EXPLORATION OF THE MITOCHONDRIA AS A POTENTIAL THERAPEUTIC TARGET IN DUCHENNE MUSCULAR DYSTROPHY

CATHERINE A. BELLISSIMO

A DISSERTATION SUBMITTED TO THE FACULTY OF GRADUATE STUDIES IN PARTIAL FULFILLMENT OF THE REQUIREMENTS FOR THE DEGREE OF DOCTOR OF PHILOSOPHY

GRADUATE PROGRAM IN KINESIOLOGY AND HEALTH SCIENCES
YORK UNIVERSITY
TORONTO, ONTARIO

April 2023

Abstract

Duchenne muscular dystrophy (DMD) is a fatal muscle wasting condition resulting from the loss of the structural protein dystrophin. The disease is characterized by severe muscle wasting and weakness that results in early death due to cardiac and/or respiratory failure. Currently, there is no cure for DMD and current standard of care (glucocorticoid steroids) only addresses secondary pathologies, and is accompanied with a myriad of negative side effects. Previous work has established the mitochondria as a contributor to dystrophic pathology and a valid therapeutic target.

The primary focus of this thesis was to examine novel therapies that modulate metabolism in DMD, to determine if secondary pathologies, including fibrosis, atrophy, weakness and mitochondrial stress are attenuated. Additionally, we aimed consider the effects of adenylates and creatine metabolism on mitochondrial permeability transition (mtPT) in a permeabilized muscle fibre system. Our study findings reveal that ATP significantly attenuates mtPT and that both creatine and ADP should be considered in buffer composition for assessment of mtPT.

Next, using the mitochondrial-enhancing compound, Olesoxime, we examined the effect of attenuating mitochondrial stress on dystrophic pathology. Unexpectedly, improvements to mitochondrial respiration and reactive oxygen species attenuation, were creatine-dependent, indicating that creatine sensitivity was preserved by Olesoxime treatment. These improvements to bioenergetics also happened in association with markers of muscle breakdown (serum creatine kinase), and improvement in muscle function (cage hand time and recovery of diaphragm force after fatigue). Finally, short-term treatment with the novel adiponectin receptor agonist, ALY688-SR, mitigated aspects of mitochondrial stress in quadriceps, diaphragm and hippocampus, while improving markers of fibrosis and muscle atrophy in the diaphragm, and recognition memory.

Overall, this thesis indicates that attenuating mitochondrial stress in dystrophic muscle and brain improves markers of muscle function and quality, while preserving cognitive function and warrants longer term treatment protocols.

Acknowledgements

Completing this dissertation has singled handedly been the most challenging yet rewarding thing I have done so far in my life. This time has been filled with many periods of joy, excitement, self-doubt, anger, pride, and gratitude- and I wouldn't change it. This thesis would not have been possible without the support and care of many individuals in my life. First, I would like to thank my supervisor, Dr. Chris Perry, who has been a constant source of guidance, mentorship, support and many many bad dad jokes. Your excitement for science and genuine care for your students is awe inspiring and I hope to one day meet your level of passion for the work I do.

Next, I would like to thank the series of students, collaborators, and mentors I have worked with throughout my graduate degrees. To the past Perry lab members, Meg, Pat and Sof, I thank you for putting up with my dumb questions and the constant patience you showed me. I genuinely enjoyed the many $10 pitchers we shared. To the present Perry Lab, Luca, Shiv, Madi, Arsh and Shahr, I thank you from the bottom of my heart for many hours we shared during our studies and next round at OEP is on me.

I would also like to thank the many collaborators that I have been able to work with, not just at York, but at Brock, UW, McMaster, PEI and many more- this thesis would not have been completed without your help. To Drs. Tom Hawke, Irena Rebalka, Rebecca MacPherson, Jeremy Simpson and Brittany Edgett, thank you for all the mentorship, time you took responding to my countless emails and the many conversations over a beer at conferences. I truly value being around so many supportive people. To my past lab mates, Emma, Dan, Val, Ian, Eric and many more, thank you for helping me fall in love with research and stay in love with it even when my westerns wouldn't work. To Russ, thank you for challenging me to progress with my research career. You encouraged me to take a chance and find new opportunities outside of where I was comfortable.

I have to also acknowledge the many friends I have made over the years both through academia and beyond it. Thank you being a support system that kept me sane when I felt that everything in my life was changing, listening to many hours of complaining about experiments and letting me drown on about the mitochondria. There is one person in particular that took the brunt of that. Thank you for being excited about my science. To the MHRC committee, most notably Dan, Shailee, Matt, and Ashley- thanks for making my time at York something special. To Dr. Dave Hood and Dr. Rolando Ceddia, I truly appreciate you both being part of my dissertation committee and I will miss our many hallway/office chats.

Lastly, I must thank my family, both those that are still with us and those I have lost- this thesis is dedicated to you all. To Mom and Dad, I cannot express how much lucky I am to have parents so supportive for my goals. To by brother Matt, thank you for all the calls and checking up on me through the years- you are the best big brother. To the many other family members (both blood-related and not) thank you for your support and love throughout these many years, but I am glad to be done being a student.

Table of Contents

List of Tables

Chapter 2

Chapter 5

Chapter 6

List of Figures

Chapter 2

Chapter 4

Chapter 5

Chapter 6

Chapter 7

List of Supplemental Figures

Chapter 5

Chapter 6

Chapter 7

List of Abbreviations

AAV	Adeno-associated viral
ACE	Angiotensin-converting enzyme
ADP	Adenosine diphosphate
AMPK	AMP-activated protein kinase
ANT	Adenosine nucleotide translocase
APAF-	Apoptotic peptidase activating factor 1
Apn	Adiponectin
ATP	Adenosine triphosphate
BAK	BCL-2 antagonist/killer 1
BAX	BCL-2 associated X protein
BCL-2	B-cell lymphoma 2
BAK	BCL2 antagonist/killer 1
BMD	Becker muscular dystrophy
Ca^{2+}	Calcium
cCK	Cytosolic creatine kinase
CNS	Central nervous system
Cr	Creatine
CyPD	Cyclophilin D
D2A	DBA/2J wildtype mouse model
D2.*mdx*	D2.B10-DMD_{mdx}/2J mouse model
dko	Utrophin-$Dystrophin^{-/-}$ mouse model
DAMP	Danger associated molecular patterns
DMD	Duchenne muscular dystrophy
ECM	Extracellular matrix
EDL	Extensor digitorum longus
EOM	Extraocular muscles
ETC	Electron transport chain
FAP	Fibro-adipogenic progenitors
$FADH_2$	Flavin adenine dinucleotide
FDA	Food and drug administration
FVC	Forced vital capacity
GPX	Glutathione peroxidase
GR	Glutathione reductase
GSH	Reduced glutathione
GSSG	Oxidized glutathione
H^+	Proton
H_2O_2	Hydrogen peroxide
IL	Interleukin
IMM	Inner mitochondrial membrane
IMS	Inner membrane space
MCU	Mitochondrial calcium uniporter
Mg^{2+}	Magnesium
mH_2O_2	Mitochondrial hydrogen peroxide
mtCK	Mitochondrial creatine kinase
mtPT	Mitochondrial permeability transition

mtPTP	Mitochondrial permeability transition pore
NAC	N-acetyl cysteine
NADH	Nicotinamide adenine dinucleotide
NADPH	Nicotinamide adenine dinucleotide phosphate
NCLX	Sodium-calcium exchanger
NF-κβ	Nuclear factor kappa beta
NO	Nitric oxide
NOR	Novel object recognition
NOX	NADPH oxidase
$O2^{\cdot -}$	Superoxide
OMM	Outer mitochondrial membrane
OXPHOS	Oxidative phosphorylation
Δp	Proton motive force
PCr	Phosphocreatine
P_i	Inorganic phosphate
PPAR-α	proliferator activated receptor-α
RIPK3	Receptor-interacting protein kinase
RNS	Reactive nitrogen species
ROS	Reactive oxygen species
RYR	Ryanodine receptor
SERCA	Sarco/endoplasmic Ca^{2+} ATPase
SMAD	Suppressor of Mothers against Decapentaplegic
SOD	Superoxide dismutase
SR	Sarcoplasmic reticulum
TALENs	Transcription activator-like effector nucleases
TCA	Tricarboxylic acid cycle
TGF-β	Transforming growth factor-β
TLR	Toll-like receptor
VDAC	Voltage-dependent anion carrier
WT	Wildtype

Chapter 1: Introduction

Duchenne muscular dystrophy (DMD) is a debilitating and fatal condition that affects more than 800 boys and young men in Canada currently [1] and between 1 in 3,500 to 1 in 5,000 live male births [2]. DMD is the most common form of muscular dystrophy, a grouping of diseases that are characterized by muscle wasting and weakness. Symptom typically arise at approximately 2 years of age, with loss of ambulation by early teens and death by early 20s. Due to a mutation in the X-linked gene encoding the structural protein dystrophin, repeated cycles of muscle degeneration and regeneration occur until muscle is replaced with fat and collagen. Currently there is no cure for DMD, however, the development of genetic therapies is ongoing with some success in human patients.

Dystrophin, a 427kDa rod-like protein, is a critical structural protein that also maintains cytoskeleton protein arrangement in cardiac and skeletal muscle [3]. Its absence impairs the integrity of the sarcolemmal membrane, rendering it susceptible to mechanical damage during contraction. The result is tearing of the sarcolemma, resulting in an influx of extracellular calcium, Ca^{2+}, that can activate a myriad of cell death pathways [4, 5] and bring about severe inflammation. Glucocorticoid steroids are the current standard of care for patients, with onset of treatment starting between the ages of 3 and 6, often before overt functional decline [6, 7]. This treatment which targets inflammation, has significantly improved lifespan and muscle function in patients [8]. Long-term treatment with glucocorticoids is associated with a multitude of negative side effects including excessive weight gain, hypertension, osteoporosis, impaired glucose metabolism, delayed puberty, behavioural changes, and cataracts [7]. Until such time that genetic therapies are easily accessible and affordable to patients, alternative treatments warrant further examination.

Beyond the genetic mutations resulting in the loss of dystrophin, abnormal Ca^{2+} homeostasis has long been considered to contribute to DMD pathology, but the manner in which alterations in Ca^{2+} leads to skeletal muscle weakness is not well understood [9, 10]. Alterations in mitochondrial Ca^{2+} handling have been shown to precede alterations in handling in the cytosolic compartment in myotubes from *mdx* mice, a murine model of DMD. Additionally, altered metabolic markers have been observed in biopsies and serum collected from patients with muscular dystrophies as early as the 1950's- prior to the understanding of the molecular basis of the disease (1986) [11-15]. Lowered mitochondrial oxygen consumption in DMD patients was first observed in 1967, and it was later

suggested that these alterations may be a secondary contributor to muscle weakness and histopathology [16]. Despite the precise cause of mitochondrial dysfunction in DMD being a topic of debate, mitochondrial therapeutics have had gained increasing attention [4]. Furthermore, understanding how non-mitochondrial targeting drugs that alter metabolism may further support the mitochondria as a contributor to muscle weakness and atrophy in DMD.

Mitochondria are key organelles within the cell, primarily responsible for energy provision, production of reactive oxygen species (ROS) and regulation of cell death pathways through Ca^{2+} homeostasis. This triad of mitochondrial function are all highly dependent on the ability of the mitochondria to maintain membrane potential ($\Delta\psi_p$) and each function can influence each other.

Alterations in ATP production [17-20], ROS emission [21-24] and mitochondrial Ca^{2+} handling [25-27], have been identified in human DMD patients and murine models of DMD (*mdx* and D2.*mdx mice)*. Oxidative stress has long been implicated in the pathogenesis of DMD as biopsies from patients reveal elevated lipid peroxidation [28-30], protein carbonylation [31, 32] and increased levels of total glutathione [21, 32, 33]. Previous work from our lab [23] has established that mitochondria are a key source of oxidative stress during oxidative phosphorylation in the D2.*mdx* mouse model. Coinciding with the increase in ROS emission, human and animal models also experience reduced ATP production [33-36] and can contribute to activation of mitochondrial derived cell death including programmed apoptosis and inflammation-induced necrosis [37-39]. Although there has been some debate in the literature concerning the role of mitochondria in dystrophic pathology, the use of mitochondrial-targeted therapies provides an opportunity to determine the contribution of this organelle to the pathogenesis of DMD.

Chapter 2: Literature Review

2.1 Overview and Introduction to Bioenergetics

2.1.1 General overview of muscle and mitochondria

Skeletal muscle comprises 40% of adult body mass and contributes considerably to daily energy expenditure (roughly ~20 to 30% of whole body basal metabolic rate) [40, 41] while providing the ability of movement and the performance of daily activities. Additionally, skeletal muscle facilitates respiratory mechanics, maintains posture and balance, and provides protection to vital organs. Thus, alterations in skeletal muscle mass can have large implications for whole body metabolism and daily life. Diseases characterized by progressive muscle loss, termed atrophy, and weakness are associated with reduced lifespan and poor quality of life. The ultimate goal of this thesis is to provide further understanding of mitochondria as a possible contributor to muscle wasting and weakness.

The mitochondria, although commonly referred to the powerhouse of the cell, is a critical organelle responsible for energy provision, but also has roles in the emission of reactive oxygen species (ROS), a necessary signaling molecule and the activation of cell death pathways. The role these functions play in the progression of the dystrophic phenotype is still being understood. A brief overview of mitochondrial bioenergetics is provided below.

2.1.2 Oxidative phosphorylation and the provision of energy

Shown to have developed over 1 billion years ago, primitive mitochondria and eukaryotes merged, forming the precursors to the modern-day cell. As the primary site of energy provision, mitochondria account for roughly 95% of the cells adenosine triphosphate (ATP) production [42]. Housed on the inner mitochondrial membrane (IMM), the electron transport chain (ETC) utilizes reducing equivalents, nicotinamide adenine dinucleotide (NADH) and flavin adenine dinucleotide ($FADH_2$) produced from ingested nutrients, to facilitate the pumping of protons from the matrix into the intermembrane space (IMS) forming an electrochemical gradient (proton motive force; Δp). The resulting gradient provides the necessary energy to drive the final complex in the ETC, generating ATP from adenosine diphosphate (ADP) and inorganic phosphate (P_i). Disruptions to

Δp can result in impairments to ATP cycling, alter the rate of reactive oxygen species (ROS) emission or initiate cell death mechanism (apoptosis).

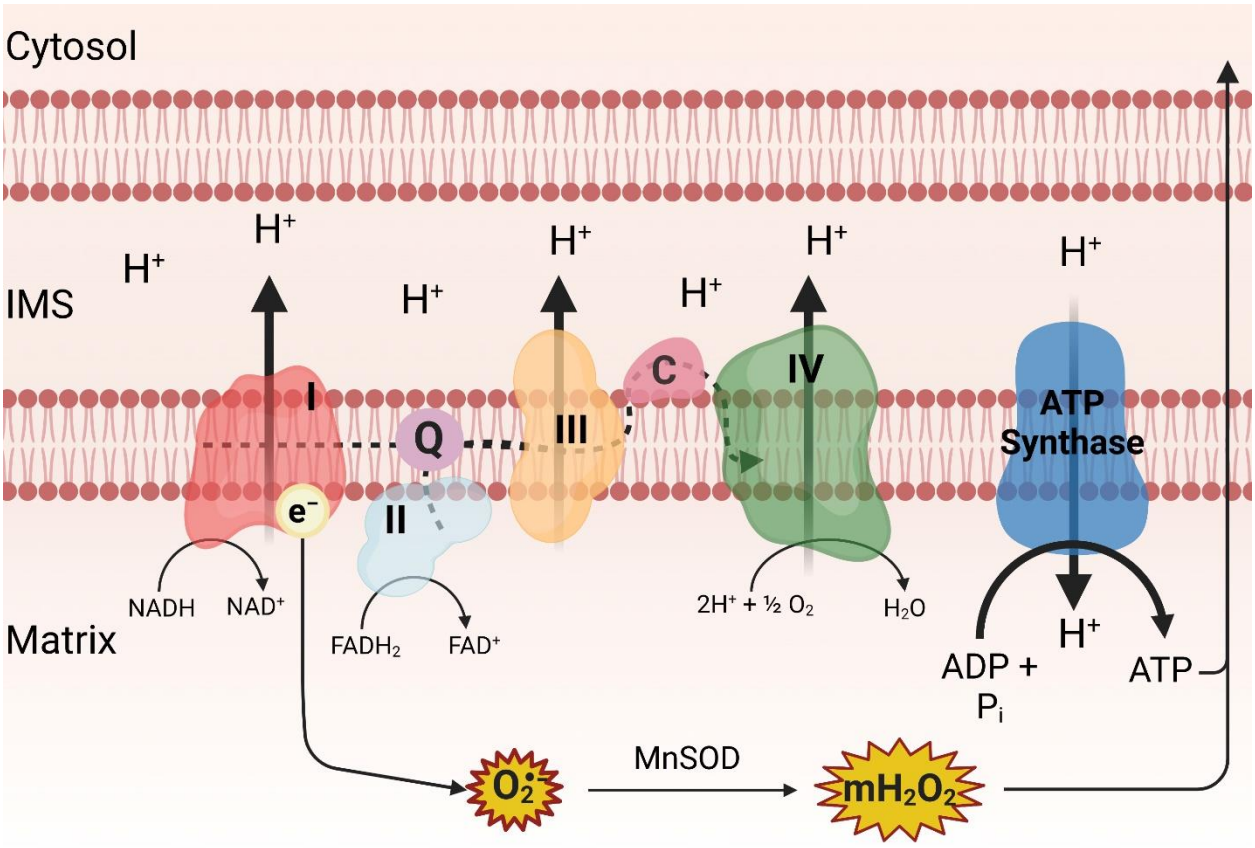

Figure 2-1: Schematic of oxidative phosphorylation and reactive oxygen species generation. The critical function of the mitochondria is to produce the cellular currency of adenosine triphosphate (ATP) from adenosine diphosphate (ADP) and inorganic phosphate (P_i). Embedded in the inner mitochondrial membrane, the electron transport chain consists of five protein complexes (I-V) and supporting electron carriers (coenzyme Q and cytochrome C) that facilitates the transfer of electrons (dashed line) through a series of redox reactions that release free energy. This free energy facilitates the pumping of protons from the mitochondrial matrix into the inner membrane space (IMS) establishing the electrochemical gradient which then powers the phosphorylation of ADP into ATP at ATP synthase (complex V). The superoxide radical ($O_2^{\bullet-}$) can be formed as a natural by product of oxidative phosphorylation which can be quickly converted into hydrogen peroxide (mH_2O_2) by manganese superoxide dismutase (MnSOD) and can then leave the mitochondria. Made with BioRender.

The movement of electrons through the ETC is facilitated by several redox reactions in proteins embedded on the IMM organized by redox potential. This mitochondrial respiratory chain is comprised of 5 complexes: complex I (NADH-UQ oxidoreductase), complex II (succinate

dehydrogenase), complex III (UQH2-cyt c oxidoreductase), complex IV (cytochrome c oxidase) and complex V (ATP synthase). The redox potential of a compound is determined by its ability to accept or donate an electron. Compounds that readily accept electrons, or are reduced, exhibit a higher redox potential than compounds that give up an electron (oxidized). The resulting organization of the ETC (Figure 2-1) allows electrons obtained from NADH at complex I, or $FADH_2$ at complex II to be transferred down the chain, facilitating pumping of protons from the negatively charged matrix across the IMM at complex I, III and IV into the IMS. The resulting movement of protons into the IMS establishes Δp sufficient enough to push protons back into the matrix through Complex V (ATP synthase), synthesizing ATP from ADP and P_i [42]. This coupling of oxidation of reducing equivalents and phosphorylation of ADP is known as oxidative phosphorylation and is a key focus of study when ATP becomes limited during disease.

There are two forms of energy transfer systems in the mitochondria that are key in maintaining cellular energy homeostasis (Figure 2-2). First, the creatine-dependent system, accounts for roughly 80% of energy transfer in the cell [43, 44] and utilizes a series of highly organized enzymes and protein channels to facilitate the transfer of P_i, from ATP to creatine (Cr) generating phosphocreatine (PCr), that can exit the mitochondria at a rate ~7x faster than ATP [45]. This process is facilitated by mitochondrial creatine kinase (mtCK), a mitochondrial specific isoform of creatine kinase that catalyzes the reversible transfer of P_i from ATP to Cr. mtCK is located in the IMS, bound to the phospholipid, cardiolipin, on the IMM and the voltage-dependent anion carrier (VDAC) on the OMM. Working in conjunction with the adenine nucleotide translocase (ANT) on the IMM, a functional substrate channel is formed allowing for efficient transport of PCr out of the mitochondria and Cr in [46-48]. Simply, ATP generated in the matrix is shuttled into the IMS through ANT, where mtCK facilitates the transfer of P_i onto Cr generating PCr. PCr then exits the mitochondria through VDAC where it can interact with cytosolic forms of CK (cCK). cCK then transfer the P_i from PCr onto ADP, quickly forming ATP which can be utilized by the working muscle [49]. The resultant Cr can then re-enter the mitochondria at a rate ~2000x faster than ADP [45] for rephosphorylation. This allows for ADP formed in the IMS to be recycled back into the matrix for ATP synthesis very swiftly. The remainder of energy transfer in the cell is dependent on ADP and ATP's ability to freely diffuse through ANT and VDAC, known as the creatine-independent pathway.

The creatine-dependent energy pathway illustrates a highly compartmentalized transfer system that overcomes diffusion limitations on substrates. In the presence of Cr, the concentration of ADP that elicits half the maximal activity of mtCK, known as K_m, is significantly reduced [50]. Interestingly, this appears to be in a fibre type specific manner, whereby cardiac and slow twitch muscle fibres exhibit this sensitivity to Cr, while fast twitch muscle shows limited reductions in K_m with Cr [51]. Despite this highly organized system, mtCK is highly susceptible to oxidative damage which has major implications for conditions characterized by oxidative stress, such as DMD [47].

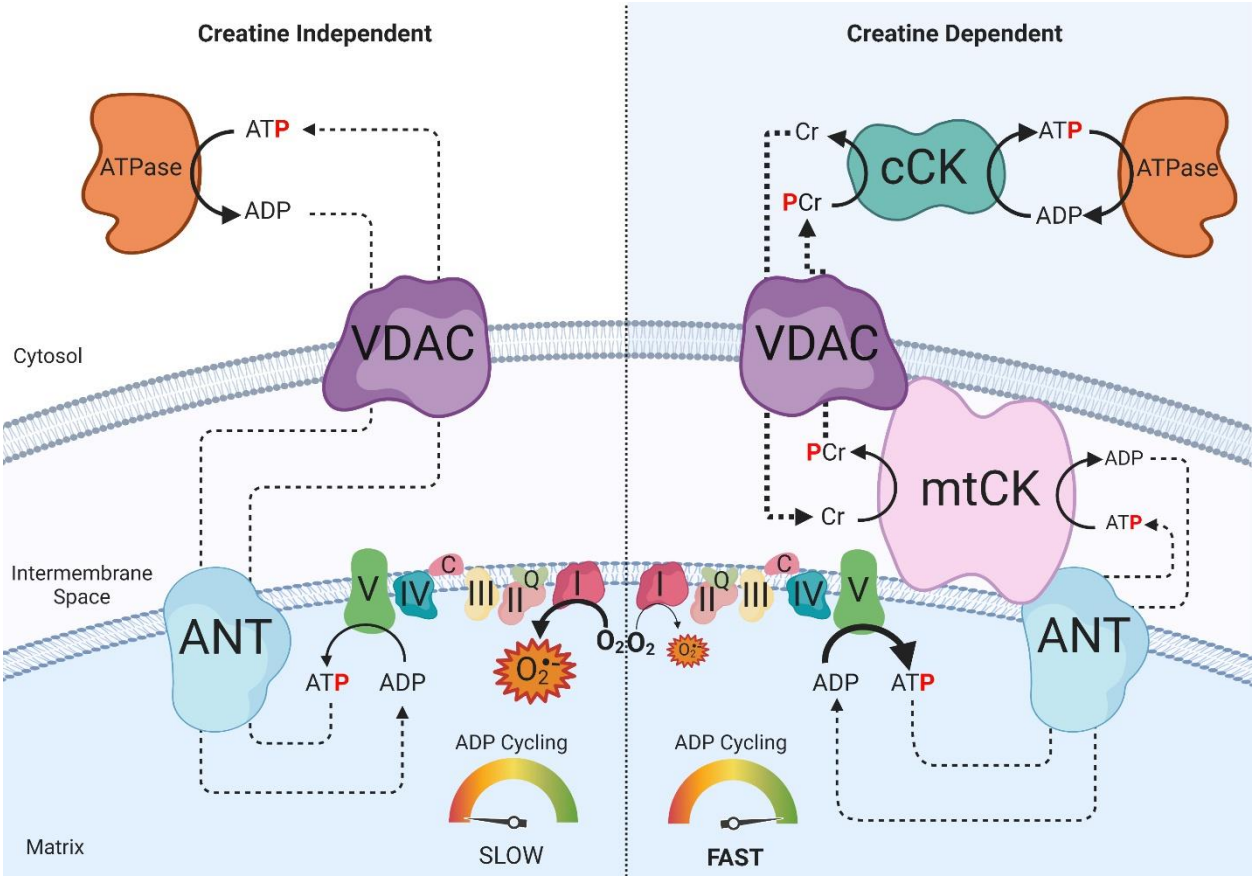

Figure 2-2: Schematic representation of creatine dependent and independent control of oxidative phosphorylation and mH_2O_2. Creatine independent phosphate shuttling between mitochondrial and cytoplasmic compartments (left) occurs via ADP/ATP cycling across the voltage-dependent anion carrier (VDAC) on the outer mitochondria membrane and adenosine nucleotide translocase (ANT) on the inner membrane. Creatine dependent phosphate shuttling (right) was facilitated by mitochondrial creatine kinase (mtCK) whereby the transfer of phosphate from ATP to Cr in the intermembrane space produces phosphocreatine (PCr) and ADP. PCr is then exported through VDAC into the cytosol and ADP is shuttled back into the matrix via ANT. The relatively faster diffusion kinetics and higher cellular concentrations of PCr/Cr vs ATP/ADP combined with a reduction of diffusion distances for the latter allow for increased energy turnover. Electrons may slip and interact with nearby oxygen forming a superoxide radical ($O_2^{\bullet-}$). The relative size between the creatine-independent (left) and -dependent (right) refers to the increased production of superoxide in the absence of creatine. C, cytochrome C; Q, coenzyme Q. Figure based on discoveries reported in References [43-46, 52-54]. Figure was created with BioRender.com.

2.1.3 Reactive oxygen species and oxidative stress

Reactive oxygen species (ROS) are a natural by-product of OXPHOS whereby electrons may slip off at several sites in the ETC prior to complex IV. After slippage, electrons may interact with oxygen forming the oxidant, superoxide ($O_2^{\bullet-}$). During state III respiration (when ADP is present in the matrix), the concentration of $O_2^{\bullet-}$ is minimal as electron are efficiently transferred down the ETC to CIV, where water is formed. However, when ADP or P_i are absent and reducing equivalents still present (termed state II), ATP production is halted, Δp becomes elevated resulting in the premature slippage of electrons and formation of $O_2^{\bullet-}$ being favoured [55, 56]. Multiple sites of $O_2^{\bullet-}$ formation have been identified across the matrix, IMM [56-58] and OMM [59], can independently contribute to oxidant formation and disease pathology.

$O_2^{\bullet-}$, despite being highly reactive, has an incredibly short half life and is impermeable to lipid membranes [60, 61], thus restricting its location and ability to interact with nearby proteins, lipids, and DNA. Within the mitochondria, $O_2^{\bullet-}$ is converted into hydrogen peroxide (H_2O_2), by manganese superoxide dismutase (MnSOD) which can then be converted into water via catalase. H_2O_2 can also leave the mitochondria and is typically quenched with the cellular antioxidant systems, glutathione and thioredoxin [62]. Under healthy conditions. H_2O_2 can be readily scavenged mitigating any potential damage, but recent evidence has suggested that H_2O_2 is a necessary cellular signal and may be required for the activation of regenerative processes [63, 64]. Additionally, H_2O_2 has also been associated with in the activation of adaptive mechanism such as increased antioxidant content [65]. Under pathological conditions, H_2O_2 emission can become elevated and may not longer be matched by antioxidant systems, leaving cells vulnerable to oxidative stress. Oxidative stress has been implicated in the activation of a number of pathways including programmed cell death (apoptosis) and endoplasmic reticulum stress [57]. Within the mitochondria specifically, mitochondrial derived ROS can contribute to cell death pathways via the triggering of mitochondrial permeability transition (mtPT) [66] described in the following section.

Similar to respiration, creatine also plays a role in mitigating ROS emission. As creatine improves ADP cycling resulting in elevation in matrix [ADP] and maintenance of a low membrane potential, the likelihood of electron slippage becomes reduced [43, 44, 67]. Interestingly, this appears to be substrate specific, whereby creatine enhances the ability of ADP to attenuate complex-I reverse

flow derived ROS [53]. Lastly, mtCK is highly susceptible to oxidative damage [68, 69] which can create a viscous cycle of impaired ADP cycling, and increased emission of mitochondrial oxidants and further damage to mtCK.

2.1.4 Mitochondrial permeability transition (mtPT) and the initiation of apoptosis

Ca^{2+} ions in skeletal muscle govern many physiological processes such as excitation-contraction [70] and operate as key second messengers [71]. Elevations of cytosolic Ca^{2+} are known to activate Ca^{2+} dependent proteases known as calpains and can trigger programmed cell death known as, apoptosis [72-74]. As such maintaining cytosolic Ca^{2+} concentrations are critical. Despite the sarcoplasmic reticulum being the primary site of Ca^{2+} storage, mitochondria act as a Ca^{2+} sink and participate in Ca^{2+} homeostasis [38].

During state III respiration, the negatively charged matrix drives the uptake of Ca^{2+} from the cytosol through the mitochondrial calcium uniporter (MCU) located on the OMM [39]. To prevent overaccumulation of matrix Ca^{2+}, the Na^{+}-Ca^{2+} exchanger (NCLX) on the IMM moves Ca^{2+} out while drawing sodium (Na^{+}) in [75]. However, when cytosolic Ca^{2+} becomes elevated, Ca^{2+} efflux can no longer match the increased Ca^{2+} influx and the mitochondria can become overloaded [75]. This results in the swelling of the organelle [76] which is a common feature of dysfunctional mitochondria and can result in subsequent activation of the mitochondrial-derived cell death pathways and the triggering mitochondrial permeability transition (mtPT) [20, 22, 23, 77-79].

Mitochondria can participate in two cell death mechanisms: the programmed, apoptotic pathway, and the un-programmed, necrosis. During times of stress, matrix Ca^{2+} becomes elevated, upsetting membrane potential and triggering of the mitochondrial permeability transition pore (mtPTP) opening [80, 81]. This results in the typically impermeable IMM, to allow the free movement of molecules less than 1.5kDA in size [82, 83] across the IMM and into the matrix [84-86]. This increase in permeability leads to rises in osmotic pressure and swelling, resulting in the unfolding of the cristae which prevents the IMM from rupturing, but ultimately causes the OMM to break.

Following this swelling, cytochrome c, a key component of the ETC that reside in the IMS, can be released into the cytosol (as depicted in Figure 2-3). This release results in the cleavage of apoptotic cell death signals, capase-9 and -3. Additionally, uncoupling of OXPHOS occurs as the IMM becomes completely permeable to protons [82]. Unless early mediation of mtPTP opening is

initiated, irreversible damage to the cell and apoptosis can occur. It is worthy to note that the concentration of Ca^{2+} required to elicit mtPTP opening varies *in vivo* and can be altered by other divalent captions, such as magnesium (Mg^{2+}), as they compete for similar binding sites as Ca^{2+} [38].

Despite the constituents of the mtPTP being debated, it is well accepted that cyclophilin-D (CyPD) remains a critical component of this pore. ATP synthase (Complex V) has also been identified as a possible component of the mtPTP. When Ca^{2+} replaces Mg^{2+} in the binding of ATP, the β-subunit of ATP synthase undergoes a conformational change of and can participate in mtPTP formation [87-89], Although Ca^{2+} is heavily implicated in mtPT, other several stressors can increase the probability of pore formation. Elevations in complex I-derived ROS can contribute to mtPT and may be prevented with complex I inhibitors such as rotenone [90]. Similarly, oxidation of pyridine nucleotides (NADH & NADPH) has been observed to promote mtPTP opening and can be mitigated using reducing agents and reductions of glutathione [66]. Lastly, changes to both matrix pH and P_i can induce mtPT [81, 91], highlighting that induction of mtPT may not be attributed to one stressor alone.

2.1.4.1 Modeling in vivo parameters during in vitro assessments of mitochondrial permeability transition pore: a need for methodological advancement?

Previous quantification of mtPT often relied on indirect measures such as quantifying mitochondrial swelling and activation of downstream apoptotic proteins such as capsase-3 and -9. While these measures are somewhat useful, they do not directly assess if mtPT has been initiated. More direct measures of mtPT often employee *in vitro* fluorescent detection of mitochondrial Ca^{2+} uptake after a single bolus or multiple small titrations of Ca^{2+} and the subsequent release through mtPTP opening. While this direct methodology provides an indication of mtPTP opening, it is susceptible to a number of limitations. Firstly, the model selection (i.e., the use of isolated mitochondria or permeabilize tissues) may alter interpretation, as different models have different affinities for metabolites. Additionally, some models retain extra-mitochondrial enzymes that may alter metabolite concentrations and equilibriums. For example, permeabilized muscle fibre bundles retain ATP hydrolyzing proteins [50] compared to isolated mitochondria, thereby affecting the equilibrium of ADP to ATP. As this equilibrium may alter membrane potential, the initiation of mtPT may also be influenced.

In isolated mitochondria from murine heart, mPTP opening is triggered at micromolar concentrations of Ca^{2+}, but partially attenuated by ADP and more firmly by ATP [92]. To directly assess the effect of ADP on mtPT, buffers was supplemented with hexokinase and 2-deoxyglucose, forming an ADP clamp, rendering [ADP] constant. In permeabilized tissues, ADP and ATP become equilibrated with each other as mitochondrially derived ATP can be hydrolyzed, which does not occur in isolated mitochondria. Despite this, it is currently unknown if adenylates attenuate mtPT in a permeabilized muscle fibre system as they do in isolated mitochondria.

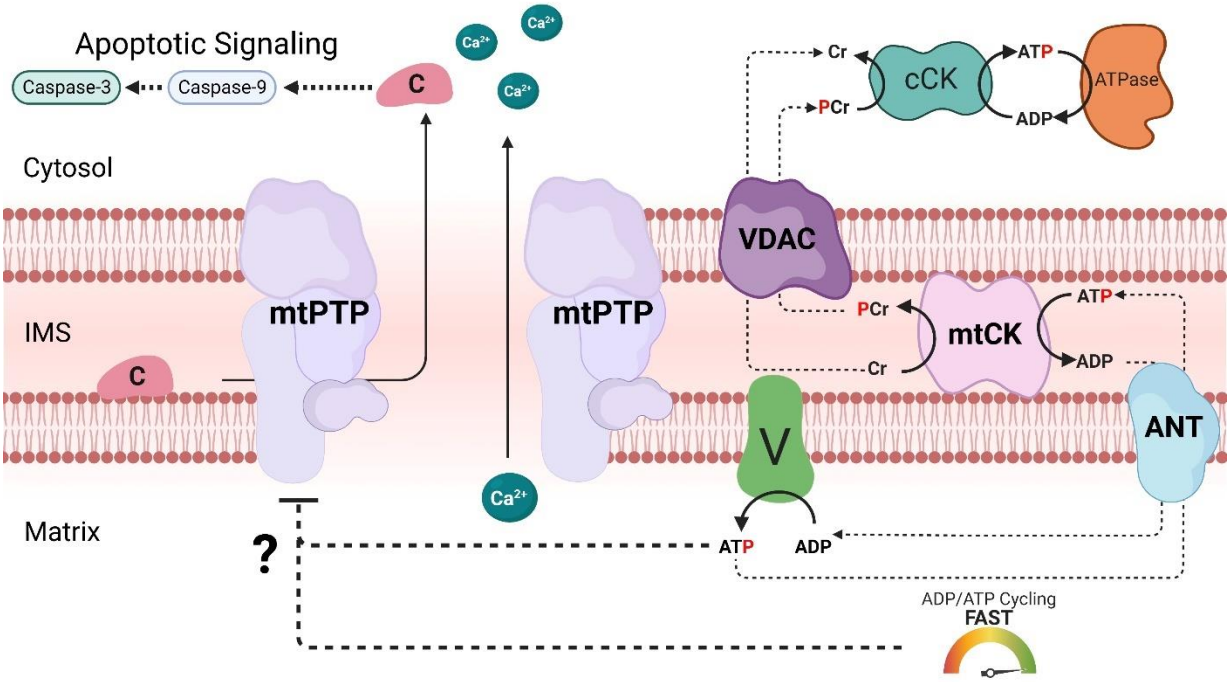

Figure 2-3: Schematic of mitochondrial permeability transition (mtPT) regulation in permeabilized skeletal muscle fibres. Triggering of the mitochondrial permeability transition pore (mtPTP) opening facilitates the release of calcium and cytochrome C from the inner membrane space (IMS), resulting in the activation of apoptotic signaling. The relative shape of the pore is reflective of potential constituents of the channel. Pore opening in permeabilize tissues may be regulated by adenylate concentration (ADP and ATP) and faster relative cycling facilated by the creatine-dependent energy transfer (depicted on the right). C, cytochrome C; mtPTP mitochondrial permeability transition pore; VDAC, voltage dependent anion carrier; ANT, adenosine nucleotide translocase; mtCK, mitochondrial creatine kinase; cCK, cytosolic creatine kinase. Figure was created with BioRender.com.

Measurements of mtPT are often made in the absence of creatine, which as described in *section 2.1.2*, accelerates ADP cycling (allowing membrane potential to remain low) by overcoming the diffusion limitation of ADP and ATP, facilitated by mtCK. While mtCK is not directly thought to be a component of mtPTP [45], proteolipid complexes of mtCK and ANT (a known component of the mtPTP), exhibit direct protective effects on mtPT [93]. This effect is thought to be attributed to the enzymatic activity of mtCK and its localization in mitochondrial complexes [94]. When present, mtCK is able to maintain high matrix [ADP] that attenuates mtPTP opening. However, these experiments were performed in isolated mitochondria, so it is unknown if mtCK protective effect on mtPT, especially in the presence of mtCK substrates, extends to permeabilized muscle fibres.

2.1.4.2 Mitochondrial initiation of apoptosis

Apoptosis commonly occurs in development and is critical in tissue homeostasis and adaptations to cellular stressors [95, 96]. In development, apoptosis is used heavily in the formation of limbs and the neural tube (reviewed in [97]). In highly proliferative tissues, such as epithelial cells of the gastrointestinal system, the role of apoptosis is integral, yet in post-mitotic tissue such as skeletal muscle, its role is less clear. Despite this uncertainty, there are two pathways in which apoptosis is activated. First, the extrinsic pathway that facilitated by the binding of a ligand to a cell membrane bound death receptors can activate down stream apoptotic events. Second, the mitochondria can activate apoptosis through an intrinsic pathway through the release of pro-apoptotic factors, known as caspases. Given the relation to mitochondria, the intrinsic pathway of apoptosis will be the focus of this review.

Caspases are a family of cysteine proteases, responsible for cleaving cellular substrates and dismantling cellular components and are known regulators of apoptosis. They are also essential in the formation of membrane blebs and apoptotic bodies that carrying these substrates and components for removal [98, 99]. Caspases are separated into two categories, initiator (caspase-8, -9 and -10) and executioner (caspase-6, -3, -7). Upon an external (caspase-8) or intrinsic stimulus (caspase-9), the initiator caspases will cleave their downstream executioner which then induces apoptosis.

The anti-apoptotic protein B-cell lymphoma 2 (BCL-2) is situated on the OMM and is a regulator of apoptosis. BCL-2 prevents activation of apoptosis through its ability to heterodimerize with pro-apoptotic proteins BCL-2 associated X protein (BAX) [100] and through direct interactions with BCL-2 antagonist/killer 1 (BAK) [101]. Upon a cellular stressor, BCL-2 becomes inactivated resulting in BAX and BAK promoting the permeabilization of the OMM. This allows for the release of cytochrome c from the intermembrane space allowing for the binding to Apoptotic Peptidase Activating Factor 1 (APAF-1) forming the apoptosome [102-105]. These apoptosomes then cleave the pro-caspase-9 rendering it functional and allows for further cleavage of pro-caspase-3 into caspase-3. Caspase-3 initiates chromatin condensation, DNA fragmentation and degradation of cytoskeleton proteins [106]. To avoid contact and damage to neighbour cells, the apoptotic cell shrinks and the membrane blebs which can be removed by phagocytic cells, such as macrophages [107]. Interestingly, blebbing is thought to be dependent on actin-myosin ATPase activity and muscle contraction [108], which may implicate changes to apoptosis with declines in muscle activity.

2.2 Duchenne muscular dystrophy

2.2.1 Molecular genetics of Duchenne muscular dystrophy (DMD)

Duchenne muscular dystrophy was first described in the first half of the 19th century but not formally characterized until 1865 by Guillaume Benjamin Amand Duchenne with prior contributions from Charles Bell, Gaetano Conte, L. Gioja, Richard Partridge, Edward Meryon and William Little across 1830-1851 (reviewed in [109]). The genetic nature of DMD was later revealed in the 1980's with seminal work performed by Lou Kunkel's laboratory including Eric Hoffman, whose work identified the protein product of the DMD gene and the first murine model of DMD [3, 110, 111]. It was with these discoveries that all work in DMD has been and will be possible.

DMD is result of a mutation to the dystrophin gene resulting in the lack of the functional protein dystrophin (see Figure 2-4). The dystrophin gene is located at Xp21.2 and contains 79 exons [110] making it the largest known human gene, which creates some difficulty for genetic editing [112]. The majority of patient present with a deletion or duplication mutation which together account for over two thirds of all mutations leading to DMD and the milder Becker muscular dystrophy (BMD) [113-115]. Within Canada from 2000-2009, most mutations involved exons 45 to 53, while

duplications tended to involved exons 2, 2-7, 2-17, 3-7, 8-11, 10, 10-11, and 12 [116]. In terms of inheritance of the mutation, two thirds of patients inherit the mutation from their mother who often unknowingly carriers. The remainder of patients are believed have a *de novo* mutation [117, 118] and thus genetic counseling and screening alone may not be effective in eliminating DMD.

Although incredible progress has been made in understanding the location and type of mutations experienced by DMD patients, a major problem still arises. The large size of the dystrophin gene and thus the cDNA that is utilized in viral vectors makes it difficult to transfect [119]. Alternative approaches such as the "micro-dystrophin" in adeno-associated viral (AAV) vectors and exon skipping using anti-sense oligonucleotides to induce alternative splicing that bypass mutated exons have been utilized and will be further discussed in *section 2.7.2 Emerging genetic therapies*.

2.2.2 In-vivo models of DMD

Preclinical models of DMD are critical for the understanding underlying mechanism of pathology and the development of novel therapies. *In vitro* models of DMD such as patient derived myoblasts and induced pluripotent stem cells are useful for assessing muscle specific improvements after genetic editing but do not provide necessary information about systemic responses and long-term outcomes. As such multiple *in-vivo* models of DMD have been identified or generated, but the degree at which these models recapitulate the human DMD phenotype varies, making it difficult to ascertain if treatments will have similar benefits in human patients. Zebrafish models of DMD are useful for high-throughput drug screening but have limited translatability to human physiology [120, 121]. Canine models of DMD offer a more closely mimetic phenotype to human patients but possess a considerable variation in phenotype and due to size have a much larger associated cost [122-124]. As a result, rodent models of DMD are the most widely used pre-clinical model, but also have several limitations to consider.

2.2.2.1 C57Bl/10-mdx mice

Discovered 1984, the *mdx* mouse arose due to spontaneous x-linked mutation arising in a C57Bl/10 reference inbred line by Bulfield et al [125]. These animals possessed elevated plasma levels of muscle creatine kinase, a clinical marker of muscle breakdown, and histological characteristics (variation in fibre size, proliferation of sarcolemmal nuclei, and infiltration by phagocytes and connective tissue cell) consistent with DMD patients [125]. Unlike their human counterparts

however, *mdx* mice show much milder clinical symptoms in limb muscles and with limited effect on lifespan (~20-25% reduction [125-127]). Also absent in DMD patients, *mdx* exhibit a phase of mass muscle fibre degeneration at 3-4 weeks of age [128-130], that is followed by compensatory muscle regeneration which outpaces the degeneration [131-134]. *Mdx* mice also exhibit compensatory utrophin upregulation that likely contributes to the milder phenotype [135]. Severe dystrophic pathology is not exhibited in *mdx* mice until approximately 15 months of age [127, 136, 137], which has resulted in the development of other murine models. Despite the limitations with this model, it is still the most used model of DMD today.

2.2.2.2 mdx/utr$^{-/-}$ mice (dko)

Utrophin, the structural homologue of dystrophin, is expressed at the neuromuscular junction in healthy muscle [138-140], with a preference to oxidative fibres. As mentioned previously, the milder phenotype observed in the *mdx* model may be attributed in part to an upregulation of utrophin. As such, to better recapitulate the human phenotype, utrophin-null (utr$^{-/-}$) mice were bred with *mdx* mice leading to *dko* model. Despite *dko* mice not being an exact genocopy of the human disease, the deficiency of both utrophin and dystrophin better resembles the phenotype seen in DMD patients, including degeneration of limb and respiratory muscles, early-onset kyphosis and premature death [141].

2.2.2.3 D2.*mdx mice*

During recent years, the D2.*mdx* mouse model has become increasingly popular for understanding dystrophic pathology. The cross breeding of *mdx* mice onto the DBA/2J background, resulted in a closer phenocopy to DMD, including extensive degeneration and fibrosis in limb and respiratory muscles at early ages [142-144], which are absent in young *mdx* mice. This is a result of a polymorphism in the latent transforming growth factor β (LTBP) 4 gene which modifies activity of transforming growth factor (TGF)-β signaling and is associated with increased suppressor of Mothers against Decapentaplegic (SMAD) signaling and fibrosis [142]. Additionally, there is a dysfunction in the *Anxa6* gene, which impairs satellite cell self-renewal ability, yielding impairments in muscles regeneration [142, 145, 146], which in *mdx* mice seemed to be enhanced leading to improved regeneration in this mode. In spite of limited time course studies having been

performed [147] in the D2.*mdx* model to understand the timing of disease progression, interventional studies in this model have already begun [148-150].

2.2.2.4 Limitation of murine models

Despite the popularity of murine models for the study of DMD and the progression made in genetic editing with them, there are still several limitations associated with these models that may make them inappropriate. Firstly, anatomical, and physiological differences between humans and mice, may limit the models from reflecting disease progression in humans. As mentioned previously, *mdx* mice show a much milder phenotype compared to human counterparts and do not show severe myopathy until 15 months of age [127, 136, 137]. Similarly, most murine models retain the ability to ambulate [136, 137, 143, 145, 147], while humans typically are wheelchair dependent by age 10-14 [151, 152]. This simple fact makes it difficult to assess if therapeutics delay loss of ambulation which is a critical milestone in the progression of DMD pathology. Additionally, there are biomechanical differences between mice and human patients. Mice are non-cursorial (specifically adapted to run), employing more flexed hip and knee postures compared to humans [153, 154]. Examination of muscle fibre length changes (fibre excursions) in humans and mice, showed that mice hindlimb muscles have smaller fibre length changes compared to human lower limb muscles during walking [155]. Given that active muscle lengthening contributes to muscle damage observed in DMD [156, 157], humans may be more predisposed to contraction-induced damaged than mice.

There are also species considerations when examining the ability of skeletal muscle to regenerate. In *mdx* mice, specifically limb muscle, a phase of mass degeneration (3-6 weeks of age) [128-130] is followed by a period of compensation wherein muscle often becomes hypertrophic [131, 133, 158, 159], which then is followed by a plateau phase until 15 months of age [127, 136, 137]. During this period of compensation, skeletal muscle regeneration can exceed degeneration, likely due to an increase in proliferation and commitment of satellite cells compared to wildtype controls [160]. In human patients however, muscle regeneration is only elevated in the first months of life [161] and is not active in later ages [160, 162-164], thus muscle regeneration is limited in human DMD patients. Other murine models of DMD (*dko,* D2.*mdx),* display impairments in muscle regeneration [145, 165, 166] that present as earlier as 5-7 weeks but still exceed the impaired in regeneration observed in humans. Lastly, the overall size of mice has made it difficult for general

experimentation, such as tissue constraint and blood draw limitations [167]. As such, rat models of DMD have recently been established.

2.2.2.5 Rat mdx model

Laboratory rats have historically been a useful species for the development of therapeutics and the evaluation of pharmacological effects and toxicity. Compared to mice, their larger body size, ability to facilitate adequate blood and tissue collections and better assessment of behaviour [168], make them ideal for pharmaceutical intervention studies. However, their usefulness in the understanding of genetic diseases had been limited. In more recent years, genetic editing techniques such as CRISPR/Cas9 and transcription activator-like effector nucleases (TALENs) have been employed in rats [169-172] resulting in the generation to rat models of DMD, henceforth known as *Dmd* rat. Recently, Nakamura et al utilized CRISPR/Cas9 systems to target exon 3 and exon 16 to generate their model [173], while Larcher et al, utilized transcription activator-like effector nucleases (TALENs) to target exon 23 [174]. Collectively, both groups demonstrated generation of a DMD rat model was possible and that the *Dmd* rat has a more severe phenotype compared to the *mdx* murine model. *Dmd* rats also exhibit impaired ambulation and cardiac function that is absent in young to middle age *mdx* mice [173-175]. The *Dmd* rat offers a more cost-efficient model than canine and porcine models, while better recapitulating the human phenotype compared to murine models.

2.3 Clinical outcomes measured in DMD

2.3.1 Skeletal muscle weakness: the impact on ambulation

As noted above, the primary deficiency in DMD is the absence of the structural protein dystrophin, that serves to stabilize the sarcolemma membrane during contraction [176]. In its absence, the plasma membrane becomes highly unstable causing damage and an influx of extracellular Ca^{2+}. The damage and subsequent activation of calcium sensitive protease pathways, leads to repeated cycles of degeneration followed by regeneration until muscle specific stem cells, known as satellite cells, become exhausted [133, 134, 156, 177]. Following this exhaustion, non-contractive connective and adipose tissue replaces muscle leading to impairments in force generation as observed primarily in skeletal (limb and respiratory) and cardiac muscle [176]. Interestingly, it was impairments in ambulation that first garnered the attention of Dr. Edward Meryon, an English

physician who document DMD prior to Duchenne himself. He noted that patients experienced difficulties in walking from an early age that progressed into inabilities to climb stairs and finally being unable to walk at all [178]. Moving forward, clinicians have separated ambulatory decline into 5 phases[179].

At birth, DMD boys are clinically asymptomatic and are termed to be in the pre-symptomatic phase (birth to 2 years old). Late in this phase, parents typically report a delay in motor milestones, namely standing and walking, with most DMD boys walking by 18 months of age. In the Early Ambulatory phase (ages 2-6 years old), patients are capable of walking, but suffer from frequent falls. When rising from supine or sitting, patients utilize Gowers' maneuver (also known as Gowers' sign), to assume an upright position. To rise from the floor, a child assumes the hands-and-knees position and then climbs to standing by "walking" his hands progressively up his shins, knees, and thighs until upright. Additionally, clinicians characterize this phase by having the ability to perform both a 10 metre walk test and to rise from supine [180]. In the next phase, Late Ambulatory (ages 6-11 years old), the speed at which loss of function is exhibited varies greatly among boys with DMD, but difficulties become progressive with age. Here, muscle strength declines, leading to inabilities to rise from the floor, with reliance on long leg braces for ambulation. By age of 11-13, boys with DMD rely on a wheelchair and enter the Early Non-Ambulatory phase.

The Early Non-Ambulatory phase (ages 10-15 years old) is characterized by progressive muscle weakness, atrophy, and the development of contractures in lower and upper limbs. At this point scoliosis becomes apparent and impacts respiratory muscle strength and function, due to the positioning of the spine. Finally patients progress into the Late Non-Ambulatory (>15 years old), where they exhibit sever upper limb weakness combined with respiratory difficulty (including declining coughing abilities) and cardiomyopathy. Often during this phase patients succumb to respiratory failure often precipitated by respiratory infection or from cardiac failure (secondary to progressive cardiomyopathy).

2.3.2 Declines in respiratory function

The most compromised muscle in DMD patients and murine models is the diaphragm. As the main respiratory pump, diaphragm failure represents one of the leading causes of death in patients [181-183]. Early signs of respiratory insufficiency in DMD patients are usually evident during sleep, as

a result of hyperventilation, leading to a variety of sleep disturbances [184, 185] and precede ventilatory failure during wakefulness. Around the age of 10 years old (during Early Non-Ambulatory phase), reduction in critical ventilatory measures such as forced vital capacity (FVC) and tidal volume become evident [186, 187], leading to reduced wall and lung compliance, hypoventilation, hypercapnia (increase in partial pressure of carbon dioxide), and hypoxemia [188-190]. Simply, structural damage to the diaphragm leads to reduced transdiaphragmatic pressure and reduced respiratory functions. As a result, strategies such as nocturnal home ventilation (typically instigated in the Late Ambulatory phase) and inspiratory muscle training (initiated during Late Ambulatory to Early Non-Ambulatory phases) have been used to varying degrees of success [190, 191]. Unfortunately, neither treatment can improve respiratory function at later ages of disease progression and patients ultimately succumb to their disease, but strides have been made in delaying this decline.

2.3.3 Development of cardiomyopathy

As respiratory failure in DMD patients has become better managed [191, 192], cardiac insufficiencies became more pronounced in patients, especially at later ages, and now are one of the major causes of death [193]. Cardiomyopathy develops in almost all DMD patients by the age of 18 years old with ECG abnormalities (defined as shorted PQ segment and prolonged QT intervals) being detected in patients as early as 6 years of age (26% of all DMD patients). As these patients age, the incidence of ECG abnormalities increases to roughly 61.5%. The observed cardiomyopathy is characterized by the thinning of the left ventricular wall, leading to progressive decline in ejection fraction [194]. At this point, roughly 26% of patients aged 10 to 14 years old and 45% of patients 14 to 18 years old are diagnosed with dilated cardiomyopathy [195]. Prophylactic treatment with angiotensin-converting enzyme (ACE) inhibitors has had promising result in clinical trials, increasing survival to 92.9% compared to the survival rate of 65.6% in patients who began ACE inhibitors later [196]. Interestingly, current standards of care for DMD, glucocorticoid steroids, do not display the same beneficial effects in cardiac muscle that is observed in limb and respiratory muscles [197]. In later stages of life (18+), 72% of patients will experience dilated cardiomyopathy with 60% exhibiting symptoms of heart failure [197-199]. In 40% of patients, heart failure will ultimately be the cause of death [200, 201].

2.3.4 Skeletal muscle atrophy

The defining characteristic of DMD is the severe muscle atrophy clearly observed in limb and respiratory muscles. Dystrophin is ubiquitously expressed by all skeletal muscle fibres, but atrophy is more predominant in specific fibre types. Human skeletal muscle consists of 3 adult fibre types when classified by myosin heavy chain expression. These fibre types include type I (oxidative), type IIA (oxidative-glycolytic) and type IIX (glycolytic). In 1985, Watkins and Cullen showed that type II fibres were preferentially affected compared to type I [202] which was later supported by others [203, 204]. Several hypotheses have been generated to explain why type I fibres are spared compared to their glycolytic counterparts. One hypothesis is that utrophin, the functional homologue to dystrophin [205], is more heavily expressed in oxidative fibres [139, 206]. Indeed in DMD patients and *mdx* mice, utrophin extends beyond the neuromuscular junction where it can stabilize the sarcolemma membrane and limit contraction induced damage [135, 207]. Utrophin upregulation has been investigated as a therapeutic intervention in DMD, either through genetic therapy [208, 209] or through calcineurin activating drugs [210].

While it is well known that the majority of DMD muscles undergo atrophy, there are select muscles that appear to undergo a paradoxical hypertrophy at early ages. In 1861, Duchenne originally described the disease as pseudo-hypertrophic muscular paralysis, as many of the boys exhibited hypertrophy of the gastrocnemius and in some reports, the vastus lateralis [211, 212]. Indeed, DMD patients exhibited larger calf circumferences than age matched healthy controls [213]. However, whether this hypertrophy was due to an increase in fibre number and size or due to an increase in non-contractile material such as fibrosis and adipose was later explored. It was established that hypertrophy in DMD is separated into two successive stages. In the first, patients exhibit true hypertrophy, involving both an increase in fibre number and size of both type I and II fibre types, which happens in young DMD patients (5-11 years old) [211]. This is followed by a pseudo-hypertrophy phase, that is a result of infiltration of inflammatory cells, adipose and collagen in the place of skeletal muscle fibres. Reasoning for this hypertrophy could be due to postural constraints, whereby boys with DMD walk on their toes due to contractures of their gastrocnemius and soleus muscle in combination with increases in passive tension of the gastrocnemius muscles [211]. As patients age and ambulation declines, muscle fibre diameter plateaus, then progressively decreases and is replaced by adipose and fibrotic tissue until death.

Additionally, there are a few muscles that are spared in DMD which may provide insight on specific mechanisms that maybe become valid therapeutic targets. Extraocular muscles (EOM) are responsible for the complex control of eye movement and are morphologically and functionally spared in DMD [211, 214]. Interestingly, these muscles are typically comprised of a unique fibre type composition (some fibres including co-expression of fast isoforms of myosin heavy chain and developmental isoforms) [215] but are suggested to be amongst the fastest to contract and the most resist to fatigue [216]. One suggested reason for this unique fibre type distribution is due to different in developmental origins, whereby limb muscle arises from the somite (blocks of paraxial mesoderm) while EOM arise from prechordal and paraxial head mesoderm [217-219]. Additionally, it has been hypothesized that EOM muscles have an enhanced ability to maintain Ca^{2+} homeostasis and to scavenge free radicals [220], which may combat the dystrophic phenotype.

2.3.5 Fibrosis

Replacement of skeletal muscle with fibrotic tissue has profound effects on muscle function and has been associated with poor survival in several conditions including DMD [221-223]. Fibrosis is characterized by the excessive deposition of extracellular matrix (ECM) proteins (such as collagen and fibronectin) that can impair tissue function. In muscle, excessive fibrosis can have detrimental effects on contraction [223-225] and has been implicated in the pathogenesis of cardiac and respiratory failure in DMD [226-229]. Fibrosis is a prominent feature of skeletal muscle in DMD patients and murine models, and the underlying mechanism have been well documented.

As ECM proteins are involved in skeletal muscle repair and development, it is likely that constant cycles of degeneration and regeneration leading to exhaustion of stem cell pools, provides the necessary queues for a pro-fibrotic environment. These queues involve growth factors and cytokines released by infiltrating immune cells which influence ECM-residing cell populations such as fibroblast and myofibroblasts [230]. One of the best known pro-fibrotic cytokines is transforming growth factor-β (TGF-β) commonly released by immune cells [231]. It has been shown TGF-β1 levels are significantly correlated with degree of pathology and clinical severity of DMD [232] and that down-regulation of TGF-β signalling is preventative for fibrosis in dystrophic models [233, 234]. The extent of fibrosis, interestingly, may limit the effectiveness of therapy, and should be a consideration on when to initiate treatment. First, replacement of muscle fibres by fibrotic tissue, results in limited available tissue for therapies to function on, which has large

implications for the timing of genetic therapies [235]. Next, fibrosis acts as a physical barrier for the access of therapeutics to the diseased regions of the muscle, specifically for hydrophilic drugs such as osphorodiamidate morpholino oligomers including the promising Eteplirsen [236, 237]. Progression of fibrosis should be a key factor on when deciding to initiate treatment especially genetic therapies.

Unfortunately, anti-fibrotic treatments that are promising in animal models have not always yielded the same results in humans. Currently, there is no effective pharmacotherapy to attenuate muscle fibrosis in DMD patient [228]. One such reasoning is the selection of murine model as described in *2.2.2 In-vivo models of DMD*. In murine models of DMD, specifically the *mdx* mouse, limb fibrosis is quite minimal until later ages, unlike in human patients that exhibit fibrosis as young as 4 years old [238]. The use of the D2.*mdx* model, which shows more extensive fibrosis may be a more suitable model for examining the anti-fibrotic therapeutics. Table 2.1 summarizes the current literature on the D2.*mdx* model and histological analysis of fibrosis, given the use of D2.*mdx* mice in this dissertation. Despite fibrosis being a main feature of the dystrophin phenotype and histology being performed, not all studies undertake quantifying the extent of fibrosis.

Table 2-1: *Progression of fibrosis (%) in various muscles of the D2.mdx model*

	Muscle						
Age (months)	Diaphragm	Tibialis Anterior	Quadriceps	Gastrocnemius	Soleus	Triceps	Heart
<1						Performed not analyzed [239]	
1-2	12-13 [23] 2 [150] 22-23† [147] 9 (Chapter 6)	9-10† [147] 1-1.5 (Chapter 6) Performed not analyzed [146]	15-17 [23] 5 [150] 25-26† [147]	20-21 [23] 18-19† [147]		Performed not analyzed [239] 20† [147]	3 [147]
3-4	32 [240] 30-31 [144] 35 [241]			10 [240] 25 [149] 19-20 [144]			Performed not analyzed [242]
5-6	32-33 [144]	4-5 [145] Performed not analyzed [146]	10-11 [145]	8-9 [145] 20-21[144]			
7-12	20-21† [147]	8-9 [145] 24-25† [147] Performed not analyzed [146]	18-19 [145]	10-11 [145] 18-19†[147]	13-14 [148]	20†[147]	
>12	30 [144]	Performed not analyzed [146]		30[144]			

†study quantified fibrosis as “unhealthy” tissue

2.4 Cellular Stressors in DMD

2.4.1 Impaired Ca^{2+} homeostasis

The lack of dystrophin in DMD causes severe membrane leading to the influx of extracellular Ca^{2+} and increased ion permeability, contributing to cytosolic Ca^{2+} overload [10, 243, 244]. Additionally, contraction-induced "micro-tears" in the plasma membrane that leads to the insertion of Ca^{2+} leak channels reinforcing a high cytosolic Ca^{2+} load [244-246]. High intracellular Ca^{2+} concentrations have cytotoxic effects that can initiate proteolytic enzymes such as calpains and caspases. Elevations in both these proteolytic enzymes have been observed in DMD and *mdx* muscle, which can contribute to the degeneration of limb and respiratory muscles and the progression of the dystrophic phenotype [4, 245-247].

Cytosolic levels of Ca^{2+} are dictated by the release of Ca^{2+} from the sarcoplasmic reticulum (SR) or from the the reuptake in the SR. Release of SR stored Ca^{2+} is facilitated by the ryanodine receptor (RYR) which physically opens to release Ca^{2+} to facilitate contraction. Reuptake of Ca^{2+} into the SR is enabled by the sarco(endo)plasmic reticulum Ca^{2+} ATPase (SERCA). Both impaired RYR and SERCA function has been document in *mdx* and D2.*mdx* mice [248, 249], including functional alterations due to oxidative damage (discussed below). Improving Ca^{2+} handling either through the overexpression of SERCA [250, 251] or through expression of the chaperone protein Hsp72 [252, 253], has attenuated the dystrophic phenotype in *mdx* mice, thus highlighting that importance of Ca^{2+} homeostasis in DMD.

The mitochondria also participate in maintaining Ca^{2+} levels. In dystrophin-deficient muscle, mitochondrial swelling due to elevations in matrix Ca^{2+} has been previously document [254]. This is thought to increase the potential for the initiation of mtPT [255] yet there have been inconsistent findings in *mdx* muscle, as discussed in our recent review [256]. Beyond the initiation of the mtPT, unregulated mitochondrial uptake of Ca^{2+} can impair oxidative phosphorylation and increase ROS formation [257] while contributing to defective mitochondrial dynamics [258]. Collectively, this indicates that the loss of dystrophin impairs Ca^{2+} homeostasis across compartments of the muscle cell.

2.4.2 Oxidative stress and sources of ROS

Despite ROS being a natural by-product of OXPHOS, in conditions where increased levels cannot be properly mitigated oxidative stress can accumulate and initiate cell death mechanisms. As described in *2.1.3 Reactive oxygen species and oxidative stress*, $O_2^{\bullet-}$ and H_2O_2 can cause irreversible damage to the cell via protein carbonylation, lipid peroxidation and DNA oxidation. In an attempt to limit irreversible damage, the muscle employs several antioxidant enzymes including superoxide dismutase (SOD), catalase (CAT), glutathione (GSH), glutathione peroxidase (GPX), glutathione reductase (GR) and thioredoxin reductase (TRX), to quench ROS or transform it into a more manageable form. Identifying the source of ROS during disease progression is essential, as conventional antioxidant treatments may not be able to access specific compartments, such as the mitochondria.

Elevated oxidative stress has been postulated to contribute to pathology in DMD since the 1970's [29] and has been supported numerous groups [29, 32, 259-264]. Biopsies from DMD patients and D2.*mdx* mice show an elevation in protein carbonylation [23, 31] and lipid peroxidation [265] which represent irreversible oxidative damage. In support, rodent models of DMD show an increase in GPX activity, levels of total GSH and antioxidant enzymes [21, 29, 266, 267], suggesting that some adaptation to quench ROS occurs during disease progression. Despite these adaptions, dystrophic muscle is more susceptible to ROS-induced damage compared to healthy controls [268]. Interestingly, treatment with the antioxidant N-acetyl cysteine (NAC) and ascorbic acid, can prevent contraction induced membrane damage in EDL from *mdx* mice [269, 270], suggesting contraction induced oxidative stress may be involved in the dystrophic phenotype. These results however do not implicate the source of ROS in DMD. One suggested source of ROS is the NADPH Oxidase (NOX), specifically NOX2, which resides on the plasma membrane [271]. In dystrophic tissue, both increased NOX expression and activity has been observed [272-274] and use of NOX inhibitors results in the improved force production and decreased Ca^{2+} influx [275]. Interestingly, treatment with global antioxidants like NAC, prevent contraction induced damage, but do not fully restore muscle function [276], suggesting some impairments still exist. In recent years, more attention has focused on the mitochondria as a source of ROS in DMD and will be discussed further in *2.5 Mitochondrial stress in DMD.*

2.4.3 The role of apoptosis and necroptosis in dystrophic pathology

As described in *section 2.1.5*, apoptosis is a form of programmed cell death that is utilized in development and tissue homeostasis [95, 96] and can be activated intrinsically via the mitochondria. Although necrosis has long be associated with myofibre death in DMD, work in the *mdx* mouse has suggested that during the acute phase of muscle degeneration, apoptosis may precede necrosis [277]. In subpopulations of regenerating fibres in 8-week-old *mdx* mice, single-strand DNA breaks, an inducer of apoptosis, have been observed [278]. The occurrence of apoptosis in skeletal muscle has also been observed in adult *mdx* mice [277, 279, 280], although it remains inconclusive if apoptosis occurs in human patients. In some reports, the presence of apoptotic cells is observed in the interstitium and not inside myofibres [281], yet others have documented the opposite where apoptosis is occurring in damaged fibres [279, 282]. Furthermore, identification of DNA fragmentation or apoptotic myonuclei, does not indicate by which pathway apoptosis has been activated. Activation of the extrinsic pathway of apoptosis involves the transmembrane receptors of the death receptor family [283]. In this pathway, Fas ligand (FasL) can induce apoptosis through its interaction with its receptor Fas, also known as CD95, and recruit caspase 8 which cleaves caspase-3 to initiate apoptosis. Increased expression of Fas was previously observed in human DMD muscle compared to controls [283, 284].

Alternatively, a genetically controlled form of necrosis known as necroptosis has been implicated in dystrophic pathology and partially overlaps with extrinsic apoptosis. TNF-α can trigger caspase-independent cell death by activating receptor interacting protein kinase-3 (RIPK3) mixed lineage kinase domain like pseudokinase (MLKL) [285]. In both *mdx* mice and DMD muscle, necroptosis is activated and may contribute more to the peak degeneration phase in *mdx* pathology [286]. Collectively, multiple forms of cell death may be initiated in DMD patients and independently contribute to the dystrophic phenotype.

2.4.4 Inflammation & necrosis

DMD is associated with a profound inflammatory cell presence that contributes to cell death in the form of necrosis. Necrosis is an energy-independent process that can induce an inflammatory response which in healthy tissue is used for clearance and repair. Necrosis evokes cellular swelling and can impair membrane integrity, resulting in the release of cytoplasmic contents, the further

recruitment of inflammatory cells such as neutrophils and macrophages and subsequent damage to neighbouring cells.

In DMD, damaged myofibers release Danger Associated Molecular Patterns (DAMPs) which serve as ligands for Toll-like receptor family (TLR), a key component of the innate immune system. This is activated through the induction of nuclear factor kappa beta (NF-κβ) pro-inflammatory pathways [287], whereby NF-κβ translocates to the nucleus and regulates the expression of pro-inflammatory cytokines including TNF-α and IL-1β. Independent of DAMPs, high concentration of ROS enhances membrane permeability through peroxidation of the plasma membrane, resulting in further exacerbation of cytosolic Ca^{2+} influx and perpetuating the necrotic signal. This results in a vicious cycle that induces further muscular necrosis and cannot be sufficiently mediated by endogenous anti-inflammatory immune cells and cytokines [287, 288].

Several immune cell types have been examined in the necrotic response in DMD including neutrophils, macrophages, eosinophils, and mast cells [288]. Neutrophils are responsible for removal of debris from the damaged myofibre and secrete necessary cytokines (TNF-α) and proteins (myeloperoxidase), that activate pro-inflammatory macrophages and aid in further recruitment of other inflammatory cells. Mast cells may further support muscle necrosis by the additional release of TNF-α [289]. In tissue, macrophages exist in a spectrum and take on specific phenotypes based on environmental queues. Pro-inflammatory signals guide macrophages to damaged myofibres, where they take on a pro-inflammatory phenotype and can boost the secretion of TNF-α and Receptor-Interacting Protein Kinase 3 (RIPK3) [290]. T regulatory cells (Treg) aid in the transition of pro-inflammatory macrophages into anti-inflammatory phenotypes, through TGF-β secretion [291].

In DMD, elevations in TGF-β are also involved in activating fibrogenic adipoprogenitor (FAP) cells that can worsen the dystrophic phenotype [292]. During the hyper-regenerative period in *mdx* mice, eosinophils are observed to be elevated which elicits IL-4 secretion. IL-4 promotes the transition of FAP into fibroblasts which may contribute to the fibrotic phenotype in DMD [293]. Although IL-4 seems to have a negative role in this context, it is important to note that IL-4 aids in myogenic differentiation [290, 294],which may have implications for muscle repair in lowered. Collectively, the innate immune system plays a large role in the necrotic response in DMD and

reductions in these cell types and cytokines have had promising results in attenuating the dystrophic phenotype [290, 293, 295-301].

2.5 Mitochondrial stress in DMD

2.5.1 Skeletal muscle mitochondrial stresses

Altered metabolic function has been observed in skeletal muscle biopsies from DMD patients since the 1950s, with further analysis showing lower mitochondrial oxygen consumption under phosphorylating conditions [11-14]. Interestingly, this was unique to DMD muscle as other forms of muscular dystrophy did not exhibit a similar defect [15]. Although the dystrophic phenotype is not caused by mitochondrial dysfunction perse, mitochondrial alterations may be a secondary contributor to muscle weakness and atrophy observed in both humans and murine models of DMD.

2.5.1.1 Attenuations oxidative phosphorylation

There are numerous reports of impaired ATP synthesis in DMD patients, either through direct measurements of ATP synthesis or indirect measures such as oxygen consumption, ETC complex activity assays, or decreased mitochondrial content [11-16, 18, 19, 36, 302]. Similar patterns are also observed in the various murine models of DMD [17, 20-27, 35, 36, 79, 258, 303-315]. However, there are still some inconsistencies within the literature concerning whether ATP concentrations and maximal mitochondrial enzyme activities are lowered in dystrophic tissue. This heterogeneity could be a result of inconsistent model use (C57Bl/10.*mdx* vs D2.*mdx*), age (young vs old) and muscle selection (oxidative vs glycolytic) [256], that may independently account for these discrepancies.

Additionally, other metabolic deficits in dystrophic muscle have been observed. This includes decreased activities of TCA cycle enzymes (succinic CoA synthetase, aconitase, malate dehydrogenase and isocitrate dehydrogenase) and glycolysis [21, 256, 301, 310], especially at later stages of disease progression. Reduced oxidation rates of glucose, pyruvate, malate, and glutamate have also been documented in DMD patients and *mdx* mice [18, 20, 21, 23, 24, 256, 301, 306, 308, 310]. This further supports an impaired ability to form ATP in dystrophic muscle, as lower quantities of reducing equivalents would be available to the ETC, combined with an impaired ability to use those equivalents.

OXPHOS is heavily affected by PCr and Cr levels which play a critical role in maintaining energy homeostasis, as described in *section 2.1.2 Oxidative phosphorylation and the provision of energy.* As previously mentioned, mtCK is extremely susceptible to modifications by oxidative stress resulting in functional impairments that could reduce energy transfer in the mitochondria [46-48]. To date, few studies have examined mtCK function in dystrophic muscle [23] but Cr supplementation has had positive effects in *mdx* mice and DMD patients [312, 316-320]. In the presence of saturating levels of Cr, oxidative muscles from *mdx* and D2.*mdx* mice exhibit reduced mitochondrial sensitivity to ADP [23, 321], indicating a potential failure in creatine-dependent energy transfer due to mtCK damage. Impairments in mtCK function also have implications for the attenuation of ROS and the activation of mtPT, thus protecting mtCK from oxidation in DMD may hold therapeutic value.

2.5.1.2 Mitochondrial reactive oxygen species emission

Despite oxidative stress being implicated in disease progression of DMD for over 40 years, the mitochondria have only recently begun to be examined as a source of ROS [21, 28-33, 266]. In an examination of basal ROS levels in the flexor digitorum brevis (FDB) fibres from *mdx* mice, the generation of ROS seems to be NOX specific [275]. However, when stimulated with osmotic shock, which occurs in dystrophic tissue, mitochondrial Ca^{2+} accumulation and mitochondrial ROS production was observed [322]. It is key to note that this study utilizes a mitochondrial-specific fluorescent probe (MitoSOX), that produces two fluorescent products, ethidium and 2-hydroxyethidium (2-OH-E+), a specific adduct of $O2^{\bullet-}$. Debate concerning if mitochondrial ROS is elevated in dystrophic muscle arose as the fluorescent spectra of these compounds overlap and when detected using confocal microscopy and is increasingly difficult to accurately measure only 2-OH-E^+ [323].

Similarly, direct measurement of mitochondrial ROS emission rates in skeletal muscle, using Amplex Red, has yielded diverging results. First, the work performed by Godin et al in the tibialis anterior from 6-week-old *mdx* mice, found no increase in H_2O_2 emission rates and a significant increase in H_2O_2 scavenging capabilities [27]. Likewise, no increase in H_2O_2 emissions in cardiac muscle from 12-week-old *mdx* mice was found [25]. However, work from our group in young D2.*mdx* mice, showed elevated H_2O_2 emission in both skeletal and cardiac muscles [22-24]. As previously mentioned, the D2.*mdx* mouse model better recapitulates the human condition

compared to the conventional *mdx* model. As such, the elevation observed in the D2.*mdx* mouse model may better recapitulate mitochondrial ROS in DMD patients and serve as a better model for therapies targeting mitochondrial ROS.

Although controversial as a mitochondrial-specific antioxidant, Idebenone, a synthetic analog to coenzyme Q10, improved cardiac and respiratory function in clinical trials in DMD patients. Idebenone may improve oxidative phosphorylation and reduce oxidative stress in these patients, as seen previously in rat and canine brain [324, 325]. Collectively, this supports the mitochondria as a contributor to dystrophic pathology through the generation of ROS and oxidative stress, and thus warrants further examination using mitochondria-specific antioxidants.

2.5.1.3 The involvement of mitochondrial permeability transition pore and apoptosis

The mtPTP can occur in response to excess Ca^{2+} stress which is a hallmark of the dystrophic phenotype [257]. Indeed, matrix Ca^{2+} influx is elevated in dystrophin-deficient muscle [255] which lead to further examination of mtPTP opening in DMD. The permeabilization of both the inner and outer mitochondrial membrane, allows for pro-apoptotic factors such as cytochrome c, to be released into the cytosol, initiating apoptosis through caspase-9 and -3 [257, 326, 327]. Although the precise components of the mtPTP are not fully resolved, there appears to be more than one combination of protein complexes [254, 328]. Nonetheless, Ca^{2+}-induced mitochondrial swelling is well known to trigger the collapse of membrane potential resulting in pore opening. The combination of impaired OXPHOS and elevated ROS emissions are thought to mediate Ca^{2+}-induced mtPTP [254, 257]. This is supported by evidence showing that depletion of adenine nucleotides (reduced OXPHOS) and presence of mitochondrial ROS, can trigger mtPTP through post-translational modifications of ANT [329, 330], however the impact of adenine nucleotides on mtPT have not been fully resolved in dystrophic muscle in permeabilized skeletal muscle fibres (see Chapter 4). However, given that dystrophic muscle exhibits impaired OXPHOS, increased ROS emission and high levels of cell death, it is likely that mtPT contributes to the dystrophic phenotype.

Interestingly, there have been inconsistent finding on whether mtPTP opening is altered in *mdx* muscle. Various studies have reported that there is increased mtPTP opening in *mdx* muscle [23, 25, 27, 79] while others report no change [22-24]. It is likely that these discrepancies may be a

result of inconsistent methodology used to assess mtPTP. Currently, no single study appears to compare multiple muscle types across multiple ages, to definitively ascertain the role of mtPT in the progression of the dystrophic phenotype. In support, pharmacological compounds known to inhibit mtPT (cyclosporin A) have improved muscle function in *mdx* mice and people with DMD, but it is likely that they exerted these effects through immunosuppression [331-334]. Interestingly, the glucocorticoid steroid, deflazacort, also increases mtPTP opening in *mdx* skeletal muscle while normalizing ATP levels to that of WT controls. Researchers attributed this to increases in content of complexes III, IV and V, with complex V being a constituent of the mtPTP. While speculative, this increase susceptibility, may result in better clearance of poor quality mitochondria [335]. Deflazacort is currently the first FDA drug approved for management of DMD in patients under the age of 2. While the majority of benefits of deflazacort are attributed to the anti-inflammatory properties, it is plausible that these mitochondrial effects, specifically the clearance of potentially poor-quality mitochondria, may contribute to the observed improvement in muscle function.

Lastly, opening of mtPTP facilitates the release of pro-apoptotic proteins such as cytochrome c. Often, assessments of mtPTP are often coupled with measurements of downstream apoptotic pathways, such as caspases. Activation of caspase-9 and -3 are believed to be linked to mtPTP and as such can be used to identify mitochondrial-facilitated apoptosis [336, 337]. In many of the studies that reported elevated mtPTP opening, a concomitant increase of caspase-9 and -3 activities are also observed [23, 25, 27]. Coupling measures of mtPT and caspase activity does provide more comprehensive evidence of the contribution of mtPT to apoptotic cell death and disease progression in DMD.

As the evidence above indicates how mtPT may contribute to cell death in DMD, the degree to which mtPT and apoptosis contribute to secondary pathologies in DMD is unknown. In some reports, cytokines controlling fibrosis can also elicit apoptosis in culture myoblasts [338] and satellite cells [339]. In combination with dystrophic muscle, dystrophic fibroblasts and FAP cells are resistant to apoptosis [340-342], thus potentially exacerbating fibrosis in dystrophic skeletal muscle. Similarly, proinflammatory cytokines such as TNF-α and IL-6 have been shown to decreased mitochondrial OXPHOS and increase mitochondrial ROS in other cell types [343-348]. Given the relationship between these two functions, mtPTP opening and apoptosis could in theory be altered as a result to circulating factors. In support, TNF-α specifically, has been shown to

require mtPTP opening to induce apoptosis in primary rat hepatocytes [349]. Given this relationship, it is plausible that TNF-α, which is chronically elevated in DMD [350-352], may trigger mtPTP opening and initiate apoptosis.

Healthy

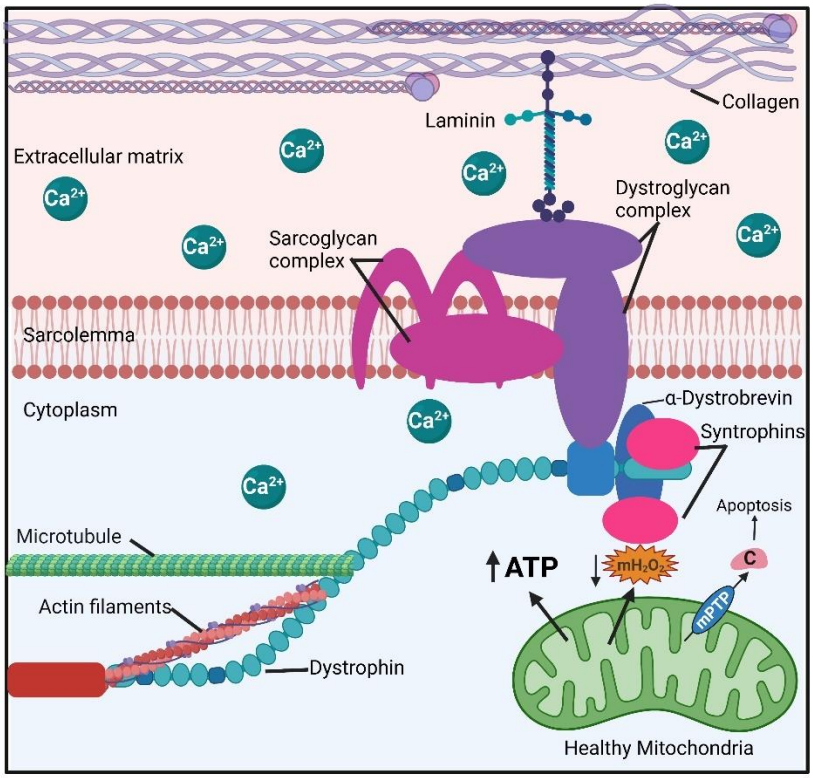

Duchenne Muscular Dystrophy

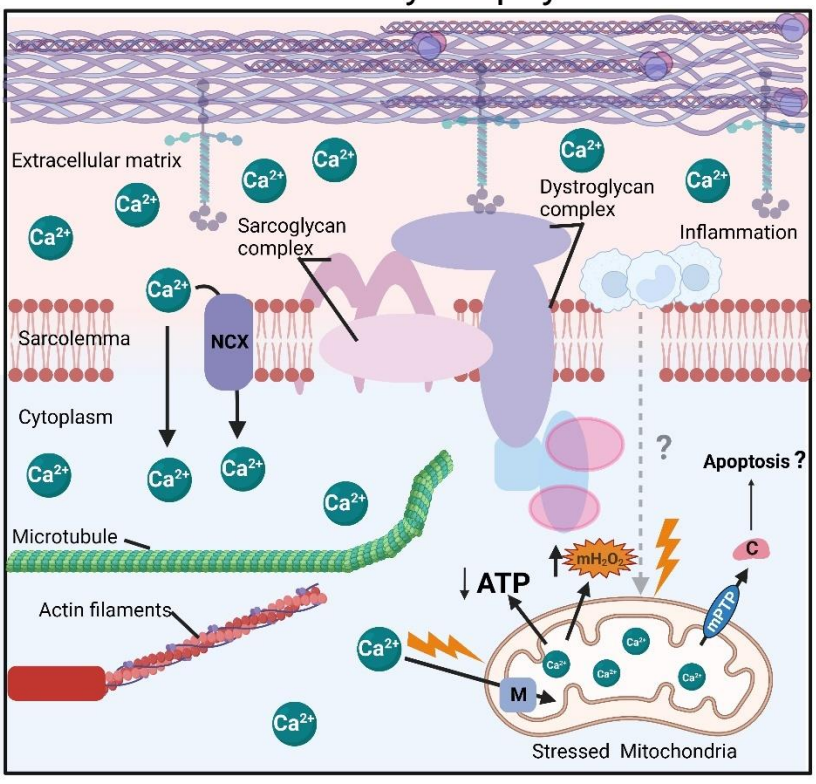

Figure 2-4: Schematic representation of physiological changes to muscle fibers in Duchenne muscular dystrophy. In healthy muscle, dystrophin provides structural support to the sarcolemma preventing excess extracellular calcium from entering the cytosol and mitochondria and provides an anchor point for microtubules and actin cytoskeleton. Dystrophin mutations destabilize the sarcolemma leading to injury during contractions. Cellular degeneration is thought to be caused by excess calcium influx that may be linked, in part, to calcium stress in mitochondria in addition to microtubule disorganization. Excess calcium influx is thought to occur through the damaged sarcolemma and through reverse flux of the sodium-calcium exchanger that is driven by excess sodium influx (not shown) [353]. Increased mitochondrial calcium uptake has been shown to occur through the mitochondrial calcium uniporter ("M" in figure [18]). Repeated cycles of tissue damage triggers inflammation and releases cytokines known to modulate mitochondrial bioenergetics, but the degree to which this causes mitochondrial stress remains uncertain. Increased extracellular matrix proteins have been reported including collagens, laminin, and others not displayed (e.g., fibronectin) [354, 355]. Furthermore, the degree to which these mechanisms contribute to mitochondrial stress across muscle types and throughout disease progression remains unresolved. ATP, adenosine triphosphate; C, cytochrome c; mH_2O_2, mitochondrial hydrogen peroxide emission; mtPTP, mitochondrial permeability transition pore; M, mitochondrial calcium uniporter; NCX, sodium-calcium exchanger. Figure was created with BioRender. Figure taken with permission from [256].

2.6 Cognitive and Behavioral Impairments in DMD

While dystrophin expression is predominant in skeletal and cardiac muscle, other tissues are also being affected in DMD, either through the direct loss of dystrophin, such as in brain [179, 356-360] and smooth muscle [179] or an indirect effect, such as in bone (through glucocorticoid treatment) [179], kidney and liver (through excessive burden of damaged muscle) [361, 362]. For the purpose of this literature review, only brain will be discussed.

In addition to the pronounced muscle atrophy and weakness observed in DMD, increasing attention is being paid to cognitive and behaviours deficits observed in boys with DMD and murine models [356, 357, 363-368]. The presence of these impairments is thought to result from the lack of dystrophin within the central nervous system (CNS), where it is normally located in the hippocampus, prefrontal cortex and the cerebellum [369]. Full length dystrophin, known as Dp427, is localized primarily to the post-synaptic neurons, while shorter length isoforms are associated to microvascular glia cells and neurons [370]. Within the CNS, dystrophin plays an important role in the clustering of neurotransmitter receptors and ion channels [371, 372].

Although first debated, cognitive impairments are now common observations in DMD patients. Several studies report an overall reduction of IQ in boys with DMD and about 30% of patients having cognitive impairments [356, 373, 374]. Additionally, other neurodivergences, such as attention-deficit hyperactivity disorder and autistic spectrum disorder, are also exhibited by 50% and 33% of patients respectively [357, 359, 375]. Deficits in linguistic functions and short- and long-term memory are also common in patients [376, 377], even when patients have normal IQ levels [378]. The varying degrees of memory impairments have been attributed to the loss of dystrophin in brain structures involved in cognition, including the cerebellum and hippocampus [363].

Examination of cognitive and behaviour function in mouse and rat models of DMD have also been undertaken. In the *mdx* mouse, long-term object recognition memory [367, 368] and memory consolidation [367] are also impaired, but task acquisition, spatial memory and procedural memory remains intact [367, 368, 379, 380]. In recent years, cognitive function of D2.*mdx* mice have also been examined, showing similar impairments to recognition memory when faced with a novel object recognition (NOR) task. These impairments were observed in association with higher soluble amyloid precursor protein β and APP in the prefrontal cortex, with lower soluble APPα in the hippocampus. Collectively this was suggestive of a shift toward a formation of amyloid plaques creating Alzheimer's disease-like phenotype in D2.*mdx* mice [381]. The biological basis of the cognitive deficits remains unclear, although it has been suggested that that altered metabolism and impaired mitochondrial function in the brain could play a role.

2.6.1 Altered mitochondrial bioenergetics in DMD brain

Altered metabolism in the brain of DMD patients has been documented as early as 1995 with work performed by Tracey et al showing increased P_i to ATP levels and P_i to PCr levels [382] which may be explained by mitochondrial abnormalities. This was supported by work in *mdx* mice that showed similar increases in P_i to PCr levels and reduced Cr concentrations [383], although other studies have reported no changes in Cr concentrations when measured with ^{1}H MRS [384, 385]. In support of altered metabolism in DMD, increased intracellular brain pH, impaired metabolism of glucose and abnormal $GABA_A$ receptors clustering have been obsrved in *mdx* mice [383]. GABA receptors are the major inhibitory neurotransmitter in the CNS which has later implication for signal transduction, while elevations in brain pH may be indicative of developmental delays.

Interestingly, no significant changes in key mitochondrial enzymes such as citrate synthase, succinate cytochrome reductase and cytochrome oxidase, were observed in *mdx* mice compared to controls [383]. This may be suggestive of an intrinsic impairment in mitochondrial function, instead of a reduction of mitochondrial content.

Mitochondrial respiratory chain activity has also been examined in brain from 3-month-old *mdx* mice. Here, complex I activity was severely reduced in the hippocampus, prefrontal cortex, cortex, striatum and cerebellum, with complex IV activity only being reduced in prefrontal cortex and striatum [386]. As these areas are involved in memory processing it is likely that the lack of dystrophin and reduced metabolism plays a role in memory impairments. In this same study, an increase in creatine kinase activity was found in all areas of the brain examined, which the authors suggested could explained by increases in mitochondrial creatine kinase activity resulting in decreases in ATP concentrations which may be protective to the brain [386].

Similar to the observations in skeletal muscle, both Ca^{2+} homeostasis and oxidative stress are also altered in *mdx* brain. A reduction in lipid and protein peroxidation were observed in the cerebellum, prefrontal cortex and striatum of 3-month-old *mdx* mice [387], which may be due to increased superoxide dismutase activity in these structures, representing a period of compensation in the brain. As only one age was examined in this study, it is unknown whether this ability to attenuate oxidative stress in the brain is maintained throughout the lifespan.

Ca^{2+} homeostasis in brain may also be affected in dystrophic brain. In *mdx* and D2.*mdx* mice SERCA activity was reduced in the hippocampus and prefrontal cortex despite no changes in SERCA expression. This may be a result of oxidative stress as heat shock protein 70 (HSP70) content was reduced [388]. HSP70 binds to SERCA1a and SERCA2a preventing inactivation in times of cellular stress [389] and has been shown to be neuroprotective [390]. Although SERCA activity and SR Ca^{2+} uptake are not direct measures of mitochondrial Ca^{2+} homeostasis, elevated cytosolic Ca^{2+} is known to increase mitochondrial Ca^{2+} uptake, which can initiate apoptosis. An increase in intracellular Ca^{2+} in cerebellar cells, but not glial cells, has been observed in *mdx* mice [391], making is plausible that Ca^{2+}-induced mitochondrial stress is observed in *mdx* brain. However, it is unknown whether mitochondrial Ca^{2+} homeostasis and mitochondrial-activated apoptosis in brain is associated with cognitive impairments in DMD. Considering the interplay of mitochondrial respiration, Ca^{2+} homeostasis and oxidative stress, it is likely that these factors do

contribute to metabolic and cognitive impairments in DMD but warrants further investigation (Chapter 7).

2.7 Therapeutics in DMD

2.7.1 Current standard of care: glucocorticoid steroids

While the underlying pathology of DMD is genetic, current standard of care for DMD targets inflammation. Glucocorticoid steroids, namely prednisone, were first used in the treatment of DMD in 1974 by Drachman et al., where walking speed, distance tolerated, and muscle strength were improved [392]. Later studies supported that long term treatment with prednisone delays loss of mobility, extends life span and increases lung function (forced vital capacity) [393-395]. Deflazacort, a derivative of prednisone, has been more recently introduced for its limited side effects and ability to improve physical milestones (stair climbing) compared to prednisone [396-398]. It currently has FDA approval for use in DMD patients as young as 2 years old. However, due to the myriad of detrimental side effects with glucocorticoids, such as cushingoid, weight gain, osteopenia, diminished stature, and behavioural issues, treatment plans among patients vary greatly [399]. Glucocorticoids have also been observed to disrupt expression of genes involved in muscle degradation and regeneration, which can lead to chronic myopathies [400], muscle weakness and atrophy [401-403], which may limit long term use.

Alternatives or adjuvant therapies have been considered in the treatment of patients and are undergoing clinical testing. Tadalafil, a vasodilator, is currently being examined (NCT05195775) to counter sympathetic vasoconstriction as an adjuvant therapy to glucocorticoids. Similarly, aerobic exercise and strength training in combination with standard care, are both being investigated in clinical trials (NCT03963453, NCT03319030, NCT04322357 & NCT02421523), with increasing evidence that exercise is safe and may slow the functional decline in DMD [404-406].

2.7.2 Emerging genetic therapies

In recent years, treatment of the underlying pathology, the genetic disruption of dystrophin, has been examined. The use of viral and non viral approaches facilitates the production of shorter dystrophin (mini or micro) isoforms that result in a milder Becker muscular dystrophy (BMD)-like pathology [407-410]. Of specific note are Food and Drug Administration (FDA) approved

antisense oligonucleotides (AON) that utilize morpholino chemistry that target exon 51 (ExonDys-51(Eteplirsen &Drisapersen), exon 53 (VyonDys-53 (Golodirsen & Viltolarsen) and exon 45 (AmonDys-45) (reviewed in [411]). The utilization of exon skipping therapies is mutation dependent and individual exon skipping therapies are only applicable to small subsets of DMD patients that possess the corresponding mutation. For example, skipping exon 51 applies to only 13-14% of patients [412, 413], the largest percentage of DMD patients. However, corresponding treatment, Eteplirsen, costs patients $300,000-400,000 (USD) per year per patient, leaving many patients unable to afford access to this drug without insurance coverage [414]. Additionally, AONs tend to have poor delivery and uptake to large tissues such as the heart and require repeated treatments [414, 415]. In Eteplirsen treated patients, a large variation in recovery of dystrophin expression is observed, with 8% to roughly 55% recovery of dystrophin (compared to healthy controls) in the biceps brachii [416]. The recovery of dystrophin expression is highly dependent on the dosage used and the amount of muscle retaining in the patient [414, 416, 417].

Lastly, oligonucleotide treatment is not curative but instead produces a milder phenotype and may delay the progression of symptoms. Opportunities to correct the underlying mutations have arisen with the development of CRISPR-Cas9 technology. CRISPR-Cas9 system consists of two main components: the CRISPR-associated (Cas) endonuclease and a single guide RNA, which guides the Cas9 to the complementary sequence in the genome. When at the appropriate sequence, the Cas9 endonuclease creates a targeted double-stranded DNA break. An exogenous DNA template may be used in homology-directed repair but is not feasible for use in post-mitotic cells such as skeletal muscle [418, 419]. In the absence of a DNA template, nonhomologous end joining (NHEJ) is utilized resulting in imprecise DNA repair [420]. Another limitation with CRISPR/Cas9 technology in its current form, is the large size of the Cas9 system (~4kb). Currently, adeno-associated viruses (AAVs) are used to deliver the Casp9 and RNA guide in two separate AAV. In addition to sizing issues, AAVs may also cause immune response, forcing this system to be administered in a single tolerable dose [419, 421]. Overall, the development of the CRISPR/Cas9 system does hold promise a therapeutic option for DMD, but many challenges remain before this therapeutic is available to patients.

2.7.3 Mitochondrial therapeutics

With more attention being drawn to genetic therapies, some considerations should be undertaken, such as potential off-target effects with genetic editing, muscle heterogeneity in receiving the genetic editing system and variable dystrophin expression across muscles. Additionally, it is unknown whether genetic editing will fully correct secondary pathologies, such as mitochondrial dysfunction.

Mitochondrial deficiencies were specifically noted in DMD as early as 1967 [15]. In our recent review [256], we highlight that mitochondrial stresses response in DMD may represent adaptive reprogramming, especially early into the disease progression, but later stages may require mitochondrial targeting compounds to improve OXPHOS, attenuation of ROS and inhibition of mtPT. Table 2-2 summarizes the current mitochondrial therapeutics being examine in pre-clinical models and DMD patients.

Table 2-2: *Mitochondrial therapeutics in the treatment of DMD*

Compound	Mechanism of Action	Model	Outcome	Reference
Idebenone	• Synthetic analog to coenzyme Q10, Improve mitochondrial oxidative phosphorylation and reduce oxidative stress	*mdx* mice	• Corrected cardiac diastolic dysfunction • Prevented mortality from cardiac pump failure • Reduced inflammation and fibrosis • Improved VWR	[422]
		DMD patients	• Increased peaked expiratory flow, FVC and peak cough flow • Increased peak systolic radial strain (when combined with glucocorticoid steroids)	[423-426]
Cyclosporine A	• Immunosuppressive, Mitochondrial permeability pore inhibitor	*mdx* mice	• Reduced plasma creatine kinase and degenerating area	[331]
		DMD patients	• Increased tetanic force and MVC	[427]

However, it is unknown how mitochondrial targeting compounds would interact with glucocorticoid therapies as it is unlikely that they would operate as a stand-alone treatment.

2.7.4 Repurposing therapeutics towards DMD: potential candidates

Clearly, limited pharmacological interventions targeting the mitochondria have been examined in the context of DMD despite a clear knowledge that mitochondria are impaired in this disease. As a result, repurposing other mitochondrial therapeutics from different diseases may provide new options to act as an adjuvant therapy to current standards of care.

2.7.4.1 Olesoxime

Olesoxime (cholest-4-en-3-one oxime, or TRO1966) is a cholesterol-like molecule, as depicted in Figure 2-5, that accumulates at the mitochondria. Olesoxime is thought to bind to the voltage dependent anion channel (VDAC), and translocator protein (TSPO) located on the outer mitochondrial membrane. In previous work it has been shown to promote motor neuron survival, improves motor performance and extend lifespan in models of amyotrophic lateral sclerosis (ALS) [428, 429]. Olesoxime has shown to have anti-mtPT effects in cultured motor neurons, [428], rat models of Huntington's [430] and cardiomyocytes [431]. Additionally, olesoxime has been observed to improve mitochondrial respiration in preclinical models of Alzheimer's and Huntington's [430, 432]. Olesoxime was already proved safe in humans as phase I clinical trials were completed [433] and progressed into phase IB [434] and phase II/III (NCT00868166) trials in ALS. Additionally, Olesoxime was used in clinical trials for spinal muscular atrophy (NCT01302600, NCT02628743), multiple sclerosis (NCT01808885), peripheral neuropathy (NCT00876538, NCT00496457) and non-alcoholic steatohepatitis (NCT00666016). Collectively, this suggests that olesoxime is safe for humans, while also improving mitochondrial respiration

and inhibiting mtPTP pore opening. This gives olesoxime merit to be examined in other conditions, such as DMD, that are characterized by poor mitochondrial function.

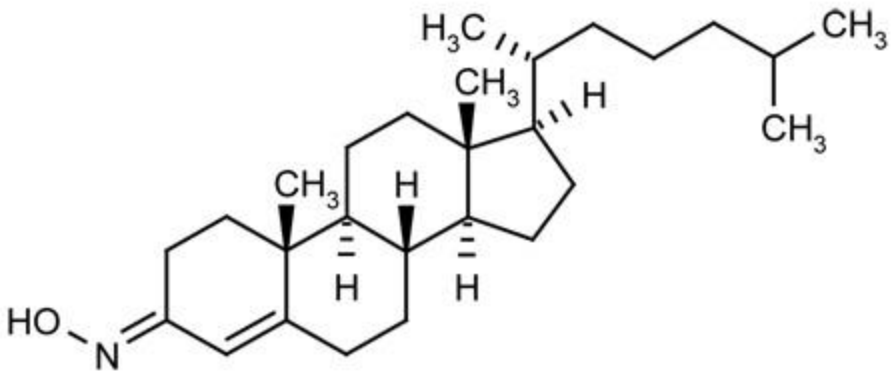

Figure 2-5: Structure of cholest-4-en-3-one oxime or Olesoxime; $C_{27}H_{45}NO$ [435]

2.7.4.2 The adiponectin receptor agonist ALY688-SR

Certain compounds may reprogram mitochondria as part of a more global umbrella of mechanisms. As glucocorticoid steroids come with a myriad of negative side-effects, alternative therapeutic options have been examined. Adiponectin (Apn), discovered in 1995, was initially thought to be an adipokine but now is known to be expressed by multiple tissues including skeletal muscle [436]. In plasma, adiponectin exists as a low molecular weight trimer that can associate with other trimers, forming a middle and high weight hexamer, each with their own biological effects [437]. Additionally, Apn can undergo proteolytic cleavage to form the functionally distinct globular Apn (gApn) [438, 439]. Lastly, Apn undergoes extensive post-translational modifications including disulfide bond formation, hydroxylation, glycosylation and which aid in the formation of the multimeric complexes [440, 441]. Apn is one of the most abundant adipokines in the plasma, circulating in the range of approximately 5 to 30 μg/mL [442]. Its most well-known role is in metabolism whereby it activates AMP-activated protein kinase (AMPK) and peroxisome

proliferator activated receptor (PPAR)-α [442-445], where it supports the production of an oxidative phenotype in muscle. It has also been examined in its influence on Ca^{2+} handling [446], muscle maintenance (including growth and repair) [439, 447-450], and the attenuation of inflammation by repressing pro-inflammatory cytokine secretion and increasing anti-inflammatory responses [451-455].

Given this influence in muscle, Apn has more thoroughly examined as a possible treatment for DMD. Initially, mice lacking Apn mice were crossed with *mdx* mice, resulting in a worsened myopathy, indicating a potential role of Apn in the dystrophic phenotype. *mdx*/*Apn-null* mice showed reduced contractile force, higher markers of muscle damage (including plasma creatine kinase and infiltrating Evans Blue Dye) and markers of oxidative stress compared to *mdx* mice [456]. Electro-transfer of the Apn gene into these mice resulted in mitigation of inflammation, oxidative stress and increased myogenic factors [456]. Likewise, genetic overexpression of Apn in *mdx* mice (*mdx/Apn*^{OE}), resulted in similar improvements to the dystrophic phenotype [457]. This highlights the potential therapeutic value of Apn in DMD, however, production of biologically active Apn or recombinant Apn proves difficult given ability of Apn to form multimeric complexes and undergo extensive posttranslational modifications. Additionally, the C-terminal globular domain and larger peptide fragments of Apn remain extremely insoluble, thus limiting the ability to use full length Apn as a therapy [458]. As such Apn receptor agonism has been examined for its treatment in disease, specifically AdipoRon and ALY688 (previously known as ADP355).

AdipoRon is an orally active synthetic small molecule Apn agonist (Figure 2-6A), which was originally proposed for the treatment of obesity related conditions [459]. AdipoRon binds to both Apn receptor (AdipoR) isoforms, with AdipoR1 activating AMPK and PGC-1α pathways and AdipoR2 activating PPAR-α, although there is greater expression of AdipoR1 in skeletal muscle

[460, 461]. AdipoRon was originally studied for its use in metabolic diseases, whereby treatment with AdipoRon corrects metabolic dysfunction in *db/db* mice, a genetic murine model of obesity [462]. Likewise in aged mice, a model of sarcopenia, AdipoRon treatment significantly improved indices of insulin sensitivity and demonstrated a transition to an oxidative phenotype in glycolytic muscles. Force production at the end of a fatigue protocol was enhanced in the EDL muscle but not the soleus during *ex vivo* contractility experiments in both old and young mice treated with AdipoRon [463].

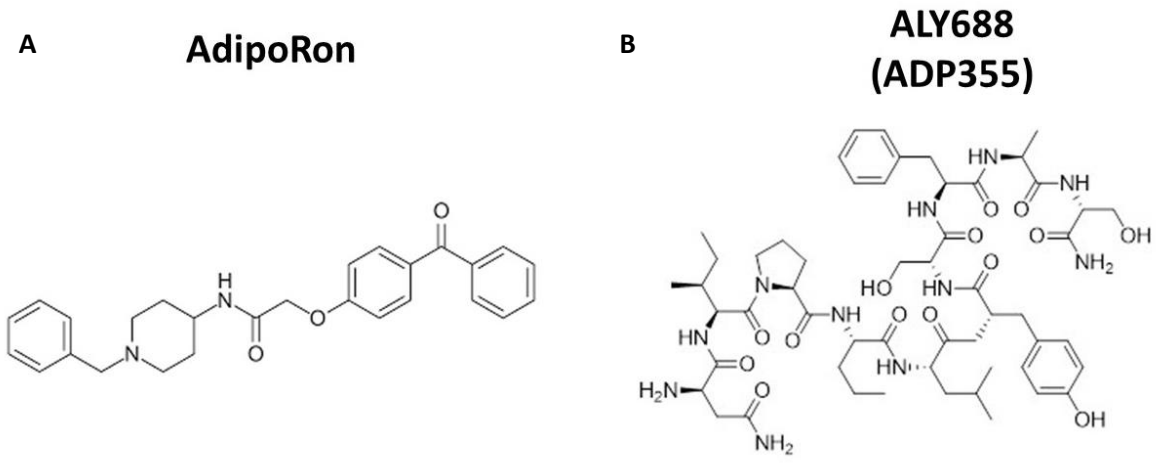

Figure 2-6: Chemical structure of AdipoRon (A) and ALY688 (ADP355) (B). *Chemical structure of slow-release formation of ALY688 (ALY688-SR) was unavailable.*

In a pivotal study by Abou-Samra et al, 8 weeks of AdipoRon treatment in *mdx* mice mitigated oxidative stress, inflammation and improved markers of muscle breakdown, regeneration, and increased muscle force [464]. Despite these benefits, it is unknown if AdipoRon treatment improves other aspects of the dystrophic phenotype including fibrosis and mitochondrial dysfunction. More importantly, it is unknown if AdipoRon treatment improves cardiac and respiratory function as assessments were only performed in skeletal muscle, specifically the tibialis anterior. Interestingly, it was recently shown that AdipoRon impaired complex I activity, induces

rapid mitochondrial Ca^{2+} overload and superoxide production, while activating necroptosis, a form of cell death with hallmarks of both apoptosis and necrosis, in pancreatic cancer cells. Although highly speculative, it is probable that AdipoRon treatment could induce the same impairments in mitochondrial function in other tissues, thus limiting its use.

ALY688, originally under the name ADP355, is another Apn-mimetic that is composed of non-natural amino acids (H-DAsn-Ile-Pro-Nva-Leu-Tyr-DSer-Phe-Ala-DSer-NH2) and was initially developed for cancer treatment [458, 465]. Similar to AdipoRon, ALY688 is activates the AMPK pathway through AdipoR1 [458] but has improved specificity to AdipoR1 and AdipoR2. In rodent models of liver fibrosis, ALY688 was shown to attenuate fibrosis by mitigating inflammation [466, 467]. These effects were associated with suppression of necroinflammation by inhibiting macrophage activation and promoting signal transducer and activator of transcription 3 (STAT3 signaling). STAT3 is involved in diverse biological processes such as proliferation, differentiation, anti-apoptosis and inflammation [468]. ALY688 reduced the activation of macrophages while supressing fibrotic TGF-β1/SMAD2 signaling. In brain, ALY688 was shown to mitigate HIV protease inhibitor-induced damage by preserving CNS physiology and mitigating metabolic dysfunction [469]. A slow-release formulation of ALY688 has been created, termed ALY688-SR, and has passed Phase I clinical trials in dry eye disease, showing low toxicity in humans (NCT 04201574). The effect of ALY688-SR on dystrophic muscle and brain is unknown and will be investigated in Chapters 5 and 6.

Chapter 3: Objectives and Hypotheses

3.1 Overview of Thesis

The overall purpose of this thesis was to examine how altering metabolism may improve muscle weakness and atrophy in a model of Duchenne muscular dystrophy (DMD). The specific objectives and hypotheses for each study are outlined below.

3.2 Objective and Hypotheses for Study 1 (CHAPTER 4)

Calcium-induced mitochondrial permeability transition pore (mPTP) opening is thought to be elevated in the muscle of DMD contributing to muscle fibre loss, but the literature is quite controversial. One explanation may be the variety of modalities and buffers used in assessing calcium-induced mPTP opening. These varying buffer compositions alter the environment in which mitochondria are exposed to and may alter adenylate concentrations, energy cycling and finally mPTP opening. The first purpose of this study was to compare mPTP assessments from permeabilized fibre bundles with and without adenylates. Next, we determined if increasing ADP/ATP cycling through the addition of creatine alters Ca^{2+}-induced mPTP opening. Lastly, we applied this to a biological context by comparing mPTP opening from permeabilized fibre bundles from D2.*mdx* mice and health controls under conditions explored in the first aim.

Hypotheses

1. The presence of adenylates (through addition of ADP and equilibration with ATP) will attenuate mPTP, marked by increased Ca^{2+} uptake in healthy skeletal muscle permeabilized fiber bundles. The presence of ADP and or ATP will increase Ca^{2+} uptake and decrease likelihood of mtPTP opening. Depleting ATP (by recycling ATP into ADP) will reduce Ca^{2+} uptake and increase likelihood of mtPTP opening.

2. The addition of creatine will further reduce susceptibility of mPTP (increased Ca^{2+} uptake), due to enhanced ADP/ATP cycling, compare to trials performed in the absence of creatine.

3. Permeabilized fibres from left ventricle of D2.*mdx* will have increased triggering of mPTP than wildtype controls.

3.3 Objective and Hypotheses for Study 2 (CHAPTER 5)

Previous work from our lab and others have identified the mitochondria to be impaired early in the disease progression of D2.*mdx* mice and suggests that mitochondria contribute to the dystrophic phenotype. Here, we aimed to examine the effect of the mitochondrial-enhancing drug Olesoxime in the D2.*mdx* model of DMD on fibrosis, muscle weakness and atrophy and the contribution of mitochondrial stress to DMD pathology.

Hypotheses

1. Short-term treatment with the mitochondrial-enhancing drug, Olesoxime in the D2.*mdx* mouse, will reduce susceptibility to Ca^{2+}-induced permeability transition pore opening, improve mitochondrial respiration and attenuation of reactive oxygen species emission compared to vehicle controls.

2. Corresponding improvements in bioenergetics will be associated with improvements to muscle weakness, atrophy, and fibrosis compared to vehicle controls.

3.4 Objective and Hypotheses for Study 3 (CHAPTER 6)

Altered metabolism including mitochondrial stress is well documented in DMD patients and rodent models of DMD and may contribute to overall pathology. As adiponectin receptor agonism has previously been shown to alter metabolism and improve dystrophic pathology, we examined the

effect of the novel adiponectin receptor agonist, ALY688-SR, in the D2.*mdx* mouse model. Specifically, we examined if short-term treatment with ALY688-SR attenuates inflammation, fibrosis, atrophy muscle weakness and mitochondrial stress in D2.*mdx* mice.

Hypotheses

1. 21 days of treatment with ALY688-SR will attenuate inflammation and fibrosis in the limb and respiratory muscles in young D2.*mdx* mice.
2. This improvement with inflammation and fibrosis will be associated with improvements in muscle weakness and atrophy compared to D2.*mdx* saline controls.
3. ALY688-SR treatment will attenuate mitochondrial stress compared to saline controls, in association with improvements to dystrophic phenotype.

3.5 Objective and Hypotheses for Study 4 (CHAPTER 7)

Although predominantly expressed in skeletal and cardiac tissue, dystrophin is expressed in the central nervous system where its specific function is not well understood. DMD patients exhibit cognitive impairments including reduced short- and long-term memory and behavioural impairments that may be exacerbated by current standard of care. Currently, no treatments target these dysfunctions. The focus of this study was to examine the effect of adiponectin-receptor agonist, ALY688-SR, on cognitive function in D2.*mdx* mice and metabolic function specifically in the hippocampus.

Hypotheses

1. 21 days of treatment with ALY688-SR will improve short term recognition memory compared to vehicle controls, as measured by novel object recognition.
2. The improvement in object recognition will be associated with an attenuation of mitochondrial stress (an increase in mitochondrial respiration) in D2.*mdx* mice.

3.6 Additional Scientific Contributions

The following work lists the additional contributions made throughout my PhD that are not included in my dissertation:

First Author -Published

Bellissimo CA, Garibotti MC, Perry CGR. Mitochondrial stress responses in Duchenne muscular dystrophy: metabolic dysfunction or adaptive reprogramming? Am J Physiol Cell Physiol. 2022 Sep 1;323(3):C718-C730. doi: 10.1152/ajpcell.00249.2022. Epub 2022 Jul 11. PMID: 35816642.

Bellissimo CA, Perry CGR. Sex differences in the regulation of hepatic mitochondrial turnover following physical activity: do males need more quality control than females? J Physiol. 2018 Dec;596(24):6125-6126. doi: 10.1113/JP276896. Epub 2018 Oct 28. PMID: 30284737; PMCID: PMC6292818.

Bellissimo, CA, Perry CGR. Regulation of skeletal muscle reactive oxygen species during exercise. In Tiidus P, LeBlanc P, Macpherson R, Josse A (Eds.) The Routledge Handbook on Biochemistry of Exercise: 1st edition. UK: Routledge, Ch. 4, 2021.

Co-Author- Published

Delfinis LJ, **Bellissimo CA**, Gandhi S, DiBenedetto SN, Garibotti MC, Thuhan AK, Tsitkanou S, Rosa-Caldwell ME, Rahman FA, Cheng AJ, Wiggs MP, Schlattner U, Quadrilatero J, Greene NP, Perry CG. Muscle weakness precedes atrophy during cancer cachexia and is linked to muscle-specific mitochondrial stress. JCI Insight. 2022 Nov 8:e155147. doi: 10.1172/jci.insight.155147. Epub ahead of print. PMID: 36346680.

Monaco CMF, **Bellissimo CA**, Hughes MC, Ramos SV, Laham R, Perry CGR, Hawke TJ. Sexual dimorphism in human skeletal muscle mitochondrial bioenergetics in response to type 1 diabetes. Am J Physiol Endocrinol Metab. 2020 Jan 1;318(1):E44-E51. doi: 10.1152/ajpendo.00411.2019. Epub 2019 Dec 3. PMID: 31794260; PMCID: PMC6985789.

Young LV, Morrison W, Campbell C, Moore EC, Arsenault MG, Dial AG, Ng S, **Bellissimo CA,** Perry CGR, Ljubicic V, Johnston AP. Loss of dystrophin expression in skeletal muscle is associated with senescence of macrophages and endothelial cells. Am J Physiol Cell Physiol. 2021 Jul 1;321(1):C94-C103. doi: 10.1152/ajpcell.00397.2020. Epub 2021 May 12. PMID: 33979211.

Co-Author- In Progress

Hughes MC, Ramos SV, **Bellissimo CA**, Dial AG, Tin E, Turnbull PC, Tadi P, Schlatter U, Hawke TJ, Perry CGR. The mitochondrial targeted peptide SBT-20 improves diaphragm and skeletal muscle pathophysiology in dystrophin-deficient mice. (*In Preparation*)

Gandhi S, Delfinis LJ, Garibotti, MC, **Bellissimo CA**, Castellani LN, Yakobov S, Edgett BA, Bacx PH, Simpson JA, Perry CGR. Adiponectin-receptor agonism mitigates chamber-specific cardiac

fibrosis and mitochondrial stress responses in the D2.*mdx* Duchenne muscular dystrophy mouse model. (*In Preparation*).

Chapter 4: The influence of adenylate cycling on mitochondrial calcium-induced permeability transition in permeabilized skeletal muscle fibers

This chapter is an original published article currently in submission. It is presented in its published form.

The influence of adenylate cycling on mitochondrial calcium-induced permeability transition pore in permeabilized skeletal muscle fibres. CA Bellissimo, S Sondergaard, MC Hughes, SV Ramos, S Larsen, CGR Perry. Bioenerg Commun. DOI: 10.26124/bec2023-0001

Author Contributions: The majority of the experiments for this study were performed by Catherine A Bellissimo (CAB). CAB maintained the breeding colony required for this project as well as subsequent studies (Chapters 5-7) after being established by MCH. CAB and SVR separated all muscle fibres used in experiments. CAB and SS performed calcium retention capacity assays and subsequent analysis. CAB and CGRP wrote the manuscript with all co-authors aiding in revision.

NOTE: Following this study, the protocol established for Calcium Retention Capacity was utilized in chapters 5 and 6.

The influence of adenylate cycling on mitochondrial calcium-induced permeability transition pore in permeabilized skeletal muscle fibres

Authors: Catherine A. Bellissimo[1], Stine Sondergaard[2], Meghan C Hughes[1], Sofhia V Ramos[1,3], Steen Larsen[2,4], Christopher GR Perry[1]*

Affiliations:

[1] School of Kinesiology & Health Science, Muscle Health Research Centre, York University, Toronto, ON, Canada, M3J 1P3.

[2] Center for Healthy Aging, Department of Biomedical Sciences, Faculty of Health and Medical Sciences, University of Copenhagen, Denmark

[3] Translational Research Institute, AdventHealth, Orlando FL, USA.

[4] Clinical Research Centre, Medical University of Bialystok, Bialystok, Poland

* Corresponding author: cperry@yorku.ca

Graphical Abstract

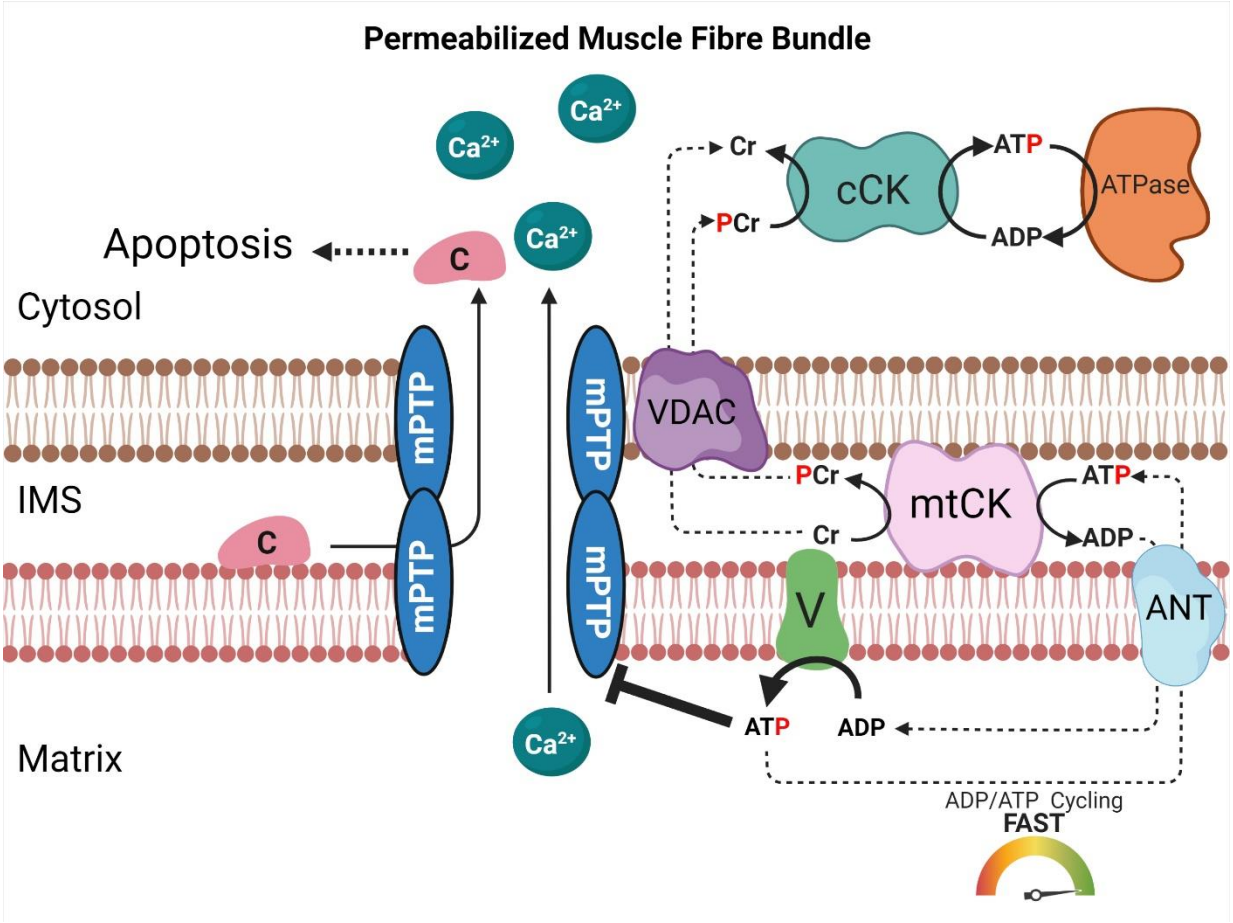

Summary

In isolated mitochondria, calcium-induced mitochondrial permeability transition pore (mPTP) opening is thought to be regulated by adenylates but the relative effects of adenylate cycling in permeabilized tissues is less explored. To determine the effect of adenylates on calcium retention capacity (CRC) as an index of mPTP in permeabilized muscle fibres, separate in vitro assessments of CRC were compared in media that did not contain ADP or received exogenous ADP that naturally equilibrated with ATP through endogenous ATP-dependent pathways (presence of both ADP and ATP). Comparisons were made to a hexokinase 2-deoxyglucose system that recycles ATP to ADP (depletion of ATP). In permeabilized mouse quadriceps fibres, we found that CRC was increased by ADP suggesting endogenous ADP-ATP equilibria attenuate mPTP. Supplementing ADP with the hexokinase ATP recycling clamp lowered CRC relative to ADP alone but had no effect relative to the absence of adenylates. This finding suggests ADP does not alter calcium-induced mPTP and that its regulation by adenylates is specific to ATP in

permeabilized mouse quadriceps fibres. Accelerating matrix ADP/ATP cycling with creatine had no effect on CRC when combined with 5mM ADP but more than doubled CRC (desensitized mPTP) when the hexokinase clamp was included. These results demonstrate the importance of considering adenylate equilibria during the design of in vitro assessments of calcium-induced mPTP in permeabilized muscle fibres.

Keywords – Permeability transition pore; Apoptosis; Metabolism; Bioenergetics; Skeletal muscle; Permeabilized muscle fibres

Introduction

Evidence suggests that mitochondria can trigger apoptosis and necrosis through formation of the permeability transition pore mPTP [470]. This event is increasingly linked to numerous cellular processes and pathologies [254, 470, 471]. mPTP is often assessed by *in vitro* fluorescent-based detection of mitochondrial calcium uptake in response to calcium titrations followed by eventual release through the mPTP once calcium retention capacity (CRC) is exceeded. As calcium-induced mPTP is influenced by adenylates [92, 94, 472-474] controlling [ADP], [ATP] and their equilibrium during *in vitro* assessments may influence mPTP measurements. Thus, comparing mPTP assessments with and without adenylates may reveal how the regulation of mPTP by ADP and/or ATP is altered in a given investigation and highlights the importance of careful consideration of *in vitro* assay conditions when assessing mPTP.

In isolated heart mitochondria, micromolar calcium triggers mPTP but this event is partially attenuated by ADP and strongly attenuated by ATP [92]. In these experiments, the addition of ADP was supplemented with hexokinase and glucose to recycle mitochondrially-derived ATP to maintain a fixed [ADP] and prevent its depletion. However, in permeabilized tissues or cells, exogenously added ADP creates an equilibrium with ATP because mitochondrially-derived ATP is hydrolyzed by extra-mitochondrial ATPases and other ATP-dependent proteins which does not exist in isolated mitochondria [50]. Thus, the addition of a fixed concentration of ADP to permeabilized samples results in the presence of both adenylates albeit in an unknown ADP:ATP equilibrium. Given calcium-induced mPTP is robustly attenuated by ATP and partially attenuated by ADP in isolated heart mitochondria [92], permitting a natural equilibria between both adenylates may offer the advantage of retaining the distinct effects of each albeit without control of the actual concentrations.

As ATP was shown to be a more potent suppressor of calcium-induced mPTP in isolated mitochondria [92], it is possible that combining ADP with a hexokinase system that recycles ATP to ADP would result in a greater mitochondrial sensitivity to calcium-induced mPTP due to depletion of ATP. In contrast, including ADP without a hexokinase clamp could lower the probability of mPTP in response to calcium due to natural equilibration with ATP in permeabilized muscle fibres. To our knowledge, these comparisons in permeabilized muscle fibres have not been performed in the literature.

Mitochondrial adenylate cycling is also sensitive to creatine [45]. By including creatine in assay media, mitochondrial creatine kinase-dependent phosphate shuttling becomes activated which ultimately accelerates matrix cycling of ADP/ATP (Figure 4-2A). Prior literature has shown that creatine combined with ADP can desensitize mitochondria to calcium-induced mPTP [94]. Other literature also supports a role for mitochondrial creatine kinase in regulating mPTP [475]. Thus, comparing the relative impact of creatine-independent and -dependent control of adenylate cycling could also provide additional insight into how mPTP is altered. The implications of *in vitro* assay design could be considerable given mPTP is altered in a growing list of diseases, stressors and biological contexts.

As the role of mitochondrial stress in contributing to muscle disorders is becoming increasingly popular, there is uncertainty over whether the influence of adenylates and creatine on mPTP is consistent across muscle types, particularly when using permeabilized muscle fibres. Furthermore, it is also unknown if altering adenylates and creatine will lead to unique conclusions of how mPTP responds in models of muscle dysfunction.

The first purpose of this investigation was to compare approaches that modulate ADP and creatine when assessing calcium-induced mPTP. Three major conditions were considered and tested in wildtype mouse muscle: (i) the absence of ADP, (ii) the inclusion of ADP (triggering equilibration with ATP), and (iii) an ATP recycling clamp using hexokinase and 2-deoxyglucose to maintain exogenously added ADP concentrations. All conditions were compared with and without creatine to accelerate matrix ADP/ATP cycling and shift the equilibrium towards ATP. The 2nd purpose of the investigation was to determine whether including ADP and creatine as physiologically relevant regulators altered the interpretation of calcium-induced mPTP events in an example biological context by comparing the D2.*mdx* mouse model of Duchenne muscular dystrophy [256] to wildtype mice.

Materials and Methods

Animal Care

Male 4–8-week-old CD1 mice were utilized from an in-house colony established at York University (Toronto, Ontario) for the first purpose. For the second purpose, 3 week-old DBA/2J WT mice were ordered directly from Jackson Laboratories (Bar Harbor, USA) due to breeding

challenges [127] and allowed to acclimate for 7 days. These mice were compared to male 4 week-old dystrophin-deficient D2.*mdx* mice were utilized from an in-house colony established at York University (Toronto, Ontario) and sourced from Jackson Laboratories. All animals were maintained on a 12:12-h light-dark cycle while being provided access to standard chow and water *ad libitum*. All experiments and procedures were approved by the Animal Care Committee at York University (AUP Approval Number 2016-18) in accordance with the Canadian Council on Animal Care.

Preparation of permeabilized muscle fibre bundles

This technique was adapted from previous methods described elsewhere [23]. Muscles were excised carefully from mice while under heavy sedation with 5% isoflurane mixed with medical air at 2.0 l/min flow followed by removal of the heart. Muscles were immediately placed into ice-cold BIOPS containing (in mM) 50 MES Hydrate, 7.23 K_2EGTA, 2.77 CaK_2EGTA, 20 imidazole, 0.5 dithiothreitol, 20 taurine, 5.77 ATP, 15 PCr, and 6.56 $MgCl_2 \cdot 6\ H_2O$ (pH 7.1). Muscles were trimmed of connective tissue and fat and separated into small bundle sizes approximately 1.0-2.5mg wet weight in size. Bundles were separated along the longitudinal axis to avoid membrane damage. Once separated and weighed, bundles were permeabilized with 40µg/uL saponin (Sigma Aldrich; Mississauga, ON) in BIOPS on a platform rotor for 30 minutes at 4°C. After permeabilization, bundles were placed in Buffer Y containing (in mM) 250 sucrose, 10 tris–HCl, 20 tris-base, 10 KH_2PO4, and 0.5 mg/mL BSA, supplemented with 4mM EGTA and washed on a rotor at 4°C for 10 min. Fibres were then placed in a second wash of Buffer Y with 10 µM blebbistatin (Cayman Chemicals) to prevent rigor [476] until substrate titrations were initiated.

Mitochondrial calcium retention capacity

Mitochondrial calcium retention capacity was performed according to protocols described previously [23, 477] with modifications outlined in section *3 Results and Discussion*. Briefly, membrane impermeable Calcium Green-5N (Invitrogen) fluorescence was measured spectrofluorometrically (QuantaMaster 80, HORIBA Scientific) in a cuvette with 300 µL assay buffer containing 1 µM Calcium Green-5N (Invitrogen), 2 µM thapsigargin, 5 µM blebbistatin, and 40 µM EGTA while maintained at 37°C with continuous stirring. Prior to the start of each experiment, the cuvette was placed on a stir plate with 500 µL of water with 10 mM EGTA for a

minimum of 10 minutes. The water was then aspirated from the cuvette and replaced with assay buffer, chelating any residual Ca^{2+}. 5 mM glutamate, 2 mM malate and varying concentrations of ADP outlined in section *3* were added to the assay buffer and minimum florescence was recorded. Calcium uptake by the mitochondria was initiated by a pulse of 8 nmol $CaCl_2$ to overcome EGTA. Additional pulses of 4 nmol of $CaCl_2$ are added until the mitochondrial permeability transition pore (mPTP) opening was observed as a spontaneous increase in fluorescence. Two pulses of 0.5 mM $CaCl_2$ were then added to saturate the fluorophore, establishing maximum saturation of the probe (F_{max}). Changes in free Ca^{2+} during mitochondrial Ca^{2+} uptake was then calculated using the known K_d for Calcium Green-5N and equations established for calculating free ion concentration [478]. Fibres are then lyophilized in a freeze-dryer (Labconco, Kansas City, MO, USA) for ≥4 h and weighed on a microbalance (Sartorius Cubis Microbalance, Gottingen, Germany). Calcium retention was then normalized to fibre dry weight in mg.

Statistics

Results are expressed as means ± SD with the level of significance established as $P < 0.05$ for all statistics. Prior to statistical analyses, outliers were omitted in accordance with ROUT testing (Q=0.5%) and then tested for normality using a D'Agostino–Pearson omnibus normality test (GraphPad Prism 7 Software, La Jolla, CA, USA). All data was found to be normally distributed. To assess statistical differences on the effect of adenylates, a one-way ANOVA was utilized followed by a two-stage step-up method of Benjamini, Krieger and Yekutieli for controlling False Discovery rate (FDR) for multiple-group comparisons. To assess the effect of creatine on CRC, a two-way ANOVA was used followed by a two-stage step-up method of Benjamini, Krieger and Yekutieli for controlling False Discovery rate (FDR) in multiple-group comparisons. Lastly, unpaired t-tests were used to assess differences between the effect of the combination of ADP and creatine on CRC.

Results and Discussion

We first examined the effect of ADP on calcium-induced mPTP. This event was assessed by titrating calcium until mitochondrial calcium retention capacity (CRC) was exceeded and mPTP opening was triggered thereby releasing calcium into the assay buffer (Figure 4-1A). Using permeabilized muscle fibres from mouse quadriceps, exogenous additions of 5mM ADP increased

CRC (Figure 4-1B) which reflects an attenuation in mPTP. This finding is consistent with a previous report in isolated heart mitochondria [92]. Notably, this addition of ADP also increased variability in CRC which may be due to the unknown degree of ADP:ATP equilibration dependent upon endogenous ATP-hydrolyzing proteins in permeabilized muscle fibres [50]. We then repeated the CRC assay in the presence of hexokinase and the glucose analogue 2-deoxyglucose. In this system, ATP synthesized by mitochondria in response to exogenous additions of ADP are immediately reconverted back to ADP (Figure 4-1C). As shown in Figure 4-1B, this hexokinase ATP recycling clamp (causing ATP depletion) led to a robust reduction in CRC compared to ADP alone (ADP:ATP equilibria) which reflects a greater propensity for calcium-induced mPTP. These results in permeabilized muscle fibres are consistent with isolated mitochondria from heart whereby ATP attenuated calcium-induced mPTP albeit using exogenous additions of ATP [92]. However, this study demonstrated only a small attenuation of mPTP when ADP was combined with the hexokinase clamp to deplete ATP suggesting ADP is much less effective than ATP at attenuating mPTP. In Figure 4-1B, we show no effect of ADP in the absence of ATP (ADP + hexokinase clamp) suggesting only ATP is effective at attenuating mPTP in permeabilized muscle fibres as noted above when ADP and ATP were permitted to equilibrate.

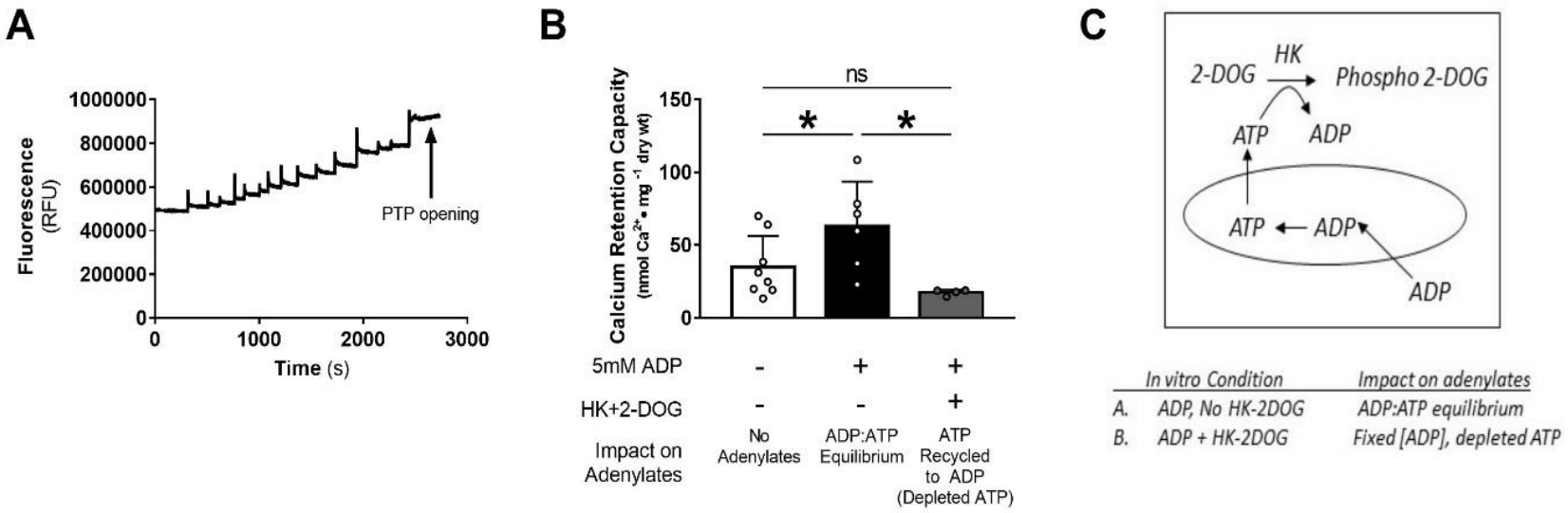

Figure 4-1. The effect of adenylates on mitochondrial calcium retention capacity in mouse permeabilized quadriceps muscle fibre bundles. (A) Representative trace of calcium titrations prior to induction of mitochondrial permeability transition pore (mPTP) opening. (B) CRC experiments were repeated in separate permeabilized fibre bundles including 5mM ADP with or without hexokinase and 2-deoxyglucose to recycle endogenously synthesized ATP from mitochondria back to ADP. (C) Addition of 2-deoxyglucose (2-DOG) and hexokinase (HK) to the media recycles ATP synthesized and exported by mitochondria (oval) using ADP that was added exogenously. Results represent mean ± SD; * P<0.05; N=4-8.

To further explore the effects of adenylate cycling on CRC, we next compared the effect of creatine on accelerating matrix ADP/ATP. In this system, mitochondrial creatine kinase utilizes mitochondrial ATP synthesized by exogenous additions of ADP, to phosphorylate creatine to phosphocreatine that is then exported for recycling by extramitochondrial creatine kinases (Figure 4-2A). This creatine-dependent phosphate shuttle shortens the distance required for the slower diffusing adenylates between matrix-inter membrane space domains, thereby accelerating matrix ADP/ATP cycling and shifting the equilibrium towards ATP. Creatine attenuated mPTP (increased CRC) in the presence of 5mM ADP fixed by the hexokinase ATP recycling clamp (depletion of ATP; Figure 4-2B). This observation is consistent with a prior report showing the combination of creatine and ADP attenuated mPTP albeit in the absence of the hexokinase clamp [94]. We then determined whether the presence of the hexokinase clamp altered the effect of creatine. By re-analyzing the data in Figure 4-1B with a separate experiment of creatine and ADP in the absence of the hexokinase clamp, we no longer observed an effect of creatine on CRC (Figure 4-2C). Thus, the ability of creatine and ADP to attenuate mPTP was observed only in the presence of the hexokinase ATP recycling clamp. While speculative, this finding suggests that creatine's influence on matrix ADP/ATP cycling is accelerated with exogenous hexokinase which might be facilitated by the higher extramitochondrial [ADP], perhaps by increasing ADP diffusion back to the mitochondria. The precise manner by which adenylate cycling achieves a balance between both kinases is unclear and could be explored in future experiments.

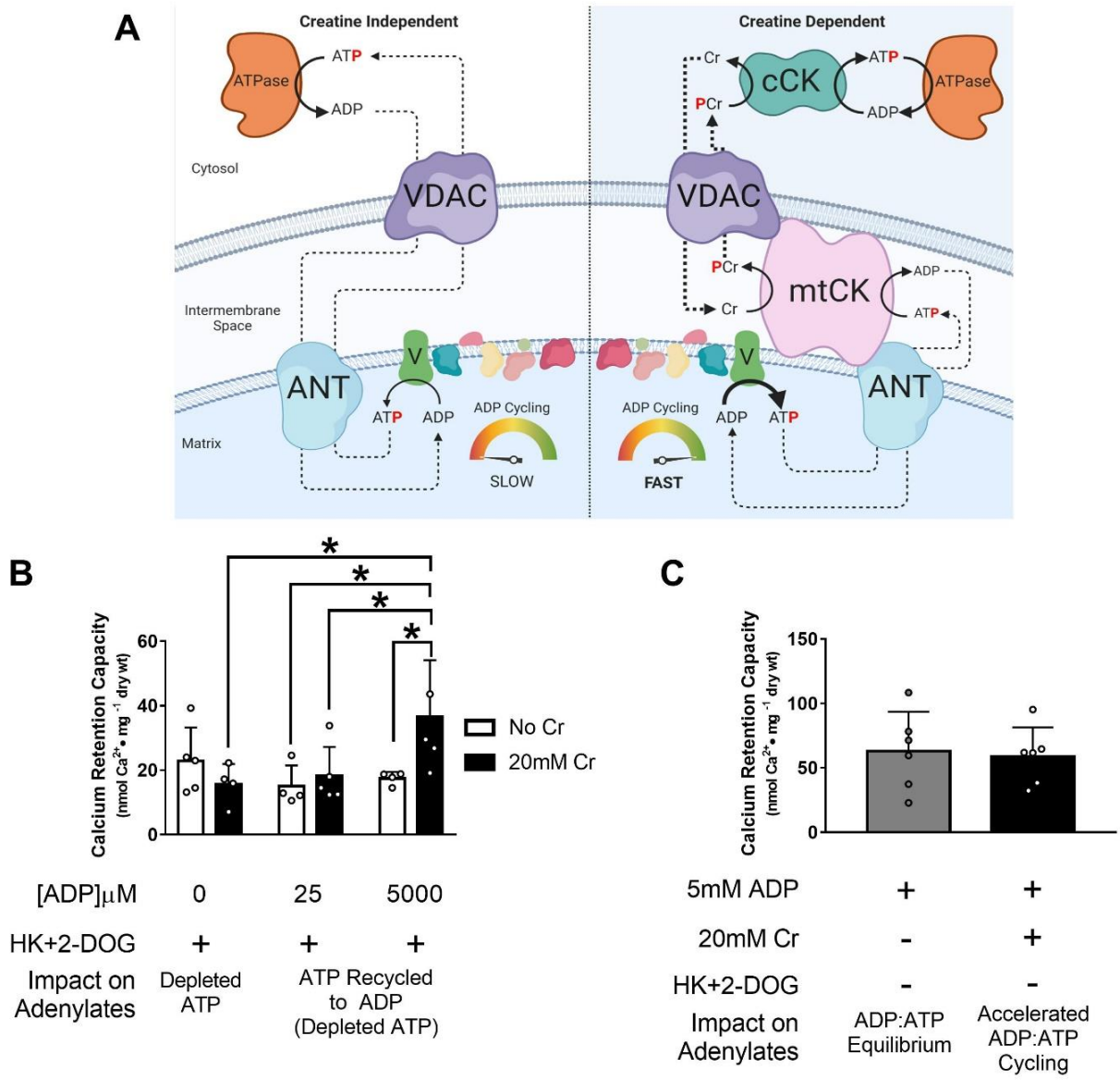

Figure 4-2. The effect of creatine on mitochondrial calcium retention capacity in mouse permeabilized quadriceps muscle fibre bundles. (A) The regulation of mitochondrial phosphate shuttling. In this system, matrix ATP is exported to the inner membrane space and dephosphorylated by mtCK. The phosphocreatine product is exported to the cytoplasm and recycled by cytosolic creatine kinases back to ATP. As creatine/phosphocreatine diffuses much faster than ADP/ATP, the system minimizes the diffusion distance of the more slowly diffusing adenylates to matrix-inner membrane space compartments and theoretically at local ATP-dependent proteins outside of the mitochondria (ATPases are depicted as only one example). The result is an accelerated turnover of matrix ADP/ATP and a higher rate of oxidative phosphorylation compared to the direct cycling of ADP and ATP between mitochondrial and cytoplasmic compartments as occurs in the absence of creatine in assay media. The experimental evidence for

this system is described previously [43-46, 53, 54, 479]. V, Complex V; mtCK, mitochondrial creatine kinase; ANT, adenine nucleotide translocase; VDAC, voltage-dependent anion carrier; cCK, cytosolic creatine kinase. Made with BioRender. (B) Mitochondrial calcium retention capacity was assessed in mouse quadriceps with creatine and ADP in assay media. All data was collected in the presence of the hexokinase 2-deoxyglucose clamp to eliminate ATP and maintain fixed concentrations of ADP. Creatine accelerates mitochondrial ADP/ATP turnover. (C) The effect of creatine on mitochondrial calcium retention capacity in the presence of ADP. Mitochondrial calcium retention capacity in the presence of ADP from Figure 4-1B was compared to a separate experiment including both ADP and creatine. Results represent mean ± SD; * $P<0.05$; n=4-6.

Thus, while the attenuation of mPTP by creatine in permeabilized fibres is similar to a previous report in isolated mitochondria [94], the requirement of the hexokinase clamp is difficult to explain and the discrepancy between both studies in the absence of the clamp is not apparent. It is unclear if these differences are related to the tissue source of isolated mitochondria wherein expression levels of mitochondrial creatine kinase might be higher in the livers that were genetically modified to express mitochondrial creatine kinase [94] as compared to quadriceps in this study, but such comparisons have not been performed. The assay conditions from this prior study also included 1mM ATP which would result in very low ADP. As creatine increases mitochondrial respiratory sensitivity to sub-maximal ADP concentrations in particular [46], future experiments could compare the effect of creatine with and without the hexokinase clamp at an even greater range of ADP concentrations used in the present study. Nevertheless, the results from Figure 4-1B and 4-1C suggest creatine attenuates CRC in permeabilized muscle fibre bundles from wildtype quadriceps when the hexokinase clamp is present.

One corollary of these findings is that the design of *in vitro* assessments of CRC might reveal distinct aspects of mPTP responses to a given biological stressor or context. For example, repeating CRC assessments with or without adenylates and/or creatine could give insight into whether their regulatory influence on mPTP is altered. To test this possibility, we compared CRC in the D2.*mdx* model of Duchenne muscular dystrophy to wildtype mice using permeabilized cardiac left ventricle fibres (Figure 4-3A-C). Previously, we demonstrated no difference between D2.*mdx* and wildtype CRC in this muscle, but the assay design did not combine ADP and creatine during *in vitro* assessments [22]. As this report also showed mitochondrial insensitivity to ADP and creatine during respiration and H_2O_2 emission, an outstanding question from this work is whether such insensitivity also applies to the regulation of mPTP. To test this possibility, we performed new

experiments in D2.*mdx* and wildtype mouse permeabilized left ventricle fibres. We excluded the hexokinase clamp to permit a natural equilibration of ADP and ATP given the results from Figure 4-1B demonstrated that an equilibrium of both adenylates is more effective at regulating CRC vs the presence of ADP alone. As shown in Figure 4-3, there were no differences between D2.*mdx* and wildtype CRC whether it was assessed with ADP with or without creatine. This suggests that the prior discovery that mitochondrial creatine insensitivity occurs during respiration and H_2O_2 emission [23] does not manifest as a loss of creatine control of mPTP, at least at this young stage of disease (4 weeks of age), in left ventricle, and when creatine is combined with high ADP concentrations (5mM). While we chose a high ADP concentration for the current experiment, we did not rule out whether creatine would have a different effect at low ADP concentrations in D2.*mdx* mice which is plausible given creatine sensitizes mitochondria to sub-maximal ADP concentrations [46]. Nevertheless, the similar results with either *in vitro* protocol strengthens the prior conclusion [22] that calcium-induced mPTP is not altered in the left ventricle at an early stage of myopathy in dystrophin deficient mice. In so doing, there is clear value in comparing multiple assay conditions when assessing CRC. Lastly, while we reached a similar conclusion with either *in vitro* assay design, our choice of model and muscle type is only one of many biological contexts that could be considered. In this light, the clear influence of ADP and creatine on CRC in quadriceps (Figures 4-1 and 4-2) demonstrates the potential opportunity of identifying unique conclusions of how CRC is regulated by adenylates and creatine when designing investigations focused on a variety of biological contexts.

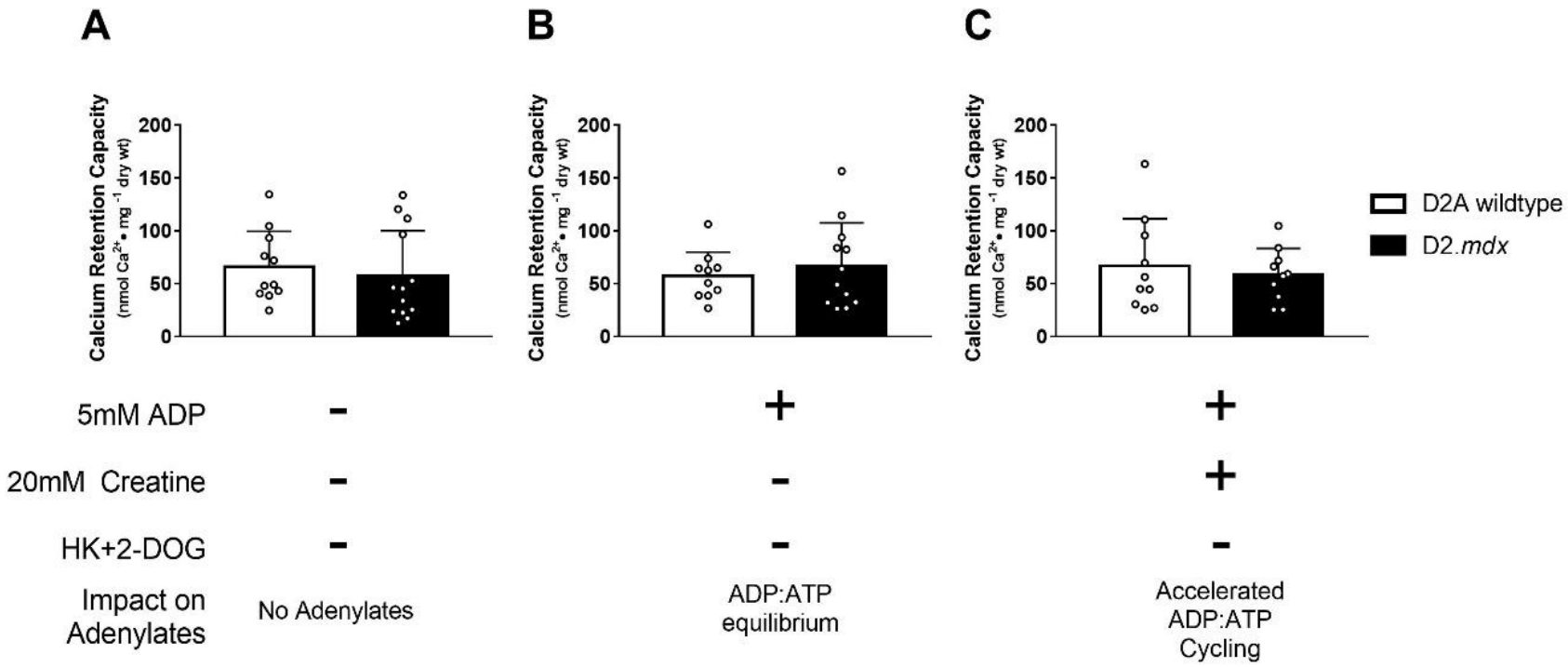

Figure 4-3. The effects of creatine and ADP on mitochondrial calcium retention capacity in mouse permeabilized left ventricle fibre bundles from D2.*mdx* mice. Mitochondrial creatine retention capacity was assessed in permeabilized fibres from 4-week-old D2A wildtype and D2.*mdx* mice. First, CRC was assessed in the absence of both ADP and creatine (A). Next, CRC was assessed in the presence of 5mM ADP and the absence (B) or presence of creatine (C). The hexokinase 2-deoxyglucose clamp was eliminated to ensure the presence of both ADP and ATP through natural equilibrium pathways endogenous to permeabilized muscle fibres. N=10-13.

Perspectives, Limitations and Conclusions

These results demonstrate that *in vitro* assessments of calcium-induced mPTP in permeabilized muscle fibres are influenced by adenylates. Specifically, calcium-induced mPTP is suppressed by exogenous additions of ADP compared to ADP combined with a hexokinase 2-deoxyglucose system of recycling ATP to ADP. As ADP equilibrates with ATP in permeabilized muscle fibres, this finding indicates that the suppression of mPTP by exogenous ADP is due to the presence and cycling of both ADP and ATP. In quadriceps muscle, combining creatine with ADP also suppresses mPTP but only when the hexokinase clamp is present. This finding warrants similar considerations for future experiments in permeabilized systems across cell types and species and using a range of ADP and creatine concentrations. Likewise, consideration of other exogenously added adenylate recycling systems could be considered including the ADP to ATP recycling clamp created by pyruvate kinase and phosphoenol pyruvate [480] or clamping ADP and ATP at calculated ratios [481].

For perspective, while the hexokinase ATP to ADP recycling system would eliminate extra-mitochondrial ATP, it is unlikely to completely eliminate matrix ATP as adenylates will continue to cycle. However, it seems likely that an attenuation of ATP occurs in the matrix which is thought to be the location where adenylates regulate mPTP. However, one study suggested there may also be an adenylate regulatory site of the mPTP outside of the matrix [474]. Overall, it seems plausible that the hexokinase clamp reduces the net exposure of mPTP to ATP as intended.

Collectively, these results demonstrate the impact of modeling adenylate cycling on calcium retention capacity-based assessments of mPTP in permeabilized muscle fibres. Careful consideration of the relevance of adenylate cycling to a given experimental question could influence the design of *in vitro* assessments in permeabilized muscle fibres with the aim of gaining greater insight into the regulation of mPTP in various biological contexts.

Abbreviations

CRC	Calcium retention capacity	mPTP	Mitochondrial permeability transition pore
H_2O_2	Hydrogen peroxide		

Acknowledgements

Funding was provided to C.G.R.P. by the Natural Science and Engineering Research Council (no. 436138-2013) and an Ontario Early Researcher Award (C.G.R.P., no. 2017-0351) with infrastructure supported by Canada Foundation for Innovation, the James. H. Cummings Foundation, and the Ontario Research Fund. M.C.H. and C.A.B. were supported by NSERC CGS and PGS scholarships, respectively. S.V.R. was supported by an Ontario Graduate Scholarship. SS was supported by the Danish Diabetes Academy supported by the Novo Nordisk Foundation research grant and Danish Diabetes Association Travel Grant.

Chapter 5: Mitochondrial creatine sensitivity is lost in the D2.*mdx* model of Duchenne muscular dystrophy and rescued by the mitochondrial-enhancing compound Olesoxime

This chapter is an original published article. It is presented in its published form.

Mitochondrial creatine sensitivity is lost in the D2.mdx model of Duchenne muscular dystrophy and rescued by the mitochondrial-enhancing compound Olesoxime. CA Bellissimo, LJ Delfinis, MC Hughes, PC Turnbull, S Gandhi, SN DiBenedetto, FA Rahman, P Tadi, C Amaral, A Dehghani, JN Cobley, J Quadrilatero, U Schlattner, and CGR Perry. American Journal of Physiology- Cell Physiology. DOI: 10.1152/ajpcell.00377.2022

Assay Development Prior to the Start of Project 1:

1. Six Minute Voluntary Movement Tracker
2. Cryosection of OCT Embedded Tissue
3. Hematoxilyn and Eosin,Picrosirius Red Staining and Immunofluorescent determination of myosin heavy chain
    a. This method adapted for in house use and was utilized in again in chapters 5 and 6. Further, this technique benefited the collaborative aspect of my PhD where I instructed laboratory members in proper cryosection and histological techniques that was utilized in Delfinis et al (2022), Chapter 6 and other projects underway. I additionally established the in-house protocol for immunofluorescent detection of myosin heavy chain that was similarly performed in this study by collaborators and utilized in Chapter 6.
4. Reduced thiol detection of mtCK

Author Contributions: The majority of the experiments for this study were performed by Catherine A Bellissimo (CAB). CAB maintained the breeding colony required for this project as well as subsequent studies (Chapters 5-7) after being established by MCH. CAB and LJD performed oral gavages and all whole body muscle function test (cage hang time, grip strength, voluntary running wheel). CA completed all voluntary movement tracking after training from

CAB. CAB completed µCT scans with PT completing analysis. CAB completed *in vitro* diaphragm force assessments and analysis. Tissue harvests were performed by CAB with LJD, AD and SND aiding in tissue processing after collection. CAB separated all muscle fibres bundles. CAB and LJD performed all mitochondrial bioenergetic assays (respiration, mH2O2 emission and calcium retention capacity) with CAB and SG performing analysis. Due to the nature of bioenergetic assessments, two people are required to perform these assays efficiently on fresh viable tissue. PCT performed all glutathione measurements with assistance from CAB on tissue preparation. CAB and SND performed all immunohistochemistry staining and analysis. FAR performed immunofluorescent detection of skeletal muscle fibre type and analysis. CAB performed all serum CK, western blotting, reduced thiol detection of mtCK, caspase assays, subsequent analyses and statistical testing. CAB and CGRP wrote the manuscript with all co-authors aiding in revision.

Mitochondrial creatine sensitivity is lost in the D2.*mdx* model of Duchenne muscular dystrophy and rescued by the mitochondrial-enhancing compound Olesoxime

C.A. Bellissimo[1], L.J. Delfinis[1], M.C. Hughes[1], P.C. Turnbull[1], S. Gandhi[1]., S.N. DiBenedetto[1], F.A. Rahman[2], P. Tadi[1], C. Amaral[1], A. Dehghani[1], J.N. Cobley[3], J. Quadrilatero[2], U. Schlattner[4], and *C.G.R. Perry[1]

[1]School of Kinesiology & Health Science, Muscle Health Research Centre, York University, Toronto, ON M3J 1P3 Canada.

[2]Faculty of Health, Department of Kinesiology and Health Sciences, University of Waterloo, Waterloo, ON N2L 3G1, Canada

[3]Redox Biology Group, University of the Highlands and Islands, Centre for Health Sciences, Inverness, IV2 3JH UK

[4]University Grenoble Alpes and Inserm U1055, Laboratory of Fundamental and Applied Bioenergetics, Grenoble, France, and Institut Universiatire de France, Paris, France

Address for correspondence:

*Christopher G. R. Perry, PhD

cperry@yorku.ca

Running Head: Enhancing mitochondria in Duchenne muscular dystrophy

Supplemental Material available at:

DOI: https://doi.org/10.6084/m9.figshare.21843543

Graphical Abstract

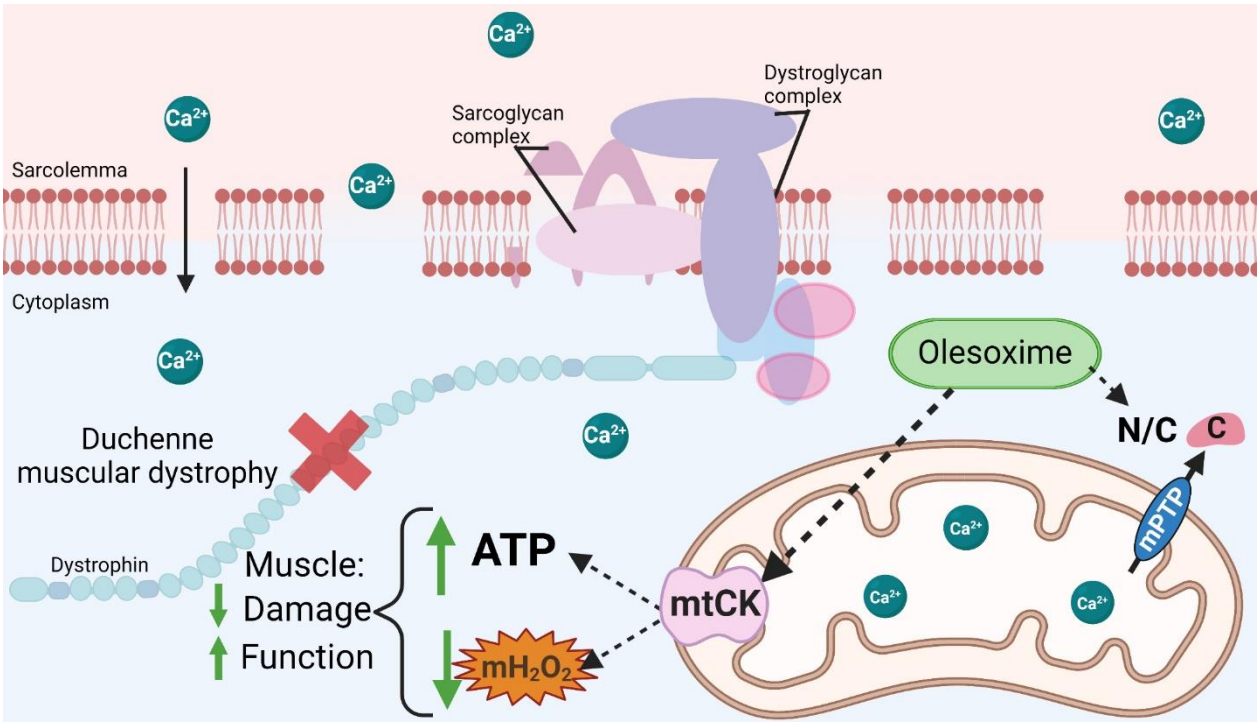

Abstract

Duchenne muscular dystrophy (DMD) is associated with distinct mitochondrial stress responses. Here, we aimed to determine whether the prospective mitochondrial-enhancing compound Olesoxime prevents early-stage mitochondrial stress in limb and respiratory muscle from D2.*mdx* mice using a proof-of-concept short-term regimen spanning 10-28 days of age. As mitochondrial-cytoplasmic energy transfer occurs via ATP- or phosphocreatine-dependent phosphate shuttling, we assessed bioenergetics with or without creatine *in vitro*. We observed that disruptions in Complex I-supported respiration and H_2O_2 emission in D2.*mdx* quadriceps and diaphragm were amplified by creatine demonstrating mitochondrial creatine insensitivity manifests ubiquitously and early in this model. Olesoxime selectively rescued or maintained creatine sensitivity in both muscles, independent of the abundance of respiration-related mitochondrial proteins or mitochondrial creatine kinase cysteine oxidation in quadriceps. Mitochondrial calcium retention capacity and glutathione were altered in a muscle-specific manner in D2.*mdx* but were generally unchanged by Olesoxime. Treatment reduced serum creatine kinase (muscle damage) and preserved cage hang-time, microCT-based volumes of lean compartments including whole body,

hindlimb and bone, recovery of diaphragm force after fatigue, and cross-sectional area of diaphragm type IIX fibre, but reduced type I fibres in quadriceps. Grip strength, voluntary wheel-running and fibrosis were unaltered by Olesoxime. In summary, locomotor and respiratory muscle mitochondrial creatine sensitivities are lost during early stages in D2.*mdx* mice but are preserved by short-term treatment with Olesoxime in association with specific indices of muscle quality suggesting early myopathy in this model is at least partially attributed to mitochondrial stress.

Introduction

Duchenne muscular dystrophy (DMD) is a debilitating and progressive muscle wasting disease resulting from a mutation in the gene encoding the protein dystrophin [111, 482]. By connecting the cytoskeleton to the sarcolemma, dystrophin promotes membrane stability during muscle contraction and is a key component of the dystroglycan complex that cross-links the cytoskeleton to the extracellular matrix. The absence of dystrophin results in cell membrane instability and muscle fibre tearing during contraction [483]. Constant cycles of fibre degeneration are associated with considerable inflammation as well as many intracellular stressors including elevated cytosolic calcium, cytoskeletal disorganization, and both redox and metabolic abnormalities. Each of these disruptions have been associated with mitochondrial stress responses [256], but the degree to which mitochondria contribute to muscle weakness in DMD remains to be determined.

The emergence of mitochondrial enhancing therapeutics provides an opportunity to revisit the role of mitochondrial stress in a variety of diseases. However, in some cases, the potential clinical efficacy of the compounds somewhat outpaces the discovery of their mechanisms of action. For example, the cholesterol-based compound Olesoxime (cholest-4-en-3-one oxime, or TRO1966) promoted motor neuron survival, improved motor performance, and extended lifespan using *in vitro* and *in vivo* models of amyotrophic lateral sclerosis (ALS) [429]. While mitochondrial assessments were not performed in these models, separate experiments in a variety of brain-derived cell lines found that Olesoxime accumulated in mitochondria [428] and interacted with the voltage dependent anion channel (VDAC) [429]. This protein was considered to be a putative component of the pro-apoptotic mitochondrial permeability transition pore (mPTP), and several effects attributed to mPTP inhibition were reported. These include reduced mitochondrial-linked apoptosis in cultured motor neurons [429], in a rat model of Huntington's [430] and camptothecin

chemotherapy exposure [431], as well as other anti-mPTP effects in HeLa cells [428] and in cardiomyocytes exposed to doxorubicin chemotherapy [428]. These lines of evidence suggest a potential to treat other conditions that present with dysregulated mPTP. However, the effect of Olesoxime on other mitochondrial bioenergetic functions in conditions causing mitochondrial stress remains unclear.

The degree to which Olesoxime may benefit muscle-weakness disorders remains uncertain. Clinical trials of spinal muscle atrophy yielded mixed results [25, 27, 484-486], while some studies in mouse models of DMD reported increased mPTP [23, 25, 27]. Thus, further investigation into the potential for Olesoxime to treat muscle weakness in *mdx* mice seems warranted, especially one with an expanded assessment of bioenergetic functions relevant to muscle weakness including oxidative phosphorylation and reactive oxygen species generation. We also assessed the ability of calcium stress to trigger mPTP given the excess cytosolic calcium in dystrophic fibres are thought to contribute to fibre degeneration, and Olesoxime's effects on calcium as a specific trigger of mPTP is less studied. As Olesoxime passed Phase I clinical trials for safety [433, 434], any potential benefit of this drug in other disorders could be translated to clinical applications more rapidly.

In this study, we employed a short-term treatment protocol as a proof-of-principle design that targets the early stages of myopathy in the D2.*mdx* mouse model of DMD given we have previously characterized several relationships between muscle dysfunction and mitochondrial stress, including mPTP, at 4 weeks of age in this model [22-24]. Here, we report a novel effect by which Olesoxime protects mitochondrial bioenergetics by preserving mitochondrial function of creatine. This effect was found in both locomotor and respiratory muscles, suggesting a ubiquitous mechanism. This improved mitochondrial creatine sensitivity was generally linked to preserving oxidative phosphorylation and attenuating increased mitochondrial hydrogen peroxide emission (mH_2O_2), but surprisingly not calcium-induced mPTP. This short-term treatment protocol at early stages of the disease led to a robust reduction in the muscle damage marker serum creatine kinase as well as modest benefits to various indices of muscle quality. The findings indicate attenuated mitochondrial creatine functions may be one component of the stressors influencing early stages of myopathy during dystrophin deficiency which warrants longer term investigations.

Materials and Methods

Animal Care

Male D2.*mdx* mice were bred from an in-house colony established at York University (Toronto, Ontario). Mice were housed with littermates until sacrifice (28 day) and then were separated for functional testing commencing 48 hours prior to sacrifice. 3 week-old DBA/2J WT mice were ordered directly from Jackson Laboratories (Bar Harbor, USA) due to low breeding performance experienced in-house as reported previously [487] and allowed to acclimatize for 7 days prior to sacrifice. Mice were maintained on a 12:12-h light-dark cycle while being provided access to standard chow and water ad libitum. All experiments and procedures were approved by the Animal Care Committee at York University (AUP Approval Number 2016-18) in accordance with the Canadian Council on Animal Care.

Olesoxime Treatment

D2.*mdx* mice were treated with Olesoxime (30mg/kg body weight/day) dissolved in corn oil [429, 435, 488] or corn oil alone via oral gavage adapted for young pups [489]. Treatment lasted from 10 days of age to 28 days (up to 30 days of age).

Body Composition and Functional Assays

In vivo computed tomography was assessed as previously described [23] with threshold for fat free mass set to 39-50 and normalized to body weight in grams. Voluntary wheel running, cage hang time and forelimb grip strength were assessed as described previously [23].

6 Minute Voluntary Movement Tracker

Voluntary ambulation was monitored according to the protocol established by Gibbs et al. [490]. Animals were placed in an open field container and movement was recorded for 6 minutes and analyzed using Kinovea software (kinovea.org). The cumulative distance moved in centimeters over the 6-minute period was recorded.

Serum Creatine Kinase

Serum creatine kinase activity (U/L) was assessed spectrofluorometrically (QuantaMaster 80, HORIBA; emission 450nm) using the Pointe Scientific Serum Creatine Kinase Kit (Pointe

Scientific, Canton, MI, USA) and calculated from the rate of NADPH production applied to a standard curve performed under the same conditions and volume dilution as samples.

In-Vitro Diaphragm Force

Assessment of *in-vitro* diaphragm force has been partially adapted from [491, 492]. Briefly, the entire diaphragm was excised and placed in ice cold Ringer solution containing (in mM) 121 NaCl, 5 KCl, 1.8 $CaCl_2$, 0.5 $MgCl_2$, 0.4 $NaHPO_4$, 24 $NaHCO_3$, 5.5 glucose and 0.1 EDTA; pH 7.3. A diaphragm strip, no more then 3-4mm in width, from the lateral costal hemidiaphragm was cut with adjacent sections of the rib and part of the central tendon as demonstrated in [493]. Silk suture was attached to the central tendons and the ribs and secured in a bath with oxygenated Ringers solution (95% O_2/5% CO_2) maintained at 25°C with ribs secured to the force transducer with an s hook and central tendon to the lever arm. The diaphragm was positioned between two platinum electrodes driven by a biphasic stimulator (Model 305C; Aurora Scientific, Inc., Aurora, ON, Canada) and allowed to acclimatize for 30 minutes. Optimal resting length (L_0) was found using single twitches until maximal force was attained. A force-frequency curve was performed (1,10,20,40,60,80, 100, 120, 140Hz) with 1 minute of rest between contractions with a final 5- minute rest period provided before a fatiguing protocol was performed (70Hz for 350ms every 2 seconds for 5 minutes). Recovery from fatigue was assessed at 5-, 10- and 15-minutes post fatigue at the frequency that elicited maximum force in the force-frequency protocol. Force production was analyzed using Dynamic Muscle Control Data Acquisition software (Aurora Scientific, Inc) and normalized to cross sectional area (CSA) of the muscle strip (m/l*d) where m is the mass of the strip devoid of the central tendon and ribs, l is the length (from the point of insert on the ribs to the myotendinous junction of the central tendon) and d is the mammalian skeletal muscle density (1.06g/mm^3) [494].

Preparation of permeabilized muscle fibre bundles

This technique was adapted from previous methods as described elsewhere [23, 495]. Quadriceps and diaphragm muscles were excised carefully from mice while under heavy sedation using isoflurane. A piece of the non-stimulated quadriceps or diaphragm was removed and placed immediately into ice-cold BIOPS containing (in mM) 50 MES Hydrate, 7.23 K_2EGTA, 2.77 CaK_2EGTA, 20 imidazole, 0.5 dithiothreitol, 20 taurine, 5.77 ATP, 15 PCr, and 6.56 $MgCl_2 \cdot 6\ H_2O$ (pH 7.1). Both muscles were trimmed of connective tissue and fat and separated along the longitudinal axis into small bundles weighing approximately 1.0-2.5mg wet weight for respiration

and mH_2O_2 and 0.5-1.4mg wet weight for calcium retention capacity. Bundles were permeabilized with 40µg/µL saponin (Sigma Aldrich; St. Louis, MI, USA) in BIOPS on a platform rotor for 30 minutes at 4°C. The permeabilized bundles were then transferred to wash buffers to remove saponin as follows: MiRO5 for mitochondrial respiration, Buffer Z for mitochondrial H_2O_2 emission (mH_2O_2), and Buffer Y for calcium retention capacity. The composition of each buffer has been described previously [23]. Fibres prepared for complex I-supported mitochondrial H_2O_2 emission (mH_2O_2) were permeabilized in the presence of 35µM 2,4-dinitrochlorobenzene (CDNB) to deplete glutathione and allow for detectable rates of mH_2O_2 [496]. All bioenergetic assays were performed within 4 hours of washing to maintain fibre viability.

Mitochondrial respiration

Mitochondrial respiration was performed as described in [23, 495]. High resolution oxygen consumption was performed in 2mL of MiRO5 supplemented with (creatine-dependent) or without (creatine independent) 20mM creatine to saturate mitochondrial creatine kinase activity [495, 497] to permit assessments of mitochondrial creatine sensitivity. O_2 consumption was measured using the Oroboros Oxygraph-2K (Oroboros Instruments, Corp., Innsbruck, Austria) while stirring at 37°C in the presence of 5µM blebbistatin to prevent spontaneous muscle fibre contraction in response to ADP [495]. Each chamber was oxygenated with 100% pure O_2 to an initial concentration of ~350 µM and experiments were completed before chamber [O_2] reached 150 µM [498, 499]. Prior to permeabilization, fibre bundles were gently and quickly blotted, weighed in ~1.5 mL of tared cold BIOPS (ATP-containing relaxing media) to ensure fibres remained relaxed. Respiration was normalized to bundle wet weight. Complex I-supported respiration was stimulated using 5mM pyruvate and 2mM malate (NADH) followed by a titration of ADP concentrations from physiological ranges (25, 100) to supraphysiological (500) and saturating to stimulate maximal coupled respiration (5000 µM). An addition of 10µM cytochrome c was added to test mitochondrial outer membrane integrity. Experiments with low ADP-stimulated respiration (bundles that did not respire in response to ADP stimulus) or high cytochrome c responses (>15% increase in respiration) were removed (17 out of 192 bundles). Lastly, 20mM succinate ($FADH_2$) was added to support complex-II respiration.

Mitochondrial H_2O_2 Emission (mH_2O_2)

mH_2O_2 emission was performed as described [23]. mH_2O_2 was determined spectrofluorometrically (QuantaMaster 40, HORIBA Scientific, Irvine, CA, USA) utilizing Buffer Z containing 10μM Amplex Ultra Red (Life Technologies; Carlsbad, CA, USA), 1U/mL horseradish peroxidase, 1mM EGTA, 40U/mL Cu/Zn SOD1, 5μM blebbistatin and 20mM Cr. Complex I-supported mH_2O_2 was initiated through the addition of 10mM pyruvate and 2mM malate (NADH; forward electron flow) and separately with 10mM succinate ($FADH_2$; reverse electron flow from Complex II to I). The ability of ADP to suppress mH_2O_2 was assessed with a titration of physiological concentrations (25, 100) and saturating for oxidant generation (500μM). All protocols were repeated without creatine in the assay buffer to permit comparisons with the creatine condition, thereby allowing assessments of mitochondrial creatine sensitivity. Bundles were lyophilized in a freeze-dryer (Labconco, Kansas City, MO, USA) for >4 h and weighed on a microbalance (Sartorius Cubis Microbalance, Gottingen, Germany).

The rate of mH_2O_2 emission was calculated and converted to [mH_2O_2] using a standard curve under the same assay conditions and then normalized to fibre bundle dry weight.

Mitochondrial calcium retention capacity

Mitochondrial calcium retention capacity was performed as previously described but with modifications [23, 477]. This assay was measured spectrofluorometrically (QuantaMaster 80, HORIBA Scientific) in a cuvette with 300μL assay buffer containing 1 μM Calcium Green-5N (Invitrogen), 2 μM thapsigargin, 5 μM blebbistatin, and 40 μM EGTA while maintained at 37°C with continuous stirring. 5mM glutamate, 2mM malate, 5mM ADP and 20mM creatine were added to the assay buffer and minimum fluorescence was recorded. 4nmol pulses of $CaCl_2$ were added until the mitochondrial permeability transition pore (mPTP) opening was observed as an increase in fluorescence corresponding to net mitochondrial calcium release, at which point saturating pulses of $CaCl_2$ were used to establish maximum fluorescence. Changes in free Ca^{2+} during mitochondrial Ca^{2+} uptake were then calculated using the known K_d for Calcium Green-5N and equations established for calculating free ion concentration [478]. Calcium retention was then normalized to fibre bundle dry weight.

Histochemical & Immunofluorescent Staining

Excised quadriceps and diaphragm were mounted for histology and immunofluorescence in Tissue Plus Optimal Cutting Temperature compound (OCT; Fisher Healthcare), frozen in isopentane chilled in liquid nitrogen and stored at -80°C. Sample collected were cut into 10µm thick serial cross sections with a cryostat (Thermo Fisher Scientific; Kalamazoo, MI, United States;) maintained at -20°C on Fisherbrand Superfrost Plus slides (Thermo Fisher Scientific). Hematoxylin and eosin (H&E) and picrosirius red (PSR) staining was used to assess muscle health and fibrosis as previously described [23]. Centralized nuclei, a marker of regenerating fibres, was analyzed by selecting five evenly spaced images throughout the muscle and averaging the result. Areas of necrosis (fibres with fragmented sarcoplasm and immune cell infiltration) were expressed as a percentage of the entire muscle section. PSR staining was used to assess fibrotic regions and was expressed as a percentage of whole muscle section. Images were taken using EVOS M7000 imager (Thermo Fisher Scientific) using 20X magnification and analyzed using ImageJ (http://imagej.nih.gov/ij/). Immunofluorescent analysis of myosin heavy chain expression was previously described [500]. Images were taken with EVOS M7000 equipped with standard red, green, blue filters cubes. Fibres that were not positively stained were considered IIX fibres. These images were then analyzed with ImageJ for fibre type distribution and cross-sectional area (CSA).

Caspase Activity

The enzymatic activities of caspase 3, 8 and 9 were measured spectrofluorometrically using substrates Ac-DVED-AMC, AC-IETD-AMC and Ac-LEHD-AMC (Enzo Life Sciences, Farmingdale, NY) respectively, as described elsewhere [501, 502]. Samples were homogenized in ice cold lysis buffer without protease inhibitors and pipetted into a 96 well plate where they were incubated with appropriate substrate. Fluorescence was read for 1 hour and maximal activity was recorded and normalized to the total protein content.

Glutathione

Reduced glutathione (GSH) and oxidized glutathione (GSSG) were assessed by UV-HPLC and fluorescent HPLC respectively using the Shimadzu Nexera X2 UHPLC system (Mandel Scientific Company Inc. Guelph, Canada). Quadriceps and diaphragm muscles were prepared according to [503] in tris buffer (50 mmol/L Tris (hydroxymethyl) amino methane buffer containing 20 mmol/L Boric acid, 2 mmol/L L-serine, 20 µmol/L Acivicin, and 5 mmol/L *N*-ethylmaleimide (NEM)) and acidified using TCA and PCA for GSH and GSSG, respectively. Separation was achieved using a

Zorbax C18 column (Agilent Technologies, Mississauga, ON, Canada). GSH was measured under isocratic conditions by monitoring NEM-GSH using a 0.25% glacial acetic acid mobile phase with 6% acetonitrile at 1.05ml/min flow rate detected at 265nm. GSSG was measured using GS-o-pthalymide (0.1%) conjugate excited at 350nm and detected at 420nm emission using HPLC/UHPLC fluorescence detector (Mandel Scientific). GSSG samples were diluted in 0.5M NaOH and run using 25mM Na_2HPO_4 in HPLC-grade H_2O with 15% methanol mobile phase at a 0.5mL/min flow rate. Distinct standard curves were applied to both GSH and GSSG and all samples were normalized to protein content measured using bicinchoninic acid protocols (Life Technologies, Carlsbad, CA, USA).

Western Blotting

Western blotting was performed to determine expression levels of VDAC, adenine nucleotide translocase (ANT), electron transport chain proteins (OXPHOS) and mitochondrial creatine kinase (mtCK) using standard SDS-PAGE procedures. Frozen sections of quadriceps and diaphragm from each muscle (approximately 10-30mg in size) were homogenized using a plastic microcentrifuge tube with tapered Teflon pestle in ice-cold buffer containing (in mM) 40 Hepes, 120 NaCl, 1 EDTA, 10 $NaHP_2O_7 \cdot 10H_2O$ pyrophosphate, 10 β-glycerophosphate, 10 NaF, and 0.3% CHAPS detergent (pH 7.1 adjusted using KOH) supplemented with protease inhibitor (1:200) and phosphatase 2/3 inhibitors (1:100). A 10% acrylamide gel was used for mtCK while all other proteins were resolved using a 12% acrylamide gel. All gels were transferred onto 0.2µm low fluorescence PVDF membrane (Bio-Rad, Mississauga, Canada) and blocked with Li-COR Odyssey Blocking Buffer (LI-COR, Lincoln NE, USA) for 1 hour. Membranes were then incubated with specific primary antibodies (listed below) overnight at 4°C. A commercially available monoclonal rodent OXPHOS Cocktail (ab110413; Abcam, Cambridge, UK, 1:250 dilution) including V-ATP5A (55 kDa), III-UQCRC2 (48 kDa), IV-MTCO1 (40 kDa), II-SDHB (30 kDa), and I-NDUFB8 (20 kDa) were used to detect electron transport chain proteins. Commercially available polyclonal antibodies were used to detect VDAC 2 (32059, 33 kDa; Santa-Cruz, 1:1000) and ANT 1 (ab180715, 32 kDa; Abcam, 1:1000). The primary antibody for mtCK was a polyclonal serum based primary antibody kindly provided by Dr Uwe Schlattner (Grenoble, France; 42 kDa, 1:1000) and has been previously validated [504]t. After overnight primary antibody incubation, membranes were washed three times (5 minutes each time) in TBS-T and incubated at room

temperature with appropriate fluorescent secondary antibody (LI-COR). Prior to detection, membranes were washed in TBS-T three times for 5 minutes and then imaged using infrared imaging (LI-COR CLx; LI-COR, Lincoln, NE, USA) and quantified by densitometry (ImageJ, http://imagej.nih.gov/ij/). All images were normalized total protein assessed between 25-75kDa from the same membrane stained using Amido Black total protein-stained membrane (A8181, Sigma). Western blots were at times performed on tissues from separate mice than those used for mitochondrial bioenergetics and histology given the very small muscles at this young age, particularly in the D2.*mdx* groups, were insufficient for all analyses in this study. As such, bioenergetics data were not normalized to western blot markers of the mitochondrial proteins outlined above.

Reduced thiol detection of mtCK

The redox state of mtCK thiols was assessed by labeling free thiol using IR-Dye 800CW-maleimide (LiCor Biotechnology, Lincoln, NE, USA) as described previously but with slight modifications [505, 506]. Briefly, quadriceps tissue was homogenized in lysis buffer (25 mM Tris-HCl pH 7.2, 150 mM NaCl, 1 mM EDTA, 1% NP-40 and 5% glycerol supplemented with a fresh protease inhibitor tablet). Samples were incubated overnight at 4°C with IR-Dye 800CW at 100nM/200µg total protein. Samples were then spun through Zeba desalting columns (Exclusion size: 7 kDa MW cutoff; Thermo Fisher Scientific) twice, to remove excess dye and small free thiols that could sequester the dye, and a protein concentration was determined using a BCA assay. 1mg of Protein G SureBeads (Bio-Rad) were incubated with 1µg s-mtCK (Santa Cruz Biotechnology) for 10 minutes at room temperature followed by 600µg of IR-Dye 800CW-labelled proteins, incubating overnight at room temperature. Bound proteins were then eluted with 20mM glycine (pH 2.0) and were subjected to 10% SDS-PAGE. The gels were scanned using infrared imaging (LI-COR CLx) and quantified by densitometry (ImageJ). In this assay (essentially macroscale ALISA [507]), target-specific redox state is calculated as (IR-MAL/Total target), with total mtCK being determined via immunoblot. An increase in reversible cysteine oxidation would manifest as a loss of IR-MAL signal.

Statistics

Results are expressed as means ± SD with the level of significance established as $P < 0.05$ for all statistics. Prior to statistical analyses, outliers were omitted in accordance with ROUT testing

(Q=0.5%) and then tested for normality using a D'Agostino–Pearson omnibus normality test (GraphPad Prism Software, La Jolla, CA, USA). State III respiration and mH_2O_2 were analyzed using a two-way ANOVA followed by uncorrected Fisher LSD post hoc testing when appropriate given the risk for false discovery rate is very low with a 3-group design [508, 509]. For all other data, statistical differences were analyzed using a one-way ANOVA (or Kruskal-Wallis for non-parametric results) between all 3 groups followed by uncorrected Fisher LSD or uncorrected Dunn's test (when non-parametric) post hoc analyses where appropriate. To assess creatine sensitivity in bioenergetic measurements, a two-way ANOVA within groups was applied to data collected at 100 and 500µM ADP were examined given that 25µM and 5mM ADP are less sensitive to creatine.

Results

Olesoxime preserves mitochondrial bioenergetics in a creatine-dependent manner

To study the effect of Olesoxime on mitochondrial bioenergetics, we determined mitochondrial respiration (a measure of oxidative phosphorylation) and H_2O_2 generation (a product of electron slip from the electron transport chain) in permeabilized fibre bundles of three experimental groups: wildtype mice (WT), D2.*mdx* mice (D2.*mdx*), and D2.*mdx* mice treated with Olesoxime for 18 d (Olesoxime). We designed *in vitro* assays that distinguish two different pathways of energy transfer between mitochondria and cytoplasm (Figure 5-1): respiratory stimulation by either ADP alone or a combination of ADP and creatine. The latter creatine-stimulated respiration accelerates intramitochondrial recycling of ADP and export of phosphocreatine, an energy-rich intermediate that is more highly concentrated and diffusible as compared to ADP [43-46, 53, 54, 479]. As the effect of creatine and mitochondrial respiration in general depend on ADP concentration, the primary signal of cellular energy turnover, we also analyzed a range of ADP concentrations.

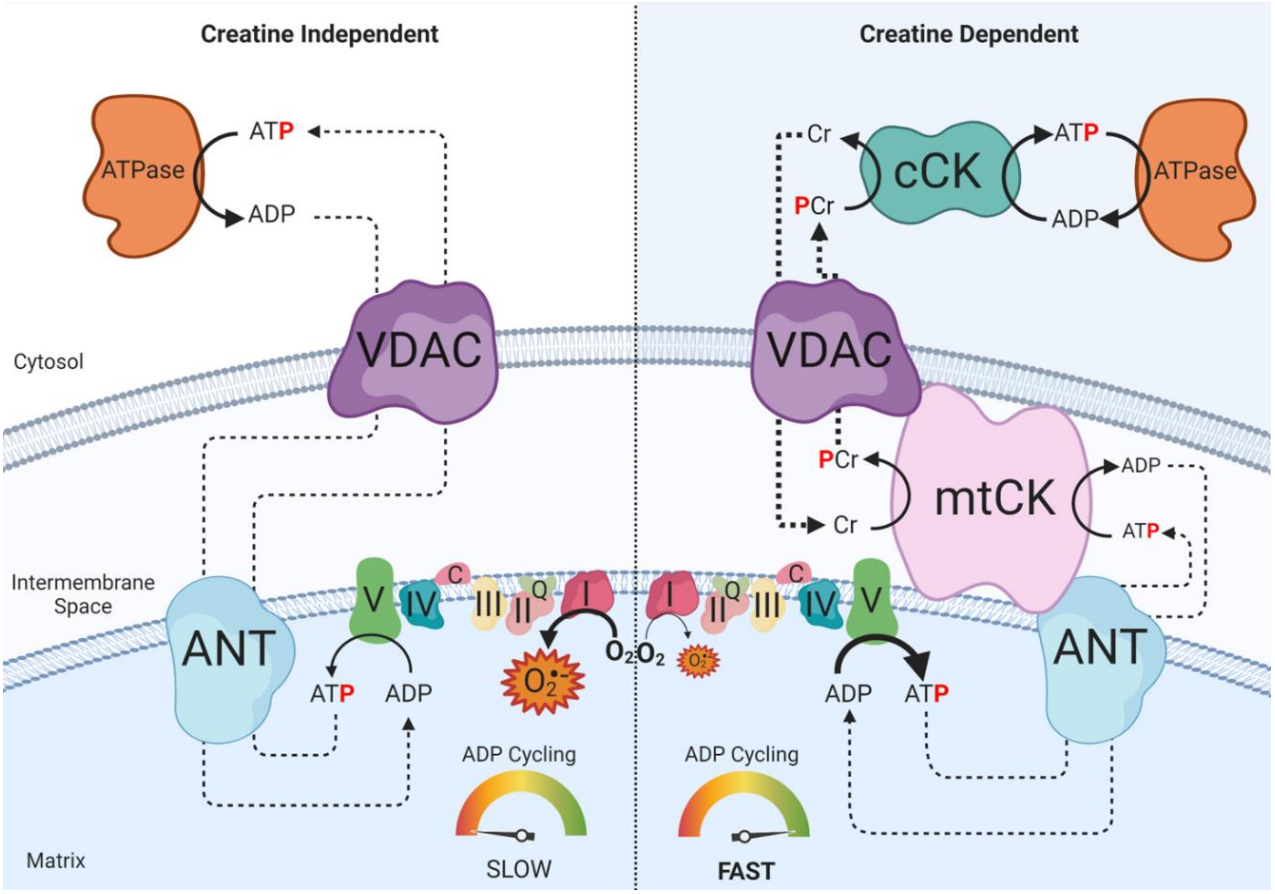

Figure 5-1. Schematic representation of creatine dependent and independent control of oxidative phosphorylation and mH_2O_2. Creatine independent phosphate shuttling between mitochondrial and cytoplasmic compartments (left) occurs via ADP/ATP cycling across the voltage-dependent anion carrier (VDAC) on the outer mitochondria membrane and adenosine nucleotide translocase (ANT) on the inner membrane. Creatine dependent phosphate shuttling (right) was facilitated by mitochondrial creatine kinase (mtCK) whereby the transfer of phosphate from ATP to Cr in the intermembrane space produces phosphocreatine (PCr) and ADP. PCr is then exported through VDAC into the cytosol and ADP is shuttled back into the matrix via ANT. The relatively faster diffusion kinetics and higher cellular concentrations of PCr/Cr vs ATP/ADP combined with a reduction of diffusion distances for the latter allow for increased energy turnover. Electrons may slip and interact with nearby oxygen forming a superoxide radical ($O_2^{\bullet-}$). The relative size between the creatine-independent (left) and -dependent (right) refers to the increase production of superoxide in the absence of creatine. Figure adapted from [43-46, 53, 54, 479]. C, cytochrome C; Q, coenzyme Q. Made with BioRender.

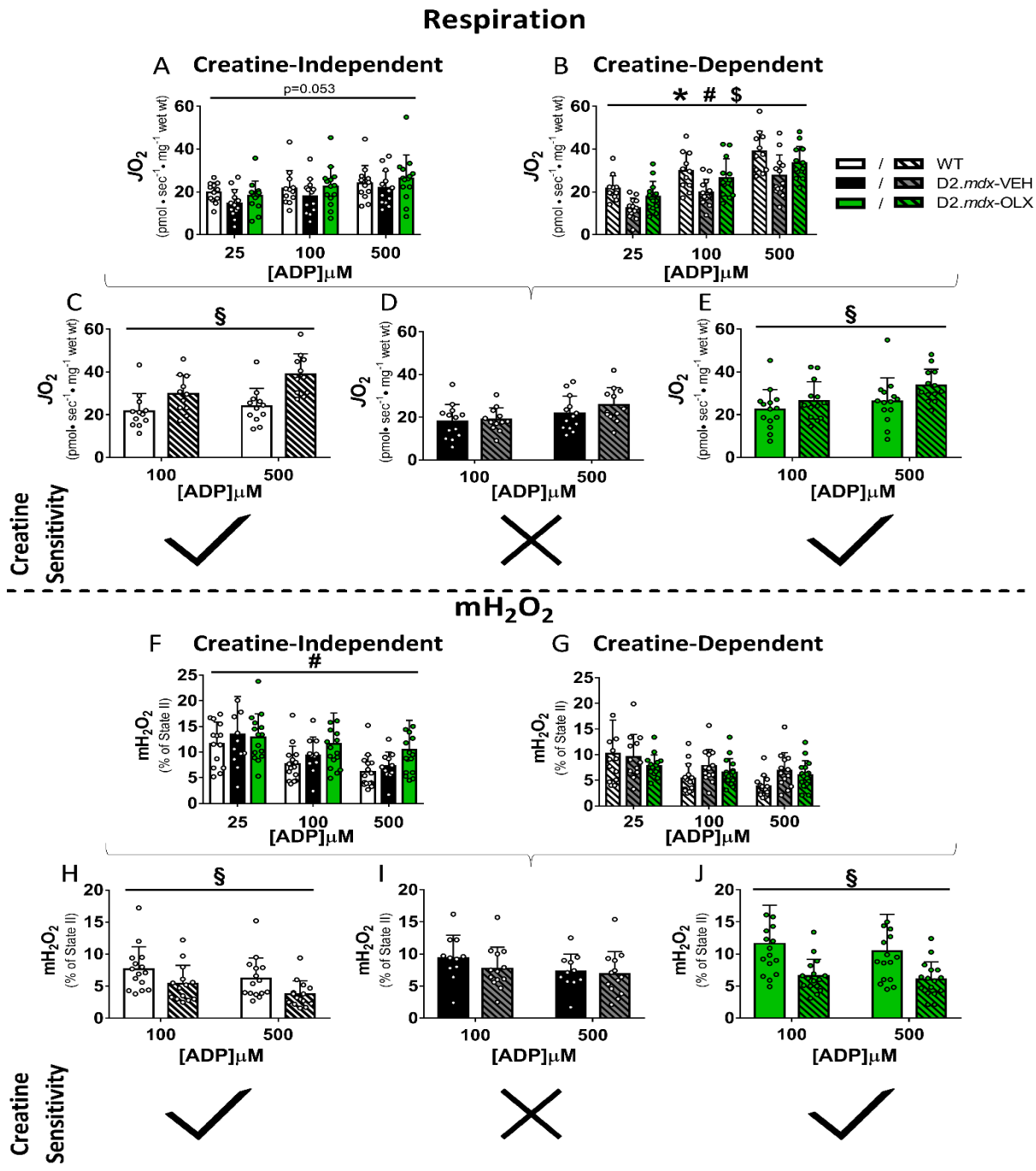

Figure 5-2. In quadriceps, Olesoxime preserves creatine sensitivity of mitochondrial respiration and mitochondrial H_2O_2 emission. (**A,B)** Complex I-supported respiration stimulated by NADH generation through 5mM pyruvate and 2mM malate (NADH) in permeabilized muscle fibres across a range of ADP concentrations that represent increasing states of metabolic demand: 25µM (resting muscle [497]); 100µM (high intensity exercise [510]) and 500µM (supramaximal) in both the absence and presence of 20mM creatine. (**C- E**) Mitochondrial

respiratory sensitivity to creatine (data replotted from A,B) at ADP concentrations that are subject to control by creatine [45] as done previously [22, 23]. (**F-J**) Similar analyses were performed to assess the ability of creatine to enhance ADP's effect on attenuating mH_2O_2 supported by 10mM succinate ($FADH_2$). Note that this stimulates Complex II, but also leads to reverse electron flow through Complex I known to generate reactive oxygen species. * $p<0.05$ WT vs D2.mdx-VEH; # $p<0.05$ WT vs D2.mdx-OLX; $ $p<0.05$ D2.mdx-VEH vs D2.mdx-OLX. § $p<0.05$ Cr vs No Cr condition. Data are shown as means ± SD, n=10-14.

In quadriceps from D2.*mdx* mice (Figure 5-2), ADP-stimulated respiration driven by pyruvate /malate (NADH, Complex I) was attenuated in both creatine-independent ($p=0.053$) and -dependent conditions ($p<0.05$) (Figures 5-2A, B) when assessed between groups. Improvements to creatine-dependent respiration were still noted after additional respiratory stimulation with 20mM succinate (representing Complex I+II, Supplemental Figure 5-1A, B). Olesoxime partially preserved respiration, but only in creatine-dependent conditions ($p<0.05$) (Figure 5-2B; Supplemental Figure 5-1B). We then directly compared the creatine-independent and -dependent condition in each experimental group (statistics assessed between these two conditions), a parameter defined here as creatine sensitivity. Such creatine sensitivity (i.e. increased respiration with creatine) was detected in WT ($p<0.05$) (Figure 5-2C), lost in D2.*mdx* (Figure 5-2D) but partially restored by addition of Olesoxime ($p<0.05$) (Figure 5-2E).

We then analyzed mH_2O_2 generation in quadriceps with succinate as substrate (allowing for reverse electron transfer through Complex I). No differences occurred between D2.*mdx* and WT (Figure 5-2F, G), whereas Olesoxime in creatine-independent conditions increased mH_2O_2 relative to WT. However, the pattern of creatine sensitivity was similar as with mitochondrial respiration: attenuation of mH_2O_2 generation by creatine [53] in WT ($p<0.05$) (Figure 5-2H) was lost in D2.*mdx* (Figure 5-2I) but rescued by Olesoxime ($p<0.05$) (Figure 5-2J). When using pyruvate/malate as substrates (forward electron flow through Complex I), mH_2O_2 generation increased in D2.*mdx* compared to WT ($p<0.05$) (Supplemental Figure 5-2 A, B), and this increase was partially attenuated by Olesoxime ($p<0.05$), but only in presence of creatine.

We then repeated the same analyses for diaphragm muscle (Figure 5-3). As in quadriceps, D2.*mdx* diaphragm showed attenuated ADP-stimulated respiration in both creatine-independent and -dependent conditions ($p<0.05$) (Figure 5-3A, B) which was rescued by Olesoxime only in the

presence of creatine ($p<0.05$) (Figure 5-3B). This pattern seen with pyruvate/malate as substrate did not reach significance when including additional succinate (Supplemental Figure 5-1C, D). However, creatine nonetheless stimulated respiration in all groups as measured by the creatine sensitivity index ($p<0.05$) (Figure 5-3C-E). Generation of mH_2O_2 in diaphragm was similar to quadriceps. Specifically, in either creatine condition, there was no difference between experimental groups with succinate as substrate (Figure 5-3F, G), while there was an increase in D2.*mdx* and Olesoxime groups with pyruvate/malate as substrates ($p<0.05$) (Supplemental Figure 5-2C, D). Importantly, the pattern of creatine sensitivity was again the same as in quadriceps: attenuation of mH_2O_2 generation by creatine in WT ($p<0.05$) (Figure 5-3H) was lost in D2.*mdx* (Figure 3I) but rescued by Olesoxime ($p<0.05$) (Figure 5-3).

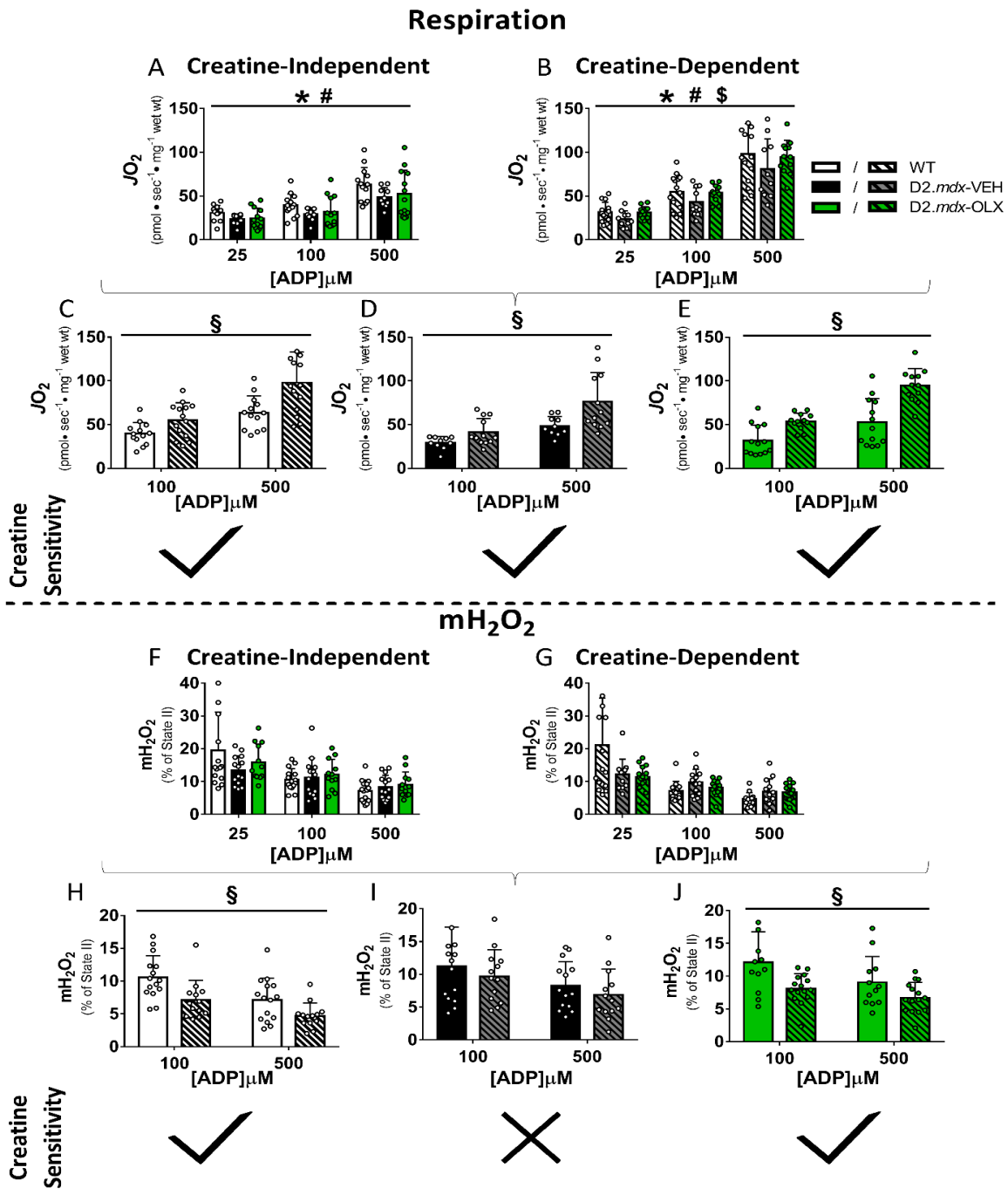

Figure 5-3. In diaphragm, Olesoxime preserves mitochondrial creatine-dependent respiration and preserves creatine sensitivity during mitochondrial H_2O_2 emission. (**A, B**) As in Figure 2, complex I-supported respiration stimulated by NADH generation through 5mM pyruvate and 2mM malate in permeabilized muscle fibres across a range of ADP concentrations that represent increasing states of metabolic demand: 25µM (resting muscle [497]); 100µM (high intensity exercise [510]) and 500µM (supramaximal) in both the absence and presence of 20mM

creatine. (**C- E**) Mitochondrial respiratory sensitivity to creatine (data replotted from A,B) at ADP concentrations that are subject to control by creatine [45] as done previously [22, 23]. (**G-K**) Similar analyses were performed to assess the ability of creatine to enhance ADP's effect on attenuating mH_2O_2 supported by 10mM succinate ($FADH_2$). Note that this stimulates Complex II, but also leads to reverse electron flow through Complex I known to generate reactive oxygen species. *p<0.05 WT vs D2.mdx-VEH; # p<0.05 WT vs D2.mdx-OLX; $ p<0.05 D2.mdx-VEH vs D2.mdx-OLX. § p<0.05 Cr vs No Cr condition. Data are shown as means ± SD, n=10-14.

We next determined whether the reduced mitochondrial creatine sensitivity in D2.*mdx* and its preservation by Olesoxime were related to altered protein levels of key components in mitochondrial energy transfer (see Figure 5-1). No differences were noted in the contents of specific subunits within Complexes I-V except for reductions within Complex III in quadriceps for both D2.*mdx* and Olesoxime relative to WT (Figure 5-4A, B). Reductions in VDAC2 and ANT1 isoforms in D2.*mdx* quadriceps and ANT1 in diaphragm ($p<0.05$) were unaltered by Olesoxime (Supplemental Figure 5-3B-E). Mitochondrial creatine kinase (mtCK) was lower in D2.*mdx* and Olesoxime vs WT in quadriceps ($p<0.05$) (Figure 5-4C) but not diaphragm (Figure 5-4D), and again unaltered by Olesoxime. Noting that mtCK is inhibited by reactive oxygen species [511], we then assessed the relative amount of exposed cysteine residues in the reduced state on immunoprecipitated mtCK (see methods). Cysteine oxidation is the first oxidative modification that occurs in the mtCK octamer upon the onset of oxidative stress [46]. However, no differences were seen for mtCK thiol redox state in any group in quadriceps ($p>0.05$) (Supplemental Figure 5-3A), suggesting differences in creatine sensitivity (Figure 5-2) were not due to redox modifications of this complex. Assessments were not performed in diaphragm given tissue limitations at this young age in the D2.*mdx* model.

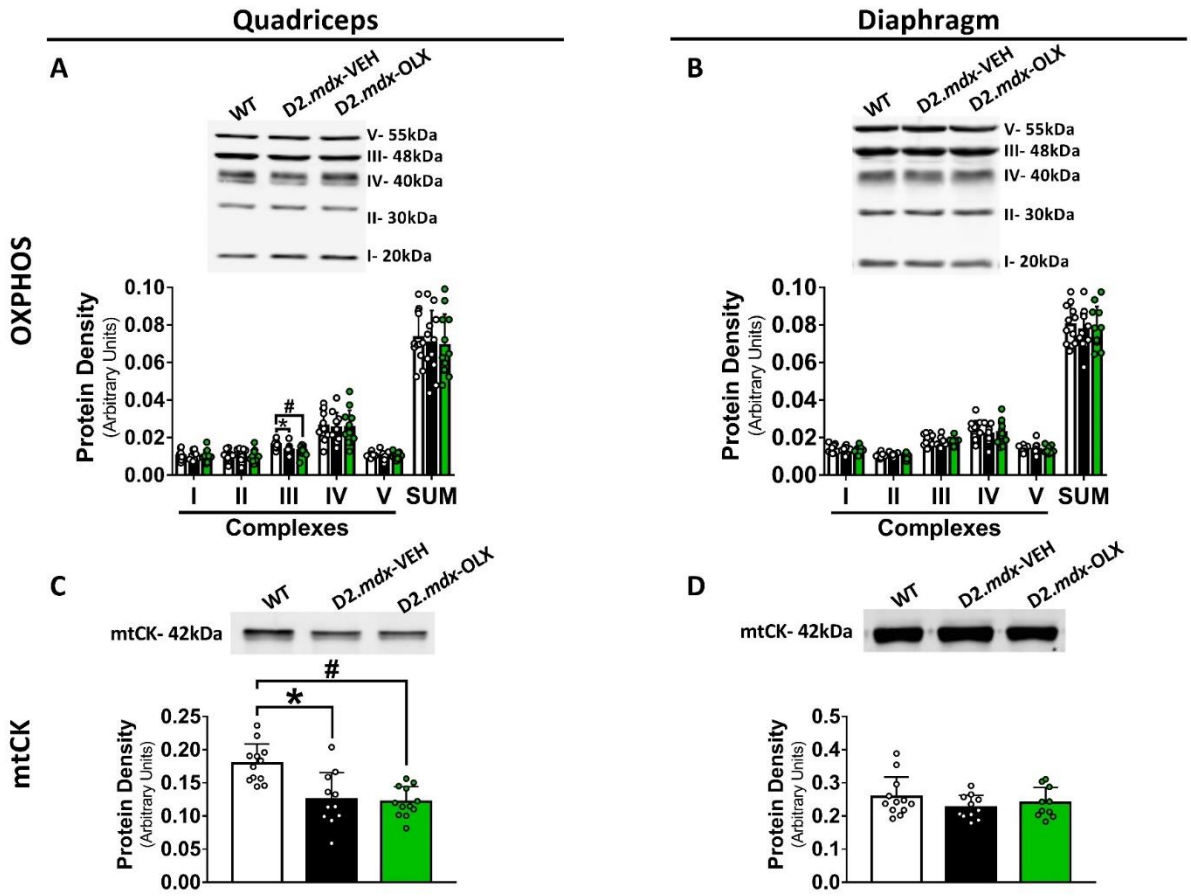

Figure 5-4. **Olesoxime did not alter contents of electron transport system proteins or mitochondrial creatine kinase in quadriceps and diaphragm**. (**A, B**) Subunits of Complexes I, II, III, IV and V (ATP Synthase) and **(C, D)** mtCK were assessed by western blot. *p<0.05 WT vs D2.mdx-VEH; #p<0.05 WT vs D2.mdx-OLX. Data are shown as means ± SD, n=10-12.

Reduced and total glutathione are increased in D2.mdx diaphragm but are not affected by Olesoxime

To determine whether alterations in creatine sensitivity during mH_2O_2 affected global cellular redox conditions, we assessed glutathione equilibria in each group. In quadriceps, there were no differences in total reduced GSH (Figure 5-5A), oxidized GSSG (Figure 5-5B), their equilibria (GSH:GSSG; Figure 5-5C) or their sum (total glutathione; Figure 5-5D). In diaphragm, reduced GSH ($p<0.05$) (Figure 5-5E) and total glutathione ($p<0.05$) (Figure 5-5H) were elevated in D2.*mdx* consistent with past reports of possible compensations in redox buffering in *mdx* mice [23, 27]. Olesoxime tended to preserve the WT levels of reduced GSH ($p=0.061$) (Figure 5-5E). There were no further differences in GSSG (Figure 5-5F) and GSH:GSSG (Figure 5-5G).

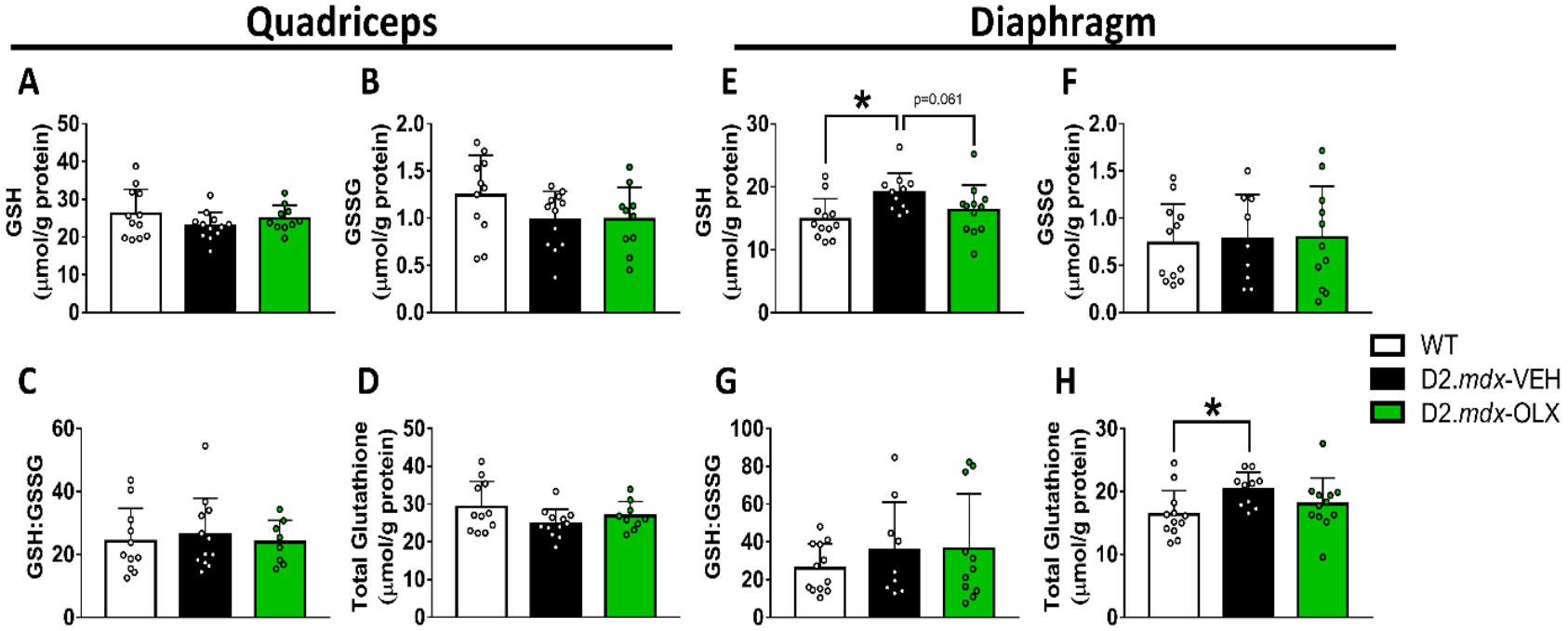

Figure 5-5. **Glutathione assessments in quadriceps and diaphragm**. (A-H) Glutathione was assessed in its reduced (GSH) and oxidized forms (GSSG), as an equilibria (GSH:GSSG) and as total content (GSH + 2xGSSG) in both quadriceps and diaphragm. * $p<0.05$ WT vs D2.mdx-VEH. Data are shown as means ± SD, n=8-12.

Olesoxime does not alter mitochondrial calcium retention capacity nor muscle necrosis or fibrosis

Prior reports suggested Olesoxime can attenuate formation of the permeability transition pore (mPTP) [428, 429, 435]. Given excess calcium stress in dystrophic fibres is thought to trigger mPTP and apoptosis as contributors to degeneration, we next compared mitochondrial calcium retention capacity, a functional readout of mPTP, to histological measures of fibre degeneration and fibrosis. We included creatine and ADP in the assay media given both are known to regulate mPTP through an attenuation effect [475, 511, 512]. In quadriceps, reductions in calcium retention capacity were noted in D2.*mdx* with and without Olesoxime ($p<0.05$) (Figure 5-6A) which reflects an increased sensitivity of mPTP to calcium stress. However, there were no changes in caspase 3 or 9 activity (Supplemental Figure 5-4A, B) which can mediate apoptosis downstream of putative mPTP opening [327, 336, 513, 514]. This observation was related to increased fibre degeneration and fibrosis ($p<0.05$) (Figure 5-6B-E). There was no effect of Olesoxime on these measures. In diaphragm, there were no differences in calcium retention capacity consistent with prior observations that this measure of mPTP is altered in a muscle specific manner in young D2.*mdx* mice [23]. Likewise, fibre degeneration and fibrosis were present in D2.*mdx* diaphragm ($p<0.05$) but were not altered by Olesoxime (Figure 5-6G-J). There were no changes in caspase 3 or 9 activity in diaphragm (Supplemental Figure 5-3D, E) or caspase 8 which is activated by extracellular stressors and can influence mPTP [515].

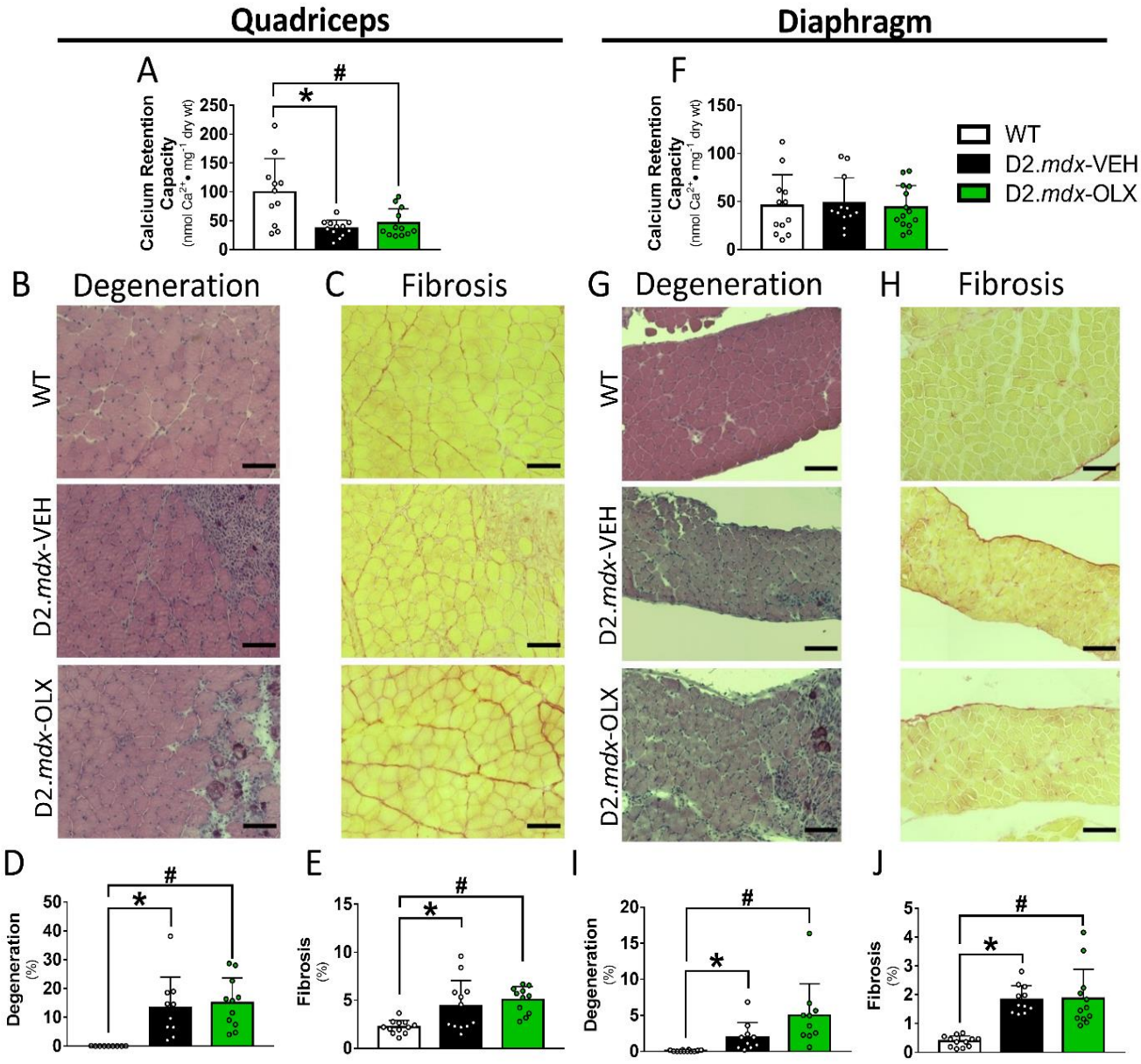

Figure 5-6. Increases in mitochondrial permeability transition pore, fibre degeneration and fibrosis in quadriceps and diaphragm of D2.mdx are not altered by Olesoxime. (A) In quadriceps, calcium retention capacity was assessed spectrofluorometrically by titrating calcium permeabilized fibres until the mPTP was triggered. (B-E) Histological assessments of muscle fibre degeneration and fibrosis were performed with hematoxylin & eosin (H&E) and picrosirius red, respectively. Representative images were obtained with 20x magnification. (F-J) Similar measures were performed in diaphragm muscle. *p<0.05 WT vs D2.mdx-VEH; #p<0.05 WT vs D2.mdx-OLX. Scale bar = 100 μm. Data are shown as means ± SD, n=9-14.

Olesoxime alters cross-sectional area and distribution in a fibre type- and muscle-specific manner

Muscle atrophy is a hallmark characteristic of DMD. Using antibodies specific for myosin heavy chain isoforms (Figure 5-7A, B, D, E), we next determined the response of specific fibres to Olesoxime. In quadriceps, atrophy was not observed in any fibre type in D2.*mdx* in contrast to a prior report at this same age and muscle showing an increased cross-sectional area averaged over all fibre types [23]. Olesoxime decreased cross sectional area of Type I fibres in quadriceps ($p<0.05$) (Figure 5-7B). The proportion of type IIA fibres (%) was elevated in D2.*mdx* ($p<0.05$), whereas Olesoxime lowered distribution in I and IIA fibres ($p<0.05$) (Figure 5-7C). In Diaphragm, D2.*mdx* showed lower cross-sectional areas in IIA and IIX fibres with the latter being preserved by Olesoxime ($p<0.05$) (Figure 5-7D, E). There were no differences in fibre type distribution between groups (Figure 5-7F).

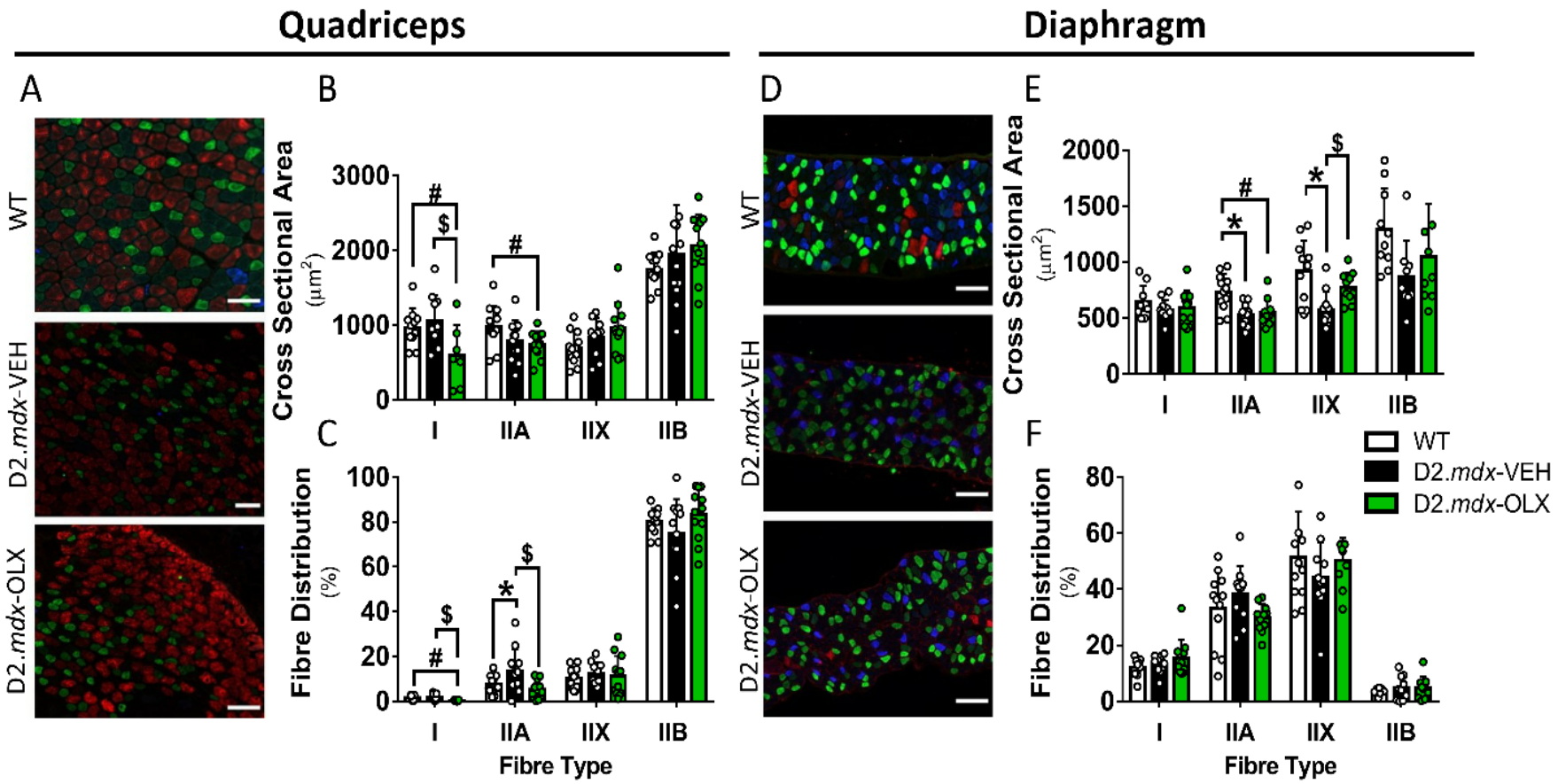

Figure 5-7. Divergent effects of Olesoxime on muscle fibre type size and distribution in quadriceps and diaphragm of D2.mdx. (**A**) Representative images of quadriceps muscle fibres stained for specific isoforms of myosin heavy chain. (**B, C**) Images were quantified to calculate cross sectional area and distribution of myosin heavy chain-specific fibres. (**D-F**) Similar measures were repeated in diaphragm fibres. *p<0.05 WT vs D2.mdx-VEH; #p<0.05 WT vs D2.mdx-OLX; $p<0.05 D2.mdx-VEH vs D2.mdx-OLX. Scale bar = 100 μm. Data are shown as means ± SD, n=10-12.

Olesoxime improves recovery from fatigue in diaphragm

We next assessed aspects of muscle force given dystrophin mutations cause severe muscle weakness which severely compromises quality of life in DMD. Diaphragm muscle strips were subjected to a series of stimulation protocols (Figure 5-8A) using force-frequency (Figure 5-8B) followed by determination of fatigue (Figure 5-8C) and recovery from fatigue (Figure 5-8D). Olesoxime improved recovery of force across 15 minutes of assessments during recovery ($p<0.05$). Due to technical limitations, assessments were not performed in quadriceps.

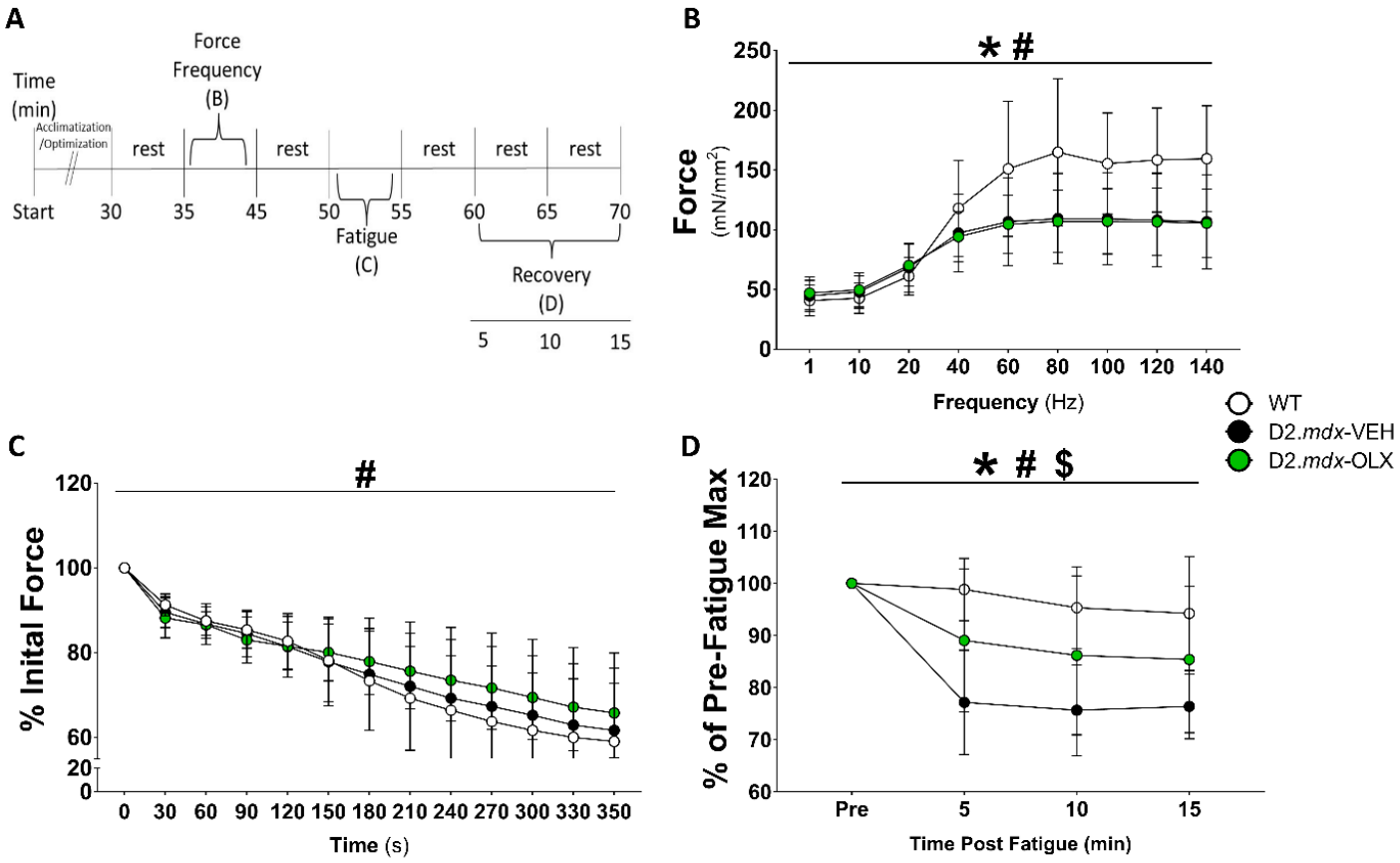

Figure 5-8. Olesoxime improves recovery of force following fatigue in diaphragm. (**A**) Muscle force was assessed using a series of force frequency, fatigue and recovery protocols. (**B**) Force frequency was assessed in-vitro using isolated diaphragm strips followed (1Hz to 140Hz for 0.2ms) by (**C**) a fatiguing protocol (70 Hz for 350 ms every 2 seconds for 5minutes). (**D**) Single stimulations were used to assess recovery from fatigue. *$p<0.05$ WT vs D2.mdx-VEH; #$p<0.05$ WT vs D2.mdx-OLX; $$p<0.05$ D2.mdx-VEH vs D2.mdx-OLX. Data are shown as means ± SD, n=9-12.

Olesoxime improves specific markers of muscle and bone health

Finally, we determined some clinically relevant measures of muscle and bone quality. Using serum creatine kinase as a marker of muscle damage, we found that increases in D2.*mdx* mice were robustly reduced by Olesoxime ($p<0.05$) (Figure 5-9A). Likewise, Olesoxime modestly improved voluntary cage hang time ($p<0.05$) (Figure 5-9B). Reductions in voluntary running wheel distance (Figure 5-9C), grip strength (Figure 5-9D), and distance explored in an open field($p<0.05$) (Figure 5-9E) were observed in D2.*mdx* but were unaltered by Olesoxime. We then used 3-dimensional microCT scans to assess aspects of body volume and composition. Modest reductions in whole body volume at this early disease stage were prevented by Olesoxime ($p<0.05$) (Figure 5-9F). Likewise, Olesoxime modestly increased hindlimb muscle volume ($p<0.05$) (Figure 5-9G). There was a general increase in whole body lean volume measures which includes muscle and visceral organs excluding lung that was accentuated by Olesoxime ($p<0.05$) (Figure 5-9H). We also assessed bone volume given reductions in bone mass are recognized as a risk in DMD. Intriguingly, reductions in hindlimb bone volume in D2.*mdx* were partially prevented by Olesoxime ($p<0.05$) (Figure 5-9I). Olesoxime did not alter adipose tissue volumes or other assessed volumetric parameters (Supplemental Table 5-1).

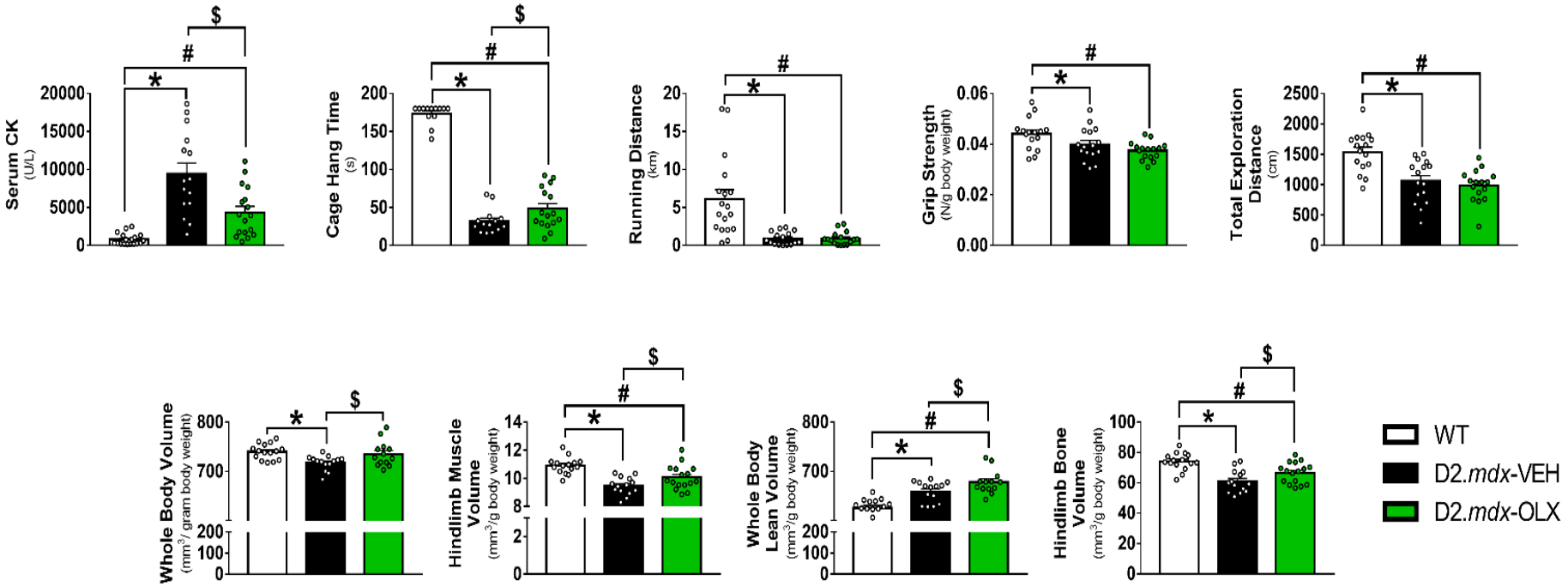

Figure 5-9. Olesoxime improves specific markers of muscle health and bone volume. (**A**) Serum creatine kinase (CK) was used as a clinically relevant marker of muscle damage. (**B**) Voluntary hang time was assessed with mice hanging to an inverted cage lid over a soft pad with assessments stopped at 180 seconds. (**C**) Voluntary running wheel distance was assessed over 24 hours. (**D**) Grip strength was assessed using a grip strength meter and normalized to body weight. (**E**) Mice were placed in open field container and video recordings were taken over 6 minutes to quantify voluntary total exploration distance. 3-dimensional microCT scans were used to assess (**F**) whole body muscle volume, (**G**) hindlimb muscle volume, (H) whole body lean volume and (**I**) hindlimb bone volume. *p<0.05 WT vs D2.mdx-VEH; #p<0.05 WT vs D2.mdx-OLX; $ p<0.05 D2.mdx-VEH vs D2.mdx-OLX. Data are shown as means ± SD, n=13-18.

Discussion

Recent reports indicate that several mitochondrial stress responses occur within the first few days of age in D2.*mdx* mice [22, 23, 311] suggesting that mitochondria may be a secondary contributor to myopathy in DMD. Here, we demonstrated that the mitochondrial enhancing compound Olesoxime can preserve (i) creatine-sensitive mitochondrial functions, in particular Complex I-supported creatine-stimulated respiration and attenuation of H_2O_2 generation, (ii) recovery from muscle fatigue, and (iii) different clinically relevant markers of muscle quality by 4 weeks of age. An overall heterogeneous effect of Olesoxime on respiratory and limb muscle quality also suggests mitochondrial influences on myopathy varies across muscle type. Thus, mitochondrial stress may have distinct influences on the progression of myopathy in DMD depending on age and muscle type.

Possible mechanisms of Olesoxime

Alterations in oxidative phosphorylation and generation of reactive oxygen species have been described for D2.*mdx* muscle [22-24] and other dystrophin deficient models [256]. For analyzing these parameters in more detail in our study, we carefully considered two different pathways of energy exchange between mitochondria and the cytoplasm: ADP/ATP vs creatine/phosphocreatine cycling. In both pathways, high energy phosphate is shuttled from the matrix to the cytoplasm albeit through different carriers (adenylates vs creatine) and at different rates (creatine/phosphocreatine being faster).

By reconstituting these pathways *in vitro* through exclusion or inclusion of creatine in the respirometric assay media as performed previously [23, 51, 495, 497, 499, 516-518], we discovered that the ability of creatine to stimulate coupled respiration is lost in D2.*mdx* quadriceps and is consistent with our previous observations in multiple muscle types in this model [22, 23]. This mitochondrial creatine insensitivity was reversed following treatment with Olesoxime (Figure 2 C-E) which is a mechanism not previously reported for this compound. Lastly, the loss of creatine sensitivity in D2.*mdx* was not observed in diaphragm in contrast to our prior report [23] which might be related to a possible variability in dynamic remodeling of muscle occurring over days to weeks at this young age. Olesoxime did not increase mtCK abundance or decrease mtCK oxidation in D2.*mdx* quadriceps. However, mtCK oxidation could be evaluated with multiple thiol labeling methodologies given the technique used in the present study detects reduced thiols which exist in

high abundance and may be less sensitive than thiol oxidation assessments such as the recently developed ALISA [507]. It is also possible that other elements of the creatine/phosphocreatine pathway (Figure 5-1) are targeted by the drug. These include the assembly of octameric mtCK within the proteolipid complex as shown in Figure 5-1 [46] or the permeability of the outer membrane VDAC pore. The latter is a likely candidate when considering the biological activity of Olesoxime as addressed below. Lastly, while we report changes in creatine-dependent respiration supported by Complex I, future work could consider whether these creatine responses are conserved across multiple substrate inputs.

Strikingly, mitochondrial H_2O_2 generation in both quadriceps and diaphragm showed the same creatine sensitivity pattern and rescue by Olesoxime as seen for quadriceps respiration. H_2O_2 is the major oxidant generated by mitochondria [519, 520] and elevations have been reported at this age in D2.*mdx* mice in association with early myopathy [22-24]. Key to the design of our *in vitro* assays was the recognition that the rate of mH_2O_2 is inversely proportional to the degree of coupled respiration [42]. We stimulated respiration across a range of ADP concentrations from low to high in presence or absence of creatine to include physiologically relevant conditions. As a key finding of our study, the observed creatine sensitivity patterns suggest that loss of creatine sensitivity occurring in D2.*mdx* mice and its rescue by Olesoxime is a general feature. This evidently raises the question as to how Olesoxime regulates creatine sensitivity.

Olesoxime seems to exert its biological activity by accumulating in mitochondrial membranes and binding to the outer membrane proteins VDAC and peripheral benzodiazepine receptor (TSPO) on the outer mitochondrial membrane TSPO [521]. Based on this interaction with VDAC, some initial reports suggested inhibition of the inner membrane mPTP as a major mechanism of Olesoxime [428-431]. However, there is now consensus that VDAC is not always a mPTP component. We did not observe an effect of Olesoxime on mitochondrial calcium retention capacity, the standard assay for mPTP calcium sensitivity, consistent with a previous report [428]. Such calcium stress was chosen as a mPTP inducer [75, 80] since dystrophin-deficient muscle shows cytosolic calcium overload [4, 5] which may cause mitochondrial stress [256]. Although we cannot exclude attenuation of mPTP by mechanisms not detectable with our calcium retention assay, it seems more likely that Olesoxime affects calcium homeostasis or cytochrome *c* release as found in other studies [429, 435] independently of mPTP. By enriching in mitochondrial outer membrane and interacting

with VDAC and TSPO, Olesoxime may more directly control the permeability of outer membrane for small molecules like calcium [521] and creatine/phosphocreatine, or cholesterol exchange and membrane fluidity. Additionally, Olesoxime may also affect the assembly of larger Bax pores which allows for efflux of macromolecules like cytochrome *c* [522, 523]. Thus, our findings add new insight into the mechanisms by which Olesoxime preserves mitochondrial bioenergetics and proposes alternative stress-related mechanisms.

Mitochondrial relationships to myopathy in D2.mdx muscle

Our study suggests that preservation of mitochondrial creatine sensitivity is linked to muscle quality in D2.*mdx* mice. While several markers showed modest improvements, the more notable responses to Olesoxime included a robust reduction in circulating serum creatine kinase – a marker of muscle injury – and improved recovery from fatigue in diaphragm. While we were unable to perform force assessments in quadriceps due to technical limitations, these findings provide a foundation to further explore the importance of mitochondrial creatine functions in regulating muscle function and contributing to weakness in dystrophin deficient muscle. Not all measures of muscle quality improved with Olesoxime, but this may not be surprising given mitochondrial stress is secondary to dystrophin deficiency and will not be the only contributor to myopathy given the known inflammatory, cytoskeletal, calcium and other stressors that arise in this disorder. While speculative, an additional consideration for future directions includes the influence of mitochondrial metabolism in cell types that modify muscle remodeling including fibroblasts, fibroadipogenic precursors and macrophages (see [256] for perspectives) particularly with longer term treatments throughout disease progression. Nevertheless, the early improvements with this short-term treatment regimen seen in the present investigation indicates that mitochondrial stress likely contributes to the early myopathy in D2.*mdx* muscle.
In this regard, the 4-week-old mice examined in this study captures a time of dynamic development as mice mature. The interaction between both developmental and disease influences on mitochondria will inevitably be complex, with the reciprocal relationship being one of many determinants of muscle quality. Nonetheless, this early age provides relevant context given myopathy develops in young children with DMD [482, 524]. The heterogeneous relationship between altered mitochondrial creatine metabolism and muscle quality in the current study also provides a foundation for exploring other mitochondrial enhancing therapies across a range of

doses and treatment durations across stages of disease development using muscle-specific comparisons.

An additional point of interest pertains to the mitochondrial calcium retention capacity measures. In vehicle-treated mice, calcium retention capacity was reduced in quadriceps but not in diaphragm compared to wildtype consistent with our previous report [23]. This finding demonstrates that mitochondrial stress responses in one muscle do not necessarily predict the response in another muscle. Such muscle-specific mitochondrial responses to dystrophin mutations are an intriguing opportunity to understand the precise mechanisms by which stress signals differ between muscles or whether mitochondrial resilience to a given stress signal is heterogeneous across the musculature (see [256] for perspective). The regulation of mitochondrial calcium cycling is of course complex and includes additional regulators not considered in this study including mitochondrial calcium uniporters. In this regard, 4-week-old C57Bl/10.mdx mice demonstrate increases in MCUb (the inactive channel subunit of the uniporter) which lowered the ratio of MCU/MCUb [26] which is thought to be a metric that regulates the mitochondrial calcium transport kinetics. Our observations of muscle-specific sensitivity or resilience to exogenous calcium stresses *in vitro* support future considerations of how MCU responses in this disease might contribute to this heterogeneity. From a broader perspective, the potential efficacy of targeting mitochondria to treat muscle weakness in DMD warrants further focus, particularly with consideration of translation from pre-clinical models to clinical trials. For example, the quinone electron shuttling drug Idebenone improved cardiac function and exercise performance in a mouse model of DMD which was subsequently shown to also improve cardiac and respiratory function in an initial clinical trial of people with DMD [423, 424]. However, subsequent clinical trials proved unsuccessful (NCT 02814019) for reasons that are not fully understood. These early attempts at targeting mitochondria demonstrate that mitochondria could be a potential therapeutic target in DMD but that additional consideration of pharmacological and biological factors influencing the translation of findings from pre-clinical models to humans will be important for continued progress in developing mitochondrial therapeutics. Nonetheless, the results from the present investigation identify mitochondrial creatine sensitivity linked to respiration and mH_2O_2 attenuation as a new direction to for continued research in pre-clinical research.

Conclusion

This study examined the efficacy of early, short-term administration of Olesoxime in the treatment of D2.*mdx* mice. In the dystrophin deficient muscle, Olesoxime preserved mitochondrial creatine sensitivity in terms of creatine-stimulated respiration and attenuated mH_2O_2 and improved markers of muscle function and quality. This suggests that mitochondria contribute to myopathy in DMD, albeit at a degree that may depend on age and muscle type, and on the relative influence of other disease stressors. However, Olesoxime did not improve mitochondrial calcium retention capacity, questioning the role of the drug in altering calcium-induced mPTP. Rather, the effect of the compound on creatine sensitivity suggests regulation of outer membrane permeability or stability of the mtCK proteolipid complex. Future studies in D2.*mdx* mice should address the mechanism underlying creatine sensitivity and the effects of longer term Olesoxime treatment on mitigation of oxidative stress and improved creatine sensitivity as a new direction in developing prospective mitochondrial enhancing therapies for Duchenne muscular dystrophy.

Funding

Funding was provided to C.G.R.P. by the National Science and Engineering Research Council (no. 436138-2013) and an Ontario Early Researcher Award (C.G.R.P., no. 2017-0351) with infrastructure supported by Canada Foundation for Innovation, the James. H. Cummings Foundation, and the Ontario Research Fund. Funding was provided to J.Q. by the National Science and Engineering Research Council (no. 258590). C.A.B. was supported by an NSERC PGS-PhD scholarship. M.C.H., P.C.T. and F.A.R. were supported by an NSERC CGS-PhD scholarships. L.J.D. was supposed by an NSERC CGS-M scholarship.

Supplemental Materials

Supplemental Table 5-1: Body weight and micro-CT assessments of adipose tissue

		Group		
COMPARTMENT		**WT**	**D2.*mdx*-VEH**	**D2.*mdx*-OLX**
	Body Weight (g)	17.07±1.89	12.53±1.38*	13.56±1.53#
Trunk	Trunk Volume (mm^3)	6218.43±907.93	4511.77±608.84*	4938.89±597.82#
	Total Trunk Adipose Volume (mm^3)	704.12±154.43	362.04±95.46*	351.04±82.98#
	Subcutaneous Adipose Volume (mm^3)	472.80±77.88	244.31±47.79*	240.26±43.91#
	Visceral Adipose Volume (mm^3)	230.24±96.72	117.02±53.98*	109.45±41.55#
	% Trunk Adipose	11.30±1.70	7.98±1.56*	7.07±1.15#
	% Subcutaneous Adipose	70.56±3.99	68.87±7.68	69.28±4.96
	% Visceral Adipose	29.30±3.98	30.94±7.66	30.34±5.13
	Normalized Total Trunk Adipose Volume (mm^3/g)	41.03±6.43	28.66±5.97*	25.45±4.80#
	Normalized Subcutaneous Adipose Volume (mm^3/g)	27.74±3.58	19.46±3.22*	17.43±2.17#
	Normalized Visceral Adipose Volume (mm^3/g)	13.23±4.59	9.14±3.61*	7.92±2.74#

Hindlimb	Hindlimb Volume (mm^3)	356.21±38.14	260.68±28.69*	286.03±33.34$^{\#,\$}$
	Hindlimb Adipose Volume (mm^3)	49.17±5.33	31.96±3.54*	33.75±4.29$^{\#}$
	% Hindlimb Adipose	13.89±0.85	12.36±1.69*	11.80±0.69$^{\#}$
	Normalized Hindlimb Adipose Volume (mm^3/g)	2.89±0.23	2.56±0.32*	2.49±0.21$^{\#}$
Whole Body	Total Volume (mm^3)	12656.92±1602.33	9029.30±1080.19*	9323.76±1186.78$^{\#,\$}$
	Total Adipose Volume (mm^3)	1967.76±438.79	656.50±87.74*	798.15±283.59$^{\#}$
	% Whole Body Adipose	15.46±2.32	7.83±1.51*	7.76±2.01$^{\#}$
	Normalized Whole Body Adipose (mm^3/g)	114.45±17.48	57.24±15.60*	56.09±10.47$^{\#}$

*p<0.05 WT vs D2.*mdx*-VEH; #p<0.05 WT vs D2.*mdx*-OLX; $p<0.05 D2.*mdx*-VEH vs D2.*mdx*-OLX. Data are shown as mean ± SD; n=12-15.

Supplemental Table 5-2: micro-CT assessments of bone volume

		Group		
COMPARTMENT		**WT**	**D2.*mdx*-VEH**	**D2.*mdx*-OLX**
Hindlimb	Hindlimb Bone Volume (mm^3)	74.07±5.72	60.94±7.33*	66.60±6.88$^{\#,\$}$
	% Hindlimb Bone	20.92±1.79	23.54±2.96*	23.52±3.09$^{\#}$
	Normalized Hindlimb Bone Volume (mm^3/g)	4.37±0.46	4.88±0.61*	4.96±0.66$^{\#}$
Whole Body	Total Bone Volume (mm^3)	583.36±92.49	509.60±126.43	567.08±135.03
	% Whole Body Bone	5.01±0.21	5.70±1.43	5.66±1.37
	Normalized Whole Body Bone (mm^3/g)	34.45±5.65	40.99±10.53	41.64±10.06

*p<0.05 WT vs D2.*mdx*-VEH; #p<0.05 WT vs D2.*mdx*-OLX; $p<0.05 D2.*mdx*-VEH vs D2.*mdx*-OLX. Data are shown as mean ± SD; n=12-15.

Supplemental Table 5-3: micro-CT assessments of lean volume

		Group		
COMPARTMENT		**WT**	**D2.*mdx*-VEH**	**D2.*mdx*-OLX**
Hindlimb	Hindlimb Lean Volume (mm^3)	186.43±24.67	119.40±18.05*	137.03±22.00$^{\#,\$}$
	% Hindlimb Lean	52.23±1.68	45.69±3.38*	47.77±3.37$^{\#}$
Whole Body	Total Lean Volume (mm^3)	10689.16±1291.97	8283.42±934.26*	9323.76±988.20$^{\#,\$}$
	% Whole Body Lean	84.54±2.32	92.17±1.51*	92.24±2.01$^{\#}$
	Normalized Whole Body Lean (mm^3/g)	625.77±20.49	658.75±21.15*	678.29±23.99$^{\#,\$}$
	Normalized Whole Body Lean (mm^3/g)	625.77±20.49	658.75±21.15*	678.29±23.99$^{\#,\$}$

*p<0.05 WT vs D2.*mdx*-VEH; #p<0.05 WT vs D2.*mdx*-OLX; $p<0.05 D2.*mdx*-VEH vs D2.*mdx*-OLX. Data are shown as mean ± SD; n=12-15.

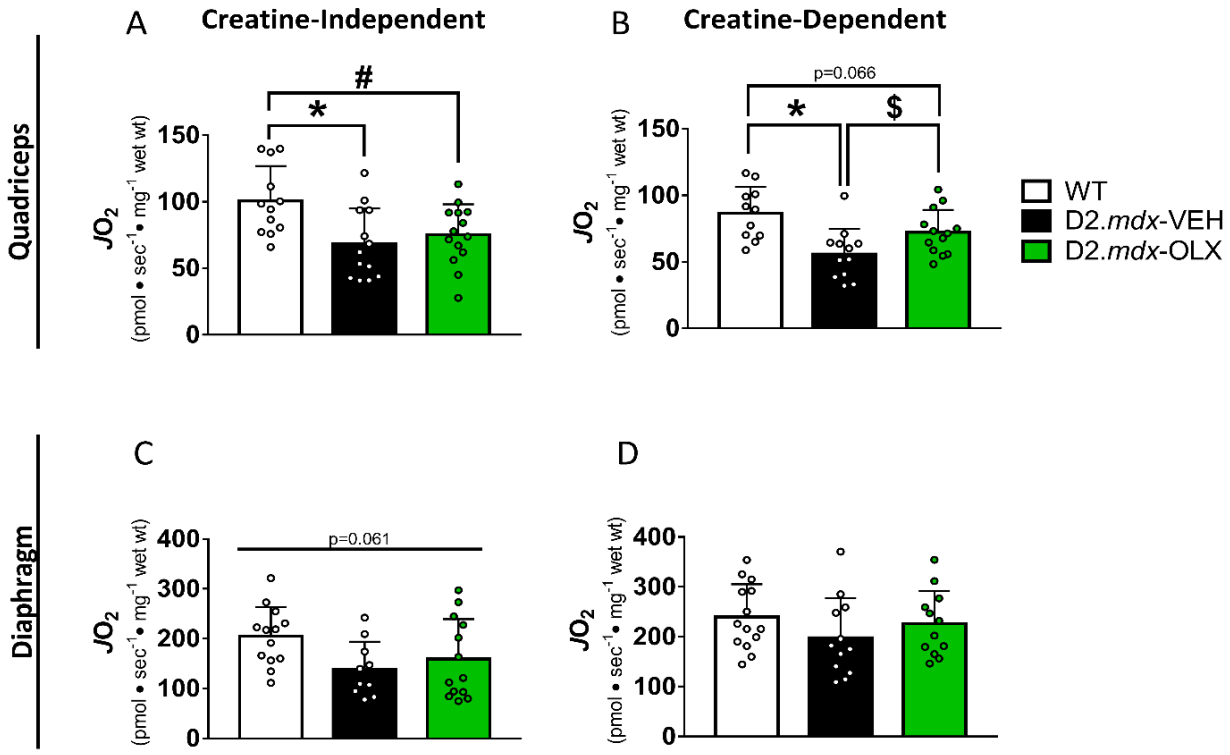

Supplemental Figure 5-1. Olesoxime improves creatine-supported complex I+II respiration in the quadriceps only. A-D Complex I+II-supported respiration was stimulated by $FADH_2$ through 20mM succinate after stimulation with 5mM Pyruvate and 2mM malate (producing NADH) in permeabilized muscle fibres at supramaximal concentrations of ADP (5,000-30,000µM) in both the absence (A, C) and presence of creatine (B, D). Assessments of respiration were completed in quadriceps (A, B) and diaphragm (C, D) muscles. * WT vs D2.mdx-VEH; # WT vs D2.mdx-OLX; $ D2.mdx-VEH vs D2.mdx-OLX. Data are shown as means ± SD; n=10-13.

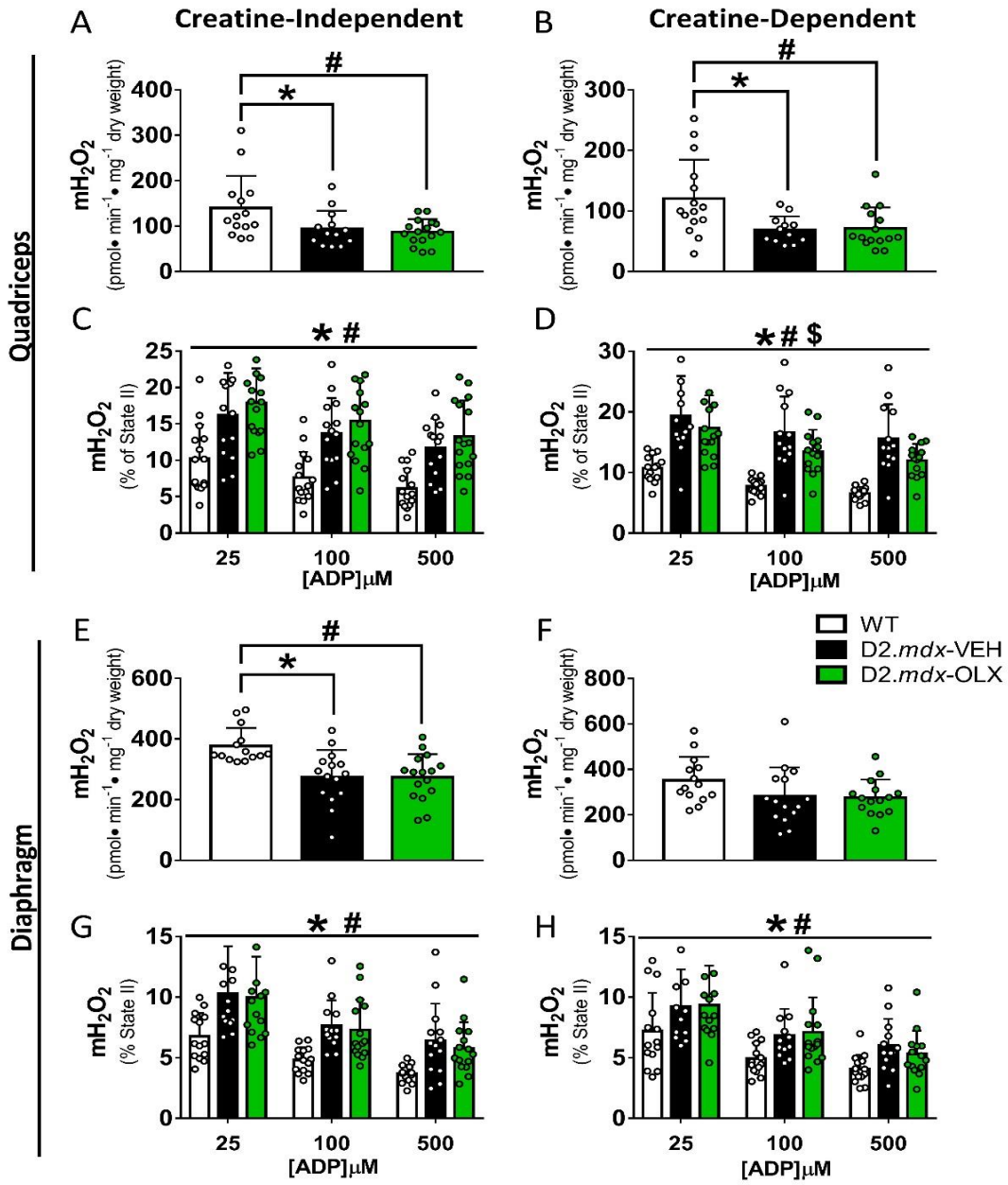

Supplemental Figure 5-2. Olesoxime improves creatine-dependent mH_2O_2 emission in quadriceps only. State II mH_2O_2 production was initiated by 5mM pyruvate and 2mM malate (NADH) to stimulate complex-I supported mH2O2 through forward electron flow from Complex I in the absence (A,E) and presence (B, F) of 20mM creatine. The ability of creatine to enhance ADP's effect on attenuating mH_2O_2 was assessed in the absence (C,G) and presence (D,H) of creatine across a range of ADP concentrations depicting increasing metabolic demand. Analyses were performed in the quadriceps (A-D) and diaphragm (E-H). *p<0.05 WT vs D2.mdx-VEH; #p<0.05 WT vs D2.mdx-OLX; $p<0.05 D2.mdx-VEH vs D2.mdx-OLX. Data are shown as means ± SD, n=11-16.

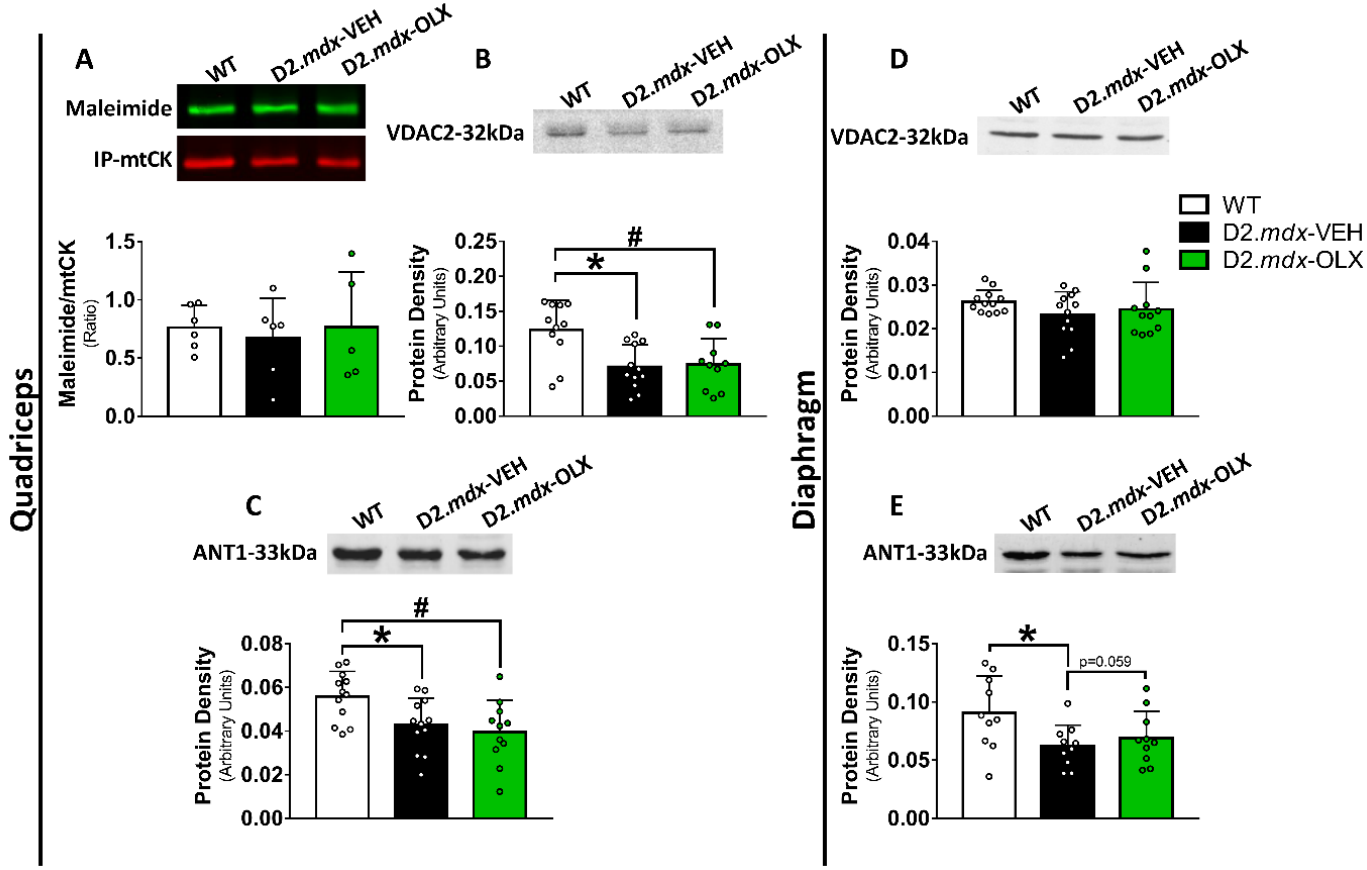

Supplemental Figure 5-3. Muscle specific changes in essential regulators of bioenergetic in D2.*mdx*. (A) Mitochondrial creatine kinase (mtCK) protein content was compared to mtCK cysteine thiol redox state assessed by labeling with IRDye 800 CW Maleimide following immunoprecipitation and PAGE. Limited tissue in small diaphragms from 4-week-old D2.mdx mice did not permit assessments of mtCK redox state in this muscle. Protein content of adenine nucleotide translocase 1 (ANT 1) on the inner mitochondrial membrane (C,E) and voltage dependent anion carrier 2 (VDAC2) on the outer mitochondrial membrane (B,D) and were quantified in the quadriceps (B-C) and diaphragm (D-E). * WT vs D2.mdx-VEH; # WT vs D2.mdx-OLX; $ D2.mdx-VEH vs D2.mdx-OLX. §Cr vs No Cr condition. Data are shown as means ± SD, n=5-12.

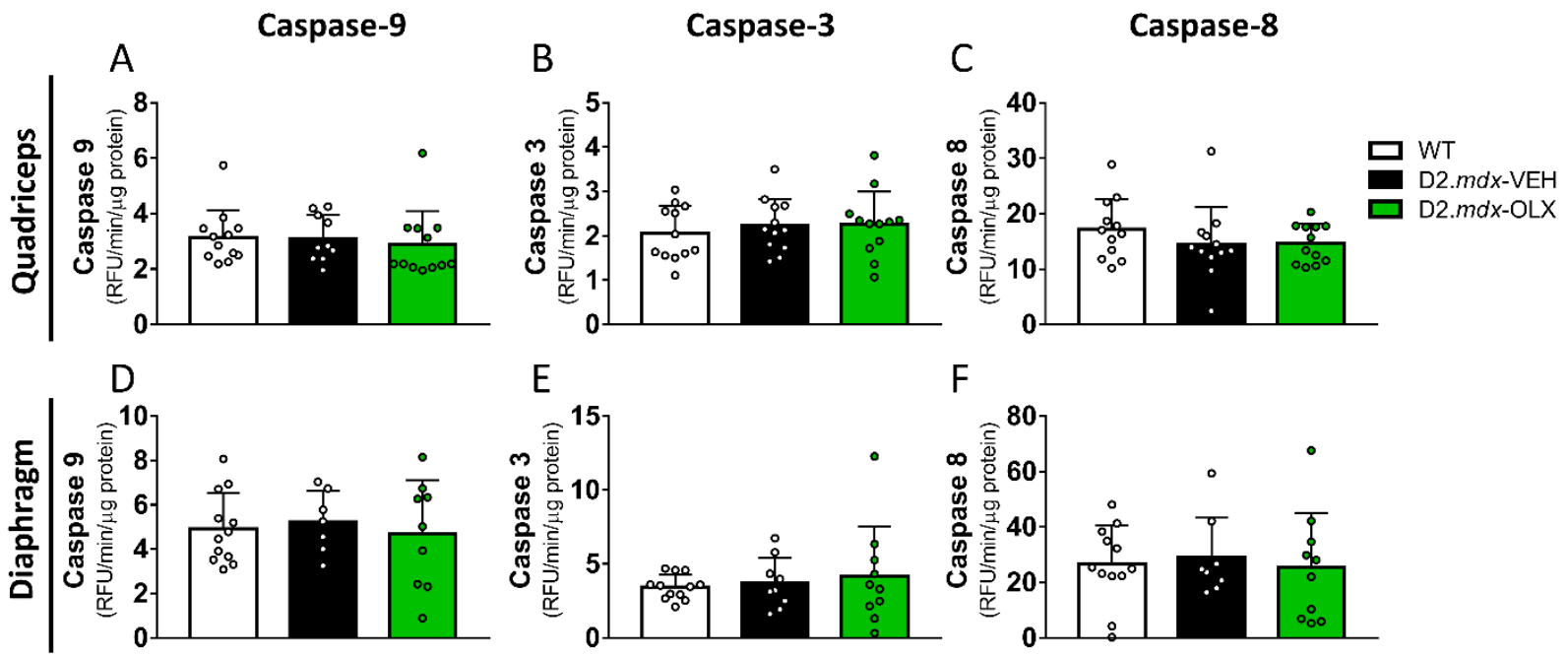

Supplemental Figure 5-4: Olesoxime treatment does not alter apoptosis-associated proteolytic enzymes in D2.mdx mice. Proteolytic enzyme activity of mitochondrial associated caspase 9 (A, D), and its downstream target caspase-3 (B, E) was assessed. Induction of non-mitochondrial sources of apoptosis was assessed through caspase-9 (C, F). Measurements of caspase activity were performed in the quadriceps (A-C) and diaphragm (D-F). Data are shown as means ± SD, n=7-12.

Supplemental Data Not Included in Manuscript

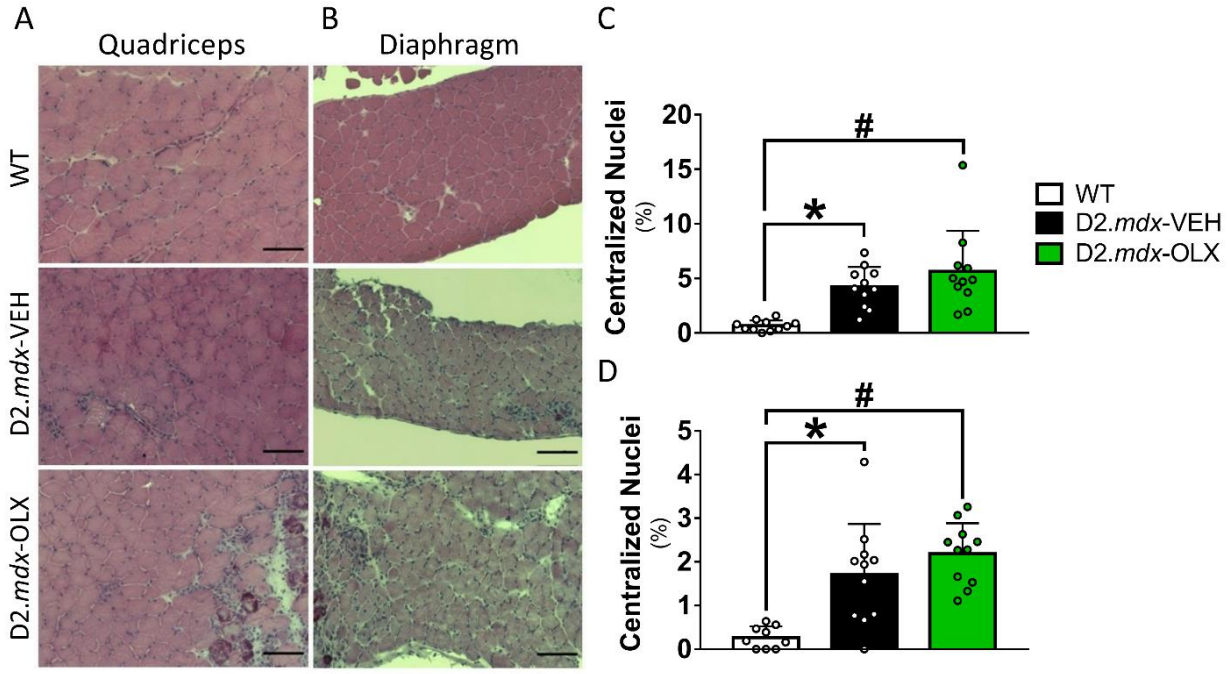

Supplemental Figure 5-5. **Olesoxime does not alter the number of regenerating fibres**. Centralized nuclei, a marker of regenerating fibres, was assessed using hematoxylin and eosin staining in the quadriceps (A,C) and (B,D) diaphragm. *p<0.05 WT vs D2.mdx-VEH; #p<0.05 WT vs D2.mdx-OLX. Scale bar = 100 μm. Data are shown as means ± SD, n=9-14.

Chapter 6: ALY688-SR attenuates diaphragm fibrosis, atrophy and mitochondrial stress in a model of Duchenne muscular dystrophy

This chapter has been written in preparation for submission to the Journal of Cachexia, Sarcopenia and Muscle. It is included in this thesis in the pre-submission format.

Assay Development Prior to the Start of Project 3:

1. Assessment of Immune Response (qPCR and Biolegend Flow Cytometry)- in collaboration with MM & LC

Author Contributions: Many of the experiments for this study were performed by Catherine A Bellissimo (CAB). CAB established and maintained the breeding colony required for this project. As tissue from these mice were shared among 3 projects (2 included in this thesis), several tasks were shared amongst two students and one post-doctoral fellow. CAB, SG and LNC performed daily drug injections and all whole-body in vivo testing. CAB performed all *in situ* quadriceps and *in vitro* diaphragm force experiments. CAB and SG conducted all tissue harvests with tissue processing from LNC, MG, LD and LJD. CAB separated all skeletal muscle fibres used for mitochondrial bioenergetics with CAB, SG and LJD performing all assessments (respiration, mH_2O_2 emission and calcium retention capacity). CAB and LNC performed all serum creatine kinase experiments. CAB, AT, MCG, YS and IAR performed all immunohistochemistry and immunofluorescent staining and assessments. CAB, MM, LC and AT conducted all qPCR and in-tissue assessment of immune presence. CAB performed all western blotting experiments. CAB and CGRP wrote the manuscript with all co-authors aiding in revision.

ALY688-SR attenuates diaphragm fibrosis, atrophy and mitochondrial stress in a model of Duchenne muscular dystrophy

Catherine A. Bellissimo[1], Shivam Gandhi[1], Laura N. Castellani[1], Mayoorey Murugathasan[1], Luca J. Delfinis[1], Arshdeep Thuhan[1], Madison C. Garibotti[1], Yeji Seo[1], Irena A. Rebalka[2], Gary Sweeney[2], Thomas J. Hawke[3], Ali A. Abdul-Sater[1] and *Christopher G.R. Perry[1]

[1]School of Kinesiology & Health Science, Muscle Health Research Centre, York University, Toronto, ON M3J 1P3 Canada.

[2]Department of Biology, Muscle Health Research Centre, York University, Toronto, ON M3J 1P3 Canada.

[3]Department of Pathology and Molecular Medicine, McMaster University, Hamilton, ON, Canada

Address for correspondence: s

*Christopher G. R. Perry, PhD

Email: cperry@yorku.ca

Tel: +1 416 736 2100

Running Head: Targeting fibrosis and atrophy in Duchenne muscular dystrophy

Keywords: Duchenne muscular dystrophy, muscle, adiponectin receptor agonism, fibrosis, atrophy, inflammation

Graphical Abstract

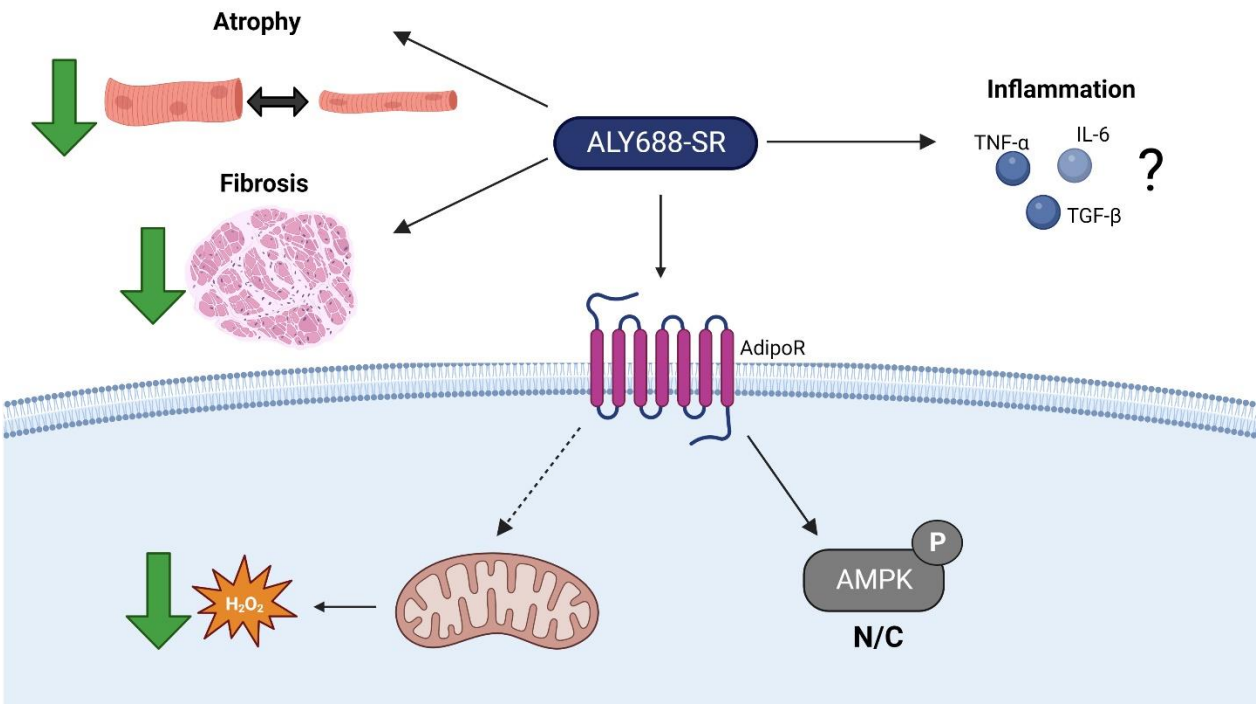

Abstract

Background Fibrosis is associated with respiratory and limb muscle atrophy in Duchenne muscular dystrophy (DMD). Current standard of care partially delays the progression of this myopathy but there remains an unmet need to develop additional therapies. Adiponectin receptor agonism has emerged as a possible therapeutic target to lower inflammation in *mdx* mouse models of DMD but the degree to which fibrosis and atrophy are prevented remain unknown. As adiponectin regulates tissue metabolism, it is also possible that adiponectin analogues may reverse metabolic disruptions in *mdx* muscle. Here, we determined whether the recently developed slow-release peptidomimetic adiponectin analogue ALY688-SR could prevent fibrosis and atrophy by attenuating inflammation and mitochondrial bioenergetic stress in diaphragm and tibialis anterior of D2.*mdx* mice.

Methods The short-term effects of ALY688-SR in early stages of disease progression were assessed by administering daily subcutaneous injections of ALY688-SR to 7-day-old male D2.*mdx* mice (n=12/group) for 21 days. Separate groups of mice received a lower dose (LD; 3mg/kg body weight), higher dose (HD; 15mg/kg body weight) or saline vehicle (VEH) and were compared to age-matched wildtype mice.

Results In VEH, diaphragm collagen was 5.5-fold greater vs wildtype (8.7% VEH, 1.3% wildtype; $p<0.05$) and an approximate doubling in tibialis anterior (1.1% VEH vs 0.5% wildtype; $p<0.05$). Both doses of ALY688-SR prevented most of the fibrosis in the diaphragm of D2.*mdx* mice (66.7-67.6% reduction of the increased collagen seen in VEH; $p<0.05$). HD partially prevented atrophy in Type I, IIA and IIB fibres from diaphragm (31.0-83.9% attenuation; $p<0.05$). Subsequent tissue analyses were performed only in HD given the dual benefits of this dose on both fibrosis and fibre size. HD lowered IL-6 mRNA (-40.0% vs VEH; $p<0.05$) but increased IL-6 and TGF-β protein contents (20.3,69.1% vs VEH, respectively; $p<0.05$) in diaphragm and lowered Complex I-stimulated H_2O_2 emission (-2.9 to -25.5% vs VEH; $p<0.05$) without changing markers of mitochondrial content suggesting decreased mitochondrial redox stress following treatment. Both doses lowered *in vitro* diaphragm force production (-3.2 to -32.5% vs VEH; $p<0.05$). In tibialis anterior, the modest fibrosis was not altered by either dose, and atrophy was not apparent at this young age.

Conclusions These results demonstrate that short-term treatment of ALY688-SR partially prevents fibrosis and atrophy in diaphragm of young D2.*mdx* mice in relation to lower mitochondrial redox stress.

Keywords: Duchenne muscular dystrophy, neuromuscular disease, dystrophin, weakness, muscle, mitochondria, adiponectin

Introduction

Duchenne muscular dystrophy (DMD) is a neuromuscular disorder estimated to occur in approximately 1 in 5,000 live male births [2]. Progressive muscle weakness in childhood usually leads to an early dependence on assistive devices as well as a reduced lifespan from respiratory or cardiac failure. Arising from an X-linked recessive mutation in dystrophin, a loss of cell membrane stability in striated muscles renders these cells susceptible to contraction-induced damage leading to repeated cycles of degeneration, systemic inflammation and fibrosis [3, 302, 525, 526]. While immunosuppression by glucocorticoids slows the progression of the disease, the considerable myopathy that remains combined with the deleterious side effects of this treatment underscores an unmet need for developing additional therapeutics.

Adiponectin is an adipokine that lowers inflammation [527, 528] and upregulates indices of fat oxidation in skeletal muscle [445, 529, 530]. Transgenic overexpression of adiponectin [457] in C57Bl/10.*mdx* mice improved whole-body measures of muscle function and reduced markers of inflammation and injury. Likewise, the orally administered small-molecule (non-peptide) adiponectin receptor (AdipoR) agonist, AdipoRon, reduced markers of inflammation and sarcolemmal damage in skeletal muscle from C57Bl/10.*mdx* mice, stimulated genomic markers of regeneration and improved whole body assessments of locomotor function using treadmill, grip strength and wire tests [464]. These effects were associated with general indices of reduced oxidative stress but the precise mechanism by which this occurred remains unknown. Also, the effects of AdipoR agonists on other hallmark signs of myopathy in *mdx* mice such as muscle-specific weakness, fibrosis, atrophy and the well-characterized state of metabolic stress (reviewed in [256]) remain unknown.

Whilst adiponectin and AdipoRon are efficacious, the former is a large multimeric protein which requires extensive posttranslational modification making it expensive to synthesize and the latter lacks potency and specificity [462, 465]. The critical receptor binding domain of adiponectin was identified and used to generate the peptidomimetic ADP355 which resulted in high specificity, was more potent than the native protein and more resistant to proteolytic degradation. ADP355, now known as ALY688, has been shown to activate adiponectin-specific signaling downstream of both AdipoR1 and AdipoR2 receptors [465, 531]. ALY688 was also shown to attenuate inflammation in various inflammatory disorders such as dry eye and liver diseases, with reduced fibrosis also seen in the latter [466, 467]. This anti-fibrotic effect is intriguing given the considerable fibrosis that occurs in DMD and murine models which may be mediated by inflammation and contribute to the progressive decline in muscle function [228, 238, 532]. As metabolic dysfunction is also apparent in DMD and *mdx* mice (reviewed in [256]), the recent finding that ALY688 improves metabolic function in skeletal muscle cells [533] and adipocytes [534] further supports consideration of this compound.

Importantly, for preclinical studies a slow-release formulation (ALY688-SR) was recently developed with improved pharmacokinetic properties enabling once daily injection (unpublished observation). The purpose of this study was to determine the effects of *in vivo* administration of ALY688-SR on fibrosis, atrophy, force production and mitochondrial bioenergetics in dystrophin-deficient muscle. Herein, we used D2.*mdx* mice – a model that demonstrates more robust muscle dysfunction compared to C57Bl/10.*mdx* mice [143, 145]. We focused specifically on the early stages of disease progression by treating mice from 1-4 weeks of age given that symptoms first manifest in young children [535] and that we have previously characterized myopathy and mitochondrial stress in 4-week-old D2.*mdx* mice [23, 24]. In the present study, we compared both diaphragm and limb muscles given their clinical relevance to respiratory and locomotor dysfunction in DMD. Here, we demonstrate that ALY688-SR attenuates fibrosis in both muscles and prevents atrophy in specific muscle fibre types from the diaphragm in relation to attenuated mitochondrial hydrogen peroxide (mH_2O_2) emission. Divergent responses in cytokine markers and reduced *in vitro* diaphragm force production were also observed. Collectively, these results suggest that adiponectin receptor agonism causes dynamic and complex muscle remodeling when administered during early stages of disease progression and at an age of rapid development. The

longer-term effects of this early attenuation in fibrosis, atrophy and mitochondrial stress on force generation capacity warrants further investigation.

Methods

Animal care

Male D2.*mdx* mice were bred from an in-house colony established at York University (Toronto, Ontario) and treated from 7 to approximately 28 days of age. 3 week-old DBA/2J wildtype (WT) mice were ordered directly from Jackson Laboratories (Bar Harbor, USA) due to low breeding performance experienced in-house as reported previously [487] and allowed to acclimatize for 7 days prior to sacrifice. All experiments and procedures were approved by the Animal Care Committee at York University (AUP Approval Number 2016-18) in accordance with the Canadian Council on Animal Care. See *Supporting Information* for more details.

ALY688-SR treatment

D2.*mdx* mice were treated with ALY688-SR (Allysta Pharmaceuticals) at two different dosages; high dose (HD; 15mg/kg body weight/day) or low dose (LD; 3mg/kg body weight/day) dissolved in saline. A separate group of mice were treated with saline alone (VEH, vehicle). Treatment was provided via subscapular subcutaneous injections from 7 days of age to 28-30 days. Wildtype mice did not receive treatment. At 28-30 days of age, mice were anaesthetized with isoflurane vaporized in medical air (21% oxygen) at a 2L/min flow rate. Due to tissue limitations in limb muscle, certain measures were performed separately in tibialis anterior and quadriceps across several phases of breeding. See *Supporting Information* for more details.

RNA isolation & quantitative PCR

All experimental details can be found in *Supporting Information*.

Cytokine profiling

Tibialis anterior and diaphragm homogenates were assessed for cytokine contents by flow cytometry as described in *Supplemental Information*.

Functional assays and serum creatine kinase

Voluntary wheel running, cage hang time and forelimb grip strength were assessed two days before sacrifice and as described previously [23, 536]. Serum derived from cardiac puncture at the time of sacrifice were assessed spectrofluorometrically for creatine kinase activity (U/L) as described in [23].

In-vitro diaphragm force

Assessment of *in-vitro* diaphragm force was partially adapted from [491, 492]. The entire diaphragm was excised, placed in ice cold Ringer solution and a strip not exceeding 3-4mm in width was cut as described previously [491]. All subsequent procedural details can be found in *Supplemental Information*.

In-situ quadriceps force

Quadriceps force protocol was adapted from previous work [537]. Mice were anaesthetized with isoflurane vaporized in medical air (21% oxygen) at a 2L/min flow rate and placed on a platform. Details of remaining procedures can be found in *Supplemental Information*.

Preparation of permeabilized muscle fibre bundles

This technique was adapted from previous methods [23, 495]. Following completion of *in situ* quadriceps force in one limb, the quadriceps from the non-stimulated limb and diaphragm were excised carefully from mice while under heavy sedation with isoflurane and placed immediately into ice-cold BIOPS buffer. Tibialis anterior was not used due to limitations in tissue availability. All subsequent procedural details and buffer composition are described in *Supplemental Information*.

Mitochondrial respiration

Mitochondrial respiration was assessed in permeabilized muscle fibres using high resolution respirometry as described in *Supplemental Information*.

Mitochondrial H_2O_2 emission (mH_2O_2)

mH_2O_2 emission was assessed in permeabilized muscle fibres using spectrofluorometry as described previously [23] and outlined in *Supplemental Information*.

Mitochondrial calcium retention capacity

Mitochondrial calcium retention capacity was assessed spectrofluorometrically as previously described but with modifications [23, 477] as outlined in Supplemental Information.

Histochemical & immunofluorescent staining

Excised muscles were mounted for histology and immunofluorescence in Tissue Plus Optimal Cutting Temperature compound (OCT; Fisher Healthcare), frozen in isopentane chilled in liquid nitrogen and stored at -80°C. All subsequent procedures are detailed in *Supplemental Information*.

Western blotting

Western blotting was performed on tissue lysate using standard SDS-PAGE procedures. Homogenization and western blot procedures are described in *Supplemental Information.*

Statistical analyses

Results are expressed as means ± SD with the level of significance established as $P < 0.05$ for all statistics. All statistical approaches are described in *Supplemental Information.*

Results

ALY688-SR treatment attenuates fibrosis in the diaphragm of D2.mdx mice

We first examined the effect of ALY688-SR treatment on diaphragm fibrosis defined as the absolute increase in collagen relative to levels observed in wildtype (WT). Using Masson's trichrome staining (Figure 6-1B), a 5.5-fold increase in collagen content was observed in diaphragm from vehicle treated D2.*mdx* mice indicating fibrosis is present at a very early stage of disease development (VEH vs WT, Figure 6-1B). Remarkably, both doses of ALY688-SR attenuated this fibrosis by 66.7-67.6%. Collagen content increased from 0.5% to 1.1% in tibialis anterior in D2.*mdx*-VEH mice compared to WT (Figure 6-1C) which indicates the diaphragm is more severely affected at this young age. Consequently, there was no detectable effect of either dose of the drug. Collectively, these findings indicate that early treatment with ALY688 decreases fibrosis in muscles severely affected by dystrophin mutation.

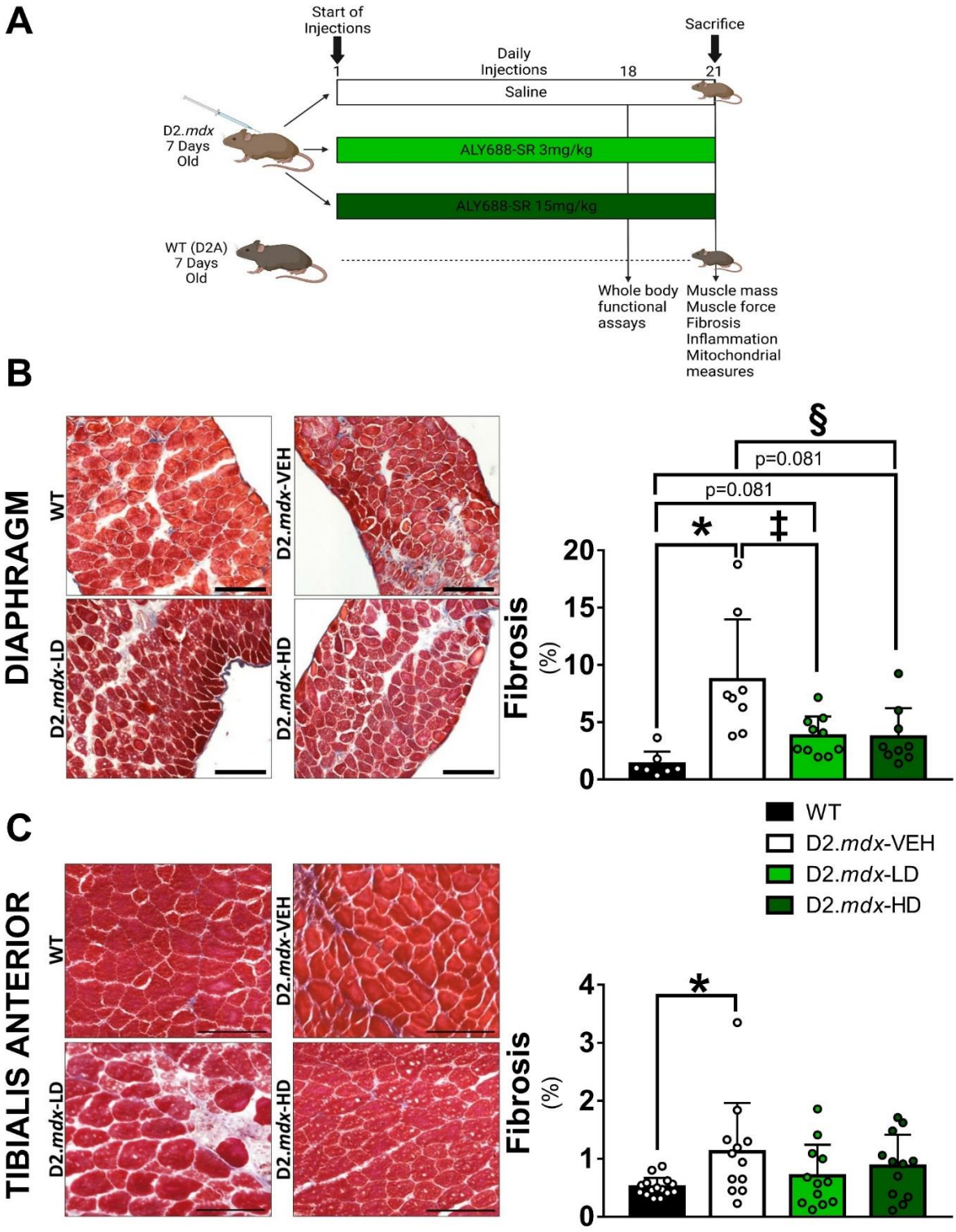

Figure 6-1. Schematic of study design and quantification of interfibrillar collagen accumulation in D2.*mdx* mice treated with ALY688-SR. A visual representation of study design is provided in (A). 7 day old D2.mdx mice received subcutaneous injections of ALY688-SR at a

low dose (LD; 3mg/kg body weight) or high dose (HD; 15mg/kg body weight) or a saline control for 21 days. Healthy D2A mice (wild type (WT)) were used as age matched controls. At day 18 of treatment, all four groups underwent whole body functional assays to assess voluntary muscle function. After 21 days of injections, all groups were sacrificed, and tissue collected for the outlined measures. Fibrosis was evaluated in diaphragm (B) and tibialis anterior (C) using Masson's trichrome staining. Results represent mean ±SD; n=7-15. All p values are FDR-adjusted by Benjamini, Krieger and Yekutieli post-hoc analyses. *$p<0.05$ WT vs D2.mdx- VEH; ‡$p<0.05$ D2.mdx-VEH vs D2.mdx- LD; §$p<0.05$ D2.mdx-VEH vs D2.mdx-HD. Representative images of diaphragm (B, magnification, ×20) and tibialis anterior (C, magnification, ×20). Scale bar =100µm.

ALY688-SR attenuates atrophy of D2.mdx diaphragm in a fibre type-specific manner

We also examined minimal feret diameter in each fibre type as a measure of muscle atrophy. The high dose of ALY688-SR completely prevented atrophy in MHC I fibres. Additionally, in IIA fibres, minimal feret diameter was reduced from 24µm in WT to 20µm in VEH compared to 22µm in HD (Figure 6-2A). In IIB fibres, minimal feret diameter was reduced from 26µm in WT to 23µm in VEH compared to 24µm in HD. A similar prevention of atrophy in IIB fibres was seen in LD.

There were no differences in minimal feret diameter in any fibre type of tibialis anterior between the groups (Figure 6-2B). This finding suggests that the modest fibrosis in tibialis anterior seen at a young age (Figure 6-1C) precedes atrophy given previous studies have shown reductions in fibre size in this muscle at later stages of disease in *mdx* mice [538].

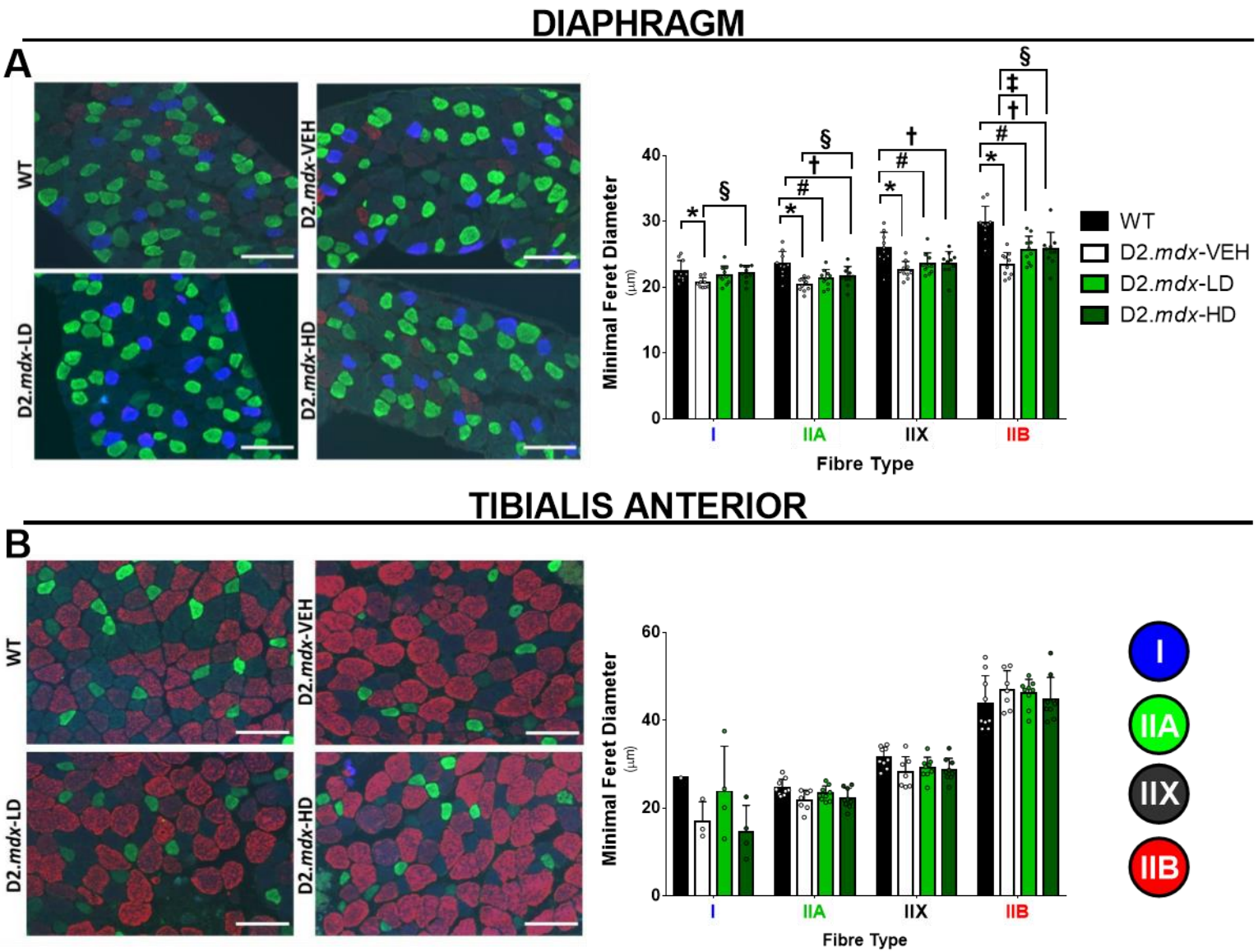
DIAPHRAGM
A
WT
D2.mdx-VEH
D2.mdx-LD
D2.mdx-HD
Minimal Feret Diameter (μm)
0
10
20
30
40
I
IIA
IIX
IIB
Fibre Type
WT
D2.mdx-VEH
D2.mdx-LD
D2.mdx-HD
TIBIALIS ANTERIOR
B
WT
D2.mdx-VEH
D2.mdx-LD
D2.mdx-HD
Minimal Feret Diameter (μm)
0
20
40
60
I
IIA
IIX
IIB
Fibre Type
I
IIA
IIX
IIB

Figure 6-2. Assessments of fibre-type specific minimal feret diameter in D2.*mdx* mice treated with ALY688-SR. Minimal feret diameter was assessed in diaphragm (A) and tibialis anterior (B) using immunofluorescent detection of myosin heavy chain isoforms. Results represent mean ±SD; n=7-10. All p values are FDR-adjusted by Benjamini, Krieger and Yekutieli post-hoc analyses. *p<0.05 WT vs D2.mdx- VEH; #p<0.05 WT vs D2.mdx- LD; †p<0.05 WT vs D2.mdx- HD; ‡p<0.05 D2.mdx-VEH vs D2.mdx- LD; §p<0.05 D2.mdx-VEH vs D2.mdx-HD. Representative images of diaphragm (A, magnification, ×20) and tibialis anterior (C, magnification, ×20). Scale bar =100µm.

ALY688-SR treatment alters markers of inflammation

We next examined the effect of ALY688-SR on markers of muscle damage and inflammation in the diaphragm and tibialis anterior. H&E staining was used to assess the degree of damaged areas consisting of areas of necrosis that often correspond to fibrosis (Figure 6-3A and Supplemental Figure 6-1A). All D2.*mdx* groups demonstrated an increase in damaged areas (3.7-to-3.9-fold change vs WT; Figure 6-3A) suggesting the attenuated fibrosis (Figure 6-1B) with the drug occurred independently of generalized fibre damage. Next, we chose to assess inflammation only with high dose ALY688-SR given that both doses were equally as effective in attenuating fibrosis but the high dose ALY688-SR was more consistent in preventing atrophy. IL-6 mRNA content was increased in diaphragm from D2.*mdx*-VEH mice which was attenuated by the high dose (51.8% increase vs WT; Figure 6-3B). In contrast, ALY688-SR increased IL-6 protein content in the diaphragm (69.1% increase vs VEH; Figure 6-3C). This result in muscle tissue lysate does not rule out the possibility that expression of IL-6 in non-muscle cell types occurred (see Discussion). Increases in IL-1β mRNA in D2.*mdx*-VEH mice (2.7-to-3.0-fold increase vs WT) were not affected by the drug (Figure 6-3B) while protein content was similar between all groups (Figure 6-3C). TNF-α and IL-10 mRNA and protein contents were not different between groups (Figure 6-3). TGF-β protein content was increased in response to the drug (20.3% increase vs VEH; Figure 3C) although mRNA contents were unchanged in all groups (Figure 6-3B).

In the tibialis anterior, robust increases in damaged areas were noted in all three D2.*mdx* groups (17.2-to-22.6-fold increase vs WT; Supplemental Figure 6-1A) in contrast to the small degree of fibrosis seen in Figure 6-1. D2.*mdx*-VEH mice demonstrated greater mRNA contents of TNF-α, IL-1β, IL-6, IL-10 and TGF-β which were paralleled by greater protein contents for TGF-β (9.7-fold increase vs VEH; Supplemental Figure 6-2B, C) compared to wildtype. The high dose of ALY688-SR attenuated TNF-α mRNA compared to VEH (41.4%; Supplemental Figure 6-1B). TNF-α protein content was not detectable in wildtype but increased to 40.6 pg/ml in VEH. HD prevented 83.9% of this increase (Supplemental Figure 6-1C).

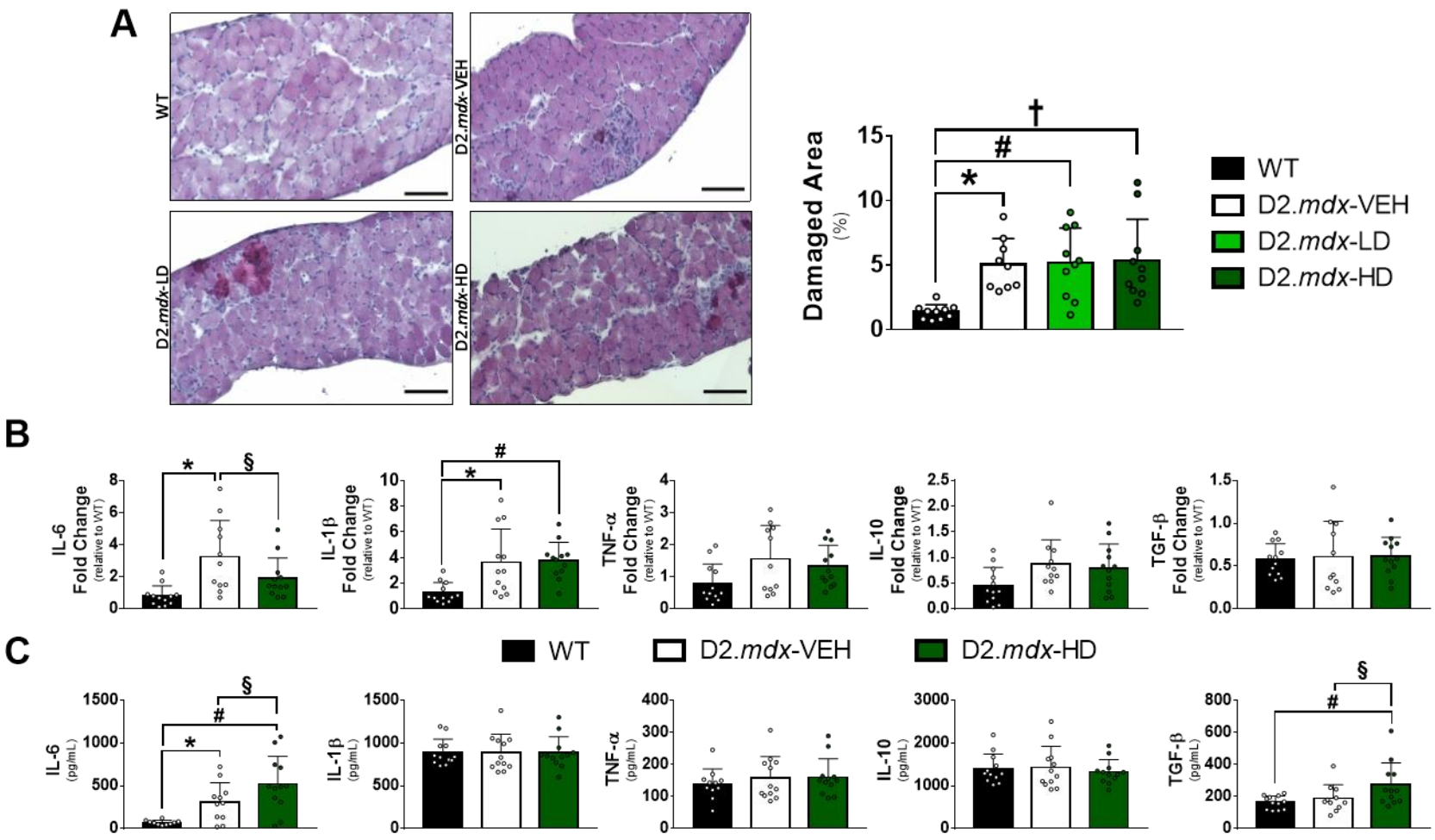
A
WT
D2.mdx-VEH
D2.mdx-LD
D2.mdx-HD
Damaged Area (%)
WT
D2.mdx-VEH
D2.mdx-LD
D2.mdx-HD
B
IL-6 Fold Change (relative to WT)
IL-1β Fold Change (relative to WT)
TNF-α Fold Change (relative to WT)
IL-10 Fold Change (relative to WT)
TGF-β Fold Change (relative to WT)
C
WT
D2.mdx-VEH
D2.mdx-HD
IL-6 (pg/mL)
IL-1β (pg/mL)
TNF-α (pg/mL)
IL-10 (pg/mL)
TGF-β (pg/mL)

Figure 6-3. Effects of ALY688 on inflammation and muscle damage in D2.*mdx* diaphragm. As both doses of ALY688 were effective in reducing fibrosis in diaphragm, only high dose groups were examined in inflammation. (A) Hematoxilyn & eosin staining were used to assess areas of muscle damaged which includes areas of necrosis and fibrosis and expressed as a percentage of total area. Scale bar =100µm. (B) qPCR were used to assess mRNA fold changes of IL-6, IL-1β, TNF-α, IL-10 and TGF-β across WT and D2.*mdx* mice treated with vehicle or high dose ALY688 treatment. qpCR results were normalized to *Rplp00,* and the subsequent ratios were presented as relative expression compared with WT values. (C) Protein levels of the same cytokines, were assessed by BioLegend Multiplex using flow cytometry. Results represent mean ±SD; n=7-12. All p values are FDR-adjusted by Benjamini, Krieger and Yekutieli post-hoc analyses. *p<0.05 WT vs D2.*mdx*- VEH; #p<0.05 WT vs D2.*mdx*- LD; †p<0.05 WT vs D2.*mdx*- HD; §p<0.05 D2.*mdx*-VEH vs D2.*mdx*-HD.

ALY688-SR lowers mitochondrial H_2O_2 emission by enhancing ADP responsiveness

Mitochondria produce H_2O_2 during oxidative phosphorylation of ADP to ATP. As cellular consumption of ATP increases, the cycling of ADP to the matrix is accelerated. Increasing matrix ADP attenuates membrane potential which in turn lowers mH_2O_2 emission given the two latter processes are inversely proportional [42]. By considering these principles, we designed *in vitro* assay conditions to capture the effect of increasing metabolic demand on oxidant generation by titrating ADP following induction of mH_2O_2 emission from mitochondria with NADH-generating substrates (pyruvate/malate) to support Complex I (Figure 6-4A). This approach revealed that mH_2O_2 emission was higher at each ADP concentration in D2.*mdx* diaphragm and quadriceps (2.0-to-9.1-fold increase vs WT; Figure 6-4B, C). This elevation was due specifically to a reduced ability of ADP to attenuate mH_2O_2 relative to wildtype muscle which is similar to our previous findings [22-24, 150]. The results suggest that dystrophin mutation leads to a greater degree of mH_2O_2 emission across a range of oxidative phosphorylation kinetics. The high dose of ALY688-SR completely preserved mitochondrial responsiveness to ADP and restored mH_2O_2 emission to normal kinetics in diaphragm (8.7 to 70.7%; Figure 6-4B). In quadriceps, both doses of the drug partially attenuated mH_2O_2 emission (45.9 to 62.3%; Figure 6-4C). mH_2O_2 emission was not assessed in tibialis anterior.

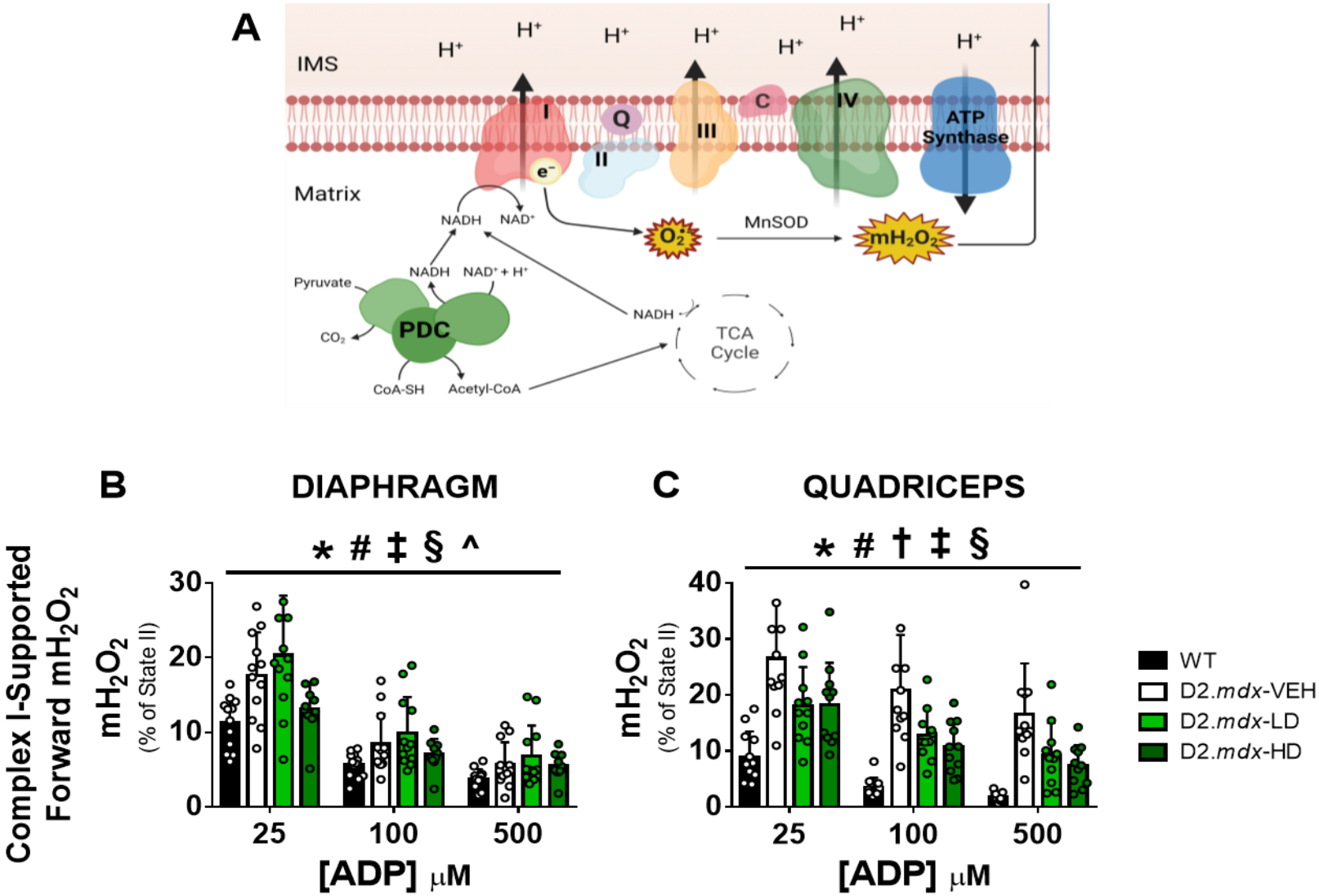
A
IMS
Matrix
H+
I
II
Q
III
C
IV
ATP Synthase
e−
NADH
NAD+
O2
MnSOD
mH2O2
Pyruvate
NADH
NAD+ + H+
CO2
PDC
CoA-SH
Acetyl-CoA
NADH
TCA Cycle
B
DIAPHRAGM
* # ‡ § ^
C
QUADRICEPS
* # † ‡ §
Complex I-Supported Forward mH2O2
mH2O2 (% of State II)
[ADP] μM
25
100
500
WT
D2.mdx-VEH
D2.mdx-LD
D2.mdx-HD

Figure 6-4. ALY688-SR enhances ADP-suppression of complex-I supported mitochondrial H_2O_2 emission. (A) Schematic representation of complex-I supported mitochondrial H_2O_2 emission (mH_2O_2) due to forward electron flow from NADH generated by pyruvate. In states of high membrane potential (low ADP), electrons at complex I may 'slip' prematurely at, for example, Complex I to produce superoxide radicals ($O_2^{\bullet-}$) which are then converted to H_2O_2 by manganese superoxide dismutase (MnSOD). 10mM pyruvate and 2mM malate (to assist with continual flux through pyruvate dehydrogenase complex (PDC)), were used to stimulate electron flow through complex I in permeabilized fibre bundles from diaphragm (B) and quadriceps (C) in the absence of ADP (state II; high membrane potential). Subsequent titrations of physiological levels of ADP ('resting muscle', 25uM; high periods of demand similar to intense exercise; 100uM) and supramaximal (500uM) attenuates mH_2O_2 by promoting forward electron flow and is expressed as a % of State II mH_2O_2 emission to reveal the degree of attenuation in response to ADP. Results represent mean ±SD; n=10-12. All p values are FDR-adjusted by Benjamini, Krieger and Yekutieli post-hoc analyses. *p<0.05 WT vs D2.*mdx*- VEH; #p<0.05 WT vs D2.*mdx*- LD; †p<0.05 WT vs D2.*mdx*- HD; ‡p<0.05 D2.*mdx*-VEH vs D2.*mdx*- LD; §p<0.05 D2.*mdx*-VEH vs D2.*mdx*-HD; ^p<0.05 D2.*mdx*-LD vs D2.*mdx*-HD. TCA= tricarboxylic cycle; PDC= pyruvate dehydrogenase complex. $O_2^{\bullet-}$= superoxide radicals

In separate *in vitro* experiments, we also used succinate ($FADH_2$; Complex II) to stimulate oxidant generation at Complex I as occurs through a unique reverse electron flow from Complex II to Complex I [539, 540]. Furthermore, we compared these kinetics in both the absence and presence of creatine given creatine accelerates matrix ADP/ATP cycling which can alter the influence of ADP in attenuating mH_2O_2, at least in response to succinate [94]. Using this approach, we found that succinate-induced mH_2O_2 emission was also elevated in D2.*mdx* diaphragm but there was no effect of either drug dose (1.1-to-2.3-fold increase vs WT; Supplemental Figure 6-2A, C). However, increased mH_2O_2 emission seen in quadriceps from D2.*mdx* mice were robustly attenuated by both doses (11.3 to 73.6%; Supplemental Figure 6-2B, D).

Thus, while high doses lowered mitochondrial H_2O_2 emission due to forward electron flow from Complex I and supported by glucose-derived substrate (pyruvate) in both muscles, succinate-induced mH_2O_2 emission by reverse electron flow to Complex I was attenuated only in the quadriceps. These findings highlight the complexity of mitochondrial redox regulation across muscle types, the overall findings demonstrate that ALY688-SR lowers mH_2O_2 by preserving mitochondrial responsiveness to ADP.

We also assessed mitochondrial respiration as an index of oxidative phosphorylation in both quadriceps and diaphragm. D2.*mdx* mice demonstrated reduced ADP-stimulated respiration in multiple substrate conditions with generally no effect of either dose in both muscles (-25.9 to -67.0% vs WT; Figure 6-5A, B; Supplemental Figure 6-3A-D; Supplemental Table 6-2). Assessments of mitochondrial content markers through western blotting of electron transport chain complexes subunits were also completed in both muscles (Figure 6-5C, D). Overall, specific subunits of complex III and V, were significantly lowered in disease state groups in both the quadriceps and diaphragm (-14.7 to -31.5% vs WT) and total sum of complexes were reduced in diaphragm (-13.8 to -19.3% vs WT). HD treatment significantly reduced total sum in quadriceps only (-29.1% vs WT) while LD treatment significantly lowered complex IV content in the diaphragm (-27.0% vs WT).

In addition to mH_2O_2 emission and respiration, we also assessed the potential for calcium-induced mitochondrial induction of apoptosis given calcium stress occurs in Duchenne muscular dystrophy [254, 541, 542]. However, there was no differences between groups when assessing mitochondrial calcium retention capacity as a marker of permeability transition pore formation (Supplemental

Figure 6-4). Collectively, these mitochondrial assessments point to a more specific relationship between muscle fibrosis, atrophy and mitochondrial redox stress underlying the effects of ALY688-SR on diaphragm in D2.*mdx* mice.

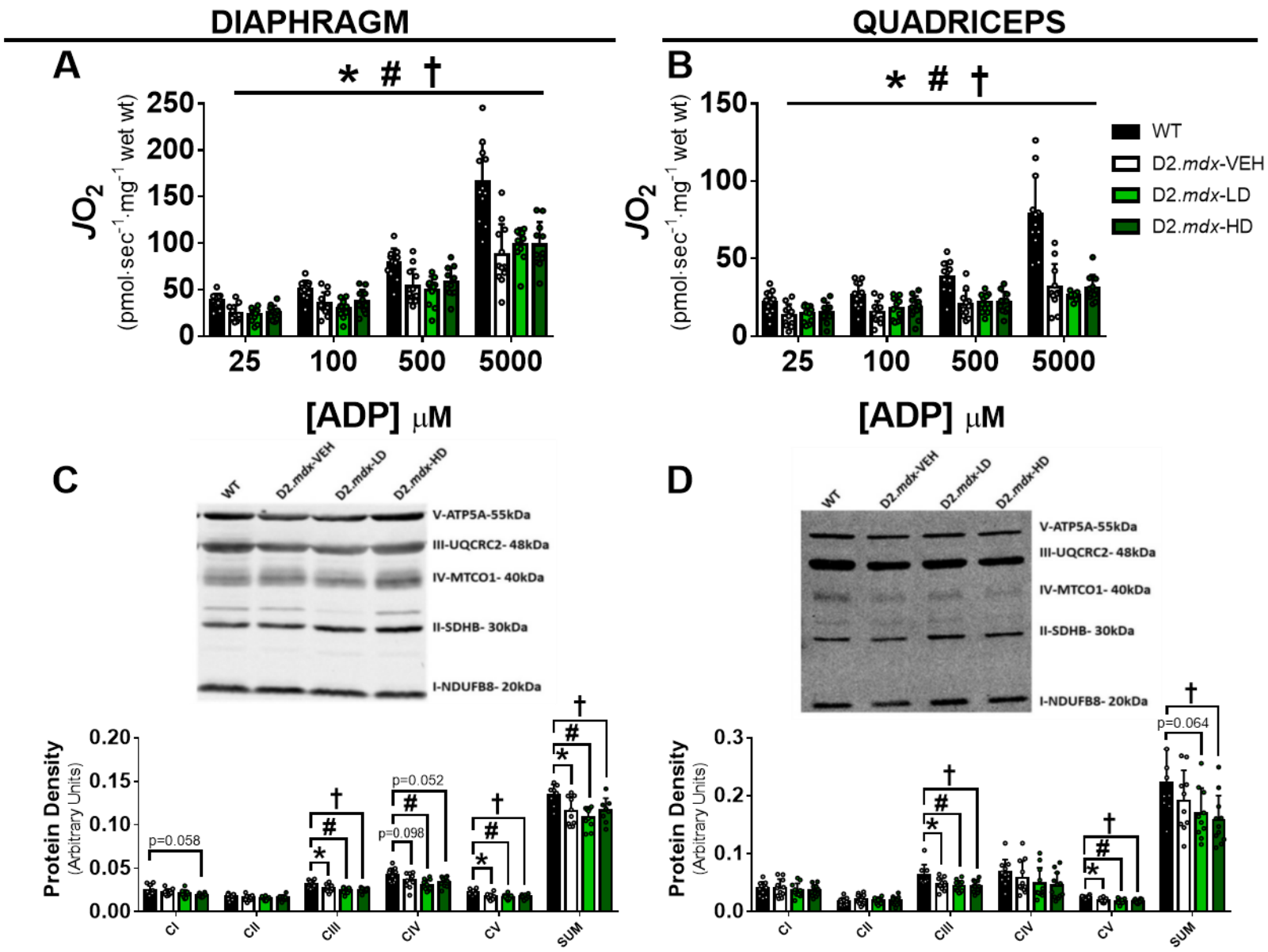
DIAPHRAGM
QUADRICEPS
A
B
C
D
* # †
JO_2 (pmol·sec^{-1}·mg^{-1} wet wt)
250
200
150
100
50
0
25
100
500
5000
[ADP] μM
WT
D2.mdx-VEH
D2.mdx-LD
D2.mdx-HD
V-ATP5A-55kDa
III-UQCRC2- 48kDa
IV-MTCO1- 40kDa
II-SDHB- 30kDa
I-NDUFB8- 20kDa
Protein Density
(Arbitrary Units)
p=0.058
p=0.098
p=0.052
p=0.064
CI
CII
CIII
CIV
CV
SUM

Figure 6-5. Reductions in pyruvate-supported mitochondrial respiration and protein markers of the electron transport chain in D2.*mdx* mice are not altered by ALY688-SR. Complex-I supported respiration (assessed by oxygen flux, JO_2) stimulated by NADH generation through 5mM pyruvate and 2mM malate in permeabilized fibre across a range of ADP concentrations representing increasing states of metabolic demand: 25μM (modeling resting muscle [497]); 100μM (modeling high intensity exercise [53]), 500uM (maximal)[510] and 5000μM (supramaximal) was assessed in the diaphragm (A) and quadriceps (B). Subunits of complexes I, II, III, IV and V were assessed by western blot in diaphragm (C) and quadriceps (D). Results represent mean ±SD; n=9-12. All p values are FDR-adjusted by Benjamini, Krieger and Yekutieli post-hoc analyses. *p<0.05 WT vs D2.*mdx*- VEH; #p<0.05 WT vs D2.*mdx*- LD; †p<0.05 WT vs D2.*mdx*- HD.

ALY688-SR remodels muscle force production

We next determined whether muscle force production was different between groups. As expected, D2.*mdx* mice demonstrated lower muscle force production in both diaphragm strips and quadriceps (Figure 6-6A, B). Both doses of ALY688-SR lowered force relative to both wildtype and D2.*mdx* in diaphragm (-2.3% to –43.0% vs VEH & WT) but had no effect on quadriceps. There was less recovery from fatigue in diaphragm with the high dose and in quadriceps with the low dose (-5.3% to -50.9%; Supplemental Figure 6-7A, B). While initially unexpected, these assessments did not translate to attenuated physical activity behaviours as noted by similar grip strength, cage hang time and voluntary wheel running between all D2.*mdx* groups (-15.1% to -91.0% vs WT Figure 6-6C-E) or serum creatine kinase (marker of muscle damage) in the high dose group despite increases seen with the low dose (3.1-to-5.2-fold increase vs WT; Figure 6-6F).

Collectively, these results suggest that the ability of ALY688-SR to attenuate both fibrosis and atrophy in diaphragm are not paralleled by increased force production. However, these force assessments were not compared to broader physiological indicators of respiratory drive and demand that may contribute to adaptive reprogramming of force generating capacity (See Discussion).

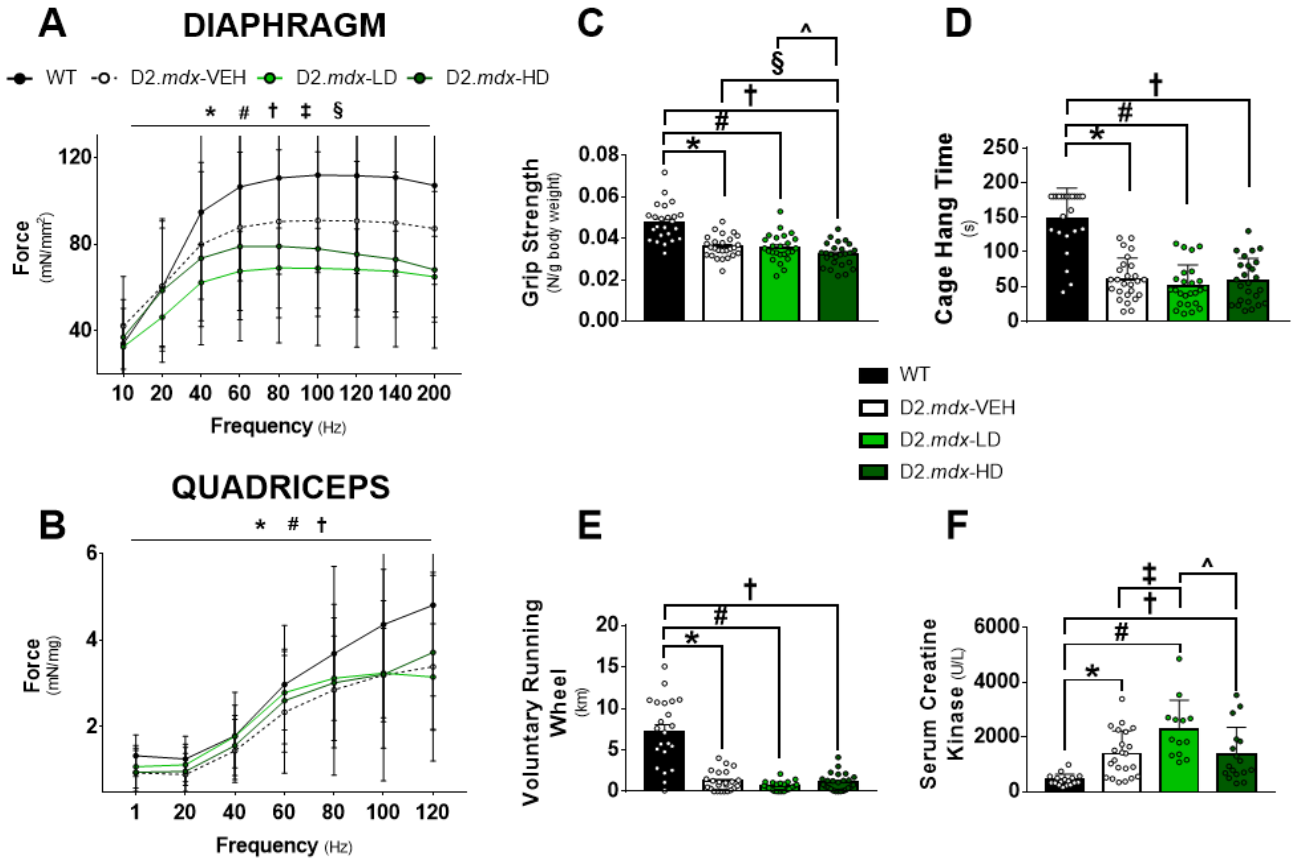

Figure 6-6. Muscle function assessments of D2.*mdx* treated with ALY688-SR. Muscle force was assessed using force frequency protocols in in-vitro diaphragm strips (A) and in-situ quadriceps preparation (B). Serum creatine kinase was assessed as a clinical marker of muscle breakdown (C). Cage hang time (D), grip strength normalized to body weight (E), and distance travelled during 24 hours of voluntary wheel running (F) were assessed as measures of voluntary motor function. Results represent mean ±SD; n=8-13 (A,B); n=13-22 (C); n=21-26 (D-F). All p values are FDR-adjusted by Benjamini, Krieger and Yekutieli post-hoc analyses. *p<0.05 WT vs D2.mdx-VEH; #p<0.05 WT vs D2.mdx- LD; †p<0.05 WT vs D2.mdx- HD; ‡p<0.05 D2.mdx-VEH vs D2.mdx- LD; §p<0.05 D2.mdx-VEH vs D2.mdx-HD; ^p<0.05 D2.mdx-LD vs D2.mdx-HD.

ALY688-SR did not alter AMPK or p38MAPK signaling in D2.mdx mice

ALY688-SR and other adiponectin receptor agonists are thought to attenuate inflammation in part by activating AMPK [443, 445, 543]. As AMPK is also activated in *mdx* mice [79], the potential combined effect of ALY688-SR and disease state in D2.*mdx* mice becomes difficult to predict. Similar to inflammatory measures, only the high dose group was assessed. As shown in Figure 6-7, AMPK phosphorylation was elevated in D2.*mdx* in both diaphragm and quadriceps (33.2% to 69.1% vs WT). The high dose of ALY688-SR had no effect in either muscle (Figure 6-7A-C, G-I). As tissues were assessed ~20-24 hours since the last injection, earlier induction of AMPK may have occurred given prior work showed rapid increases in AMPK phosphorylation in L6 skeletal muscle cells after 30 minutes of treatment [544]. Phosphorylation of p38 MAPK was also assessed given ALY688-SR has been shown to activate this pathway in previous studies [545-547]. However, there were no differences in this measure between any of the groups.

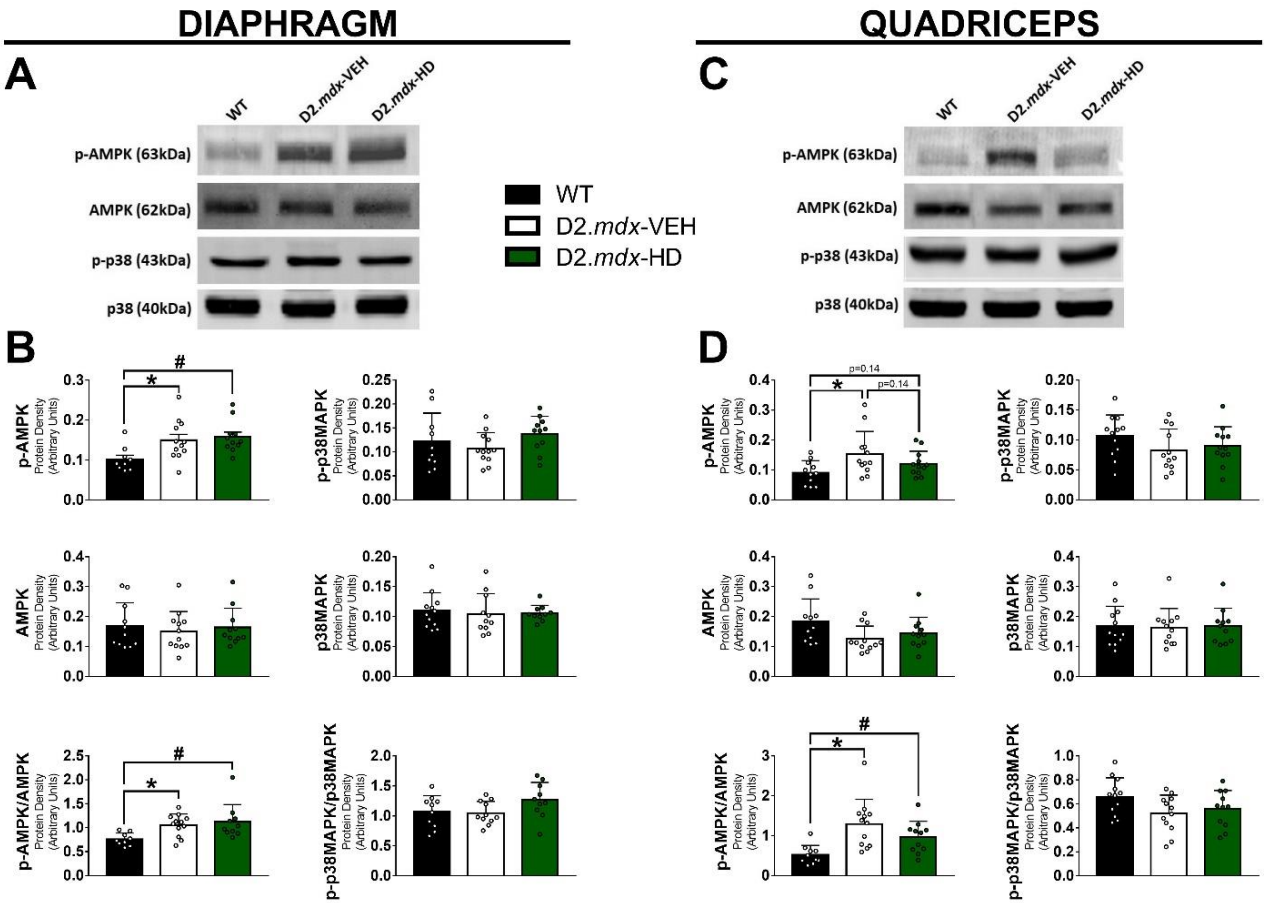

Figure 6-7. Effects of ALY688-SR treatment on AMPK and p38MAPK activity in D2.*mdx* mice. Western blotting was used to quantify the active phosphorylated form of AMPK, total AMPK, phosphorylated p38MAPK, p38MAPK with normalization of phosphorylated forms to total contents as an index of activity in the diaphragm (A,B) and quadriceps (C,D). Low-dose treated animals were excluded in this analysis as high dose treatment attenuated more aspects of dystrophic pathology. Results represent mean ±SD; n=9-12. All p values are FDR-adjusted by Benjamini, Krieger and Yekutieli post-hoc analyses. *p<0.05 WT vs D2.*mdx*- VEH; #p<0.05 WT vs D2.*mdx*- LD.

Discussion

Progressive fibrosis in diaphragm and limb muscles is believed to contribute to muscle dysfunction in people with DMD and dystrophin-deficient *mdx* mice [548-550]. While chronic glucocorticoid treatment is associated with delayed age-related increases in fibrosis, at least in heart [551], there remains an unmet need to therapeutically prevent fibrosis in addition to preserving muscle mass and function. Here, we identify the adiponectin receptor agonist ALY688-SR as an anti-fibrotic that reduced collagen content in the diaphragm by 66.7-67.6% of very young D2.*mdx* mice after 3 weeks of daily treatment. ALY688-SR also partially attenuated diaphragm atrophy in multiple fibre types. These effects were associated with lower diaphragm mitochondrial reactive oxygen species which suggests a relationship exists between mitochondrial stress and myopathy in this model.

Disease-modifying effects of ALY688-SR are more apparent in the severely fibrotic diaphragm

The partial prevention of fibrosis and atrophy in the diaphragm was not observed in the tibialis anterior. However, this is likely due to the minimal disease effects noted in this muscle at this young age demonstrating a heterogeneous response of muscle at this early stage of disease progression in the D2.*mdx* mouse. Specifically, when comparing D2.*mdx* vehicle-treated mice to wildtype, collagen content was many-fold higher in diaphragm but only two-fold higher in tibialis anterior. The results indicate that ALY688-SR is effective at partially preventing fibrosis and atrophy when a robust disease state is present in muscle (e.g. diaphragm). Future studies could consider longer term treatment effects of ALY688-SR in muscles that develop more robust fibrosis and atrophy.

These effects in the diaphragm suggest that adiponectin receptor agonism can regulate muscle fibre size and fibrosis. As ALY688 is known to attenuate markers of inflammation [467], we determined whether such preservations were related to lower inflammation. While ALY688-SR lowered mRNA content of IL-6, increases in IL-6 protein were also observed compared to vehicle-treated D2.*mdx* mice. This finding is difficult to explain given IL-6 has been shown to be directly associated with fibrosis [552-556]. While speculative, this divergent response in IL-6 mRNA and protein measured in diaphragm lysate may be related to differential effects of the drug on muscle fibre expression of IL-6 distinct from production in other cell types such as fibroblasts and immune cells. While recombinant adiponectin was shown to increase IL-6 production in human bronchial epithelial cells [557], the role of IL-6 in regulating fibrosis is also somewhat controversial given

this cytokine is known to have both pro-inflammatory and anti-inflammatory effects depending on the type of experimental model, disease state or systemic stressor [558]. However, mononuclear cell infiltrate assessed by H&E staining was not affected by the drug suggesting changes in fibroblast or immune cell cytokine production may be due to altered activity independent of the cellular contents in muscle tissue.

TGF-β protein content was also increased by ALY688-SR in the diaphragm while mRNA content was not altered, again suggesting a possible increase in production from other cell types within muscle. TGF-β plays an important role in activating fibrosis [339], and was previously shown to be induced by the adiponectin receptor [559, 560]. Additionally, TGF-β is a pleiotropic cytokine that can activate complex signaling pathways with crosstalk at multiple levels leading to highly context-dependent and multifaceted role in health and disease. For example, TGF-β production from tissue resident macrophages and other sources inhibits immune responses, either directly by inhibiting the functions of Th1 and Th2 CD4+ effector cells and NK cells, or indirectly by promoting regulatory T cells (Treg) generation and function[561-563]. These examples demonstrate the opportunity for further investigation into the involvement of other immune cell types by which skeletal muscle in D2.*mdx* mice were remodeled by adiponectin receptor agonism. Overall, the diverse responses in inflammatory factors may be related to the dynamic interplay between early disease progression in the diaphragm and the rapid development and remodeling of muscle that occurs in young D2.*mdx* mice.

In tibialis anterior, ALY688-SR attenuated TNF-α mRNA and protein suggesting a possible direct effect in fibres of this muscle. As there was little fibrosis and no apparent atrophy in this muscle, these results may add further credence to determining whether such early effects of treatment translate into longer-term prevention of the eventual pathology in D2.*mdx* mice that likely manifests in other muscles at later stages of disease progression. For example, atrophy of tibialis anterior fibres was reported as early as 12 weeks [143].

Reduced diaphragm fibrosis and atrophy are related to attenuated mitochondrial redox stress

Mitochondrial H_2O_2 emission in diaphragm muscle fibres was reduced with ALY688-SR treatment. This assessment was performed with NADH-generating substrates which specifically target Complex I of the electron transport chain. The findings add to previous reports that Complex I is dysfunctional in muscle from *mdx* mouse strains [20, 22, 23].

The mechanism of lower Complex I-supported H_2O_2 emission was related to mitochondrial responsiveness to ADP. When ATP is used in muscle by ATP-hydrolyzing pathways generally located outside the mitochondria, as occurs at basal rates in resting/sedentary muscle or at increasing rates during progressively greater muscle contractions, the resulting ADP product cycles back to mitochondria to combine with inorganic phosphate to re-synthesize ATP. The resulting entry of protons from the inner membrane space through ATP synthase into the matrix lowers mitochondrial membrane potential. This event triggers a dual response in the electron transport chain whereby proton pumping from matrix to inner membrane space ensues in tandem with forward electron flux from NADH (Complex I) or other reducing equivalents at other sites. This forward electron flow reduces the probability of premature electron 'slip' onto oxygen to generate superoxide and its dismutated product, H_2O_2. Being membrane permeable, this reactive oxygen species can then be scavenged by mitochondrial antioxidants or emitted into the cytoplasm. In this way, a rise in energy demand manifested as ADP ultimately lowers H_2O_2 emission. The discovery reported herein reveals that *in vivo* administration of ALY688-SR enhanced the ability of ADP to attenuate mH_2O_2 assessed *in vitro* in both diaphragm and quadriceps of D2.*mdx* mice. However, the ability of ADP to stimulate respiration was not altered by ALY688-SR for reasons that are unclear. Nevertheless, this finding suggests that adiponectin receptor regulates some component of the phosphorylation system related to ADP's control of bioenergetics, but the manner by which this occurs either directly or indirectly requires further investigation. The precise mechanism by which mitochondrial H_2O_2 contributes to atrophy and fibrosis in muscle is likely multi-factorial but is increasingly associated with myopathy in muscular dystrophies as discussed elsewhere [256].

Lastly, mitochondria can also export phosphate in the form of phosphocreatine with creatine cycling back for re-phosphorylation by ATP in the matrix. This pathway was assessed by including creatine in the media during assessments and compared to assessments in the absence of creatine as discussed above. As similar conclusions were made in both assay conditions, the results do not suggest that ALY688-SR rescue mitochondrial creatine metabolism in this study design[150].

The relationship between histopathology and muscle force responses to ALY688-SR

The attenuation of diaphragm fibrosis and atrophy occurred concurrently with lower *in vitro* force production. The reason for this lower force production response to short-term treatment of the drug is not apparent but may be related to several factors. First, treatment commenced at 7 days of age

up to 28 days of age. This period of development involves rapid remodeling of muscle tissue that is regulated by extensive coordination of fibroblasts and immune cells. As these cell types are known to be influenced by adiponectin [564, 565], it becomes difficult to predict how adiponectin agonists may influence the balance between muscle mass, extracellular matrix components such as collagen and, force generating capacity. Second, this dynamic period of remodeling is exacerbated by the presence of early-stage disease stressors arising from a lack of dystrophin expression in this model. While speculative, when considering the increased work of breathing that occurs in people with muscular dystrophies [566], we did not determine whether the reduced *in vitro* force production in diaphragm was a result of reduced work of breathing following drug treatment. In line with this speculation, adiponectin-deficient mice have lower dynamic lung compliance [567] predicting that a greater amount of force would be required to increase lung volume. Whether this means that adiponectin lowers the work of breathing remains to be determined but this possibility could explain whether the lower diaphragm force in response to ALY688-SR was an adaptive response to lower demands. However, the reduced recovery from fatigue would not align with this and remains difficult to explain. The attenuation of diaphragm fibrosis and atrophy nonetheless align with clinical interest in these specific outcomes, and their preservation seen herein points to a need for further investigation to determine if longer-term treatment eventually preserves force production once adolescence is complete.

Conclusion

In summary, these results suggest that the recently developed adiponectin receptor agonist ALY688-SR prevents much of the fibrosis in diaphragm and partially prevents atrophy in multiple fibre types. These effects were observed after 3 weeks of short-term treatment in young mice at early stages of the disease. This remodeling was related to dynamic changes in inflammatory markers and attenuated mitochondrial H_2O_2 emission – a known metabolic stressor that occurs in D2.*mdx* muscle. These results warrant further investigation into the longer-term effects of ALY688-SR on other muscles that eventually develop fibrosis and atrophy as well as the relationship of these effects to force production in limb muscle and diaphragm in relation to dynamic work as occurs *in vivo*.

Online supplemental material

Additional supporting information pertaining to methodologies and results are available online. In line with journal requirements, additional references beyond those listed below are available in the supplemental package.

Acknowledgements

ALY688-SR was provided by Allysta Pharmaceuticals.

Author Contributions

Experimental work and or analyses were performed by all authors. All authors contributed to preparing the manuscript.

Funding

Funding was provided to C.G.R.P. by Allysta Pharmaceuticals, the National Science and Engineering Research Council (no. 2019-06687) and an Ontario Early Researcher Award (C.G.R.P., no. 2017-0351) with infrastructure supported by Canada Foundation for Innovation, the James. H. Cummings Foundation, and the Ontario Research Fund. Funding was provided by the National Science and Engineering Research Council to A.A.A.S. (no. 2017-05073) and T.J.H (2018-06324 and 2018-522456) and by the Canadian Institutes of Health Research to G.S. Scholarships were awarded to C.A.B. (NSERC PGS-PhD, MITACS Accelerate), L.N.C. (MITACS Accelerate), L.J.D. (NSERC CGS-D), S.G. and A.T. (Ontario Graduate Scholarships).

Conflicts of Interest and Statement of Contributions

This study was partially funded by Allysta Pharmaceuticals. G.S. is a Scientific Advisor for Allysta Pharmaceuticals. Study design and conception were prepared by C.A.B., S.G., G.S., C.G.R.P and Allysta Pharmaceuticals. Experimental work and analyses were performed by all authors except G.S. The manuscript was written by C.A.B. and C.G.R.P. All authors contributed to the manuscript and approved the final version. The authors of this manuscript certify that they comply with the ethical guidelines for authorship and publishing in the Journal of Cachexia, Sarcopenia and Muscle [568].

Supporting Methods

Animal Care

Mice were housed with littermates until functional testing (commencing 48 hours prior to sacrifice) and then sacrifice (~28 -30 days of age). Mice were maintained on a 12:12-h light-dark cycle while being provided access to standard chow and water ad libitum. Given small tissue size, multiple phases of breeding were required for sufficient masses for analyses. As a result, two phases of breeding and treatments were required.

ALY688-SR treatment

Following the treatment protocol, *in situ* quadriceps force assessments were then performed in one limb followed by removal of the quadriceps from the other limb for mitochondrial assessments, diaphragm for *in vitro* force assessments and finally other tissues for further processing as described below. Muscle and visceral organs weights were normalized to tibia length. Tissue collected from the first phase were utilized in force, histological, mitochondrial measures (respiration, mH_2O_2 and calcium retention capacity) and western analyses (diaphragm and quadriceps only). A second phase was then collected and utilized for cytokine profiling, qPCR analyses and additional westerns (TA only). Serum was collected from both phase 1 and 2 and utilized for serum CK analysis. All animals were utilized in *in vivo* functional assays (grip strength, cage hang time and voluntary wheel running).

Histochemical analysis of muscle regeneration

Centralized nuclei, a marker of regenerating fibres, was analyzed by selecting five evenly spaced images throughout the muscle and averaging the result.

RNA isolation & quantitative PCR

Samples were lysed using TRIzol reagent and RNA was separated to aqueous phase using chloroform. The aqueous layer containing RNA was then mixed with isopropanol and loaded to Aurum Total RNA Mini Kit columns (Bio-Rad, Mississauga, ON, Canada). Total RNA was then extracted according to the manufacturer's instructions and concentration was assessed on the nanodrop attachment for the Varioskan LUX Multimode Microplate reader (Thermo Scientific). Reverse transcription of RNA into cDNA was performed by M-MLV reverse transcriptase and

oligo(dT) primers (Qiagen). cDNA was then amplified in a CFX384 Touch Real-Time PCR Detection Systems (Bio-Rad) with a SYBR Green master mix and specific primers, listed below in Table 6-1. Standard curves were created by plotting log DNA concentrations against Ct values from a 1:5 serial dilutions with CFX Manager Software. Gene expression was normalized to a *Rplp0* control [569], and relative differences were determined using the ΔΔCt method [570]. Values are presented as fold increases relative to WT group.

Table 6-1: Primers for Cytokine (listed 5' to 3')

Gene	***Primer***
IL-1β	*Forward* *GCAGCACATCAACAAGAG* *Reverse* *CAGCAGGTTATCATCATCATC*
TNF-α	*Forward* *AGAATGAGGCTGGATAAGAT* *Reverse* *GAGGCAACAAGGTAGAGA*
TGF-β	*Forward* *CCTGCAAGACCATCGACATG* *Reverse* *TGTTGTACAAAGCGAGCACC*
IL-6	*Forward* *ACAGAAGGAGTGGCTAAG* *Reverse* *AGAGAACAACATAAGTCAGATAC*
IL-10	*Forward* *ATAACTGCACCCACTTCCCA* *Reverse* *GGGCATCACTTCTACCAGGT*
Rplp0	*Forward* *TTGGAGTGACATCGTCTT* *Reverse* *ATCTTGAGGAAGTAGTTGGA*

Cytokine profiling

Tibialis anterior and diaphragm samples were homogenized in lysis buffer containing (in mM) (20 Tris/HCl, 150 NaCl, 1 EDTA, 1 EGTA, 1% Triton X-100, 2.5 $Na_4O_7P_2$, 1 Na_3VO_4, pH 7.0) supplemented with protease (Roche) and phosphatase inhibitors (Sigma). Samples were diluted two-fold in the assay buffer before loading to the plates with beads. According to the manufacturer's instructions, levels of TGF-β, TNF-α, IL-1β, IL-6 and IL-10 in the homogenates were measured using LEGENDplexTM Mouse Custom Panel. Assay was performed in the Attune NxT flow cytometer (Thermo Fisher). The FCS files generated on the flow cytometer were analyzed using the LEGENDplex™ cloud-based analysis software.

In-vitro diaphragm force

A silk suture was attached to the central tendons and the ribs and secured in a bath with oxygenated Ringers solution containing (in mM) 121 NaCl, 5 KCl, 1.8 $CaCl_2$, 0.5 $MgCl_2$, 0.4 $NaHPO_4$, 24 $NaHCO_3$, 5.5 glucose and 0.1 EDTA; pH 7.3 (95% O_2/5% CO_2) maintained at 25°C with ribs secured to the force transducer with an s-hook and central tendon to the lever arm. The diaphragm was positioned between two platinum electrodes driven by a biphasic stimulator (Model 305C; Aurora Scientific, Inc., Aurora, ON, Canada) and allowed to acclimatize for 30 minutes. Optimal resting length (L_0) was found using single twitches until maximal force was attained. A force-frequency curve was performed (1, 10, 20, 40, 60, 80, 100, 120, 140, 200 Hz) with 1 minute of rest between contractions with a final 5- minute rest period provided before a fatiguing protocol was performed (70Hz for 350ms every 2 seconds for 5 minutes). After the force-frequency protocol was assessed, a 5 minute rest period was provided before a fatiguing protocol was performed (70Hz for 350ms every 2 seconds for 5 minutes). Recovery from fatigue was assessed at 5-, 10- and 15-minutes post fatigue at the frequency that elicited maximum force in the force-frequency protocol. Force production was analyzed using Dynamic Muscle Control Data Acquisition software (Aurora Scientific, Inc) and normalized to cross sectional area (CSA) of the muscle strip (m/l*d) where ‘m’ is the mass of the strip devoid of the central tendon and ribs, ‘l’ is the length (from the point of insert on the ribs to the myotendinous junction of the central tendon) and ‘d’ is the mammalian skeletal muscle density (1.06g/mm^3) [494].

In-situ quadriceps force

Body temperature was maintained using an overhead heat lamp. Once fully sedated, hair was removed from the knee and a small vertical incision was made above the knee to expose the patellar tendon. The tendon was then secured with a suture (4/0; Fine scientific instruments, North Vancouver, Canada), with a loop at the end. The tendon was then severed, and the loop was then attached to an Aurora Scientific 305C muscle lever arm with an s-hook (Aurora, Ontario, Canada). A 27 G needle was pierced from the lateral side of the knee through the femoral epicondyles immobilizing the knee joint. The knee was then secured with a vertical knee clamp and quadriceps contraction was facilitated through percutaneous stimulation of the femoral nerve. Optimal resting length (L_0) was determined using single twitches (pulse width=0.2ms) at varying muscle lengths at the maximal stimulation current. Force was assessed across increasing frequencies (1, 40, 60, 80, 100, 120 Hz) using a biphasic stimulator (Model 710B, Aurora Scientific, Inc., ON, Canada), with one minute rest between each frequency. After a five minute rest period, a fatigue protocol (70Hz stimulation once every 1.5s for 120 contractions) was initiated. Recovery from fatigue was assessed 5, 10 and 15 minutes after the last contraction of the fatigue protocol at the frequency that elicited max force. Data were analyzed using Dynamic Muscle Control Data Acquisition software (Aurora Scientific, Inc) and normalized to quadriceps weight in mg.

Preparation of permeabilized muscle fibre bundles

The quadriceps from the non-stimulated limb and the diaphragm were collected and quickly placed in a buffer containing (in mM) 50 MES Hydrate, 7.23 K_2EGTA, 2.77 CaK_2EGTA, 20 imidazole, 0.5 dithiothreitol, 20 taurine, 5.77 ATP, 15 PCr, and 6.56 $MgCl_2 \cdot 6\ H_2O$ (pH 7.1). Both muscles were trimmed of connective tissue and fat and separated along the longitudinal axis into small bundles weighing approximately 1.0-2.5mg wet weight for respiration and mH_2O_2 and 0.5-1.5mg wet weight for calcium retention capacity. Bundles were permeabilized with 40µg/µL saponin (Sigma Aldrich; St. Louis, MI, USA) in BIOPS on a platform rotor for 30 minutes at 4°C. The permeabilized bundles were then transferred to wash buffers to remove saponin as follows: MiRO5 for mitochondrial respiration, Buffer Z for mitochondrial H_2O_2 emission (mH_2O_2), and Buffer Y for calcium retention capacity. The composition of each buffer has been described previously [23]. Fibres prepared for pyruvate-supported mitochondrial H_2O_2 emission (mH_2O_2) were permeabilized in the presence of 35µM 2,4-dinitrochlorobenzene (CDNB) to deplete glutathione and enhance the

detection of mH_2O_2 [496]. All bioenergetic assays were performed within 4 hours of washing to maintain fibre viability.

Mitochondrial respiration

High resolution oxygen consumption (an index of mitochondrial respiration) was performed in 2mL of MiRO5 supplemented with (creatine-dependent) or without (creatine independent) 20mM creatine to saturate mitochondrial creatine kinase activity [495, 497]. O_2 consumption was measured using the Oroboros Oxygraph-2K (Oroboros Instruments, Corp., Innsbruck, Austria) while stirring at 37°C in the presence of 5µM blebbistatin to prevent muscle fibre contraction by rigor in response to ADP [495]. Each chamber was oxygenated with 100% pure O_2 to an initial concentration of ~350 µM and experiments were completed before chamber [O_2] reached 150 µM [495, 498, 499, 571, 572]. Prior to permeabilization, fibre bundles were gently and quickly blotted dry, weighed in ~1.5 mL of tared cold BIOPS (ATP-containing relaxing media) to ensure fibres remained relaxed. Respiration was normalized to bundle wet weight. Complex I-supported respiration was stimulated using 5mM pyruvate and 2mM malate (NADH; State II respiration) followed by a titration of ADP concentrations (State III) from physiological ranges (25, 100µM) to supraphysiological (500 µM) and saturating to stimulate maximal coupled respiration (5000 µM). An addition of 10µM cytochrome *c* was added to test mitochondrial outer membrane integrity. Experiments with very low ADP-stimulated respiration and high cytochrome c responses were removed. Lastly, 10mM succinate ($FADH_2$) was added to support complex-II respiration.

Mitochondrial H_2O_2 emission (mH_2O_2)

Briefly, mH_2O_2 was determined spectrofluorometrically (QuantaMaster 40, HORIBA Scientific, Irvine, CA, USA) utilizing Buffer Z containing 10µM Amplex Ultra Red (Life Technologies; Carlsbad, CA, USA), 1U/mL horseradish peroxidase, 1mM EGTA, 40U/mL Cu/Zn SOD1, 5µM blebbistatin and 20mM Cr. Complex I-supported mH_2O_2 was initiated through the addition of 10mM pyruvate and 2mM malate (NADH; forward electron flow) and separately with 10mM succinate ($FADH_2$; reverse electron flow from Complex II to I). The ability of ADP to suppress mH_2O_2 was assessed with a titration of physiological concentrations (25, 100) and saturating for oxidant generation (500µM). All protocols were repeated without creatine in the assay buffer to permit comparisons with the creatine condition, thereby allowing assessments of mitochondrial creatine sensitivity. Bundles were lyophilized in a freeze-dryer (Labconco, Kansas City, MO, USA)

for >4 h and weighed on a microbalance (Sartorius Cubis Microbalance, Gottingen, Germany). The rate of mH_2O_2 emission was calculated using a standard curve under the same assay conditions and then normalized to fibre bundle dry weight.

Mitochondrial calcium retention capacity

This assay was measured spectrofluorometrically (QuantaMaster 80, HORIBA Scientific) in a cuvette with 300µL assay buffer containing 1 µM Calcium Green-5N (Invitrogen), 2 µM thapsigargin, 5 µM blebbistatin, and 40 µM EGTA while maintained at 37°C with continuous stirring. 5mM glutamate, 2mM malate, 5mM ADP and 20mM creatine were added to the assay buffer and minimum fluorescence was recorded. 4nmol pulses of $CaCl_2$ were added until the mitochondrial permeability transition pore (mPTP) opening was observed as an increase in fluorescence corresponding to net mitochondrial calcium release, at which point saturating pulses of $CaCl_2$ were used to establish maximum fluorescence. Changes in free Ca^{2+} during mitochondrial Ca^{2+} uptake were then calculated using the known K_d for Calcium Green-5N and equations established for calculating free ion concentration [478]. Calcium retention was then normalized to fibre bundle dry weight.

Histochemical & Immunofluorescent Staining

Samples collected were cut into 8µm thick serial cross sections with a cryostat (Thermo Fisher Scientific; Kalamazoo, MI, United States;) maintained at -20°C on Fisherbrand Superfrost Plus slides (Thermo Fisher Scientific). Hematoxylin and eosin (H&E) and Masson's trichrome staining was used to assess muscle health and fibrosis as previously described [23]. Centralized nuclei, a marker of regenerating fibres, was analyzed by selecting five evenly spaced images throughout the muscle and averaging the result. Areas of damage (fibres with fragmented sarcoplasm and immune cell infiltration) were expressed as a percentage of the entire muscle section. Images were taken using EVOS M7000 imager (Thermo Fisher Scientific) using 20X magnification and analyzed using ImageJ (http://imagej.nih.gov/ij/). To determine fibrotic area, skeletal muscle sections were stained with Masson's Trichrome (fibrotic regions stain blue for collagen) and expressed as a percentage of a region of interest, which included the entire muscle section with any artifacts removed. Sections were imaged Nikon 90i-eclipse microscope (Nikon Inc., Melville, NY) and analysed with the NIS Elements AR software (v4.6, Nikon). Immunofluorescent analysis of myosin heavy chain expression was previously described [500]. Images were taken with EVOS M7000

equipped with standard red, green, blue filters cubes. Fibres that were not positively stained were considered IIX fibres. These images were then analyzed with ImageJ for minimal Feret's diameter as an index of muscle atrophy [131].

Western blotting

Frozen sections of quadriceps and diaphragm from each muscle (approximately 10-30mg in size) were homogenized using a plastic microcentrifuge tube with tapered Teflon pestle in ice-cold lysis buffer containing (in mM) (20 Tris/HCl, 150 NaCl, 1 EDTA, 1 EGTA, 1% Triton X-100, 2.5 $Na_4O_7P_2$, 1 Na_3VO_4, pH 7.0) supplemented with protease (Sigma) and phosphatase inhibitors (Roche). A 12% gel was used to separate electron transport chain proteins and all other proteins were separated on a 10% gel. Following, all gels were transferred onto 0.2µm low fluorescence PVDF membrane (Bio-Rad, Mississauga, Canada) and blocked with Li-COR Intercept Blocking Buffer (LI-COR, Lincoln NE, USA) for 1 hour. Membranes were then incubated with specific primary antibodies (listed below) overnight at 4°C. A commercially available monoclonal rodent OXPHOS Cocktail (ab110413; Abcam, Cambridge, UK, 1:250 dilution) including V-ATP5A (55 kDa), III-UQCRC2 (48 kDa), IV-MTCO1 (40 kDa), II-SDHB (30 kDa), and I-NDUFB8 (20 kDa) were used to detect electron transport chain proteins. Commercially available polyclonal antibodies were used to detect p-AMPKα (Thr172; 62kDa) (2535, Cell Signaling Technologies (CST), 1:1000), AMPKα (62 kDa; 2532, CST, 1:500), p-p-38MAPK (Thr180/Tyr182;43 kDa;) (9211, CST, 1:1000) and p38MAPK (40 kDa; 9212, CST, 1:500). After overnight primary antibody incubation, membranes were washed three times (5 minutes each time) in TBS-T and incubated at room temperature with appropriate fluorescent secondary antibody (LI-COR). Prior to detection, membranes were washed in TBS-T three times for 5 minutes and then imaged using infrared imaging (LI-COR CLx; LI-COR, Lincoln, NE, USA) and quantified by densitometry (ImageJ, http://imagej.nih.gov/ij/). All images were normalized total protein from the same membrane stained using Amido Black total protein-stained membrane (A8181, Sigma).

Statistical analyses

Prior to statistical analyses, outliers were omitted in accordance with ROUT testing (Q=0.5%) and then tested for normality using a D'Agostino–Pearson omnibus normality test (GraphPad Prism Software, La Jolla, CA, USA). State III respiration and mH_2O_2 were analyzed using a two-way ANOVA followed by a two-stage step-up method of Benjamini, Krieger and Yekutieli for

controlling False Discovery rate (FDR) for multiple-group comparisons. For all other data, statistical differences were analyzed using a one-way ANOVA between all groups followed by a two-stage step-up method of Benjamini, Krieger and Yekutieli post hoc analyses where appropriate. All reported p-values are FDR-adjusted p values (traditionally termed ‘q’).

Supplemental Results

Supplemental Table 6-1: Anthropometrics effects of ALY688-SR treatment

	Wild-Type	**D2.*mdx*-VEH**	**D2.*mdx*-LD**	**D2.*mdx*-HD**
Body Weight (g)	15.8 ± 2.6	13.2 ± 1.5*	12.4 ± 1.3$^{\#}$	13.3 ± 1.6†^
Tibial Length (mm)	15 ± 0.7	14 ± 0.6*	14 ± 0.5$^{\#}$	14 ± 0.5†
Muscle (mg/mm)				
Quadriceps	6.4 ± 1.0	6.7 ± 1.3	6.1 ± 0.7	6.7 ± 0.9
Extensor Digitorum Longus	0.3 ± 0.1	0.3 ± 0.1	0.3 ± 0.1	0.3 ± 0.1
Tibialis Anterior	1.7 ± 0.2	1.7 ± 0.3	1.6 ± 0.3	1.6 ± 0.3
Soleus	0.3 ± 0.1	0.3 ± 0.1	0.3 ± 0.1	0.3 ± 0.1
Plantaris	0.5 ± 0.1	0.5 ± 0.2	0.5 ± 0.1	0.5 ± 0.1
Gastrocnemius	3.8 ± 0.4	3.6 ± 0.5	3.5 ± 0.3	3.6 ± 0.4
Triceps	3.1 ± 0.8	3.5 ± 1.3	3.3 ± 0.8	3.8 ± 0.9†
Adipose Pad (mg/mm)				
Inguinal	7.2 ± 2.0	3.1 ± 1.1*	2.9 ± 0.7$^{\#}$	3.6 ± 0.8†
Epididymal	8.9 ± 3.7	1.5 ± 0.5*	1.1 ± 0.4$^{\#}$	1.8 ± 0.6†
Viscera (mg/mm)				

Spleen	5.4 ± 1.2	5.0 ± 1.3	4.3 ± 1.07$^{\#\ddagger}$	5.1 ± 1.0^
Kidney	8.3 ± 1.9	7.1 ± 1.4*	6.6 ± 1.0$^{\#}$	7.3 ± 1.0†
Liver	55.0 ± 7.5	55.7 ± 9.4	48.1 ± 4.6$^{\#\ddagger}$	59.2 ± 9.0†^

Results represent mean ±SD; n=7-10. All p values are FDR-adjusted by Benjamini, Krieger and Yekutieli post-hoc analyses. *p<0.05 WT vs D2.*mdx*- VEH; #p<0.05 WT vs D2.*mdx*- LD; †p<0.05 WT vs D2.*mdx*- HD; ‡p<0.05 D2.*mdx*-VEH vs D2.*mdx*- LD; §p<0.05 D2.*mdx*-VEH vs D2.*mdx*-HD; ^p<0.05 D2.*mdx*-LD vs D2.*mdx*-HD

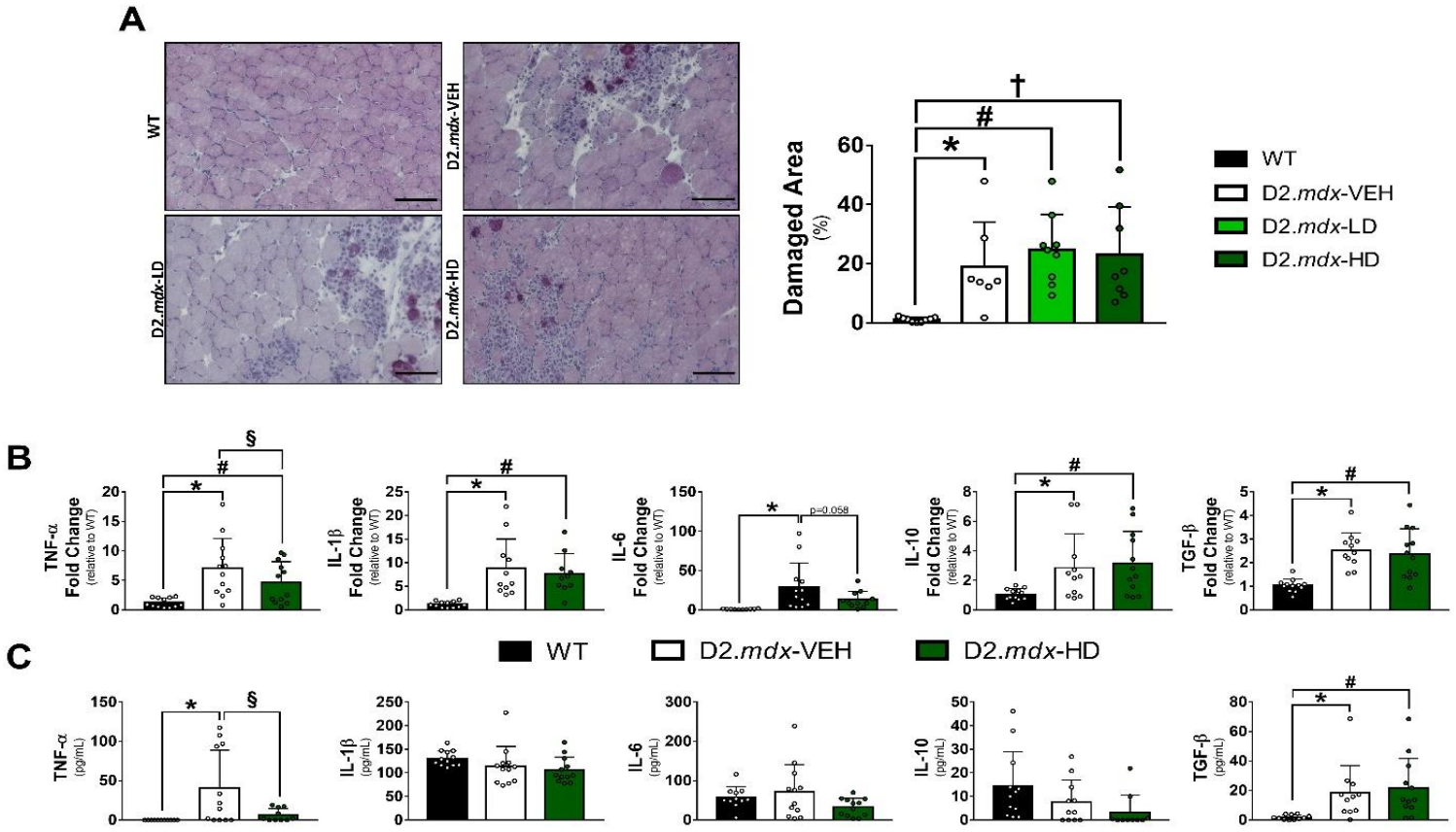

Supplemental Figure 6-1. Effects of ALY688 on inflammation and muscle damage in D2.*mdx* tibialis anterior. (A) Hematoxylin & eosin staining were used to assess areas of muscle damage which includes areas of necrosis and fibrosis and expressed as a percentage of total area. Scale bar =100µm. (B) qPCR were used to assess mRNA fold changes of TNF-α, IL-1β, IL-6, IL-10 and TGF-β across WT and D2.*mdx* mice treated with vehicle or high dose ALY688 treatment. qPCR results were normalized to *Rplp0*, and the subsequent ratios were presented as relative expression compared with WT values. (C) Protein levels of the same cytokines, were assessed by BioLegend Multiplex using flow cytometry. Results represent mean ±SD; n=7-12. All p values are FDR-adjusted by Benjamini, Krieger and Yekutieli post-hoc analyses. *p<0.05 WT vs D2.*mdx*- VEH; #p<0.05 WT vs D2.*mdx*- LD; †p<0.05 WT vs D2.*mdx*- HD; §p<0.05 D2.*mdx*-VEH vs D2.*mdx*-HD.

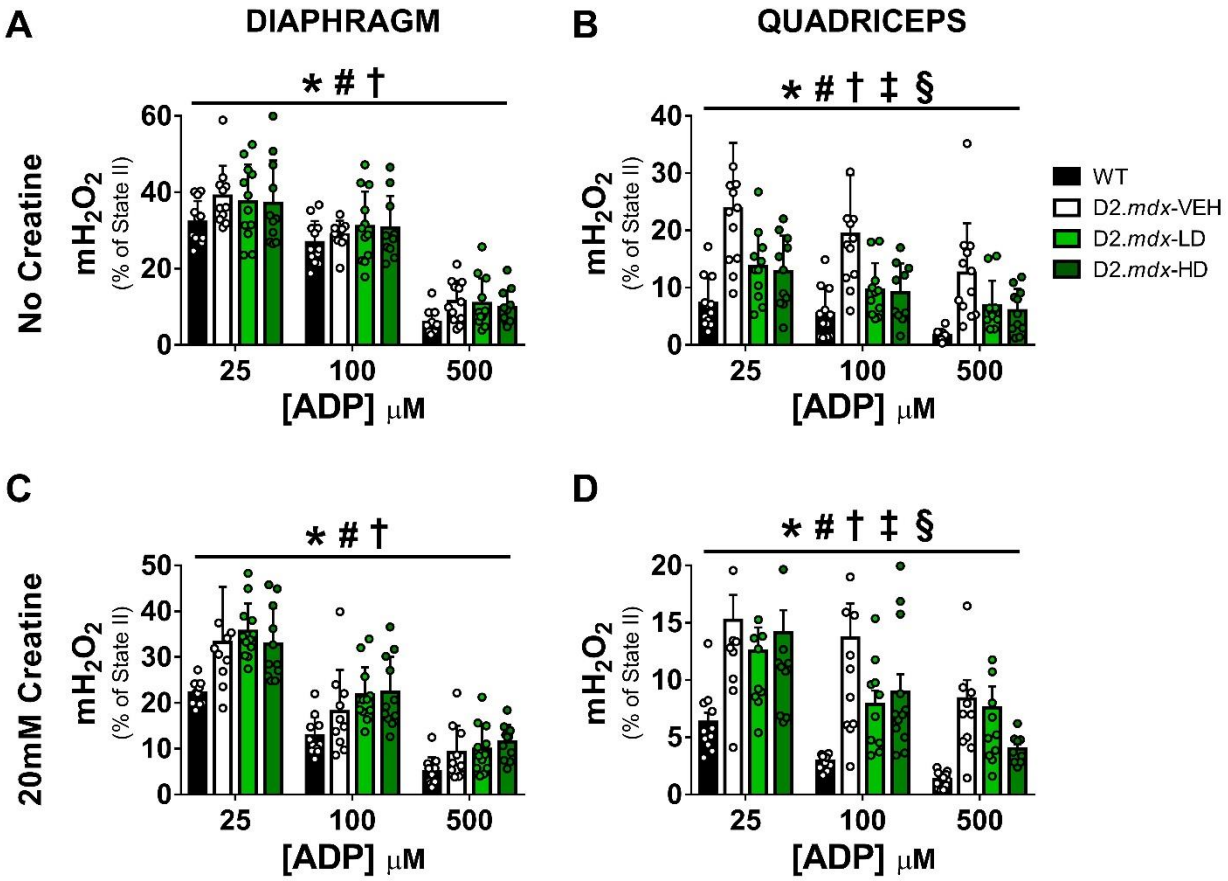

Supplemental Figure 6-2. **ALY688-SR enhances ADP attenuation of mitochondrial H_2O_2 emission supported by succinate in quadriceps.** The ability of ADP to attenuate mitochondrial H_2O_2 emission (mH_2O_2) stimulated by succinate was assessed in permeabilized fibres of diaphragm (A,B) and quadriceps (C,D). 10mM succinate ($FADH_2$) was used to stimulate electron flow in reverse direction from complex II to complex I to generate superoxide that is dismutated to H_2O_2. ADP's attenuation of mH_2O_2 was assessed in the absence (A,C) and presence (B,D) of creatine (accelerator of matrix ADP/ATP cycling) across a range of ADP concentrations depicting increasing metabolic demand [45, 497, 510]. Analyses were performed in the diaphragm (A,B) and quadriceps (C,D). Results represent mean ±SD; n=10-12. All p values are FDR-adjusted by Benjamini, Krieger and Yekutieli post-hoc analyses. *p<0.05 WT vs D2.*mdx*- VEH; #p<0.05 WT vs D2.*mdx*- LD; †p<0.05 WT vs D2.*mdx*- HD; ‡p<0.05 D2.*mdx*-VEH vs D2.*mdx*- LD; §p<0.05 D2.*mdx*-VEH vs D2.*mdx*-HD.

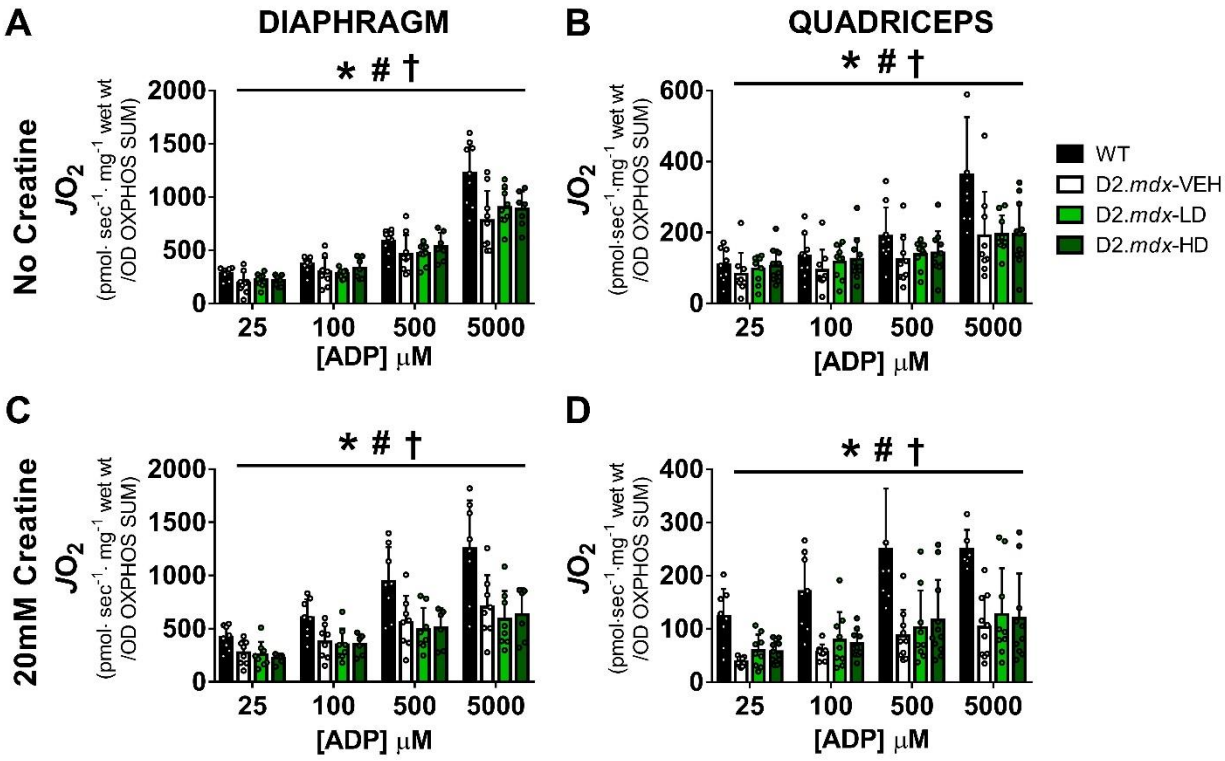

Supplemental Figure 6-3. Mitochondrial respiration normalized to mitochondrial content markers is not altered by ALY688-SR treatment. Complex-I supported respiration (assessed by oxygen flux, JO_2) normalized to protein markers of the electron transport chain (from Figure 6-6B) as an index of mitochondrial content in diaphragm (A,B) and quadriceps (C,D) in the absence (A,C) and presence (B,D) of 20mM creatine (to accelerate ADP/ATP cycling) across a range of increasing metabolic demand (ADP concentrations) [45, 497, 510]. Results represent mean ±SD; n=9-12. All p values are FDR-adjusted by Benjamini, Krieger and Yekutieli post-hoc analyses. *p<0.05 WT vs D2.*mdx*- VEH; #p<0.05 WT vs D2.*mdx*- LD; †p<0.05 WT vs D2.*mdx*- HD.

Supplemental Table 6-2: Reductions in creatine-accelerated mitochondrial respiration supported by pyruvate and succinate are not altered by ALY688-SR.

	Diaphragm				**Quadriceps**			
[ADP] (μM)	WT	D2.*mdx*-VEH	D2.*mdx*-LD	D2.*mdx*-HD	WT	D2.*mdx*-VEH	D2.*mdx*-LD	D2.*mdx*-HD
Creatine-dependent Complex I-supported respiration (pyruvate) (pmol $O_2 \cdot sec^{-1} \cdot mg^{-1}$ wet weight)								
0 (State II)	39.9± 12.0	21.4± 8.2*	19.4± 9.9$^{\#}$	20.4± 4.4†	12.5± 4.8	5.0± 1.8*	5.8± 3.1$^{\#}$	7.0± 2.5†
25	55.4± 15.9	30.9± 13.4*	21.6± 5.0$^{\#,\ddagger}$	27.7± 5.5†	25.3± 6.7	8.0± 3.4*	9.8± 5.3$^{\#}$	10.15± 6.0†
100	81.0± 25.4	45.3± 17.7*	30.5± 7.2$^{\#,\ddagger}$	42.2± 9.0†	35.8± 9.1	11.5± 4.5*	13.4± 8.4$^{\#}$	12.6± 7.3†
500	126. 7± 45.4	68.4± 28.2*	50.2± 18.3$^{\#}$	64.1± 20.2†	54.2± 13.3	15.1± 7.1*	17.8± 10.6$^{\#}$	17.3± 10.7†
5000	174.2± 66.0	84.7± 34.9*	62.0± 23.2$^{\#}$	85.7± 34.8†	74.6± 22.5	18.7± 10.0*	22.2± 12.9$^{\#}$	22.0± 16.2†
Creatine-dependent Complex I+II-supported respiration (pyruvate, glutamate, succinate) (pmol $O_2 \cdot sec^{-1} \cdot mg^{-1}$ wet weight)								
Max	215.3± 79.7	161.7± 55.1$^{\#}$	135.3± 37.7	159.9± 33.8	122.7± 51.7	60.3± 17. 6*	60.1± 21.0$^{\#}$	64.9± 19.1†

Creatine accelerates matrix-ADP/ATP cycling through mitochondrial creatine kinase activation [43-46, 52-54] in contrast to data in Figure 6-6 which was assessed in the absence of creatine (slower state of ADP/ATP cycling). Complex-I supported respiration stimulated

by NADH generation (5mM pyruvate and 2mM malate) in permeabilized fibres across a range of ADP concentrations representing increasing states of metabolic demand: 25μM (modeling resting muscle [497]); 100μM (modeling high intensity exercise [53, 510]), 500uM (maximal) and 5000μM (supramaximal) was assessed in the diaphragm (A) and quadriceps (B). Following ADP titrations, 20mM succinate was added to generate $FADH_2$ which stimulates forward electron flow (due to presence of ADP) from Complex II (yielding Complex I+II supported respiration). Results represent mean ±SD; n=9-12. All p values are FDR-adjusted by Benjamini, Krieger and Yekutieli post-hoc analyses. *p<0.05 WT vs D2.*mdx*- VEH; #p<0.05 WT vs D2.*mdx*- LD; †p<0.05 WT vs D2.*mdx*- HD; ‡p<0.05 D2.mdx-VEH vs D2.mdx- LD.

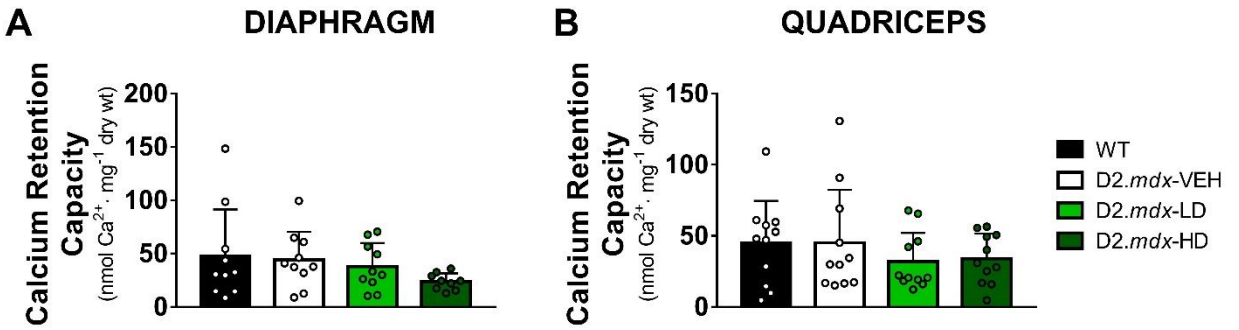

Supplemental Figure 6-4. Calcium-induced mitochondrial permeability transition pore opening in D2.*mdx* mice after ALY688-SR. Calcium retention capacity was measured spectrofluorometrically by titrating calcium chloride into permeabilized muscle fibres from diaphragm (A) and quadriceps (B) until mitochondrial permeability transition pore opening was triggered. Results represent mean ±SD; n=9-11.

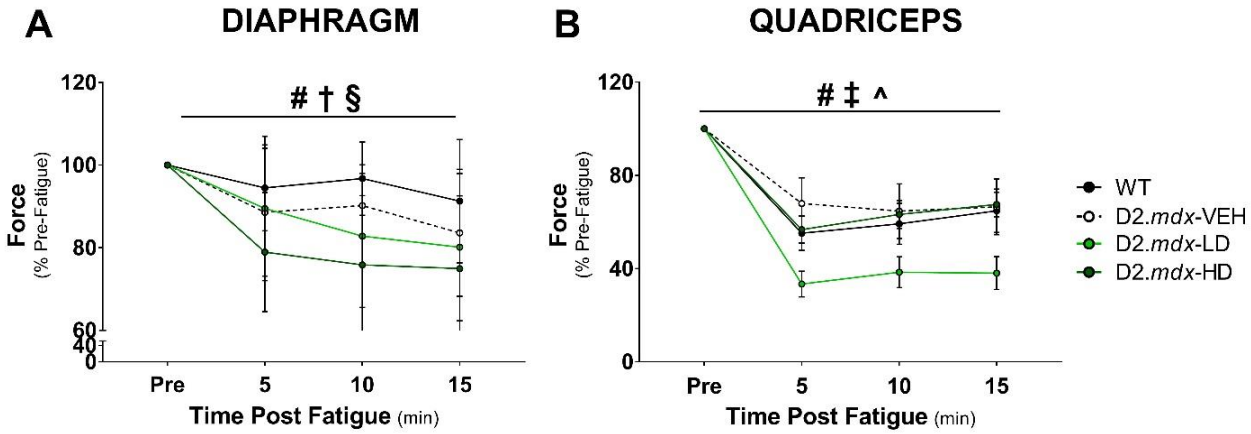

Supplemental Figure 6-5. Effects of ALY688-SR treatment on recovery after muscle fatigue in D2.*mdx* mice. *In-vitro* diaphragm strips (A) and *in-situ* quadriceps (B) underwent fatiguing protocols (70 Hz for 350 ms every 2 seconds for 5minutes). Prior to fatigue, 5-,10- and 15 minutes post fatigue, single stimulations were used to assess recovery and expressed as a % of pre-fatigue contraction. Results represent mean ±SD; n=8-11. All p values are FDR-adjusted by Benjamini, Krieger and Yekutieli post-hoc analyses. *p<0.05 WT vs D2.*mdx*- VEH; #p<0.05 WT vs D2.*mdx*-LD; †p<0.05 WT vs D2.*mdx*- HD; ‡p<0.05 D2.*mdx*-VEH vs D2.*mdx*- LD; §p<0.05 D2.*mdx*-VEH vs D2.*mdx*-HD; ^p<0.05 D2.*mdx*-LD vs D2.*mdx*-HD

Supplemental Data Not Included in Manuscript

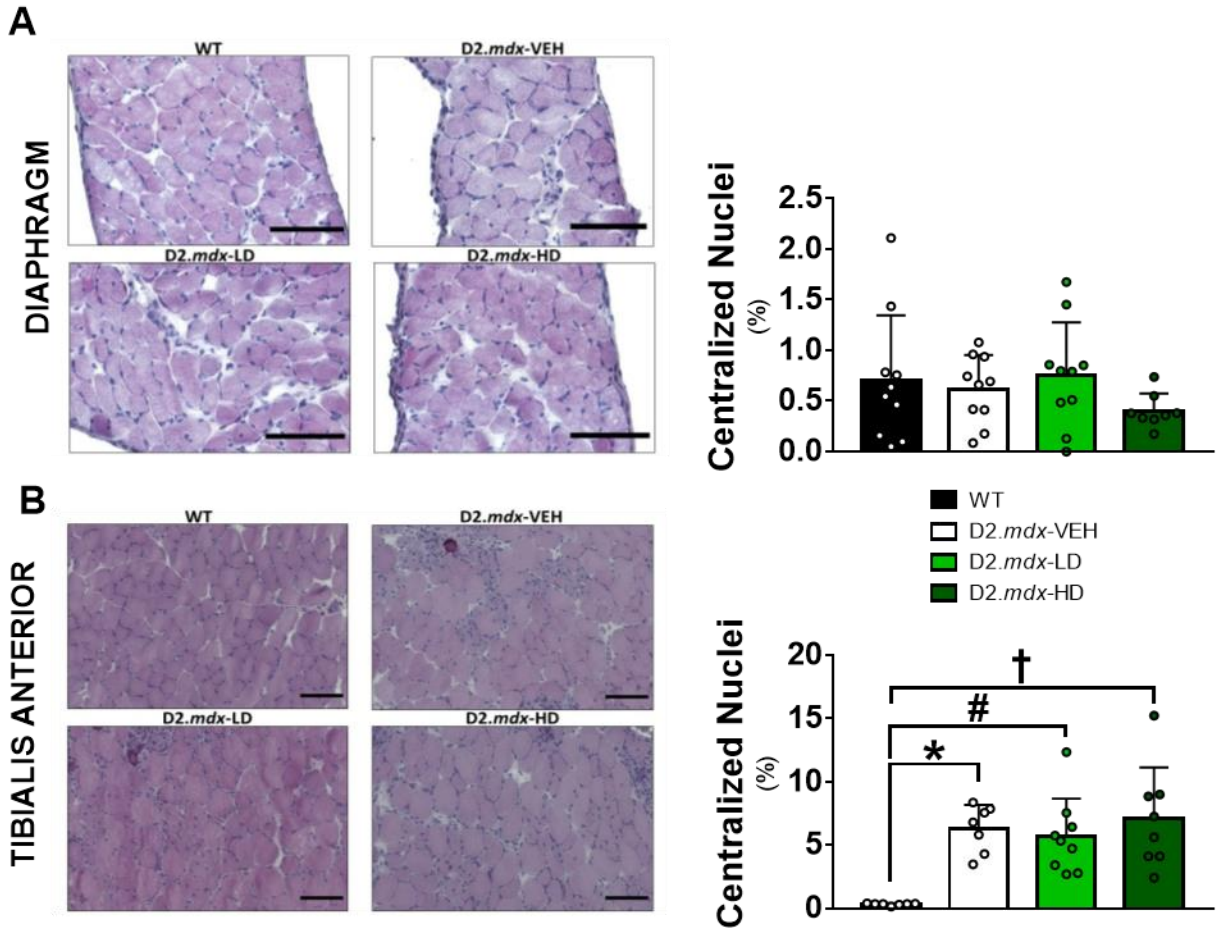

Supplemental Figure 6-6. Effects of ALY688 on muscle regeneration in the diaphragm and tibialis anterior. Hematoxylin & eosin staining were used to assess number of centrally nucleated fibres, a marker of muscle fibre regeneration in (A) diaphragm and (B) tibialis anterior. Scale bar =100µm. Results represent mean ±SD; n=7-10. All p values are FDR-adjusted by Benjamini, Krieger and Yekutieli post-hoc analyses. *p<0.05 WT vs D2.*mdx*- VEH; #p<0.05 WT vs D2.*mdx*-LD; †p<0.05 WT vs D2.*mdx*- HD.

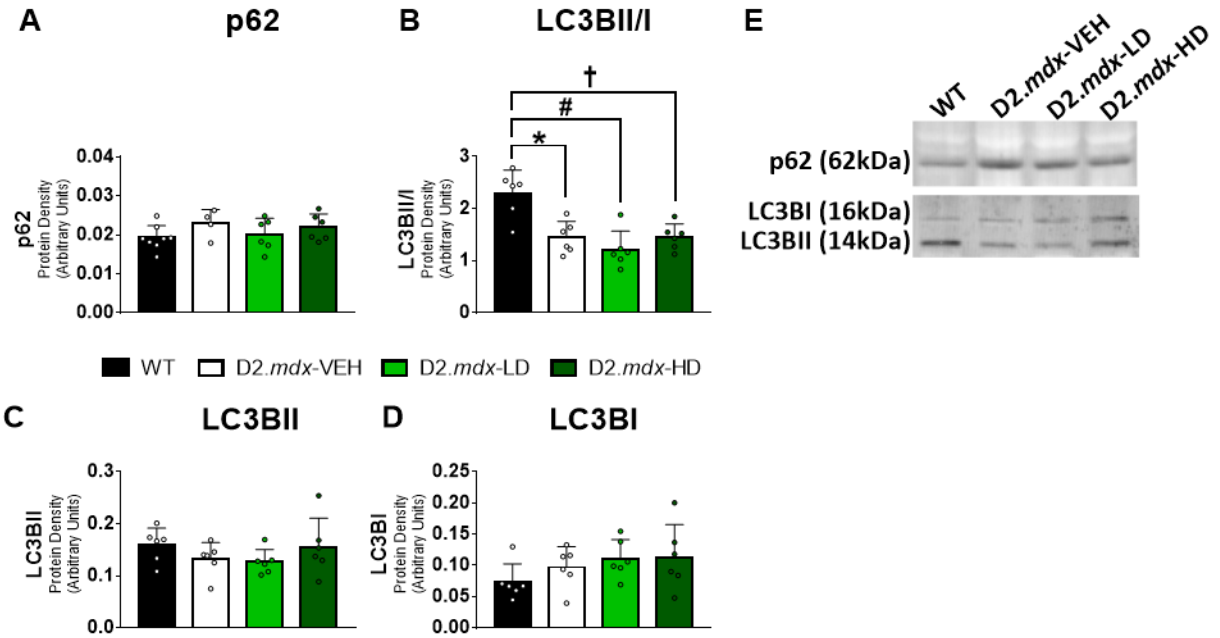

Supplemental Figure 6-7. Effects of ALY688 on autophagy in diaphragm. Western blotting was used to assess marker of autophagy in the diaphragm examining (A) p62, (B) LC3BII/I ratios (C) LC3BII and (D) LC3BI. Results represent mean ±SD; n=4-8. All p values are FDR-adjusted by Benjamini, Krieger and Yekutieli post-hoc analyses. *p<0.05 WT vs D2.*mdx*- VEH; #p<0.05 WT vs D2.*mdx*- LD; †p<0.05 WT vs D2.*mdx*- HD.

Chapter 7: Memory impairment in the D2.mdx mouse model of Duchenne muscular dystrophy is prevented by the adiponectin receptor agonist ALY688

This chapter has been written in preparation for submission to the Journal of Experimental Physiology. It is included in this thesis in the pre-submission format.

Assay Development Prior to the Start of Project 4:

1. Novel Object Recognition- in collaboration with LNC

Author Contributions: Many of the experiments for this study were performed by Catherine A Bellissimo (CAB). CAB established and maintained the breeding colony required for this project. As tissue from these mice were shared among 3 projects, several tasks were shared amongst two students and one post-doctoral fellow. CAB, SG and LNC performed daily drug injections. Novel object recognition testing and analysis was performed by LNC. CAB, LNC and SG conducted all tissue harvests. LNC prepared hippocampal tissue for mitochondrial respiration. LNC and CAB performed all mitochondrial respirometry. CAB, MM and LNC conducted all qPCR and in tissue assessment of immune presence. CAB and MF performed all western blotting experiments. CAB and CGRP wrote the manuscript with all co-authors aiding in revision.

Memory impairment in the D2.*mdx* mouse model of Duchenne muscular dystrophy is prevented by the adiponectin receptor agonist ALY688

Catherine A. Bellissimo[1], Laura N. Castellani[1], Michael S. Finch[2], Mayoorey Murugathasan[1], Shivam Gandhi[1], Gary Sweeney[3], Ali A. Abdul-Sater[1], Rebecca E.K. MacPherson[2], and Christopher G.R. Perry[1]

[1]School of Kinesiology & Health Science and the Muscle Health Research Centre, York University, Toronto, ON M3J 1P3 Canada.
[2]Department of Health Sciences, Brock University, St. Catharines, ON L2S 3A1 Canada
[3]Department of Biology, Muscle Health Research Centre, York University, Toronto, ON M3J 1P3 Canada.

Corresponding author:
Christopher G. R. Perry, PhD
Email: cperry@yorku.ca
ORCID ID: https://orcid.org/0000-0002-5745-5888

Running Title: Adiponectin receptor agonism improves memory in D2.mdx mice

Key words: Duchenne muscular dystrophy, memory, cognition, mitochondria

Graphical Abstract

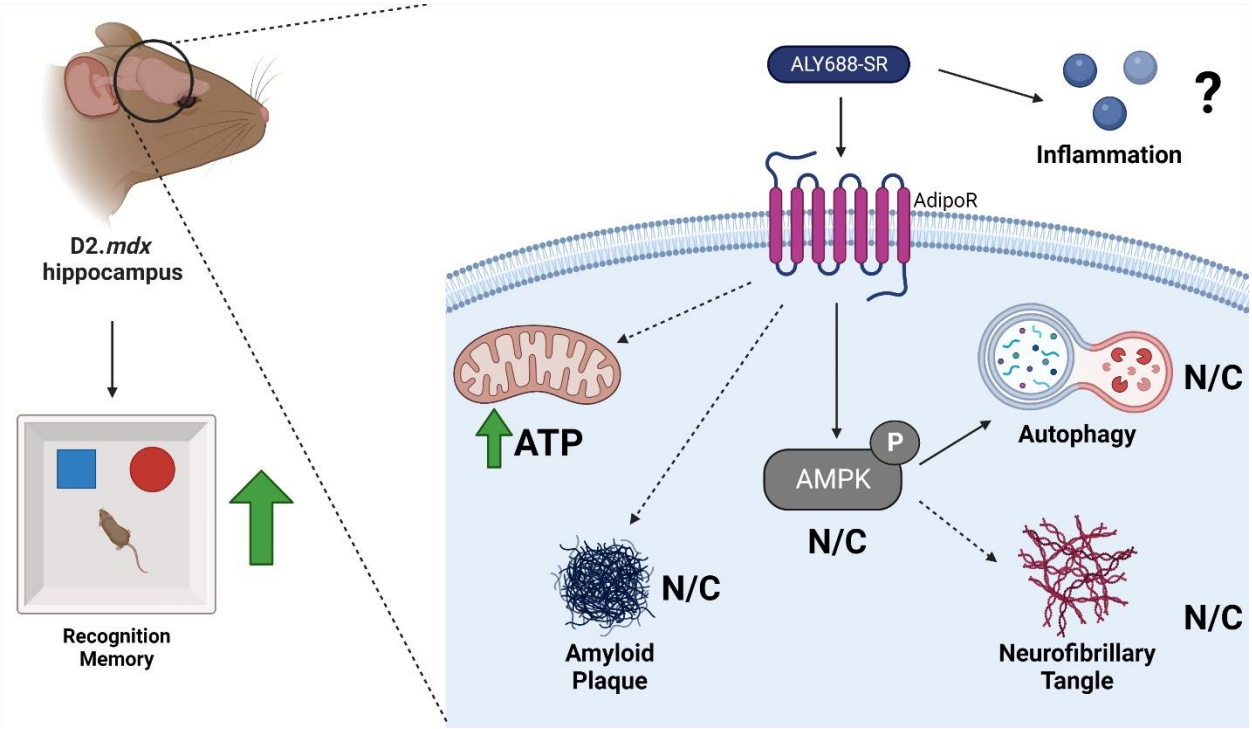

New Findings

What is the central question of this study?

Can adiponectin receptor agonism improve recognition memory in a mouse model of Duchenne muscular dystrophy?

What is the main finding and its importance?

Short-term treatment with the novel adiponectin receptor agonist, ALY688, improves recognition memory in D2.*mdx* mice. This finding suggests further investigation into adiponectin receptor agonism is warranted given there remains an unmet need for clinical approaches to treat this cognitive dysfunction in people with Duchenne muscular dystrophy.

Abstract

Memory impairments have been well-documented in people with Duchenne muscular dystrophy (DMD). However, the underlying mechanisms are poorly understood, and there is an unmet need to develop new therapies to treat this condition. Using a novel object recognition test, we show that recognition memory impairments in D2.*mdx* mice are completely prevented by daily treatment with the novel adiponectin receptor agonist ALY688 from days 7-28 of age. Compared to age-matched wildtype mice, untreated D2.*mdx* mice demonstrated lower hippocampal mitochondrial respiration (carbohydrate substrate), greater serum IL-6 cytokine content and greater hippocampal total tau and raptor protein contents. Each of these measures were partially or fully preserved following treatment with ALY688. Collectively, these results indicate that adiponectin receptor agonism improves recognition memory in young D2.*mdx* mice.

Introduction

Duchenne muscular dystrophy (DMD) is a severe progressive muscle wasting disorder that results from mutations to the gene for the protein dystrophin [111, 125, 178]. By compromising cell membrane stability and cytoskeletal architecture, a variety of cell stressors arise, including metabolic dysfunction which may contribute to muscle weakness (reviewed in [256, 550]). Dystrophin is also expressed in the central nervous system including the hippocampus and other regions that regulate memory processing [369].

Previous reports estimate ~30% of people with DMD exhibit cognitive dysfunction including memory impairments [366, 573]. Similar observations have been reported in murine models of DMD, including C57Bl/10ScSn-*mdx* and D2.*mdx* mice [367, 381]. Such cognitive impairments may be related to disruptions in brain energy homeostasis given separate investigations using non-invasive magnetic resonance spectroscopy reported elevated inorganic phosphate (Pi) to ATP and Pi to phosphocreatine (PCr) in boys with DMD [382]. Similar observations were reported in C57Bl/10ScSn-*mdx* mice [383]. In the latter study, maximal activities of mitochondrial enzymes in the brain were not different from wildtype mice suggesting that the capacity of specific mitochondrial pathways might be preserved. However, functional assessments of oxidative phosphorylation using intact mitochondria have not been performed. Such approaches have revealed attenuations in mitochondrial substrate oxidation in muscle from *mdx* mice and muscle from people with DMD (reviewed in [256]).

Glucocorticoids (GC) are the current standard of care for slowing the progression of muscle weakness in males with DMD [574-576] by reducing inflammation [577]. The effects of GC on memory in DMD is not fully resolved in the literature, but memory impairments attributed to GC therapy have been identified more broadly in other populations (reviewed in [578]). As such, there is an unmet need to develop new therapies that improve memory in addition to muscle function in DMD. In this regard, adiponectin receptor (AdipoR) agonism was recently shown to improve markers of muscle quality in *mdx* mice [464]. The agonist ALY688 in particular attenuates inflammation in various inflammatory disorders such as dry eye and liver diseases [466, 467] and reprograms substrate metabolism [534]. Given adiponectin-deficient mice have impaired recognition memory [579], we hypothesized that a recently developed slow-release formulation (ALY688-SR) with improved pharmacokinetic properties enabling once daily injection

(unpublished observations) would improve memory during early disease stages in young D2.*mdx* mice in association with lower inflammation and enhanced mitochondrial metabolism.

Methods & Materials

Animals

Male D2.*mdx* mice originated from a colony maintained at York University (Toronto, Canada) and sourced from Jackson Laboratories (Stock Number 013141, Bar Harbor, United States). Mice were treated daily from days 7 to 28 of age with ALY688-SR at 15 mg/kg b.w. (Allysta Pharmaceuticals, Bellevue, WA; D2.*mdx*-ALY688-SR) or saline control (D2.*mdx*-VEH). This age was chosen given it captures an early stage of disease progression in cardiac and skeletal muscle [22-24, 143, 150]. Mice were sacrificed 20-24 hr after the last dose. Breeding of wildtype mice was unsuccessful, similar to a previous report [487]. Instead, three-week-old wildtype DBA/2J WT mice (D2A) were obtained from Jackson Laboratories (Stock number 000671, Bar Harbor, United States) and allowed to acclimatize for one week before sacrifice. Mice were housed in standard 12:12-hr light:dark cycles and were allowed access to standard rodent chow and water *ad libitum*. 4 days prior to sacrifice, all groups underwent novel object recognition acclimatization and testing as described below. Mice were anesthetized under 5% isoflurane vaporized in medical air (21% oxygen) at a flow rate of 2L/min and then maintained at 2-3% prior to euthanasia by exsanguination. Muscles were removed and used for another investigation (under review at the time of this submission). The right and left hippocampus were then quickly dissected from the brain with a portion placed immediately into ice-cold BIOPS, containing (in mM): 50 MES Hydrate, 7.23 K_2EGTA, 2.77 CaK_2EGTA, 20 imidazole, 0.5 dithiothreitol, 20 taurine, 5.77 ATP, 15 PCr, and 6.56 $MgCl_2 \cdot 6\ H_2O$ (pH 7.1) or flash-frozen in liquid nitrogen and stored at -80°C for RNA isolation and western blotting. All experiments and procedures were approved by the Animal Care Committee at York University (AUP Approval Number 2016-18) in accordance with the Canadian Council on Animal Care.

Novel Object Recognition test

The novel object recognition test (NOR) was performed as previously described [363, 381, 580, 581]. Briefly, animals were placed in an open field area (40cm x 40cm x 40cm). Sessions were

recorded with a cell-phone video camera secured above the apparatus. Testing was performed in 3 stages: acclimation, habituation and testing as previously described [363, 381, 580, 581]. During acclimation, mice were placed into the arena and allowed to freely move for 5 minutes each day for 4 days preceding testing. The following day, habituation was performed, where two identical objects (Object 1) were placed in opposite corners of the arena and mice were left to explore for 10 minutes. Objects were similar in size to the animals and were chosen to ensure novelty in all trials. Following a habituation period, mice were returned to a neutral cage for 30 minutes. Thereafter, mice were placed back in the arena with one familiar object and one novel object (Object 2) and allowed to explore for 10 minutes. Object exploration time was defined as the time the mouse interacted with the object, defined by sniffing or touching the object when the mouse is less than 2 cm from the object. Sitting or standing on the object was not included unless the mouse sniffed the object while climbing on it. For the trial to be considered the animal must have interacted with the object for greater than 20 seconds. Discrimination ratio (DR) was calculated as follows: DR = (Time (object 2) –Time (object 1))/Total time.

High-Resolution Respirometry

Mitochondrial oxygen consumption (respiration) was measured using the *in situ* brain permeabilization previous described [582] with some modification. Following weighing, a portion of the hippocampus samples were quickly minced with scissors in a chilled tube containing BIOPS buffer followed by immediate placement into an Oxygraph-2K respirometer (Oroboros Instruments, Austria) containing MiR05 respiration medium (0.5mM EGTA, 3mM $MgCl_2$, 10mM KH_2PO_4, 20mM HEPES, 60mM K-lactobionate, 110mM sucrose, 1g/L BSA; pH 7.2) at 37°C with constant stirring at 750rpm. Samples were equilibrated in respiration buffer for 10 minutes before the addition of 50µg/mL saponin to facilitate permeabilization of the tissue. Following permeabilization, pyruvate-stimulated respiration was examined in the brain using 5mM pyruvate & 2mM malate to generate NADH and saturate electron entry into Complex I. To examine State III respiration as an index of oxidative phosphorylation, ADP was then added at a concentration of 15uM to approximate the concentrations reported in human brains using non-invasive MRS assessments [583]. Cytochrome *c* was added as a test of mitochondrial outer membrane integrity. All experiments demonstrated <10% increase in respiration. Each protocol was initiated with a starting $[O_2]$ of ~350 µM and was completed before the oxygraph chamber $[O_2]$ reached 150 µM

as done previously [495, 499]. Polarographic oxygen measurements were acquired in 2s intervals with the rate of respiration derived from 40 data points and expressed as pmol/s/mg wet weight. Chemicals and reagents were purchased from Sigma (St. Louis, Mo., USA), BioShop (Burlington, ONT, Canada).

RNA isolation & quantitative PCR

Total RNA was isolated from hippocampus using the Aurum Total RNA Mini Kit (Bio-Rad; Mississauga, ON, Canada) according to manufacturer's instructions, and reverse transcribed into cDNA by M-MLV reverse transcriptase and oligo(dT) primers (Qiagen). cDNA was then amplified in a CFX384 Touch Real-Time PCR Detection Systems (Bio-Rad) with a SYBR Green master mix and specific primers. Gene expression was normalized to a *Rplp0* control [569] and relative differences were determined using the ΔΔCt method [570], normalized to D2A expression. The primers used to probe for mouse cytokines are as follows: IL-1β Forward 5'-GCAGCACATCAACAAGAG-3', Reverse 5'-AGCAGGTTATCATCATCATC-3'; TNF-α Forward 5'-AGAATGAGGCTGGATAAGAT-3', Reverse 5'-GAGGCAACAAGGTAGAGA-3'; IL-6 Forward 5'-ACAGAAGGAGTGGCTAAG-3', Reverse 5'-AGAGAACAACATAAGTCAGATAC-3'; IL-10 Forward 5'-ATAACTGCACCCACTTCCCA-3', Reverse 5'-GGGCATCACTTCTACCAGGT-3'; Rplp0 Forward 5'-TTGGAGTGACATCGTCTT-3', Reverse 5'-ATCTTGAGGAAGTAGTTGGA-3'.

Cytokine Profiling

Protein contents of TGF-β, TNF-α, IL-1β, IL-6 and IL-10 in serum were measured by flow cytometry using LEGENDplexTM Mouse Custom Panel (BioLegend; San Diego, CA, USA). Serum, collected from all groups, was diluted four-fold in the assay buffer. Assay was completed according to the manufacturer's instructions on the Attune NxT flow cytometer (Thermo Fisher). The FCS files generated on the flow cytometer were analyzed using the LEGENDplex™ cloud-based analysis software.

Western blotting

Hippocampus tissue (collected from the same mice utilized in high-resolution respirometry experiments) was homogenized in cold lysis buffer containing (in mM; 20 Tris/HCl, 150 NaCl, 1 EDTA, 1 EGTA, 1% Triton X-100, 2.5 $Na_4O_7P_2$, 1 Na_3VO_4, pH 7.0) supplemented with protease

and phosphatase inhibitors (Sigma) according to the protocol established in [23]. Detection of electron transport chain complex subunits were performed according to the procedure in [23]. For detection of total AMPK, p-AMPK, p-ULK1, p62, and LC3BII/I, proteins were transferred to a 0.2µm low fluorescence polyvinylidene difluoride membrane using a Bio-Rad Trans Blot Turbo. Membranes were then blocked in Licor Intercept Blocking buffer diluted 1:1 in PBS. Membranes were then incubated with appropriate primaries diluted in blocking buffer (LI-COR, Lincoln NE, USA) as follows: p-AMPK (1:1000; t192 CST 2535), total AMPK (1:500; CST 2532), p-ULK1 (ser757, the target of Raptor; 1:500; CST14202), p62 (1:1000; CST 5114) and LC3B (1:1000; CST 2775) overnight at 4°C. Membranes were then washed three times for 5mins in TBS-T and incubated at room temperature with appropriate fluorescent secondary antibody (LI-COR). The same washing protocol was repeated and then membranes were detected using infrared imaging (LI-COR CLx; LI-COR, Lincoln, NE, USA) and quantified by densitometry (ImageJ, http://imagej.nih.gov/ij/). All images were normalized to total protein from the same membrane stained using Amido Black total protein stain (A8181, Sigma).

All remaining proteins were detected on 0.45µm nitrocellulose and blocked with 5% nonfat dry milk in TBS-T. Membranes were incubated with the appropriate primary antibodies as follows: APP (BioLegend 825001), soluble APPα (IBL 11088), soluble APPβ (BioLegend 813401), BACE1 (CST 5606), ADAM10 (Abcam ab1997), p-tau (serine 202; CST 11834), total tau (CST 4019), p-Raptor (serine 792; CST 2083), total Raptor (CST 2280), p-p70s6K (thr389; CST 9206S), total p70s6k (Santa Cruz SC-230), NeuN (CST 24307) and pro-BDNF (SC SC-65514) diluted to 1:1000 in 5% BSA overnight at 4°C. Following primary antibody incubation and washing, membranes were incubated in horseradish peroxidase secondary antibodies diluted 1: 5000 in 1% nonfat dry milk-TBS-T. Membranes were washed (3 × 5 min in TBST) and protein bands were imaged using enhanced chemiluminescence (Western lightning Plus-ELC; PerkinElmer, 105001EA) and ChemiDoc Imaging System (Bio-Rad). All proteins were normalized to total protein obtained from ponceau stain. Images were analyzed via AlphaView Software (ProteinSimple).

Statistics

Results are expressed as means ± SD. The level of significance was set to $p < 0.05$ for all statistics. D'Agostino-Pearson normality tests (GraphPad Prism Software, La Jolla, CA, USA) confirmed

that all data were normally distributed, one-way ANOVAs were utilized with two-stage step-up method of Benjamini, Krieger and Yekutieli post-hoc analyses for False Discovery rate (FDR) corrections in multiple-group comparisons. All reported p-values are FDR-adjusted p values (traditionally termed ‘q’).

Results

D2.*mdx*-VEH mice demonstrated impaired recognition memory as shown by a lower discrimination index in the NOR test (Figure 7-1A, B). This decrement was completely prevented by ALY688-SR (Figure 7-1A, B). Hippocampal mitochondrial pyruvate-supported respiration stimulated by ADP at physiological concentrations (see methods) was lower in D2.*mdx*-VEH but completely preserved by ALY688-SR (Figure 7-1C). These differences between groups likely reflect adaptive reprogramming intrinsic to mitochondria given electron transport chain subunit contents were similar in all groups (Figure 7-1D, E).

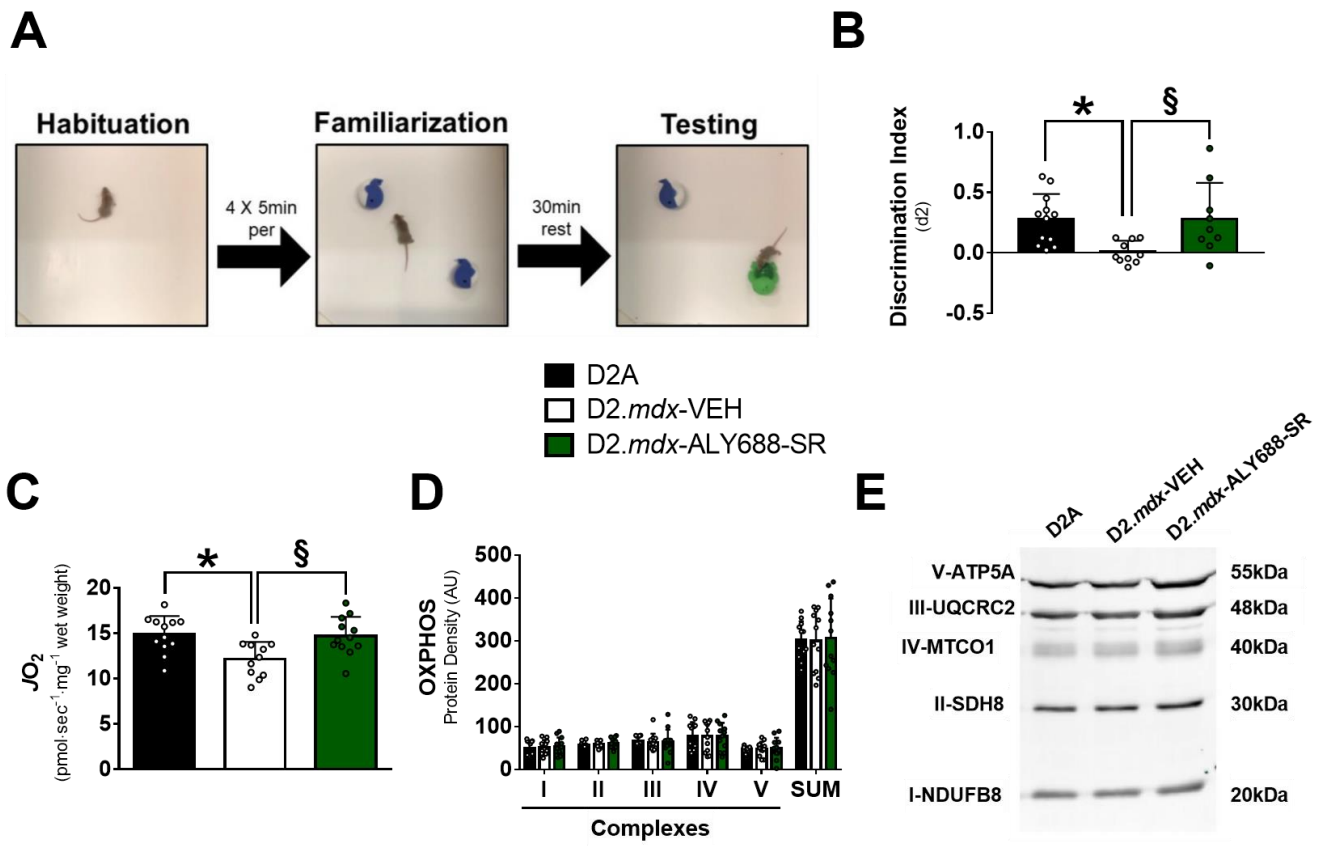

Figure 7-1. Novel object recognition (NOR) testing and hippocampal Complex I-supported respiration are preserved by ALY688-SR in 4-week-old D2.*mdx* mice. (A) Representative image of the NOR task with habituation (left), familiarization (middle) and testing (right). (B) Discrimination index was reduced in D2.*mdx*-VEH mice and was normalized with ALY688-SR treatment. (C) State III respiration was supported by Complex I substrates (NADH) pyruvate (5mM) and malate (2mM) and stimulated by a physiological concentration of ADP (15µM). (D, E) Protein content of electron transport chain components was quantified in the hippocampus. Data expressed as mean ± SD with n = 9-12 per group. *p ≤ 0.05 WT vs D2.*mdx*-VEH; §p≤0.05 D2.*mdx*-VEH vs D2.*mdx*-ALY688-SR.

We then assessed cytokine markers given the parent compound of ALY688-SR (ALY688) has been shown to have anti-inflammatory effects. No significant changes were observed in hippocampal mRNA of IL-6, IL-1β, TNF-α or IL-10 (Figure 7-2A-D). Cytokine protein contents were assessed in serum due to tissue limitations in the hippocampus. Serum IL-6 and TNF-α were significantly elevated in D2.*mdx*-VEH mice vs D2A controls (Figure 7-2E, G). ALY688-SR attenuated IL-6 (Figure 7-2E) and increased IL-1β relative to D2.*mdx*-VEH while also increasing IL-10 vs wildtype. (Figure 7-2F, H).

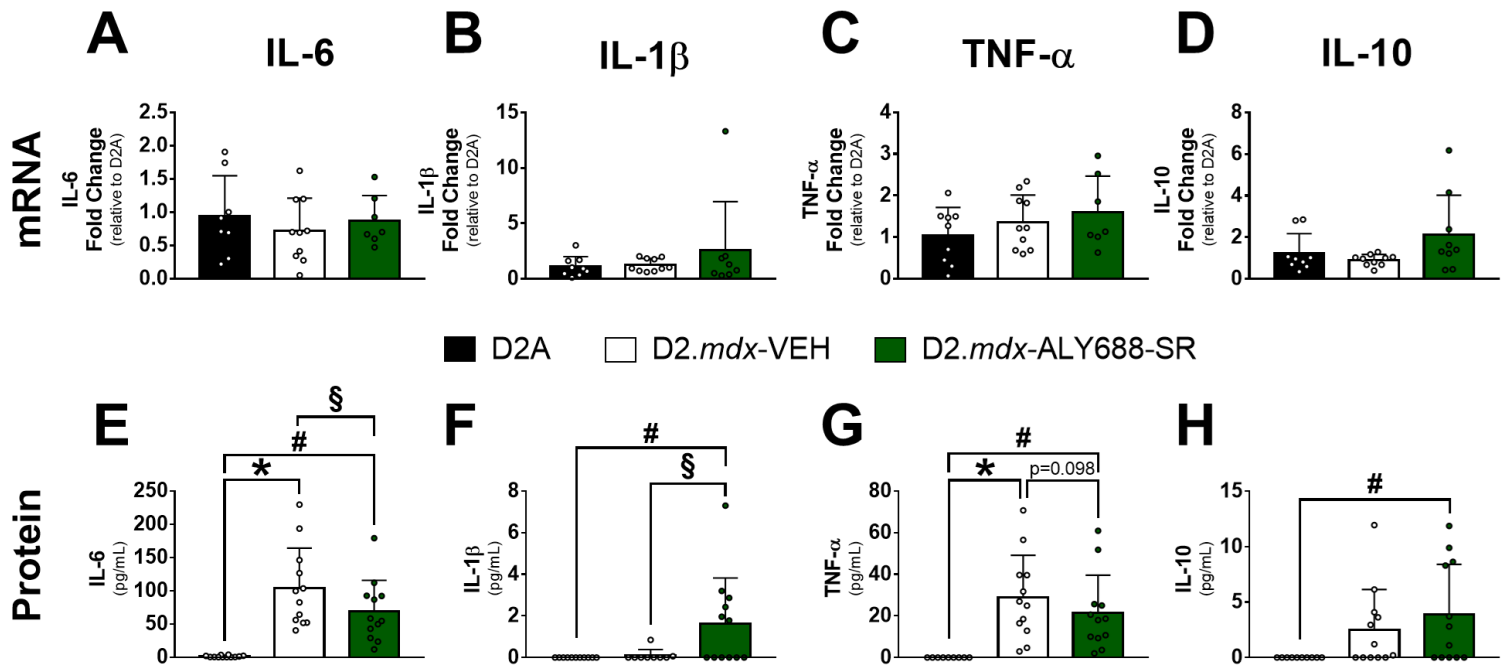

Figure 7-2. Hippocampus and serum inflammatory cytokine expression and contents. (A-D) Hippocampal mRNA fold changes of IL-6, IL-1β, TNF-α and IL-10 were expressed relative to D2A expression. (E-H) Serum levels of IL-6, IL-1β, TNF-α and IL-10 were quantified. Data expressed as mean ± SD with n = 7-12 per group. *p ≤ 0.05 WT vs D2.*mdx*-VEH; #p≤0.05 WT vs D2.*mdx*-VEH; §p≤0.05 D2.*mdx*-VEH vs D2.*mdx*-ALY688-SR. IL-6- interleukin-6, IL-1β- Interleukin-1 beta, TNF-α- tumor necrosis factor-alpha, IL-10- interleukin-10

We next assessed markers of potential pathways linking AMPK or inflammation to neural function given AdipoR agonism activates AMPK signaling in various models [464, 534] and lowers inflammation as noted above. As shown in Figure 7-3 (B, C), total AMPK protein was lower following treatment with ALY688-SR. While difficult to explain, the degree of activation (p-AMPK or p-AMPK/AMPK) was not altered. ALY688-SR also completely prevented the increases in protein contents of total tau (marker of neurofibrillary tangles) and total raptor (upstream regulator of tangles and autophagy) seen in D2.*mdx* vs WT. However, phosphorylation (both absolute and relative to total protein) of tau, Raptor (serine 792; an AMPK specific phosphorylation site [584]) were similar in all groups (Figure 7-3A-C). Markers of amyloidogenesis (Figure 7-4A-C) were similar in all groups as were BDNF and NeuN (data not shown).

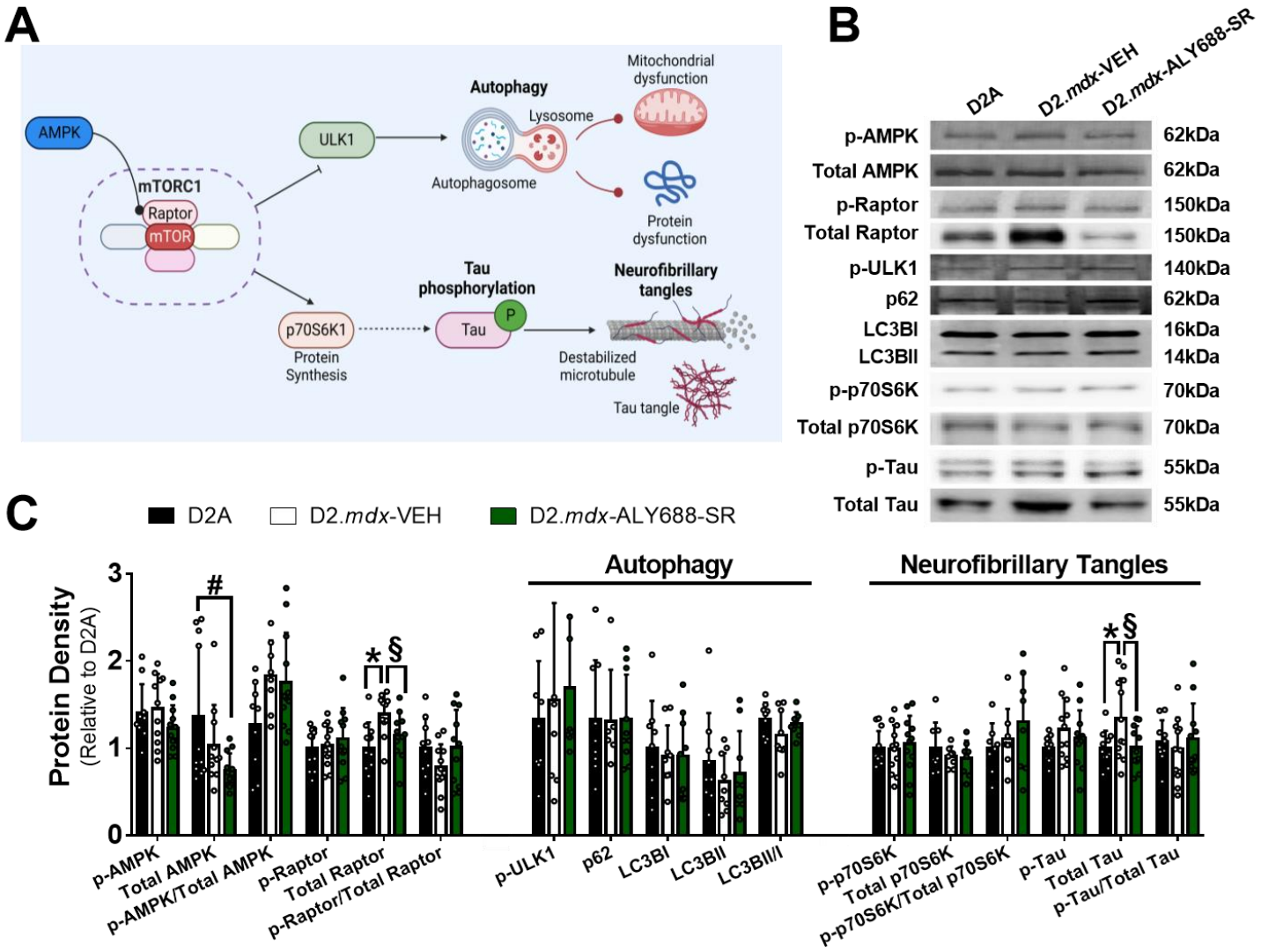
A
AMPK
mTORC1
Raptor
mTOR
ULK1
Autophagy
Lysosome
Autophagosome
Mitochondrial dysfunction
Protein dysfunction
p70S6K1
Protein Synthesis
Tau
P
Tau phosphorylation
Neurofibrillary tangles
Destabilized microtubule
Tau tangle
B
D2A
D2.mdx-VEH
D2.mdx-ALY688-SR
p-AMPK 62kDa
Total AMPK 62kDa
p-Raptor 150kDa
Total Raptor 150kDa
p-ULK1 140kDa
p62 62kDa
LC3BI 16kDa
LC3BII 14kDa
p-p70S6K 70kDa
Total p70S6K 70kDa
p-Tau 55kDa
Total Tau 55kDa
C
D2A
D2.mdx-VEH
D2.mdx-ALY688-SR
Protein Density
(Relative to D2A)
Autophagy
Neurofibrillary Tangles
p-AMPK
Total AMPK
p-AMPK/Total AMPK
p-Raptor
Total Raptor
p-Raptor/Total Raptor
p-ULK1
p62
LC3BI
LC3BII
LC3BII/I
p-p70S6K
Total p70S6K
p-p70S6K/Total p70S6K
p-Tau
Total Tau
p-Tau/Total Tau

Figure 7-3. AMPK and downstream protein markers related to autophagy and neurofibrillary tangles. (A) Theoretical cascade linking AMPK – an adiponectin receptor target – to factors related to autophagy and neurofibrillary tangles. The AMPK target, Raptor is rendered inactive upon its phosphorylation, allowing for the induction of autophagy through the phosphorylation of ULK-1, allowing for clearance of dysfunctional mitochondria and proteins (Lee et al., 2010; Norwitz et al., 2020). Alternatively, activation of the mTORC1 complex leads to increased protein synthesis via p70s6k1 which has been implicated in tau phosphorylation, the destabilization of microtubules and the generation of neurofibrillary tangles (Iqbal et al., 2010; Pei et al., 2006). Made with BioRender. (B, C) Western blot markers for targets outlined in assessed in hippocampus tissue (A). Data expressed as mean ± SD with n = 6-12 per group. *$p \leq 0.05$ WT vs D2.mdx-VEH; §$p \leq 0.05$ D2.mdx-VEH vs D2.mdx-ALY688-SR. AMPK- AMP kinase, mTORC1- mammalian target of rapamycin complex 1, Raptor- Regulatory-associated protein of mTOR, ULK1-Unc-51 like autophagy activating kinase, p70s6k1- Ribosomal protein S6 kinase β 1

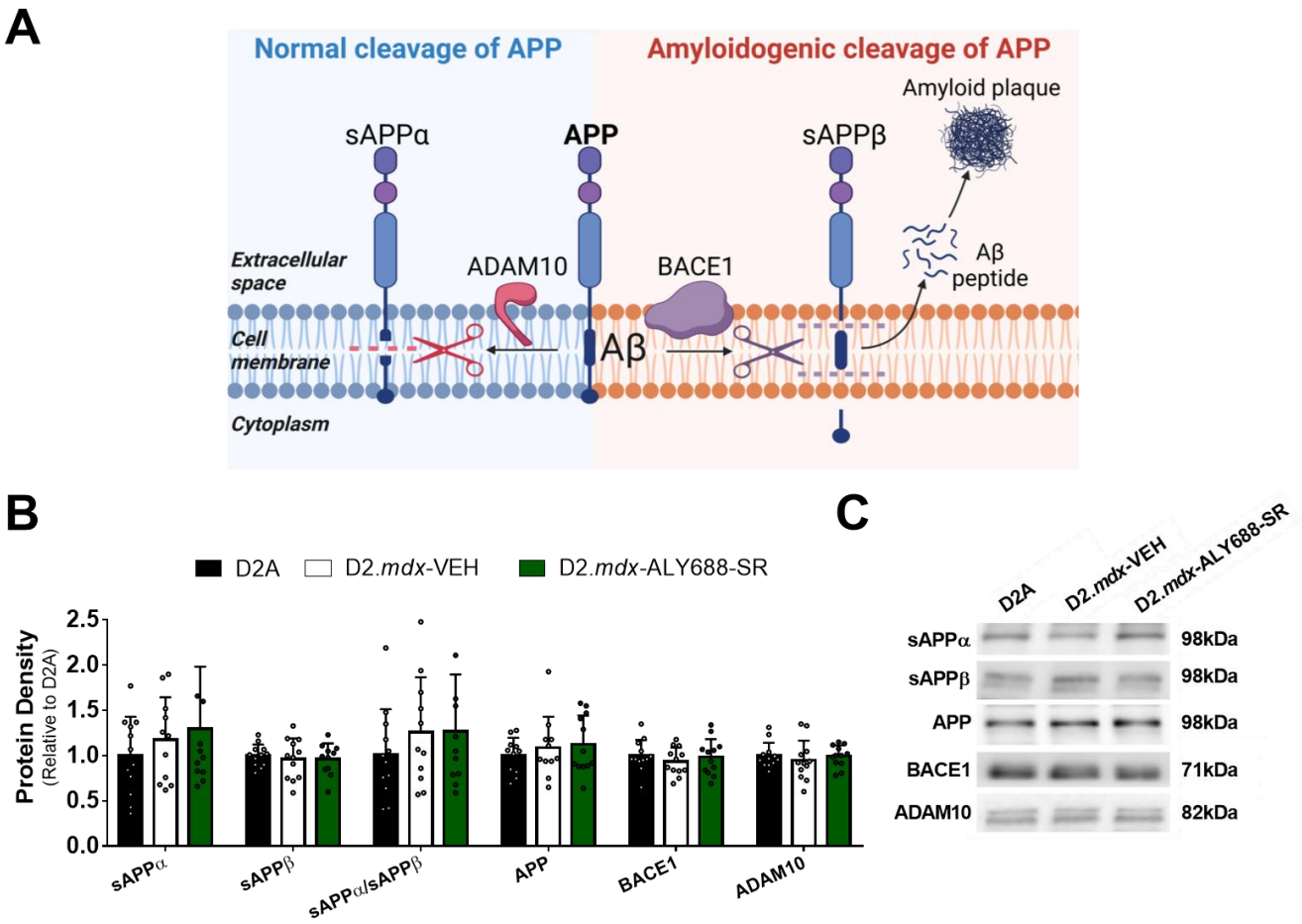

Figure 7-4. Protein markers of amyloidogenic cascade. (A) The development of neuritic plaques occurs when cleavage of amyloid precursor protein (APP) into amyloid beta (Aβ) peptides and soluble APPβ (sAPPβ) via beta-secretase 1 (BACE1) (right) is favoured over conventional cleavage of APP (left). Adapted from [585]. Made with BioRender. (B, C) Western blot markers for targets outlined in assessed in hippocampus tissue (A). Data expressed as mean ± SD with n = 11-12 per group. APP- amyloid precursor protein, sAPPα- soluble APP- alpha, ADAM10- A Disintegrin and Metalloproteinase 10, sAPPβ- soluble APP-beta, BACE1- beta-secretase 1, Aβ- amyloid beta.

Discussion

Here, we show that the novel AdipoR agonist, ALY688-SR improved recognition memory in young D2.*mdx* mice following a short-term 21-day treatment paradigm. This effect was associated with a complete restoration of hippocampal pyruvate-supported mitochondrial respiration (index of glucose oxidation) when stimulating ATP synthesis with an ADP concentration matching the level reported *in vivo* in human brain [382]. This finding is interesting given the high dependency of neurons on glucose as a fuel source. As this protocol partially depends on Complex I oxidation of NADH, the finding may also implicate Complex I dysfunction occurs in the hippocampus similar to reports in muscle from D2.*mdx* mice [22-24, 150] as well as in other regions of the brain in C57Bl/10ScSn-*mdx* mice [386]. Hippocampal mitochondrial relationships to NOR have also been previously reported. For example, reduced NOR and hippocampal mitochondrial structural dynamics were altered in aging-related neurodegeneration [586], whereas improvements in pyruvate-supported respiration and NOR were observed in a model of erythropoietin overexpression [587].

The precise relationship between dystrophin mutations and mitochondrial stress in the brain is not clear but may be informed by previous discoveries in *mdx* muscle which generally implicate calcium overload, redox stress, and inflammation as possible links [550]. Increases in serum IL-6 and reductions in mitochondrial pyruvate oxidation in the present study aligns with this paradigm, particularly given ALY688-SR partially attenuated IL-6 while completely preserving respiration and recognition memory. While hippocampal inflammatory markers were unchanged, the reductions in serum IL-6 with ALY688-SR presents the possibility that systemic inflammation caused by the well-characterized muscle damage in D2.*mdx* mice [23, 143, 145, 150] might contribute a trigger separate from the direct effects of the dystrophin mutation in the hippocampus. Indeed, pharmacological inhibition of IL-6 in the hippocampus improved long-term memory in rats [463] but the effects on mitochondrial bioenergetics were not examined.

Improved recognition memory was also related to increased contents of tau protein and the inhibitory complex of mTOR, raptor, both of which are downstream of AdipoR signaling [584, 588]. The lack of change in their phosphorylation state does not necessarily rule out a potential role for these pathways in mediating the disease or treatment effects given the tissues were harvested 20-24 hrs after the last dose. Assessing the activity of these and other signaling cascades shortly

after dosing may provide more insight into their potential contributions. This timing consideration may also explain why AMPK itself was not phosphorylated in response to the drug despite being a known downstream target of AdipoR [443, 589] and considering both AMPK and p38MAPK are phosphorylated after 30 minutes of ALY688 treatment in L6 muscle cells [544]. Future experiments could extend these findings to incubations in neurons.

Limitations

In addition to the hippocampus, the NOR test is dependent on multiple regions of the brain not investigated in the present study such as the prefrontal cortex. While we were unable to obtain sufficient sample of this region given the small size of the brain at 4 weeks of age, prior research has shown greater markers of amyloidogenesis occur in this region compared to only one marker in the hippocampus at 8 weeks of age in D2.*mdx* mice [381]. The present study found no changes in any such marker in the hippocampus which may be related to the younger age, and we cannot rule out the possibility that reduced NOR in D2.*mdx*-VEH was related to such markers in the prefrontal cortex. Lastly, the lack of change in protein markers of autophagy and neurotrophic factors do not reflect the activity of these pathways which require assessments of their kinetics aspects with additional methodologies. As such, these processes could still be considered in future research with respect to how dystrophin mutations impair recognition memory, and how ALY688-SR restores this cognitive function given AdipoRs and/or AMPK (a target of AdipoR) have been linked to autophagy, neurofibrillary tangles or amyloidogenesis [590-593].

Conclusions

ALY688-SR completely prevented impairments in recognition memory following 21-days of treatment in young D2.*mdx* mice. Given there is an unmet need for therapies that improve memory and other cognitive functions in DMD, these findings lay the foundation for continued exploration into the mechanisms, and potential, of adiponectin receptor agonism in treating cognitive dysfunction separately from the myopathy in this debilitating disease.

Author Contributions

Study design and conception were prepared by C.A.B., L.N.C., S.G., G.S., C.G.R.P and Allysta Pharmaceuticals, and all authors contributed to the rationale for specific measurements. Experimental work and/or analyses were performed by all authors. The manuscript was written by C.A.B. and C.G.R.P. All authors contributed to the manuscript and approved the final version.

Acknowledgements

ALY688-SR was provided by Allysta Pharmaceuticals.

Funding

Funding for this research was provided to C.G.R.P. by Allysta Pharmaceuticals, the National Science and Engineering Research Council (no. 2019-06687), Ontario Early Researcher Award (C.G.R.P., no. 2017-0351) and a MITACS Accelerate award with infrastructure supported by Canada Foundation for Innovation, the James. H. Cummings Foundation, and the Ontario Research Fund. Funding was provided by the National Science and Engineering Research Council to A.A.S. (no. 2017-05073), to R.E.K.M by (2017-03904) and by the Canadian Institutes of Health Research to G.S. Scholarships and awards were awarded to C.A.B. (NSERC PGS-PhD, MITACS Accelerate), L.N.C. (MITACS Accelerate), M.S.F. (NSERC CGS-M), and S.G. (Ontario Graduate Scholarship).

Conflicts of Interest

This study was partially funded by Allysta Pharmaceuticals. G.S. is a Scientific Advisor for Allysta Pharmaceuticals.

Data Availability Statement

Data can be made available upon reasonable request to the corresponding author.

Supplemental Data Not Included in Manuscript

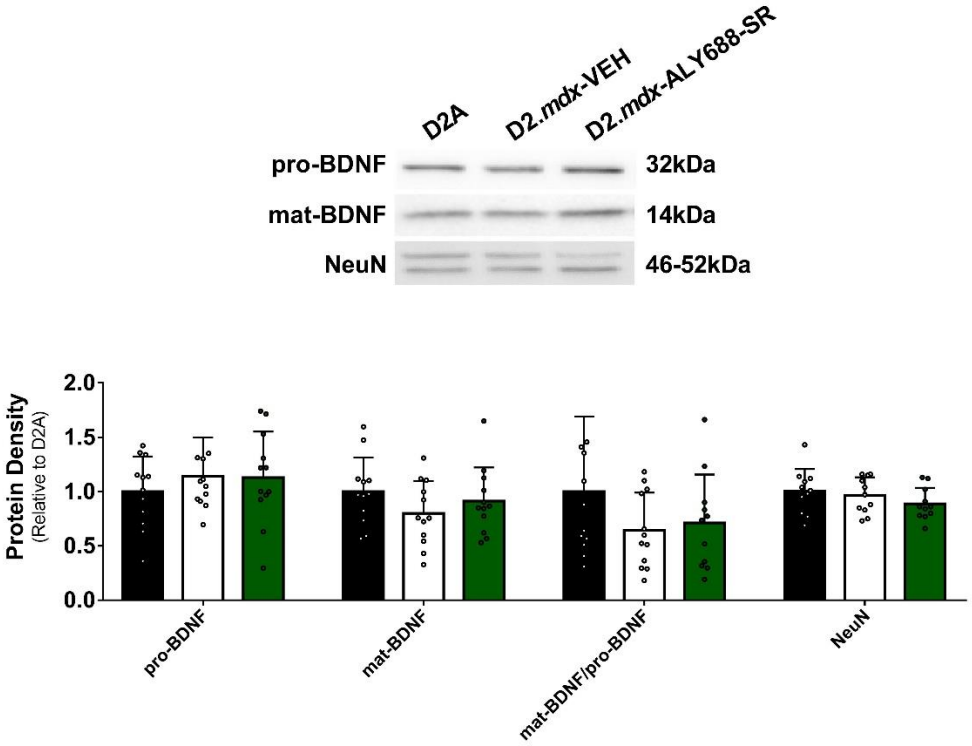

Supplemental Figure 7-1. Protein markers of neurogenesis. Western blot markers for targets outlined in assessed in hippocampus tissue. Data expressed as mean ± SD with n = 11-12 per group.

Chapter 8: Summary of Findings

8.1 General Discussion

Duchenne muscular dystrophy (DMD) is a fatal disease resulting from the loss of the structural protein dystrophin. Early in life, patients exhibit progressive muscle weakness, resulting in loss in ambulation followed by premature death due to cardiac and or respiratory failure. Currently there is no cure for this disease, although genetic therapies have made great strides in recent years. Unfortunately, there are several uncertainties about the long-term effectiveness of these therapies and due to costs, may not be widely available to all patients once fully approved. As such, alternative treatments are being investigated, including drugs that target metabolism, which has long been identified as impaired in DMD patients. The first goal of this thesis was to improve methodologies in examining mitochondrial permeability transition in permeabilized muscle fibres (Chapter 4) by considering the presence of adenylates and creatine. We then applied this to a biological context and then utilized that methodology in subsequent chapters. Next, we examined the how attenuating metabolic stress in a mouse model of DMD alters pathology by utilizing two pharmaceutical compounds: Olesoxime (Chapter 5) and the novel adiponectin receptor agonist ALY688-SR (Chapter 6 & 7).

The findings from this thesis indicate that the natural cycling of ADP and ATP in permeabilized muscle fibres attenuates mtPT and should be considered in buffer composition during measures of mtPT. Next, short-term treatment with the mitochondrial enhancing drug, Olesoxime, improves mitochondrial creatine sensitivity which may contribute to attenuation of mitochondrial stress and muscle weakness. Lastly, adiponectin receptor agonism has tissue specific effects in D2.*mdx* mice on mitochondrial respiration and reactive oxygen species emissions while reducing atrophy and fibrosis in the diaphragm and improving recognition memory. Collectively, these short-term treatment paradigms in young dystrophic mice provide further support that mitochondrial stress, including creatine insensitivity, may contribute to the dystrophic phenotype, but longer-term treatments are required to assess if these drugs may be viable for translation into DMD patients.

Modeling in vivo conditions in in vitro assays in assessments of mitochondrial permeability transition

In numerous publications [23, 24, 499], including chapters 4 and 5 of thesis this, we have highlighted that modelling *in vivo* conditions (ADP, creatine, etc) during *in vitro* assessments of mitochondrial function should be considered during study design as it may reveal how key regulators of mitochondrial bioenergetics impact respiration, mtPT and may highlight new therapeutic opportunities in disease.

Our recent review [256] highlights inconsistencies in the literature on the influence of mitochondrial permeability pore opening in the dystrophic phenotype. One reason for the inconsistencies in the literature may be attributed to buffer design and model selection. mtPT is often assessed by *in vitro* fluorescent based detection of mitochondrial calcium uptake. In such an assay, several small boluses of calcium are titrated and the eventual release of calcium from the mitochondria once retention capacity is exceeded is identified as mPTP opening. Conversely, one single large bolus can be titrated and time to mPTP opening can be used [27].

Previous reports in isolated mitochondria indicate that adenylates (ADP and ATP) can attenuate mPTP opening [92], but whether the same effect was consistent in permeabilized fibre bundles was unknown and lead to Study 1 (Chapter 4). In this chapter, we reveal that ADP is less effective at attenuating mPTP compared to ATP and the exclusion of ADP clamping systems such as hexokinase 2-deoxyglucose should be considered during assay design. Additionally, the effect of creatine, which accelerates matrix ADP/ATP cycling, is only apparent in the presence of ADP clamping, for unknown reasons. In our hands, calcium retention capacity was unaltered between D2.*mdx* and wildtype (D2A) left ventricle when creatine and 5mM ADP are provided in the absence of a hexokinase clamp. As creatine only increases respiration at submaximal concentrations of ADP [497], using a lower concentration may reveal significant differences between genotypes. As a result of these findings, creatine and ADP were supplemented in CRC assay buffer in the absence of an ADP clamp. This buffer design was then utilized in subsequent chapters of this dissertations but may also be applied to other disease pathologies.

Examining creatine impairments in dystrophic tissue

One of the most significant findings of this thesis is the restoration of creatine sensitivity with a mitochondrial enhancing compound Olesoxime. To assess this, mitochondrial respiration was performed in the presence and absence of 20mM creatine, allowing the comparison of the efficient

creatine-dependent energy transfer system and the creatine-independent system (Figure 2-2). Consistent with previous work from our laboratory, D2.*mdx* mice exhibit an impairment in creatine sensitivity in quadriceps which happens in association with the presence of muscle weakness [23]. However, unlike previous reports, the diaphragm appears to maintain creatine sensitivity during ADP stimulated respiration, which may be a consequence of age. Hughes and colleagues utilized mice at 28 days of age, while Chapter 5, utilized up to 30 days of age. While this difference seems minimal, this is a period of dynamic remodeling, which may contribute changes in creatine sensitivity throughout the life span [23]. Creatine sensitivity was lost in both muscles when examining the attenuation of mH_2O_2 emissions in the presence of varying concentrations of ADP. This may represent that sensitivity to creatine is lost earlier in some functions of the mitochondria compared to others.

Interestingly, improvements of creatine sensitivity could not be attributed to the mitigation of mtCK oxidation as evaluated by the detection of reduced thiols, where a decrease in signaling indicates an increase in oxidation. Newly developed methods, such as ALISA and RedoxiFluor [507, 594], which directly quantify oxidation may be more sensitive (better discussed in *8.2 Limitations*). Additionally, improvements observed in creatine sensitivity with olesoxime could be a result of other elements of the creatine/phosphocreatine pathways, namely the assembly of octameric mtCK [47] and association with the phospholipid cardiolipin.

MtCK resides in the mitochondrial inner membrane space (IMS) as an octamer where it physically associates with VDAC and ANT and facilitates the shuttling of PCr and Cr in and out of the mitochondria, and ATP and ADP in and out of the matrix. In highly oxidative tissues such as the heart, sarcomeric-mtCK, the main isoform in muscle, can account for 25% of total CK activity, representing the highest value among all tissues [49, 595], thus any impairment to mtCK may have drastic metabolic effects. MtCK is also highly susceptible to oxidative stress [46] and results in inactivation, disassembly of mtCK octamers and reduced affinity for phospholipids such as cardiolipin [68, 596-598]. In models of ischemia, increased levels of superoxide and peroxynitrite leads to enzymatic inactivation of s-mtCK and dissociations of octamers, further contributing to energy depletion [68, 599, 600] and have been observed to effect cytosolic ion pumping, specifically Ca^{2+} [601-603]. As DMD is characterized by loss of Ca^{2+} homeostasis, further impairments in mtCK function, may contribute to greater cytosolic Ca^{2+} overload and ROS

emission, producing a vicious cycle of mtCK inactivity, metabolic impairments and abhorrent Ca^{2+} handling, potentially furthering the dystrophic phenotype. It is plausible that as Olesoxime improved attenuation of mH_2O_2, maintained mitochondrial respiration by preventing mtCK inactivation, that was not detectable via the current methodologies used.

Another facet in which mtCK function may be altered is through modifications to cardiolipin. Cardiolipin, a unique phospholipid found on the inner mitochondrial membrane, interacts with mtCK and ANT, facilitating a proteolipid complex with VDAC. This complex regulates energy exchange, reduces ROS emission, and prevents permeability transition pore opening [46]. Like mtCK, cardiolipin is highly susceptible to oxidative modifications, and when oxidized, dissociates from the proteolipid complex [93, 596]. Previous work by Hughes et al, revealed that the cardiolipin targeting compound SBT-20 improved creatine-dependent respiration in the quadriceps while attenuating fibrosis in the diaphragm [604]. Collectively, it is possible that improvements to creatine-dependent respiration and mH_2O_2 attenuation with Olesoxime are facilitated by mitigation of oxidation to cardiolipin preventing its release from the proteolipid complex with mtCK. Although not directly examined in this thesis, the possible effect Olesoxime on cardiolipin oxidation warrants further examination.

Disease modifying effects of Olesoxime & ALY688-SR may be related to attenuated mitochondrial stress – why one might not be enough

This thesis employees two different approaches in the treatment of DMD. The first focuses on enhancing mitochondrial function (Chapter 5) which improved mitochondrial respiration and the ability of ADP to attenuate reactive oxygen species emissions but not calcium-induced mPTP opening. These improvements to mitochondrial stress happen in parallel with modest enhancements to indices of muscle quality and function, while significantly reducing markers of muscle breakdown. However, this did not translate to improvements in histopathology which may suggest that further treatments are needed in combination with Olesoxime to address other aspects of the dystrophic pathology. Adjuvant therapies in DMD are currently being explored in a number of clinical trials (NCT04322357 & NCT05195775) but none have included a mitochondrial therapeutic. Potentially combining Olesoxime with either current standard of care, prednisone or

deflazacort, or other anti-inflammatories may address multiple secondaries in one treatment plan but remains highly speculative.

Chapter 6 examines the impact of attenuating metabolic deficiencies through adiponectin receptor agonism in respiratory and locomotor muscle. Adiponectin and adiponectin receptor agonism has been well studied in its use for treatment of metabolic disease through its anti-inflammatory properties [605, 606]. Given the profound and chronic inflammation associated with DMD, adiponectin was more thoroughly examined as a treatment [456, 457, 543, 607]. However, there are several limitations to full length adiponectin and the common adiponectin receptor agonist, AdipoRon, which have led to the development of newer agonist, such as ALY688-SR. In diaphragm, treatment with ALY688-SR resulted in improvements to the dystrophic environment, specifically reduced fibrosis and inflammation, that does not fully address impaired mitochondrial function. This highlights that mitochondrial stress remains despite improvements to other secondary pathologies and implies that more direct mitochondrial therapeutics may be required. The minimal effects of ALY688-SR in limb muscle (quadriceps and tibialis anterior) may be a result of a limited pathology due to the young age utilized and is further discussed in *8.2 Limitations*. Consistent with this, the more heavily used diaphragm, shows increased fibrosis in D2.*mdx* as demonstrated in Table 2-1, and is similar to comparisons made between muscles in the C57Bl/10.*mdx* model [158, 608, 609]. These improvements happen in associations with some alleviation to mitochondrial stress in both the quadriceps and diaphragm.

Unlike Olesoxime, creatine sensitivity is not restored with ALY688-SR which implies a mitochondrial targeting compound may be specifically required to improve this aspect of mitochondrial function. This again highlights the potential need to combine therapies to address the several secondary pathologies observed in DMD. This will be future discussed in *8.3 Future directions.*

ALY688-SR as a novel therapy for memory deficiencies in DMD

Like muscle, dystrophin is also expressed in the brain and central nervous system, but its function remains obscure [610]. DMD patients present with variable degrees of cognitive impairments, including speech delays, learning disabilities and memory impairments [357, 404] that may be related to metabolic deficiencies and inflammation [382, 383, 573, 611]. Treatment with ALY688-SR completely attenuated reductions in recognition memory and mitochondrial respiration

observed in D2.*mdx* mice. However, the mechanisms by which these improvements arose from remain obscure as well-known targets of adiponectin receptor agonism, such as AMPK, were unchanged in the hippocampus. Similarly, there were no changes in the activation of autophagy and the development of amyloidogenic plaques, both which are downstream of AMPK [612-614].

The development of neurofibrillary tangles was also examined as a possible mechanism behind the improvement to recognition memory. Neurofibrillary tangles have been implicated in the pathogenesis of Alzheimer's disease [615] and have been observed in a case study of a DMD patient [616]. These tangles typically consist of abnormal accumulation of hyperphosphorylated tau [617, 618] which was not observed in this study. An elevation of total tau was observed in D2.*mdx* mice, and although highly speculative, may be in response to increases in neuroinflammation as previously demonstrated in a murine model of Alzheimer's disease [619]. Consistent with this, circulating levels of IL-6 were elevated in D2.*mdx* mice and attenuated with ALY688-SR. Despite the complexity of these result, Chapter 7 provides initial evidence that adiponectin receptor agonism may improve recognition memory, but longer-term studies are required.

Lastly, due to logistical constraints, cognitive testing in D2.*mdx* mice were limited to recognition memory using the novel object recognition test despite other cognitive deficits being identified in DMD patients. As the hippocampus is heavily involved in recognition memory [381], we focused our biochemical and bioenergetic assessments on this area of the brain. As limited cognitive testing has been performed in the D2.*mdx* model, further studies are required to ascertain whether these mice recapitulate deficiencies in other cognitive functions such as learning and memory impairments that could be explored using the Morris water maze test [620]. Analyses could then be expanded to include areas of the brain involved with learning, memory etc. Nonetheless, the results form Chapter 7, provide preliminary evidence the young D2.*mdx* mice demonstrate impaired recognition memory that may be related to compromised mitochondrial respiration.

8.2 Limitations

Age and treatment lengths

In all studies, a relatively new model of D2.*mdx* mice were utilized as it is thought to better recapitulate the dystrophic phenotype observed in humans. The D2.*mdx* mice demonstrate a more

severe pathology than the traditional C57Bl/10-*mdx* model, due to a natural mutation in TGF-β binding protein 4 in the D2A background strain [143, 145]. To date, very few groups have utilized this model specifically at young ages, which makes it difficult to ascertain if any compensation is occurring during our therapeutic window. Notably, a period of compensation at 4-6 weeks of age until 15 months of age is well documented in the C57Bl/10-*mdx* strain [158, 621, 622] but has not been thoroughly identified in D2.*mdx* mice, beyond work performed in our laboratory (Hughes et al unpublished). A single time course study has been completed in D2.*mdx* but focused on 10 week and 34-week-old time points, so it is unknown if compensation has occurred prior to this time point [147]. As such, the early therapeutic timepoint of 4 weeks of age provides a unique opportunity to examine if short term treatments limit or delay dystrophic pathology but comes with several constraints.

This time point results in small body size and limited tissue weights, requiring multiple rounds of breeding and injections to gain sufficient quantities for bioenergetic, histological and biochemical analyses. This was abundantly clear in Chapter 5 where oxidation of mtCK could not be performed in the diaphragm. Similarly, in Chapter 7, mitochondrial respiration, inflammation, and signal transduction in the hippocampus could not be assessed within the same animal. This may have contributed to minor increases in variability, and well as preventing certain assessments to be performed.

This age also poses another technical challenge as it is relatively early in the disease progression resulting in limited pathology in specific muscles. In the limb muscles examined in this thesis (quadriceps, Chapter 5, and quadriceps and tibialis anterior, Chapter 6) minimal fibrosis and muscle damage are observed at 4-weeks of age, leaving little be corrected with therapeutics. Similarly, a profound inflammatory response could not be consistently found across all tissues at this timepoint, despite elevations in inflammatory cytokines being well documented across murine models [127, 623, 624]. Although some markers of inflammation, for example, TNF-α in the tibialis anterior and IL-6 in the diaphragm appear to be attenuated by ALY688-SR. This result was not consistent when protein levels of these cytokines were examined. But given that many of these cytokines are necessary signals during muscle repair, perhaps the divergent changes are a result of that dynamic remodeling in the tissue.

Finally, these included studies are relatively short-term treatment protocols (18 days for Olesoxime and 21 days for ALY688-SR), which may account for the somewhat limited changes to disease pathology. Longer duration studies are needed to examine if long term efficacy of these drugs remains and is further discussed in *8.3 Future Directions*.

Improved methodologies for assessing oxidative modifications

We initially hypothesized that olesoxime treatment would result in improvements to creatine-dependent bioenergetic measures by alleviating oxidation of mtCK. Surprisingly, we did not observe a reduction in oxidation of mtCK with Olesoxime treatment. This in part may be due to the sensitivity of the thiol labeling technique used in Chapter 5. This technique relied on the assessment of reduced thiols which exist in high abundance and may make it difficult to assess increases in thiol oxidation. Newer techniques that utilize less tissue and directly measure oxidized thiols, such as ALISA and RedoxiFluor [507, 594], may reveal mtCK was in fact oxidized in D2.*mdx* mice and protected with Olesoxime treatment. These techniques also offer the opportunity to examine other redox sensitive proteins that may impact the dystrophic phenotype such as Nrf2, a redox sensitive protein that upregulates many cytoprotective genes products in response to oxidants and other toxic stressors and has been previously examined in DMD [625].

Tissue constraints resulted in prioritization of protocols

Although careful attention was paid to the design of buffers and protocols used for bioenergetic assessments in all studies, this is by no means a comprehensive assessment of oxidative phosphorylation and reactive oxygen species emission in part due to tissue limitations. Previous work from Hughes et al [23] identified complex I as a site of dysfunction in D2.*mdx* mice which aided in prioritizing assessments performed in Chapters 5-7. However, fatty acid oxidation was not thoroughly investigated during this thesis, yet it is known to be impaired in DMD patients and C57Bl/10.*mdx* mice [626-628]. To date no studies have thoroughly examined fatty acid oxidation in the D2.*mdx* model at any age, so it is unknown if the drug treatments examined in this thesis would have improved this. Given adiponectin is involved with increasing fatty acid oxidation [443], treatment with ALY688-SR may have improved fatty acid oxidation in dystrophic skeletal muscle. Another limitation faced was the logistical constraints of the behavioural testing performed. As Chapter 6 and 7 utilized the same mice, limited behavioural and cognitive testing could be performed due to the time consuming nature of mitochondrial bioenergetic assessments

and muscle function measures. Further studies may consider utilizing multiple cohorts of mice that may undergo more thorough behavioural testing independent of mitochondrial measures.

8.3 Future Directions

Although this thesis makes further progress in examining treatment options for secondary pathologies and highlights the potential importance of treating creatine insensitivity in DMD, further research is still required to determine the long-term efficacy of the highlighted drugs. Several considerations are also highlighted for future study design.

Firstly, delaying the age at which animals are studied and prolonging treatment protocols may better reveal differences between vehicle controls and treated animals, as disease pathology would have progressed, specifically in limb muscles. For example, beyond 7 weeks of age in D2.*mdx* mice, fibrosis becomes more extensive across limb muscles. Given that ALY688-SR attenuated early onset fibrosis in the diaphragm, a longer treatment protocol may reveal a similar effect in limbs muscles. Likewise, extending treatment protocols with Olesoxime may result in further recovery of voluntary force measures and recovery of creatine-dependent respiration in the quadriceps. As such, longer treatment protocols should be considered for both Olesoxime and ALY688-SR.

The analyses of this thesis were limited to brain, respiratory and limb muscles in 4-week-old mice but does not include assessment of cardiac tissue. The heart is heavily impacted in DMD [629], with almost all patients exhibiting some form of cardiomyopathy in later stages of the disease [630-632]. Additionally, cardiac tissue is highly sensitive to creatine [51]. Collectively this suggests that that creatine-dependent improvements of Olesoxime would be most pronounced in cardiac tissue and may reveal improvements to histopathology and contractility that were not observed in limb and respiratory muscles. Additional future studies should examine chamber-specific alterations, as recent evidence has shown that the right ventricle exhibits elevated fibrosis at this time point (Gandhi et al, unpublished), while the left ventricle exhibits reduced ADP-stimulated respiration and ADP attenuation of H_2O_2 [22] in 4-week-old D2.*mdx* mice. Future studies should include assessment of cardiac, limb and respiratory muscles to fully ascertain the efficacy of the drugs being investigated, before translation to clinical trials.

In Chapter 4, we investigated the role of adenylates and creatine on calcium-induced mitochondrial permeability transition pore opening in permeabilized skeletal muscle fibres. Here we reveal that ATP alone attenuates mtPTP opening in the quadriceps of CD1 mice, with creatine only having an effect in the presence of an ADP clamp. However, there are limitation to this conclusion as this experiment was performed at supramaximal levels of ADP (5mM). Creatine is known to increase mitochondrial respiration at submaximal concentrations of ADP [497]. Future experiments should be repeated at lower ADP concentrations (~100μM) to assess if increasing ADP/ATP cycling through the creatine-dependent energy transfer system sufficiently attenuates mtPT. Additionally, comparisons of mtPT should be made in the presence and absence of creatine to identify if the creatine-dependent energy transfer is involved in calcium-induced mtPTP opening. Once optimal buffer composition is identified, comparisons between WT and D2.*mdx* mice can be made to fully examine the role of mtPT in disease progression.

As previously mentioned, Olesoxime did not appear to alter the redox status of mtCK in the quadriceps, but this lack of effect does not eliminate the possibility of Olesoxime prevents oxidative damage. This methodology does not directly measure oxidation of mtCK and therefore may not be sensitive enough to detect minute changes in oxidation that result in functional improvements to mitochondrial respiration. Future work should utilize methodologies such as RedoxiFluor [594] that directly measure protein redox status in cardiac, limb and respiratory muscles. Alternatively, for measurements octameric mtCK content, native blue gel staining which retains these protein structures [633], could be performed.

This thesis paid specific attention to protocol design when assessing mitochondria bioenergetics. In the hippocampus, tissue limitations prevented analysis of creatine-dependent respiration and any assessment of mH_2O_2 emission (Chapter 7). As the brain (including the hippocampus) expresses high levels of ubiquitous mtCK (u-mtCK) [47], future assessments of mitochondrial bioenergetics should be performed in the presence and absence of saturating levels of creatine to assess if the brain also exhibits creatine insensitivity, similar to skeletal muscle. Furthermore, only one study to date has examined cognitive function in D2.*mdx* mice [381], while no studies have examined mitochondria respiration or oxidative stress in the brain of this model. Future studies in D2.*mdx* mice, should first characterize if the mitochondria represent a major site of ROS production in the dystrophic brain and then identify specific sites of ROS generation within the mitochondria. While

oxidative stress is thought to play a role in cognitive decline in *mdx* mice [384], further studies are required definitively identify the mitochondria as the source. Following this, similar treatment paradigms used in Chapter 7 can be used to assess if improvements to recognition memory with ALY688-SR treatment is related to attenuation of reactive oxygen species. Furthermore, assessments of metabolism, inflammation and amyloidogenic signaling and should expand beyond the hippocampus to include other areas of the brain such as the prefrontal cortex that are involved in recognition memory.

Lastly, current treatment plans for DMD patients often combine glucocorticoid steroids, mobility aids (braces, walkers, wheelchairs), modest exercise and respiratory support (nighttime ventilation), but despite these, patients still succumb to rapid declines and early death. Combining therapies such as anti-inflammatories, anti-fibrotic drugs with mitochondrial targeting compounds may address may be more efficacious than treatment with one alone. Based on evidence from this thesis, combining traditional therapeutics such as prednisone or deflazacort or utilizing new age anti-inflammatories, such as adiponectin receptor agonists, with mitochondrial therapies (such as Olesoxime), may address multiple pathologies and warrants further studies.

8.4 Conclusions

Building off previous work, this thesis continues to support that mitochondrial stress contributes to the general pathology observed in D2.*mdx* mice but adds that creatine sensitivity may be a valid therapeutic target. Careful attention to buffer composition may also reveal impairments in dystrophic tissue and provide new therapeutic avenues. Furthermore, the novel adiponectin receptor agonist ALY688-SR improves some aspects of mitochondrial stress in skeletal muscle while attenuating fibrosis and atrophy. Lastly, ALY688-SR also improves some aspects of cognitive dysfunction and mitochondrial impairments, albeit through an unclear mechanism. Future studies with Olesoxime and ALY688-SR either independent or as a cocktail therapy, should include longer term studies that extend to later time points to reveal if further improvements are observed.

References

1. Hodgkinson, V., et al., *The Canadian Neuromuscular Disease Registry 2010-2019: A Decade of Facilitating Clinical Research Througha Nationwide, Pan-NeuromuscularDisease Registry.* J Neuromuscul Dis, 2021. **8**(1): p. 53-61.
2. Crisafulli, S., et al., *Global epidemiology of Duchenne muscular dystrophy: an updated systematic review and meta-analysis.* Orphanet Journal of Rare Diseases, 2020. **15**(1): p. 141.
3. Hoffman, E.P., R.H. Brown, Jr., and L.M. Kunkel, *Dystrophin: the protein product of the Duchenne muscular dystrophy locus.* Cell, 1987. **51**(6): p. 919-28.
4. Robert, V., et al., *Alteration in calcium handling at the subcellular level in mdx myotubes.* J Biol Chem, 2001. **276**(7): p. 4647-51.
5. Leijendekker, W.J., et al., *Regulation of cytosolic calcium in skeletal muscle cells of the mdx mouse under conditions of stress.* Br J Pharmacol, 1996. **118**(3): p. 611-6.
6. Lamb, M.M., et al., *Corticosteroid Treatment and Growth Patterns in Ambulatory Males with Duchenne Muscular Dystrophy.* J Pediatr, 2016. **173**: p. 207-213.e3.
7. Goemans, N. and G. Buyse, *Current treatment and management of dystrophinopathies.* Curr Treat Options Neurol, 2014. **16**(5): p. 287.
8. Matthews, E., et al., *Corticosteroids for the treatment of Duchenne muscular dystrophy.* Cochrane Database Syst Rev, 2016. **2016**(5): p. Cd003725.
9. Duncan, C.J., *Role of intracellular calcium in promoting muscle damage: a strategy for controlling the dystrophic condition.* Experientia, 1978. **34**(12): p. 1531-5.
10. Culligan, K. and K. Ohlendieck, *Abnormal calcium handling in muscular dystrophy.* BAM-PADOVA-, 2002. **12**(4): p. 151-162.
11. Vignos, P.J., Jr. and M. Lefkowitz, *A biochemical study of certain skeletal muscle constituents in human progressive muscular dystrophy.* J Clin Invest, 1959. **38**(6): p. 873-81.
12. Tada, K., Y. Watanabe, and H. Chikaoka, *Demonstration of Defect of Creatinephosphokinase in Muscle of Progressive Muscular Dystrophy.* The Tohoku Journal of Experimental Medicine, 1961. **75**(3): p. 299-308.
13. Scholte, H.R. and H.F. Busch, *Early changes of muscle mitochondria in Duchenne dystrophy. Partition and activity of mitochondrial enzymes in fractionated muscle of unaffected boys and adults and patients.* J Neurol Sci, 1980. **45**(2-3): p. 217-34.
14. Dreyfus, J.C., G. Schapira, and F. Schapira, *Biochemical study of muscle in progressive muscular dystrophy.* J Clin Invest, 1954. **33**(5): p. 794-7.
15. Ionăşescu, V., N. Luca, and O. Vuia, *RESPIRATORY CONTROL AND OXIDATIVE PHOSPHORYLATION IN THE DYSTROPHIC MUSCLE.* Acta Neurologica Scandinavica, 1967. **43**(5): p. 564-572.
16. Hoagland, C.L., R.E. Shank, and G.I. Lavin, *THE HISTOPATHOLOGY OF PROGRESSIVE MUSCULAR DYSTROPHY AS REVEALED BY ULTRAVIOLET PHOTOMICROGRAPHY.* J Exp Med, 1944. **80**(1): p. 9-18.
17. Kuznetsov, A.V., et al., *Impaired mitochondrial oxidative phosphorylation in skeletal muscle of the dystrophin-deficient mdx mouse.* Mol Cell Biochem, 1998. **183**(1-2): p. 87-96.
18. Sperl, W., et al., *High resolution respirometry of permeabilized skeletal muscle fibers in the diagnosis of neuromuscular disorders.* Mol Cell Biochem, 1997. **174**(1-2): p. 71-8.

19. Olson, E., et al., *Oxidative phosphorylation of skeletal muscle in human muscular dystrophy.* The Journal of Laboratory and Clinical Medicine, 1968. **71**(2): p. 220-231.
20. Rybalka, E., et al., *Defects in mitochondrial ATP synthesis in dystrophin-deficient mdx skeletal muscles may be caused by complex I insufficiency.* PLoS One, 2014. **9**(12): p. e115763.
21. Dudley, R.W., et al., *Dynamic responses of the glutathione system to acute oxidative stress in dystrophic mouse (mdx) muscles.* Am J Physiol Regul Integr Comp Physiol, 2006. **291**(3): p. R704-10.
22. Hughes, M.C., et al., *Impairments in left ventricular mitochondrial bioenergetics precede overt cardiac dysfunction and remodelling in Duchenne muscular dystrophy.* The Journal of Physiology, 2020. **598**(7): p. 1377-1392.
23. Hughes, M.C., et al., *Early myopathy in Duchenne muscular dystrophy is associated with elevated mitochondrial H2O2 emission during impaired oxidative phosphorylation.* Journal of Cachexia, Sarcopenia and Muscle, 2019. **10**(3): p. 643-661.
24. Ramos, S.V., et al., *Mitochondrial bioenergetic dysfunction in the D2.mdx model of Duchenne muscular dystrophy is associated with microtubule disorganization in skeletal muscle.* PLOS ONE, 2020. **15**(10): p. e0237138.
25. Ascah, A., et al., *Stress-induced opening of the permeability transition pore in the dystrophin-deficient heart is attenuated by acute treatment with sildenafil.* American Journal of Physiology-Heart and Circulatory Physiology, 2011. **300**(1): p. H144-H153.
26. Dubinin, M.V., et al., *Duchenne muscular dystrophy is associated with the inhibition of calcium uniport in mitochondria and an increased sensitivity of the organelles to the calcium-induced permeability transition.* Biochim Biophys Acta Mol Basis Dis, 2020. **1866**(5): p. 165674.
27. Godin, R., et al., *Peroxisome proliferator-activated receptor γ coactivator 1-α gene transfer restores mitochondrial biomass and improves mitochondrial calcium handling in post-necrotic mdx mouse skeletal muscle.* The Journal of physiology, 2012. **590**(21): p. 5487-5502.
28. Disatnik, M.H., et al., *Evidence of oxidative stress in mdx mouse muscle: studies of the pre-necrotic state.* J Neurol Sci, 1998. **161**(1): p. 77-84.
29. Kar, N.C. and C.M. Pearson, *Catalase, superoxide dismutase, glutathione reductase and thiobarbituric acid-reactive products in normal and dystrophic human muscle.* Clin Chim Acta, 1979. **94**(3): p. 277-80.
30. Ragusa, R.J., C.K. Chow, and J.D. Porter, *Oxidative stress as a potential pathogenic mechanism in an animal model of Duchenne muscular dystrophy.* Neuromuscul Disord, 1997. **7**(6-7): p. 379-86.
31. Haycock, J.W., et al., *Oxidative damage to muscle protein in Duchenne muscular dystrophy.* Neuroreport, 1996. **8**(1): p. 357-61.
32. Murphy, M.E. and J.P. Kehrer, *Oxidation state of tissue thiol groups and content of protein carbonyl groups in chickens with inherited muscular dystrophy.* Biochem J, 1989. **260**(2): p. 359-64.
33. Austin, L., et al., *Potential oxyradical damage and energy status in individual muscle fibres from degenerating muscle diseases.* Neuromuscular Disorders, 1992. **2**(1): p. 27-33.
34. Cole, M.A., et al., *A quantitative study of bioenergetics in skeletal muscle lacking utrophin and dystrophin.* Neuromuscul Disord, 2002. **12**(3): p. 247-57.

35. Percival, J.M., et al., *Defects in mitochondrial localization and ATP synthesis in the mdx mouse model of Duchenne muscular dystrophy are not alleviated by PDE5 inhibition.* Hum Mol Genet, 2013. **22**(1): p. 153-67.
36. Shuttlewood, R.J. and J.R. Griffiths, *The purine nucleotide profile in mouse, chicken and human dystrophic muscle: an abnormal ratio of inosine plus adenine nucleotides to guanine nucleotides.* Clin Sci (Lond), 1982. **62**(1): p. 113-5.
37. Nikoletopoulou, V., et al., *Crosstalk between apoptosis, necrosis and autophagy.* Biochimica et Biophysica Acta (BBA) - Molecular Cell Research, 2013. **1833**(12): p. 3448-3459.
38. Zulian, A., et al., *Forty years later: Mitochondria as therapeutic targets in muscle diseases.* Pharmacological Research, 2016. **113**: p. 563-573.
39. Scarpa, A. and G.F. Azzone, *The Mechanism of Ion Translocation in Mitochondria.* European Journal of Biochemistry, 1970. **12**(2): p. 328-335.
40. Zurlo, F., et al., *Skeletal muscle metabolism is a major determinant of resting energy expenditure.* J Clin Invest, 1990. **86**(5): p. 1423-7.
41. Rolfe, D.F. and G.C. Brown, *Cellular energy utilization and molecular origin of standard metabolic rate in mammals.* Physiol Rev, 1997. **77**(3): p. 731-58.
42. Nicholls, D.G. and S.J. Ferguson, *Bioenergetics 4*. 2013: Elsevier.
43. Aliev, M., et al., *Molecular system bioenergics of the heart: experimental studies of metabolic compartmentation and energy fluxes versus computer modeling.* Int J Mol Sci, 2011. **12**(12): p. 9296-331.
44. Guzun, R., et al., *Regulation of respiration in muscle cells in vivo by VDAC through interaction with the cytoskeleton and MtCK within Mitochondrial Interactosome.* Biochimica et Biophysica Acta (BBA) - Biomembranes, 2012. **1818**(6): p. 1545-1554.
45. Wallimann, T., M. Tokarska-Schlattner, and U. Schlattner, *The creatine kinase system and pleiotropic effects of creatine.* Amino Acids, 2011. **40**(5): p. 1271-96.
46. Schlattner, U., L. Kay, and M. Tokarska-Schlattner, *Mitochondrial Proteolipid Complexes of Creatine Kinase.* Subcell Biochem, 2018. **87**: p. 365-408.
47. Schlattner, U., M. Tokarska-Schlattner, and T. Wallimann, *Mitochondrial creatine kinase in human health and disease.* Biochimica et Biophysica Acta (BBA)-Molecular Basis of Disease, 2006. **1762**(2): p. 164-180.
48. Schlattner, U. and T. Wallimann, *Octamers of mitochondrial creatine kinase isoenzymes differ in stability and membrane binding.* J Biol Chem, 2000. **275**(23): p. 17314-20.
49. Wyss, M., et al., *Mitochondrial creatine kinase: a key enzyme of aerobic energy metabolism.* Biochim Biophys Acta, 1992. **1102**(2): p. 119-66.
50. Saks, V.A., et al., *Control of cellular respiration in vivo by mitochondrial outer membrane and by Creatine Kinase. A new speculative hypothesis: possible involvement of mitochondrial-cytoskeleton interactions.* Journal of Molecular and Cellular Cardiology, 1995. **27**(1): p. 625-645.
51. Kuznetsov, A.V., et al., *Striking differences between the kinetics of regulation of respiration by ADP in slow-twitch and fast-twitch muscles in vivo.* European journal of biochemistry, 1996. **241**(3): p. 909-915.
52. Bessman, S. and A.t. Fonyo, *The possible role of the mitochondrial bound creatine kinase in regulation of mitochondrial respiration.* Biochemical and biophysical research communications, 1966. **22**(5): p. 597-602.

53. Meyer, L.E., et al., *Mitochondrial creatine kinase activity prevents reactive oxygen species generation: antioxidant role of mitochondrial kinase-dependent ADP re-cycling activity.* J Biol Chem, 2006. **281**(49): p. 37361-71.
54. Meyer, R.A., H.L. Sweeney, and M.J. Kushmerick, *A simple analysis of the "phosphocreatine shuttle".* Am J Physiol, 1984. **246**(5 Pt 1): p. C365-77.
55. Korshunov, S.S., V.P. Skulachev, and A.A. Starkov, *High protonic potential actuates a mechanism of production of reactive oxygen species in mitochondria.* FEBS Lett, 1997. **416**(1): p. 15-8.
56. Lambert, A.J. and M.D. Brand, *Superoxide production by NADH:ubiquinone oxidoreductase (complex I) depends on the pH gradient across the mitochondrial inner membrane.* Biochem J, 2004. **382**(Pt 2): p. 511-7.
57. Brand, M.D., *Mitochondrial generation of superoxide and hydrogen peroxide as the source of mitochondrial redox signaling.* Free Radic Biol Med, 2016. **100**: p. 14-31.
58. Wong, H.S., et al., *Production of superoxide and hydrogen peroxide from specific mitochondrial sites under different bioenergetic conditions.* J Biol Chem, 2017. **292**(41): p. 16804-16809.
59. Maggiorani, D., et al., *Monoamine Oxidases, Oxidative Stress, and Altered Mitochondrial Dynamics in Cardiac Ageing.* Oxid Med Cell Longev, 2017. **2017**: p. 3017947.
60. Turrens, J.F., *Mitochondrial formation of reactive oxygen species.* J Physiol, 2003. **552**(Pt 2): p. 335-44.
61. Murphy, M.P., *How mitochondria produce reactive oxygen species.* Biochem J, 2009. **417**(1): p. 1-13.
62. Lu, J. and A. Holmgren, *The thioredoxin antioxidant system.* Free Radic Biol Med, 2014. **66**: p. 75-87.
63. Schieber, M. and N.S. Chandel, *ROS function in redox signaling and oxidative stress.* Curr Biol, 2014. **24**(10): p. R453-62.
64. Horn, A., et al., *Mitochondrial redox signaling enables repair of injured skeletal muscle cells.* Sci Signal, 2017. **10**(495).
65. Duddy, W., et al., *Muscular dystrophy in the mdx mouse is a severe myopathy compounded by hypotrophy, hypertrophy and hyperplasia.* Skelet Muscle, 2015. **5**: p. 16.
66. Chernyak, B.V. and P. Bernardi, *The mitochondrial permeability transition pore is modulated by oxidative agents through both pyridine nucleotides and glutathione at two separate sites.* Eur J Biochem, 1996. **238**(3): p. 623-30.
67. Saks, V.A., et al., *Metabolic compartmentation and substrate channelling in muscle cells. Role of coupled creatine kinases in in vivo regulation of cellular respiration--a synthesis.* Mol Cell Biochem, 1994. **133-134**: p. 155-92.
68. Soboll, S., et al., *Octamer-dimer transitions of mitochondrial creatine kinase in heart disease.* J Mol Cell Cardiol, 1999. **31**(4): p. 857-66.
69. Wendt, S., U. Schlattner, and T. Wallimann, *Differential effects of peroxynitrite on human mitochondrial creatine kinase isoenzymes. Inactivation, octamer destabilization, and identification of involved residues.* J Biol Chem, 2003. **278**(2): p. 1125-30.
70. Tupling, A.R., *Excitation-Contraction Coupling*, in *Encyclopedia of Neuroscience*, M.D. Binder, N. Hirokawa, and U. Windhorst, Editors. 2009, Springer Berlin Heidelberg: Berlin, Heidelberg. p. 1479-1483.
71. Gailly, P., *New aspects of calcium signaling in skeletal muscle cells: implications in Duchenne muscular dystrophy.* Biochim Biophys Acta, 2002. **1600**(1-2): p. 38-44.

72. Harr, M.W. and C.W. Distelhorst, *Apoptosis and autophagy: decoding calcium signals that mediate life or death.* Cold Spring Harb Perspect Biol, 2010. **2**(10): p. a005579.
73. Altamirano, F., et al., *Increased resting intracellular calcium modulates NF-κB-dependent inducible nitric-oxide synthase gene expression in dystrophic mdx skeletal myotubes.* J Biol Chem, 2012. **287**(25): p. 20876-87.
74. Spencer, M.J., D.E. Croall, and J.G. Tidball, *Calpains are activated in necrotic fibers from mdx dystrophic mice.* J Biol Chem, 1995. **270**(18): p. 10909-14.
75. Pozzan, T., M. Bragadin, and G.F. Azzone, *Disequilibrium between steady-state Ca2+ accumulation ratio and membrane potential in mitochondria. Pathway and role of Ca2+ efflux.* Biochemistry, 1977. **16**(25): p. 5618-25.
76. Crofts, A.R. and J.B. Chappell, *CALCIUM ION ACCUMULATION AND VOLUME CHANGES OF ISOLATED LIVER MITOCHONDRIA. REVERSAL OF CALCIUM ION-INDUCED SWELLING.* Biochem J, 1965. **95**(2): p. 387-92.
77. Elustondo, P.A., et al., *Mitochondrial permeability transition pore induction is linked to formation of the complex of ATPase C-subunit, polyhydroxybutyrate and inorganic polyphosphate.* Cell Death Discov, 2016. **2**: p. 16070.
78. Halestrap, A.P., et al., *Mitochondria and cell death.* Biochemical Society Transactions, 2000. **28**(2): p. 170-177.
79. Pauly, M., et al., *AMPK activation stimulates autophagy and ameliorates muscular dystrophy in the mdx mouse diaphragm.* The American journal of pathology, 2012. **181**(2): p. 583-592.
80. Wrogemann, K. and S.D.J. Pena, *MITOCHONDRIAL CALCIUM OVERLOAD: A GENERAL MECHANISM FOR CELL-NECROSIS IN MUSCLE DISEASES.* The Lancet, 1976. **307**(7961): p. 672-674.
81. Bernardi, P., et al., *The Mitochondrial Permeability Transition Pore: Channel Formation by F-ATP Synthase, Integration in Signal Transduction, and Role in Pathophysiology.* Physiol Rev, 2015. **95**(4): p. 1111-55.
82. Halestrap, A.P., S.J. Clarke, and S.A. Javadov, *Mitochondrial permeability transition pore opening during myocardial reperfusion--a target for cardioprotection.* Cardiovasc Res, 2004. **61**(3): p. 372-85.
83. Halestrap, A.P. and P. Pasdois, *The role of the mitochondrial permeability transition pore in heart disease.* Biochim Biophys Acta, 2009. **1787**(11): p. 1402-15.
84. Haworth, R.A. and D.R. Hunter, *The Ca2+-induced membrane transition in mitochondria: II. Nature of the Ca2+ trigger site.* Archives of Biochemistry and Biophysics, 1979. **195**(2): p. 460-467.
85. Hunter, D.R. and R.A. Haworth, *The Ca2+-induced membrane transition in mitochondria. I. The protective mechanisms.* Arch Biochem Biophys, 1979. **195**(2): p. 453-9.
86. Hunter, D.R. and R.A. Haworth, *The Ca2+-induced membrane transition in mitochondria. III. Transitional Ca2+ release.* Arch Biochem Biophys, 1979. **195**(2): p. 468-77.
87. Giorgio, V., et al., *Ca(2+) binding to F-ATP synthase β subunit triggers the mitochondrial permeability transition.* EMBO Rep, 2017. **18**(7): p. 1065-1076.
88. Neginskaya, M.A., et al., *ATP Synthase C-Subunit-Deficient Mitochondria Have a Small Cyclosporine A-Sensitive Channel, but Lack the Permeability Transition Pore.* Cell Rep, 2019. **26**(1): p. 11-17.e2.
89. Amodeo, G.F., M.E. Solesio, and E.V. Pavlov, *From ATP synthase dimers to C-ring conformational changes: unified model of the mitochondrial permeability transition pore.* Cell Death & Disease, 2017. **8**(12): p. 1.

90. Fontaine, E., et al., *Regulation of the permeability transition pore in skeletal muscle mitochondria. Modulation By electron flow through the respiratory chain complex i.* J Biol Chem, 1998. **273**(20): p. 12662-8.
91. Javadov, S., *The calcium-ROS-pH triangle and mitochondrial permeability transition: challenges to mimic cardiac ischemia-reperfusion.* Frontiers in Physiology, 2015. **6**.
92. Duchen, M.R., et al., *On the involvement of a cyclosporin A sensitive mitochondrial pore in myocardial reperfusion injury.* Cardiovasc Res, 1993. **27**(10): p. 1790-4.
93. Dolder, M., S. Wendt, and T. Wallimann, *Mitochondrial creatine kinase in contact sites: interaction with porin and adenine nucleotide translocase, role in permeability transition and sensitivity to oxidative damage.* Biol Signals Recept, 2001. **10**(1-2): p. 93-111.
94. Dolder, M., et al., *Inhibition of the mitochondrial permeability transition by creatine kinase substrates: requirement for microcompartmentation.* Journal of Biological Chemistry, 2003. **278**(20): p. 17760-17766.
95. Kerr, J.F., A.H. Wyllie, and A.R. Currie, *Apoptosis: a basic biological phenomenon with wide-ranging implications in tissue kinetics.* Br J Cancer, 1972. **26**(4): p. 239-57.
96. Festjens, N., T. Vanden Berghe, and P. Vandenabeele, *Necrosis, a well-orchestrated form of cell demise: signalling cascades, important mediators and concomitant immune response.* Biochim Biophys Acta, 2006. **1757**(9-10): p. 1371-87.
97. Voss, A.K. and A. Strasser, *The essentials of developmental apoptosis.* F1000Res, 2020. **9**.
98. Coleman, M.L., et al., *Membrane blebbing during apoptosis results from caspase-mediated activation of ROCK I.* Nat Cell Biol, 2001. **3**(4): p. 339-45.
99. Salvesen, G.S. and V.M. Dixit, *Caspases: intracellular signaling by proteolysis.* Cell, 1997. **91**(4): p. 443-6.
100. Yin, X.M., Z.N. Oltvai, and S.J. Korsmeyer, *BH1 and BH2 domains of Bcl-2 are required for inhibition of apoptosis and heterodimerization with Bax.* Nature, 1994. **369**(6478): p. 321-3.
101. Westphal, D., R.M. Kluck, and G. Dewson, *Building blocks of the apoptotic pore: how Bax and Bak are activated and oligomerize during apoptosis.* Cell Death & Differentiation, 2014. **21**(2): p. 196-205.
102. Bao, Q. and Y. Shi, *Apoptosome: a platform for the activation of initiator caspases.* Cell Death & Differentiation, 2007. **14**(1): p. 56-65.
103. Li, P., et al., *Cytochrome c and dATP-dependent formation of Apaf-1/caspase-9 complex initiates an apoptotic protease cascade.* Cell, 1997. **91**(4): p. 479-89.
104. Eguchi, Y., S. Shimizu, and Y. Tsujimoto, *Intracellular ATP levels determine cell death fate by apoptosis or necrosis.* Cancer Res, 1997. **57**(10): p. 1835-40.
105. Nikoletopoulou, V., et al., *Crosstalk between apoptosis, necrosis and autophagy.* Biochim Biophys Acta, 2013. **1833**(12): p. 3448-3459.
106. Porter, A.G. and R.U. Jänicke, *Emerging roles of caspase-3 in apoptosis.* Cell Death Differ, 1999. **6**(2): p. 99-104.
107. McConkey, D.J., *Biochemical determinants of apoptosis and necrosis.* Toxicol Lett, 1998. **99**(3): p. 157-68.
108. Wickman, G.R., et al., *Blebs produced by actin–myosin contraction during apoptosis release damage-associated molecular pattern proteins before secondary necrosis occurs.* Cell Death & Differentiation, 2013. **20**(10): p. 1293-1305.
109. Tyler, K.L., *Origins and early descriptions of "Duchenne muscular dystrophy".* Muscle Nerve, 2003. **28**(4): p. 402-22.

110. Ahn, A.H. and L.M. Kunkel, *The structural and functional diversity of dystrophin.* Nat Genet, 1993. **3**(4): p. 283-91.
111. Hoffman, E.P., *The discovery of dystrophin, the protein product of the Duchenne muscular dystrophy gene.* Febs j, 2020. **287**(18): p. 3879-3887.
112. Koenig, M., et al., *Complete cloning of the Duchenne muscular dystrophy (DMD) cDNA and preliminary genomic organization of the DMD gene in normal and affected individuals.* Cell, 1987. **50**(3): p. 509-17.
113. Koenig, M., et al., *The molecular basis for Duchenne versus Becker muscular dystrophy: correlation of severity with type of deletion.* Am J Hum Genet, 1989. **45**(4): p. 498-506.
114. Den Dunnen, J.T., et al., *Topography of the Duchenne muscular dystrophy (DMD) gene: FIGE and cDNA analysis of 194 cases reveals 115 deletions and 13 duplications.* Am J Hum Genet, 1989. **45**(6): p. 835-47.
115. Takeshima, Y., et al., *Mutation spectrum of the dystrophin gene in 442 Duchenne/Becker muscular dystrophy cases from one Japanese referral center.* J Hum Genet, 2010. **55**(6): p. 379-88.
116. Mah, J.K., et al., *A population-based study of dystrophin mutations in Canada.* Can J Neurol Sci, 2011. **38**(3): p. 465-74.
117. Lee, T., et al., *Differences in carrier frequency between mothers of Duchenne and Becker muscular dystrophy patients.* J Hum Genet, 2014. **59**(1): p. 46-50.
118. Hanson, B., M.J.A. Wood, and T.C. Roberts, *Molecular correction of Duchenne muscular dystrophy by splice modulation and gene editing.* RNA Biol, 2021. **18**(7): p. 1048-1062.
119. Duan, D., *Systemic AAV Micro-dystrophin Gene Therapy for Duchenne Muscular Dystrophy.* Mol Ther, 2018. **26**(10): p. 2337-2356.
120. Berger, J., et al., *Dystrophin-deficient zebrafish feature aspects of the Duchenne muscular dystrophy pathology.* Neuromuscul Disord, 2010. **20**(12): p. 826-32.
121. Kornegay, J.N., et al., *Muscular dystrophy in a litter of golden retriever dogs.* Muscle Nerve, 1988. **11**(10): p. 1056-64.
122. Schatzberg, S.J., et al., *Molecular analysis of a spontaneous dystrophin 'knockout' dog.* Neuromuscul Disord, 1999. **9**(5): p. 289-95.
123. Kornegay, J.N., et al., *Canine models of Duchenne muscular dystrophy and their use in therapeutic strategies.* Mamm Genome, 2012. **23**(1-2): p. 85-108.
124. Cooper, B.J., et al., *The homologue of the Duchenne locus is defective in X-linked muscular dystrophy of dogs.* Nature, 1988. **334**(6178): p. 154-156.
125. Bulfield, G., et al., *X chromosome-linked muscular dystrophy (mdx) in the mouse.* Proc Natl Acad Sci U S A, 1984. **81**(4): p. 1189-92.
126. Chamberlain, J.S., et al., *Dystrophin-deficient mdx mice display a reduced life span and are susceptible to spontaneous rhabdomyosarcoma.* Faseb j, 2007. **21**(9): p. 2195-204.
127. McGreevy, J.W., et al., *Animal models of Duchenne muscular dystrophy: from basic mechanisms to gene therapy.* Dis Model Mech, 2015. **8**(3): p. 195-213.
128. Karpati, G., et al., *Localization and quantitation of the chromosome 6-encoded dystrophin-related protein in normal and pathological human muscle.* J Neuropathol Exp Neurol, 1993. **52**(2): p. 119-28.
129. Head, S.I., *Branched fibres in old dystrophic mdx muscle are associated with mechanical weakening of the sarcolemma, abnormal Ca2+ transients and a breakdown of Ca2+ homeostasis during fatigue.* Exp Physiol, 2010. **95**(5): p. 641-56.
130. Williams, M.S. and J. Kwon, *T cell receptor stimulation, reactive oxygen species, and cell signaling.* Free Radic Biol Med, 2004. **37**(8): p. 1144-51.

131. Briguet, A., et al., *Histological parameters for the quantitative assessment of muscular dystrophy in the mdx-mouse.* Neuromuscul Disord, 2004. **14**(10): p. 675-82.
132. McDonald, A.A., et al., *Disease course in mdx:utrophin+/- mice: comparison of three mouse models of Duchenne muscular dystrophy.* Physiol Rep, 2015. **3**(4).
133. Carnwath, J.W. and D.M. Shotton, *Muscular dystrophy in the mdx mouse: histopathology of the soleus and extensor digitorum longus muscles.* J Neurol Sci, 1987. **80**(1): p. 39-54.
134. Coulton, G.R., et al., *The mdx mouse skeletal muscle myopathy: I. A histological, morphometric and biochemical investigation.* Neuropathol Appl Neurobiol, 1988. **14**(1): p. 53-70.
135. Tinsley, J.M., et al., *Amelioration of the dystrophic phenotype of mdx mice using a truncated utrophin transgene.* Nature, 1996. **384**(6607): p. 349-53.
136. Deconinck, N. and B. Dan, *Pathophysiology of duchenne muscular dystrophy: current hypotheses.* Pediatr Neurol, 2007. **36**(1): p. 1-7.
137. Straub, V., et al., *Animal models for muscular dystrophy show different patterns of sarcolemmal disruption.* J Cell Biol, 1997. **139**(2): p. 375-85.
138. Campanelli, J.T., et al., *A role for dystrophin-associated glycoproteins and utrophin in agrin-induced AChR clustering.* Cell, 1994. **77**(5): p. 663-74.
139. Gramolini, A.O., J. Wu, and B.J. Jasmin, *Regulation and functional significance of utrophin expression at the mammalian neuromuscular synapse.* Microsc Res Tech, 2000. **49**(1): p. 90-100.
140. Takemitsu, M., et al., *Dystrophin-related protein in the fetal and denervated skeletal muscles of normal and mdx mice.* Biochem Biophys Res Commun, 1991. **180**(3): p. 1179-86.
141. Deconinck, A.E., et al., *Utrophin-Dystrophin-Deficient Mice as a Model for Duchenne Muscular Dystrophy.* Cell, 1997. **90**(4): p. 717-727.
142. Heydemann, A., et al., *Latent TGF-beta-binding protein 4 modifies muscular dystrophy in mice.* J Clin Invest, 2009. **119**(12): p. 3703-12.
143. Coley, W.D., et al., *Effect of genetic background on the dystrophic phenotype in mdx mice.* Hum Mol Genet, 2016. **25**(1): p. 130-45.
144. Hammers, D.W., et al., *The D2.mdx mouse as a preclinical model of the skeletal muscle pathology associated with Duchenne muscular dystrophy.* Scientific Reports, 2020. **10**(1): p. 14070.
145. Fukada, S., et al., *Genetic background affects properties of satellite cells and mdx phenotypes.* Am J Pathol, 2010. **176**(5): p. 2414-24.
146. Rodrigues, M., et al., *Impaired regenerative capacity and lower revertant fibre expansion in dystrophin-deficient mdx muscles on DBA/2 background.* Sci Rep, 2016. **6**: p. 38371.
147. van Putten, M., et al., *Natural disease history of the D2-mdx mouse model for Duchenne muscular dystrophy.* Faseb j, 2019. **33**(7): p. 8110-8124.
148. Spaulding, H.R., et al., *Nutraceutical and pharmaceutical cocktails did not improve muscle function or reduce histological damage in D2-mdx mice.* J Appl Physiol (1985), 2019. **127**(4): p. 1058-1066.
149. Ward, C.W., et al., *GsMTx4-D provides protection to the D2.mdx mouse.* Neuromuscul Disord, 2018. **28**(10): p. 868-877.
150. Bellissimo, C.A., et al., *Mitochondrial creatine sensitivity is lost in the D2.mdx model of Duchenne muscular dystrophy and rescued by the mitochondrial-enhancing compound Olesoxime.* Am J Physiol Cell Physiol, 2023.

151. Kohler, M., et al., *Disability and survival in Duchenne muscular dystrophy.* J Neurol Neurosurg Psychiatry, 2009. **80**(3): p. 320-5.
152. Manzur, A.Y., M. Kinali, and F. Muntoni, *Update on the management of Duchenne muscular dystrophy.* Arch Dis Child, 2008. **93**(11): p. 986-90.
153. Akay, T., et al., *Degradation of mouse locomotor pattern in the absence of proprioceptive sensory feedback.* Proc Natl Acad Sci U S A, 2014. **111**(47): p. 16877-82.
154. Kadaba, M.P., H.K. Ramakrishnan, and M.E. Wootten, *Measurement of lower extremity kinematics during level walking.* J Orthop Res, 1990. **8**(3): p. 383-92.
155. Hu, X., et al., *Are mice good models for human neuromuscular disease? Comparing muscle excursions in walking between mice and humans.* Skelet Muscle, 2017. **7**(1): p. 26.
156. Petrof, B.J., et al., *Dystrophin protects the sarcolemma from stresses developed during muscle contraction.* Proc Natl Acad Sci U S A, 1993. **90**(8): p. 3710-4.
157. Moens, P., P.H. Baatsen, and G. Maréchal, *Increased susceptibility of EDL muscles from mdx mice to damage induced by contractions with stretch.* J Muscle Res Cell Motil, 1993. **14**(4): p. 446-51.
158. Stedman, H.H., et al., *The mdx mouse diaphragm reproduces the degenerative changes of Duchenne muscular dystrophy.* Nature, 1991. **352**(6335): p. 536-9.
159. Torres, L.F. and L.W. Duchen, *The mutant mdx: inherited myopathy in the mouse. Morphological studies of nerves, muscles and end-plates.* Brain, 1987. **110 (Pt 2)**: p. 269-99.
160. Turk, R., et al., *Muscle regeneration in dystrophin-deficient mdx mice studied by gene expression profiling.* BMC Genomics, 2005. **6**: p. 98.
161. Pescatori, M., et al., *Gene expression profiling in the early phases of DMD: a constant molecular signature characterizes DMD muscle from early postnatal life throughout disease progression.* The FASEB Journal, 2007. **21**(4): p. 1210-1226.
162. Webster, C. and H.M. Blau, *Accelerated age-related decline in replicative life-span of Duchenne muscular dystrophy myoblasts: implications for cell and gene therapy.* Somat Cell Mol Genet, 1990. **16**(6): p. 557-65.
163. Hoffman, E.P., *Genotype/phenotype correlations in Duchenne/Becker dystrophy.* Mol Cell Biol Hum Dis Ser, 1993. **3**: p. 12-36.
164. Blau, H.M., C. Webster, and G.K. Pavlath, *Defective myoblasts identified in Duchenne muscular dystrophy.* Proc Natl Acad Sci U S A, 1983. **80**(15): p. 4856-60.
165. Lu, A., et al., *Rapid depletion of muscle progenitor cells in dystrophic mdx/utrophin-/- mice.* Hum Mol Genet, 2014. **23**(18): p. 4786-800.
166. Young, L.V., et al., *Loss of dystrophin expression in skeletal muscle is associated with senescence of macrophages and endothelial cells.* Am J Physiol Cell Physiol, 2021. **321**(1): p. C94-c103.
167. Collins, C.A. and J.E. Morgan, *Duchenne's muscular dystrophy: animal models used to investigate pathogenesis and develop therapeutic strategies.* Int J Exp Pathol, 2003. **84**(4): p. 165-72.
168. Abbott, A., *Laboratory animals: the Renaissance rat.* Nature, 2004. **428**(6982): p. 464-6.
169. Tesson, L., et al., *Knockout rats generated by embryo microinjection of TALENs.* Nat Biotechnol, 2011. **29**(8): p. 695-6.
170. Li, W., et al., *Simultaneous generation and germline transmission of multiple gene mutations in rat using CRISPR-Cas systems.* Nat Biotechnol, 2013. **31**(8): p. 684-6.
171. Li, D., et al., *Heritable gene targeting in the mouse and rat using a CRISPR-Cas system.* Nat Biotechnol, 2013. **31**(8): p. 681-3.

172. Fujii, W., et al., *Efficient generation of large-scale genome-modified mice using gRNA and CAS9 endonuclease.* Nucleic Acids Res, 2013. **41**(20): p. e187.
173. Nakamura, K., et al., *Generation of muscular dystrophy model rats with a CRISPR/Cas system.* Sci Rep, 2014. **4**: p. 5635.
174. Larcher, T., et al., *Characterization of Dystrophin Deficient Rats: A New Model for Duchenne Muscular Dystrophy.* PLOS ONE, 2014. **9**(10): p. e110371.
175. Iyer, S.R., et al., *Muscle phenotype of a rat model of Duchenne muscular dystrophy.* Muscle Nerve, 2020. **62**(6): p. 757-761.
176. Cohn, R.D. and K.P. Campbell, *Molecular basis of muscular dystrophies.* Muscle & nerve, 2000. **23**(10): p. 1456-1471.
177. Coirault, C., et al., *Severe muscle dysfunction precedes collagen tissue proliferation in mdx mouse diaphragm.* J Appl Physiol (1985), 2003. **94**(5): p. 1744-50.
178. Emery, A.E., *Duchenne muscular dystrophy—Meryon's disease.* Neuromuscular Disorders, 1993. **3**(4): p. 263-266.
179. Suthar, R. and N. Sankhyan, *Duchenne Muscular Dystrophy: A Practice Update.* Indian J Pediatr, 2018. **85**(4): p. 276-281.
180. Iff, J., et al., *Disease Progression Stages and Burden in Patients with Duchenne Muscular Dystrophy Using Administrative Claims Supplemented by Electronic Medical Records.* Adv Ther, 2022. **39**(6): p. 2906-2919.
181. Van Ruiten, H.J., et al., *Why are some patients with Duchenne muscular dystrophy dying young: An analysis of causes of death in North East England.* Eur J Paediatr Neurol, 2016. **20**(6): p. 904-909.
182. Passamano, L., et al., *Improvement of survival in Duchenne Muscular Dystrophy: retrospective analysis of 835 patients.* Acta Myol, 2012. **31**(2): p. 121-5.
183. Kieny, P., et al., *Evolution of life expectancy of patients with Duchenne muscular dystrophy at AFM Yolaine de Kepper centre between 1981 and 2011.* Ann Phys Rehabil Med, 2013. **56**(6): p. 443-54.
184. Hukins, C.A. and D.R. Hillman, *Daytime predictors of sleep hypoventilation in Duchenne muscular dystrophy.* Am J Respir Crit Care Med, 2000. **161**(1): p. 166-70.
185. Smith, P.E., P.M. Calverley, and R.H. Edwards, *Hypoxemia during sleep in Duchenne muscular dystrophy.* Am Rev Respir Dis, 1988. **137**(4): p. 884-8.
186. Phillips, M.F., et al., *Changes in spirometry over time as a prognostic marker in patients with Duchenne muscular dystrophy.* Am J Respir Crit Care Med, 2001. **164**(12): p. 2191-4.
187. De Bruin, P.F., et al., *Diaphragm thickness and inspiratory strength in patients with Duchenne muscular dystrophy.* Thorax, 1997. **52**(5): p. 472-5.
188. Rideau, Y., L.W. Jankowski, and J. Grellet, *Respiratory function in the muscular dystrophies.* Muscle Nerve, 1981. **4**(2): p. 155-64.
189. Gozal, D. and P. Thiriet, *Respiratory muscle training in neuromuscular disease: long-term effects on strength and load perception.* Med Sci Sports Exerc, 1999. **31**(11): p. 1522-7.
190. Lo Mauro, A., et al., *Abdominal volume contribution to tidal volume as an early indicator of respiratory impairment in Duchenne muscular dystrophy.* Eur Respir J, 2010. **35**(5): p. 1118-25.
191. Eagle, M., et al., *Survival in Duchenne muscular dystrophy: improvements in life expectancy since 1967 and the impact of home nocturnal ventilation.* Neuromuscul Disord, 2002. **12**(10): p. 926-9.

192. Jeppesen, J., et al., *The Duchenne muscular dystrophy population in Denmark, 1977-2001: prevalence, incidence and survival in relation to the introduction of ventilator use.* Neuromuscul Disord, 2003. **13**(10): p. 804-12.
193. Lee, J.J., S.M. Patel, and S.F. Saba, *X marks the spot: Duchenne's cardiomyopathy.* The American Journal of Medicine, 2014. **127**(7): p. e13-e14.
194. Judge, D.P., et al., *Pathophysiology and Therapy of Cardiac Dysfunction in Duchenne Muscular Dystrophy.* American Journal of Cardiovascular Drugs, 2011. **11**(5): p. 287-294.
195. Bäckman, E. and E. Nylander, *The heart in Duchenne muscular dystrophy: a non-invasive longitudinal study.* Eur Heart J, 1992. **13**(9): p. 1239-44.
196. Duboc, D., et al., *Perindopril preventive treatment on mortality in Duchenne muscular dystrophy: 10 years' follow-up.* Am Heart J, 2007. **154**(3): p. 596-602.
197. Bushby, K., et al., *Diagnosis and management of Duchenne muscular dystrophy, part 1: diagnosis, and pharmacological and psychosocial management.* Lancet Neurol, 2010. **9**(1): p. 77-93.
198. Verhaert, D., et al., *Cardiac involvement in patients with muscular dystrophies: magnetic resonance imaging phenotype and genotypic considerations.* Circ Cardiovasc Imaging, 2011. **4**(1): p. 67-76.
199. D'Amario, D., et al., *A current approach to heart failure in Duchenne muscular dystrophy.* Heart, 2017. **103**(22): p. 1770-1779.
200. Nigro, G., et al., *Prospective study of X-linked progressive muscular dystrophy in Campania.* Muscle Nerve, 1983. **6**(4): p. 253-62.
201. Nigro, G., et al., *The incidence and evolution of cardiomyopathy in Duchenne muscular dystrophy.* Int J Cardiol, 1990. **26**(3): p. 271-7.
202. WATKINS, S.C. and M.J. CULLEN, *HISTOCHEMICAL FIBRE TYPING AND ULTRASTUCTURE OF THE SMALL FIBRES IN DUCHENNE MUSCULAR DYSTROPHY.* Neuropathology and Applied Neurobiology, 1985. **11**(6): p. 447-460.
203. Webster, C., et al., *Fast muscle fibers are preferentially affected in Duchenne muscular dystrophy.* Cell, 1988. **52**(4): p. 503-513.
204. Minetti, C., E. Ricci, and E. Bonilla, *Progressive depletion of fast alpha-actinin-positive muscle fibers in Duchenne muscular dystrophy.* Neurology, 1991. **41**(12): p. 1977-81.
205. Blake, D.J., J.M. Tinsley, and K.E. Davies, *Utrophin: a structural and functional comparison to dystrophin.* Brain Pathol, 1996. **6**(1): p. 37-47.
206. Chakkalakal, J.V., et al., *Expression of utrophin A mRNA correlates with the oxidative capacity of skeletal muscle fiber types and is regulated by calcineurin/NFAT signaling.* Proc Natl Acad Sci U S A, 2003. **100**(13): p. 7791-6.
207. Jasmin, B.J., et al., *Multiple regulatory events controlling the expression and localization of utrophin in skeletal muscle fibers: insights into a therapeutic strategy for Duchenne muscular dystrophy.* J Physiol Paris, 2002. **96**(1-2): p. 31-42.
208. Sengupta, K., et al., *Genome Editing-Mediated Utrophin Upregulation in Duchenne Muscular Dystrophy Stem Cells.* Mol Ther Nucleic Acids, 2020. **22**: p. 500-509.
209. Miura, P. and B.J. Jasmin, *Utrophin upregulation for treating Duchenne or Becker muscular dystrophy: how close are we?* Trends Mol Med, 2006. **12**(3): p. 122-9.
210. St-Pierre, S.J., et al., *Glucocorticoid treatment alleviates dystrophic myofiber pathology by activation of the calcineurin/NF-AT pathway.* Faseb j, 2004. **18**(15): p. 1937-9.
211. Cros, D., et al., *Muscle hypertrophy in Duchenne muscular dystrophy. A pathological and morphometric study.* J Neurol, 1989. **236**(1): p. 43-7.

212. Baloh, R. and P.A. Cancilla, *An appraisal of histochemical fiber types in Duchenne muscular dystrophy.* Neurology, 1972. **22**(12): p. 1243-52.
213. Beenakker, E.A., et al., *Quantitative assessment of calf circumference in Duchenne muscular dystrophy patients.* Neuromuscul Disord, 2002. **12**(7-8): p. 639-42.
214. Kaminski, H.J., et al., *Extraocular muscles are spared in advanced Duchenne dystrophy.* Ann Neurol, 1992. **32**(4): p. 586-8.
215. Wicke, W., et al., *Histochemical and immunohistochemical study on muscle fibers in human extraocular muscle spindles.* Exp Eye Res, 2007. **84**(4): p. 670-9.
216. Porter, J.D., et al., *Extraocular muscles: basic and clinical aspects of structure and function.* Survey of ophthalmology, 1995. **39**(6): p. 451-484.
217. Couly, G.F., P.M. Coltey, and N.M. Le Douarin, *The developmental fate of the cephalic mesoderm in quail-chick chimeras.* Development, 1992. **114**(1): p. 1-15.
218. Verma, M., K. Fitzpatrick, and L.K. McLoon, *Extraocular Muscle Repair and Regeneration.* Curr Ophthalmol Rep, 2017. **5**(3): p. 207-215.
219. Burden, S.J., *The formation of neuromuscular synapses.* Genes & Development, 1998. **12**(2): p. 133-148.
220. Andrade, F.H., J.D. Porter, and H.J. Kaminski, *Eye muscle sparing by the muscular dystrophies: lessons to be learned?* Microsc Res Tech, 2000. **48**(3-4): p. 192-203.
221. Judge, S.M., et al., *Skeletal Muscle Fibrosis in Pancreatic Cancer Patients with Respect to Survival.* JNCI Cancer Spectr, 2018. **2**(3): p. pky043.
222. Dulai, P.S., et al., *Increased risk of mortality by fibrosis stage in nonalcoholic fatty liver disease: Systematic review and meta-analysis.* Hepatology, 2017. **65**(5): p. 1557-1565.
223. Desguerre, I., et al., *Endomysial Fibrosis in Duchenne Muscular Dystrophy: A Marker of Poor Outcome Associated With Macrophage Alternative Activation.* Journal of Neuropathology & Experimental Neurology, 2009. **68**(7): p. 762-773.
224. Bernasconi, P., et al., *Expression of transforming growth factor-beta 1 in dystrophic patient muscles correlates with fibrosis. Pathogenetic role of a fibrogenic cytokine.* J Clin Invest, 1995. **96**(2): p. 1137-44.
225. Finsterer, J. and C. Stöllberger, *The heart in human dystrophinopathies.* Cardiology, 2003. **99**(1): p. 1-19.
226. Huebner, K.D., et al., *Functional resolution of fibrosis in mdx mouse dystrophic heart and skeletal muscle by halofuginone.* Am J Physiol Heart Circ Physiol, 2008. **294**(4): p. H1550-61.
227. Percival, J.M., et al., *Sildenafil reduces respiratory muscle weakness and fibrosis in the mdx mouse model of Duchenne muscular dystrophy.* J Pathol, 2012. **228**(1): p. 77-87.
228. Zhou, L. and H. Lu, *Targeting fibrosis in Duchenne muscular dystrophy.* J Neuropathol Exp Neurol, 2010. **69**(8): p. 771-6.
229. Tandon, A., et al., *Myocardial fibrosis burden predicts left ventricular ejection fraction and is associated with age and steroid treatment duration in duchenne muscular dystrophy.* J Am Heart Assoc, 2015. **4**(4).
230. Klingler, W., et al., *The role of fibrosis in Duchenne muscular dystrophy.* Acta Myol, 2012. **31**(3): p. 184-95.
231. Lieber, R.L. and S.R. Ward, *Cellular mechanisms of tissue fibrosis. 4. Structural and functional consequences of skeletal muscle fibrosis.* Am J Physiol Cell Physiol, 2013. **305**(3): p. C241-52.
232. Song, Y., et al., *Expression levels of TGF-β1 and CTGF are associated with the severity of Duchenne muscular dystrophy.* Exp Ther Med, 2017. **13**(4): p. 1209-1214.

233. Taniguti, A.P., et al., *Prevention of muscle fibrosis and myonecrosis in mdx mice by suramin, a TGF-β1 blocker.* Muscle Nerve, 2011. **43**(1): p. 82-7.
234. Lorts, A., et al., *Deletion of periostin reduces muscular dystrophy and fibrosis in mice by modulating the transforming growth factor-β pathway.* Proc Natl Acad Sci U S A, 2012. **109**(27): p. 10978-83.
235. Kharraz, Y., et al., *Understanding the process of fibrosis in Duchenne muscular dystrophy.* Biomed Res Int, 2014. **2014**: p. 965631.
236. Fortunato, F., et al., *Innovative Therapeutic Approaches for Duchenne Muscular Dystrophy.* J Clin Med, 2021. **10**(4).
237. Bersini, S., et al., *Tackling muscle fibrosis: From molecular mechanisms to next generation engineered models to predict drug delivery.* Adv Drug Deliv Rev, 2018. **129**: p. 64-77.
238. Desguerre, I., et al., *Endomysial fibrosis in Duchenne muscular dystrophy: a marker of poor outcome associated with macrophage alternative activation.* J Neuropathol Exp Neurol, 2009. **68**(7): p. 762-73.
239. Mázala, D.A.G., et al., *TGF-β–driven muscle degeneration and failed regeneration underlie disease onset in a DMD mouse model.* JCI Insight, 2020. **5**(6).
240. Verhaart, I.E.C., et al., *A modified diet does not ameliorate muscle pathology in a mouse model for Duchenne muscular dystrophy.* PLoS One, 2019. **14**(4): p. e0215335.
241. Hayes, H.M., et al., *Preserved Left Ventricular Function despite Myocardial Fibrosis and Myopathy in the Dystrophin-Deficient D2.B10-Dmd (mdx) /J Mouse.* Oxid Med Cell Longev, 2022. **2022**: p. 5362115.
242. Kennedy, T.L., et al., *Micro-utrophin Improves Cardiac and Skeletal Muscle Function of Severely Affected D2/mdx Mice.* Mol Ther Methods Clin Dev, 2018. **11**: p. 92-105.
243. Allen, D.G., et al., *Calcium and the damage pathways in muscular dystrophy.* Can J Physiol Pharmacol, 2010. **88**(2): p. 83-91.
244. Whitehead, N.P., E.W. Yeung, and D.G. Allen, *Muscle damage in mdx (dystrophic) mice: role of calcium and reactive oxygen species.* Clin Exp Pharmacol Physiol, 2006. **33**(7): p. 657-62.
245. Alderton, J.M. and R.A. Steinhardt, *How calcium influx through calcium leak channels is responsible for the elevated levels of calcium-dependent proteolysis in dystrophic myotubes.* Trends Cardiovasc Med, 2000. **10**(6): p. 268-72.
246. Turner, P.R., et al., *Increased protein degradation results from elevated free calcium levels found in muscle from mdx mice.* Nature, 1988. **335**(6192): p. 735-8.
247. Bonuccelli, G., et al., *Proteasome inhibitor (MG-132) treatment of mdx mice rescues the expression and membrane localization of dystrophin and dystrophin-associated proteins.* Am J Pathol, 2003. **163**(4): p. 1663-75.
248. Mareedu, S., et al., *Abnormal Calcium Handling in Duchenne Muscular Dystrophy: Mechanisms and Potential Therapies.* Front Physiol, 2021. **12**: p. 647010.
249. Cleverdon, R.E.G., et al., *Sarco(endo)plasmic reticulum Ca(2+)-ATPase function is impaired in skeletal and cardiac muscles from young DBA/2J mdx mice.* iScience, 2022. **25**(9): p. 104972.
250. Goonasekera, S.A., et al., *Mitigation of muscular dystrophy in mice by SERCA overexpression in skeletal muscle.* J Clin Invest, 2011. **121**(3): p. 1044-52.
251. Mázala, D.A., et al., *SERCA1 overexpression minimizes skeletal muscle damage in dystrophic mouse models.* Am J Physiol Cell Physiol, 2015. **308**(9): p. C699-709.
252. Gehrig, S.M., et al., *Hsp72 preserves muscle function and slows progression of severe muscular dystrophy.* Nature, 2012. **484**(7394): p. 394-8.

253. Dremina, E.S., V.S. Sharov, and C. Schöneich, *Heat-shock proteins attenuate SERCA inactivation by the anti-apoptotic protein Bcl-2: possible implications for the ER Ca2+-mediated apoptosis.* Biochem J, 2012. **444**(1): p. 127-39.
254. Bernardi, P., M. Carraro, and G. Lippe, *The mitochondrial permeability transition: Recent progress and open questions.* The FEBS Journal, 2021. **n/a**(n/a).
255. Angebault, C., et al., *Metformin Reverses the Enhanced Myocardial SR/ER–Mitochondria Interaction and Impaired Complex I-Driven Respiration in Dystrophin-Deficient Mice.* Frontiers in Cell and Developmental Biology, 2021. **8**.
256. Bellissimo, C.A., M.C. Garibotti, and C.G.R. Perry, *Mitochondrial Stress Responses in Duchenne muscular dystrophy: Metabolic Dysfunction or Adaptive Reprogramming?* Am J Physiol Cell Physiol, 2022.
257. Bernardi, P. and S. von Stockum, *The permeability transition pore as a Ca(2+) release channel: new answers to an old question.* Cell Calcium, 2012. **52**(1): p. 22-7.
258. Kang, C., et al., *Deficit in PINK1/PARKIN-mediated mitochondrial autophagy at late stages of dystrophic cardiomyopathy.* Cardiovasc Res, 2018. **114**(1): p. 90-102.
259. Hunter, M.I. and J.B. Mohamed, *Plasma antioxidants and lipid peroxidation products in Duchenne muscular dystrophy.* Clin Chim Acta, 1986. **155**(2): p. 123-31.
260. Matkovics, B., A. László, and L. Szabó, *A comparative study of superoxide dismutase, catalase and lipid peroxidation in red blood cells from muscular dystrophy patients and normal controls.* Clinica Chimica Acta, 1982. **118**(2): p. 289-292.
261. Salminen, A. and M. Kihlström, *Increased susceptibility to lipid peroxidation in skeletal muscles of dystrophic hamsters.* Experientia, 1989. **45**(8): p. 747-749.
262. Jackson, M., D. Jones, and R. Edwards, *Techniques for studying free radical damage in muscular dystrophy.* Medical biology, 1984. **62**(2): p. 135-138.
263. Jackson, M.J., *Free Radicals and Skeletal Muscle Disorders.* Oxygen radicals: systemic events and disease processes, 1990: p. 149-171.
264. Reyes, J., et al., *Enhanced urinary spontaneous luminescence in Duchenne muscular dystrophy.* Free Radic Biol Med, 1994. **16**(6): p. 851-3.
265. Grosso, S., et al., *Isoprostanes in dystrophinopathy: Evidence of increased oxidative stress.* Brain Dev, 2008. **30**(6): p. 391-5.
266. Burr, I.M., K. Asayama, and G.M. Fenichel, *Superoxide dismutases, glutathione peroxidase, and catalase in neuromuscular disease.* Muscle Nerve, 1987. **10**(2): p. 150-4.
267. Austin, L., et al., *Potential oxyradical damage and energy status in individual muscle fibres from degenerating muscle diseases.* Neuromuscul Disord, 1992. **2**(1): p. 27-33.
268. Rando, T.A., et al., *Muscle cells from mdx mice have an increased susceptibility to oxidative stress.* Neuromuscul Disord, 1998. **8**(1): p. 14-21.
269. Whitehead, N.P., et al., *N-Acetylcysteine ameliorates skeletal muscle pathophysiology in mdx mice.* J Physiol, 2008. **586**(7): p. 2003-14.
270. Tonon, E., et al., *Ascorbic acid protects the diaphragm muscle against myonecrosis in mdx mice.* Nutrition, 2012. **28**(6): p. 686-90.
271. Javeshghani, D., et al., *Molecular characterization of a superoxide-generating NAD(P)H oxidase in the ventilatory muscles.* Am J Respir Crit Care Med, 2002. **165**(3): p. 412-8.
272. Spurney, C.F., et al., *Dystrophin-deficient cardiomyopathy in mouse: expression of Nox4 and Lox are associated with fibrosis and altered functional parameters in the heart.* Neuromuscul Disord, 2008. **18**(5): p. 371-81.
273. Tseng, B.S., et al., *Regenerated mdx mouse skeletal muscle shows differential mRNA expression.* J Appl Physiol (1985), 2002. **93**(2): p. 537-45.

274. Jung, C., et al., *Dystrophic cardiomyopathy: amplification of cellular damage by Ca2+ signalling and reactive oxygen species-generating pathways.* Cardiovasc Res, 2008. **77**(4): p. 766-73.
275. Whitehead, N.P., et al., *Skeletal muscle NADPH oxidase is increased and triggers stretch-induced damage in the mdx mouse.* PLoS One, 2010. **5**(12): p. e15354.
276. Burns, D.P., et al., *N-acetylcysteine Decreases Fibrosis and Increases Force-Generating Capacity of mdx Diaphragm.* Antioxidants (Basel), 2019. **8**(12).
277. Tidball, J.G., et al., *Apoptosis precedes necrosis of dystrophin-deficient muscle.* Journal of Cell Science, 1995. **108**(6): p. 2197-2204.
278. Coulton, G.R., et al., *In situ localisation of single-stranded DNA breaks in nuclei of a subpopulation of cells within regenerating skeletal muscle of the dystrophic mdx mouse.* J Cell Sci, 1992. **102 (Pt 3)**: p. 653-62.
279. Matsuda, R., A. Nishikawa, and H. Tanaka, *Visualization of dystrophic muscle fibers in mdx mouse by vital staining with Evans blue: evidence of apoptosis in dystrophin-deficient muscle.* J Biochem, 1995. **118**(5): p. 959-64.
280. Sandri, M., et al., *Apoptosis, DNA damage and ubiquitin expression in normal and mdx muscle fibers after exercise.* FEBS Lett, 1995. **373**(3): p. 291-5.
281. Migheli, A., et al., *Muscle apoptosis in humans occurs in normal and denervated muscle, but not in myotonic dystrophy, dystrophinopathies or inflammatory disease.* Neurogenetics, 1997. **1**(2): p. 81-7.
282. Sandri, M., et al., *Apoptotic myonuclei in human Duchenne muscular dystrophy.* Lab Invest, 1998. **78**(8): p. 1005-16.
283. Tews, D.S. and H.H. Goebel, *DNA-fragmentation and expression of apoptosis-related proteins in muscular dystrophies.* Neuropathol Appl Neurobiol, 1997. **23**(4): p. 331-8.
284. Behrens, L., et al., *Cytotoxic mechanisms in inflammatory myopathies. Co-expression of Fas and protective Bcl-2 in muscle fibres and inflammatory cells.* Brain, 1997. **120 (Pt 6)**: p. 929-38.
285. Vanden Berghe, T., B. Hassannia, and P. Vandenabeele, *An outline of necrosome triggers.* Cell Mol Life Sci, 2016. **73**(11-12): p. 2137-52.
286. Morgan, J.E., et al., *Necroptosis mediates myofibre death in dystrophin-deficient mice.* Nat Commun, 2018. **9**(1): p. 3655.
287. Ambrósio, C.E., et al., *Identification of three distinguishable phenotypes in golden retriever muscular dystrophy.* Genet Mol Res, 2009. **8**(2): p. 389-96.
288. Tripodi, L., et al., *The Immune System in Duchenne Muscular Dystrophy Pathogenesis.* Biomedicines, 2021. **9**(10).
289. Giuliani, G., M. Rosina, and A. Reggio, *Signaling pathways regulating the fate of fibro/adipogenic progenitors (FAPs) in skeletal muscle regeneration and disease.* Febs j, 2022. **289**(21): p. 6484-6517.
290. Dong, Y., et al., *Glucocorticoids increase adipocytes in muscle by affecting IL-4 regulated FAP activity.* The FASEB Journal, 2014. **28**(9): p. 4123-4132.
291. Flanigan, K.M., et al., *Anti-dystrophin T cell responses in Duchenne muscular dystrophy: prevalence and a glucocorticoid treatment effect.* Hum Gene Ther, 2013. **24**(9): p. 797-806.
292. Engel, A.G. and G. Biesecker, *Complement activation in muscle fiber necrosis: demonstration of the membrane attack complex of complement in necrotic fibers.* Ann Neurol, 1982. **12**(3): p. 289-96.

293. Hodgetts, S., et al., *Reduced necrosis of dystrophic muscle by depletion of host neutrophils, or blocking TNFalpha function with Etanercept in mdx mice.* Neuromuscul Disord, 2006. **16**(9-10): p. 591-602.
294. Horsley, V., et al., *IL-4 acts as a myoblast recruitment factor during mammalian muscle growth.* Cell, 2003. **113**(4): p. 483-94.
295. Hindi, S.M., et al., *Distinct roles of TRAF6 at early and late stages of muscle pathology in the mdx model of Duchenne muscular dystrophy.* Hum Mol Genet, 2014. **23**(6): p. 1492-505.
296. Gussoni, E., et al., *Specific T cell receptor gene rearrangements at the site of muscle degeneration in Duchenne muscular dystrophy.* J Immunol, 1994. **153**(10): p. 4798-805.
297. Hale, J.S. and P.J. Fink, *Back to the thymus: peripheral T cells come home.* Immunol Cell Biol, 2009. **87**(1): p. 58-64.
298. Gorospe, J.R., et al., *Dystrophin-deficient myofibers are vulnerable to mast cell granule-induced necrosis.* Neuromuscul Disord, 1994. **4**(4): p. 325-33.
299. Granchelli, J.A., et al., *Cromolyn increases strength in exercised mdx mice.* Res Commun Mol Pathol Pharmacol, 1996. **91**(3): p. 287-96.
300. De Paepe, B. and J.L. De Bleecker, *Cytokines and chemokines as regulators of skeletal muscle inflammation: presenting the case of Duchenne muscular dystrophy.* Mediators Inflamm, 2013. **2013**: p. 540370.
301. Chen, Y.W., et al., *Expression profiling in the muscular dystrophies: identification of novel aspects of molecular pathophysiology.* J Cell Biol, 2000. **151**(6): p. 1321-36.
302. Allen, D.G., N.P. Whitehead, and S.C. Froehner, *Absence of Dystrophin Disrupts Skeletal Muscle Signaling: Roles of Ca2+, Reactive Oxygen Species, and Nitric Oxide in the Development of Muscular Dystrophy.* Physiol Rev, 2016. **96**(1): p. 253-305.
303. Samaha, F.J., B. Davis, and B. Nagy, *Duchenne muscular dystrophy.* Adenosine triphosphate and creatine phosphate content in muscle, 1981. **31**(7): p. 916-916.
304. Barker, R.G., et al., *Mitochondrial content is preserved throughout disease progression in the mdx mouse model of Duchenne muscular dystrophy, regardless of taurine supplementation.* Am J Physiol Cell Physiol, 2018. **314**(4): p. C483-c491.
305. Chinet, A.E., P.C. Even, and A. Decrouy, *Dystrophin-dependent efficiency of metabolic pathways in mouse skeletal muscles.* Experientia, 1994. **50**(6): p. 602-5.
306. Even, P.C., A. Decrouy, and A. Chinet, *Defective regulation of energy metabolism in mdx-mouse skeletal muscles.* Biochem J, 1994. **304 (Pt 2)**(Pt 2): p. 649-54.
307. Gaglianone, R.B., et al., *Reduced mitochondrial respiration and increased calcium deposits in the EDL muscle, but not in soleus, from 12-week-old dystrophic mdx mice.* Sci Rep, 2019. **9**(1): p. 1986.
308. Glesby, M.J., et al., *Serum CK, calcium, magnesium, and oxidative phosphorylation in mdx mouse muscular dystrophy.* Muscle Nerve, 1988. **11**(8): p. 852-6.
309. Khairallah, M., et al., *Metabolic and signaling alterations in dystrophin-deficient hearts precede overt cardiomyopathy.* Journal of Molecular and Cellular Cardiology, 2007. **43**(2): p. 119-129.
310. Matsumura, C.Y., et al., *Isobaric Tagging-Based Quantification for Proteomic Analysis: A Comparative Study of Spared and Affected Muscles from mdx Mice at the Early Phase of Dystrophy.* PLOS ONE, 2013. **8**(6): p. e65831.
311. Moore, T.M., et al., *Mitochondrial Dysfunction Is an Early Consequence of Partial or Complete Dystrophin Loss in mdx Mice.* Frontiers in Physiology, 2020. **11**.

312. Passaquin, A.C., et al., *Creatine supplementation reduces skeletal muscle degeneration and enhances mitochondrial function in mdx mice.* Neuromuscul Disord, 2002. **12**(2): p. 174-82.
313. Schuh, R.A., et al., *Measuring mitochondrial respiration in intact single muscle fibers.* Am J Physiol Regul Integr Comp Physiol, 2012. **302**(6): p. R712-9.
314. Timpani, C.A., A. Hayes, and E. Rybalka, *Revisiting the dystrophin-ATP connection: How half a century of research still implicates mitochondrial dysfunction in Duchenne Muscular Dystrophy aetiology.* Med Hypotheses, 2015. **85**(6): p. 1021-33.
315. Vila, M.C., et al., *Mitochondria mediate cell membrane repair and contribute to Duchenne muscular dystrophy.* Cell Death & Differentiation, 2017. **24**(2): p. 330-342.
316. Pulido, S.M., et al., *Creatine supplementation improves intracellular Ca2+ handling and survival in mdx skeletal muscle cells.* FEBS Lett, 1998. **439**(3): p. 357-62.
317. Tarnopolsky, M.A. and M.F. Beal, *Potential for creatine and other therapies targeting cellular energy dysfunction in neurological disorders.* Ann Neurol, 2001. **49**(5): p. 561-74.
318. Felber, S., et al., *Oral creatine supplementation in Duchenne muscular dystrophy: a clinical and 31P magnetic resonance spectroscopy study.* Neurol Res, 2000. **22**(2): p. 145-50.
319. Tarnopolsky, M.A., et al., *Creatine monohydrate enhances strength and body composition in Duchenne muscular dystrophy.* Neurology, 2004. **62**(10): p. 1771-7.
320. Tarnopolsky, M.A., B.D. Roy, and J.R. MacDonald, *A randomized, controlled trial of creatine monohydrate in patients with mitochondrial cytopathies.* Muscle Nerve, 1997. **20**(12): p. 1502-9.
321. Braun, U., et al., *Lack of dystrophin is associated with altered integration of the mitochondria and ATPases in slow-twitch muscle cells of MDX mice.* Biochim Biophys Acta, 2001. **1505**(2-3): p. 258-70.
322. Shkryl, V.M., et al., *Reciprocal amplification of ROS and Ca(2+) signals in stressed mdx dystrophic skeletal muscle fibers.* Pflugers Arch, 2009. **458**(5): p. 915-28.
323. Dikalov, S.I. and D.G. Harrison, *Methods for Detection of Mitochondrial and Cellular Reactive Oxygen Species.* Antioxidants & Redox Signaling, 2014. **20**(2): p. 372-382.
324. Sugiyama, Y., et al., *EFFECTS OF IDEBENONE (CV-2619) AND ITS METABOLITES ON RESPIRATORY ACTIVITY AND LIPID PEROXIDATION IN BRAIN MITOCHONDRIA FROM RATS AND DOGS.* Journal of Pharmacobio-Dynamics, 1985. **8**(12): p. 1006-1017.
325. Suno, M. and A. Nagaoka, *Inhibition of lipid peroxidation by a novel compound (CV-2619) in brain mitochondria and mode of action of the inhibition.* Biochem Biophys Res Commun, 1984. **125**(3): p. 1046-52.
326. Cai, J., J. Yang, and D. Jones, *Mitochondrial control of apoptosis: the role of cytochrome c.* Biochimica et Biophysica Acta (BBA) - Bioenergetics, 1998. **1366**(1): p. 139-149.
327. Tantral, L., et al., *Intracellular calcium release is required for caspase-3 and -9 activation.* Cell Biochem Funct, 2004. **22**(1): p. 35-40.
328. Carrer, A., et al., *Defining the molecular mechanisms of the mitochondrial permeability transition through genetic manipulation of F-ATP synthase.* Nat Commun, 2021. **12**(1): p. 4835.
329. Mailloux, R.J., X. Jin, and W.G. Willmore, *Redox regulation of mitochondrial function with emphasis on cysteine oxidation reactions.* Redox Biol, 2014. **2**: p. 123-39.
330. McStay, G.P., S.J. Clarke, and A.P. Halestrap, *Role of critical thiol groups on the matrix surface of the adenine nucleotide translocase in the mechanism of the mitochondrial permeability transition pore.* Biochem J, 2002. **367**(Pt 2): p. 541-8.

331. De Luca, A., et al., *A multidisciplinary evaluation of the effectiveness of cyclosporine a in dystrophic mdx mice.* Am J Pathol, 2005. **166**(2): p. 477-89.
332. Millay, D.P., et al., *Genetic and pharmacologic inhibition of mitochondrial-dependent necrosis attenuates muscular dystrophy.* Nat Med, 2008. **14**(4): p. 442-7.
333. Reutenauer, J., et al., *Investigation of Debio 025, a cyclophilin inhibitor, in the dystrophic mdx mouse, a model for Duchenne muscular dystrophy.* Br J Pharmacol, 2008. **155**(4): p. 574-84.
334. Sharma, K.R., M.A. Mynhier, and R.G. Miller, *Cyclosporine increases muscular force generation in Duhenne muscular dystrophy.* Neurology, 1993. **43**(3 Part 1): p. 527-527.
335. Dubinin, M.V., et al., *The Effect of Deflazacort Treatment on the Functioning of Skeletal Muscle Mitochondria in Duchenne Muscular Dystrophy.* Int J Mol Sci, 2020. **21**(22).
336. Petronilli, V., et al., *The Mitochondrial Permeability Transition, Release of Cytochrome c and Cell Death.* Journal of Biological Chemistry, 2001. **276**(15): p. 12030-12034.
337. Budihardjo, I., et al., *Biochemical pathways of caspase activation during apoptosis.* Annu Rev Cell Dev Biol, 1999. **15**: p. 269-90.
338. Cencetti, F., et al., *TGFβ1 evokes myoblast apoptotic response via a novel signaling pathway involving S1P4 transactivation upstream of Rho-kinase-2 activation.* Faseb j, 2013. **27**(11): p. 4532-46.
339. Li, Y., et al., *Transforming growth factor-β1 induces the differentiation of myogenic cells into fibrotic cells in injured skeletal muscle: a key event in muscle fibrogenesis.* The American journal of pathology, 2004. **164**(3): p. 1007-1019.
340. Zanotti, S., S. Gibertini, and M. Mora, *Altered production of extra-cellular matrix components by muscle-derived Duchenne muscular dystrophy fibroblasts before and after TGF-beta1 treatment.* Cell Tissue Res, 2010. **339**(2): p. 397-410.
341. Zanotti, S., et al., *Fibroblasts from the muscles of Duchenne muscular dystrophy patients are resistant to cell detachment apoptosis.* Exp Cell Res, 2011. **317**(17): p. 2536-47.
342. Lemos, D.R., et al., *Nilotinib reduces muscle fibrosis in chronic muscle injury by promoting TNF-mediated apoptosis of fibro/adipogenic progenitors.* Nat Med, 2015. **21**(7): p. 786-94.
343. Qualls, A.E., W.M. Southern, and J.A. Call, *Mitochondria-cytokine crosstalk following skeletal muscle injury and disuse: a mini-review.* Am J Physiol Cell Physiol, 2021. **320**(5): p. C681-c688.
344. Pelosi, L., et al., *Increased Circulating Levels of Interleukin-6 Induce Perturbation in Redox-Regulated Signaling Cascades in Muscle of Dystrophic Mice.* Oxid Med Cell Longev, 2017. **2017**: p. 1987218.
345. Pelosi, L., et al., *Increased levels of interleukin-6 exacerbate the dystrophic phenotype in mdx mice.* Hum Mol Genet, 2015. **24**(21): p. 6041-53.
346. Pelosi, L., et al., *Functional and Morphological Improvement of Dystrophic Muscle by Interleukin 6 Receptor Blockade.* EBioMedicine, 2015. **2**(4): p. 285-93.
347. Abid, H., et al., *Extramyocellular interleukin-6 influences skeletal muscle mitochondrial physiology through canonical JAK/STAT signaling pathways.* Faseb j, 2020. **34**(11): p. 14458-14472.
348. Li, Y.P., et al., *Mitochondria mediate tumor necrosis factor-alpha/NF-kappaB signaling in skeletal muscle myotubes.* Antioxid Redox Signal, 1999. **1**(1): p. 97-104.
349. Bradham, C.A., et al., *The Mitochondrial Permeability Transition Is Required for Tumor Necrosis Factor Alpha-Mediated Apoptosis and Cytochrome c Release.* Molecular and Cellular Biology, 1998. **18**(11): p. 6353-6364.

350. Messina, S., et al., *Activation of NF-kappaB pathway in Duchenne muscular dystrophy: relation to age.* Acta Myol, 2011. **30**(1): p. 16-23.
351. Porreca, E., et al., *Haemostatic abnormalities, cardiac involvement and serum tumor necrosis factor levels in X-linked dystrophic patients.* Thromb Haemost, 1999. **81**(4): p. 543-6.
352. Tews, D.S. and H.H. Goebel, *Cytokine expression profile in idiopathic inflammatory myopathies.* J Neuropathol Exp Neurol, 1996. **55**(3): p. 342-7.
353. Deval, E., et al., *Na(+)/Ca(2+) exchange in human myotubes: intracellular calcium rises in response to external sodium depletion are enhanced in DMD.* Neuromuscul Disord, 2002. **12**(7-8): p. 665-73.
354. Hantaï, D., et al., *Fibronectin, Laminin, Type I, III and IV Collagens in Duchenne's Muscular Dystrophy, Congenital Muscular Dystrophies and Congenital Myopathies: An Immunocytochemical Study.* Connective Tissue Research, 1985. **13**(4): p. 273-281.
355. Rooney, J.E., et al., *Severe muscular dystrophy in mice that lack dystrophin and α7 integrin.* Journal of Cell Science, 2006. **119**(11): p. 2185-2195.
356. Cotton, S., N.J. Voudouris, and K.M. Greenwood, *Intelligence and Duchenne muscular dystrophy: full-scale, verbal, and performance intelligence quotients.* Dev Med Child Neurol, 2001. **43**(7): p. 497-501.
357. Pane, M., et al., *Attention deficit hyperactivity disorder and cognitive function in Duchenne muscular dystrophy: phenotype-genotype correlation.* J Pediatr, 2012. **161**(4): p. 705-9.e1.
358. Anderson, J.L., et al., *Brain function in Duchenne muscular dystrophy.* Brain, 2002. **125**(Pt 1): p. 4-13.
359. Ricotti, V., et al., *Neurodevelopmental, emotional, and behavioural problems in Duchenne muscular dystrophy in relation to underlying dystrophin gene mutations.* Dev Med Child Neurol, 2016. **58**(1): p. 77-84.
360. Pane, M., et al., *Early neurodevelopmental assessment in Duchenne muscular dystrophy.* Neuromuscul Disord, 2013. **23**(6): p. 451-5.
361. Braat, E., et al., *Renal function in children and adolescents with Duchenne muscular dystrophy.* Neuromuscul Disord, 2015. **25**(5): p. 381-7.
362. Tay, S.K., H.T. Ong, and P.S. Low, *Transaminitis in Duchenne's muscular dystrophy.* Ann Acad Med Singap, 2000. **29**(6): p. 719-22.
363. Bagdatlioglu, E., et al., *Cognitive impairment appears progressive in the mdx mouse.* Neuromuscul Disord, 2020. **30**(5): p. 368-388.
364. Hendriksen, J.G., et al., *Psychosocial adjustment in males with Duchenne muscular dystrophy: psychometric properties and clinical utility of a parent-report questionnaire.* J Pediatr Psychol, 2009. **34**(1): p. 69-78.
365. Muntoni, F., A. Mateddu, and G. Serra, *Passive avoidance behaviour deficit in the mdx mouse.* Neuromuscul Disord, 1991. **1**(2): p. 121-3.
366. Snow, W.M., J.E. Anderson, and L.S. Jakobson, *Neuropsychological and neurobehavioral functioning in Duchenne muscular dystrophy: A review.* Neuroscience & Biobehavioral Reviews, 2013. **37**(5): p. 743-752.
367. Vaillend, C., J.M. Billard, and S. Laroche, *Impaired long-term spatial and recognition memory and enhanced CA1 hippocampal LTP in the dystrophin-deficient Dmd(mdx) mouse.* Neurobiol Dis, 2004. **17**(1): p. 10-20.
368. Vaillend, C., et al., *Influence of dystrophin-gene mutation on mdx mouse behavior. I. Retention deficits at long delays in spontaneous alternation and bar-pressing tasks.* Behav Genet, 1995. **25**(6): p. 569-79.

369. Doorenweerd, N., et al., *Timing and localization of human dystrophin isoform expression provide insights into the cognitive phenotype of Duchenne muscular dystrophy.* Sci Rep, 2017. **7**(1): p. 12575.
370. Blake, D.J., et al., *Different dystrophin-like complexes are expressed in neurons and glia.* J Cell Biol, 1999. **147**(3): p. 645-58.
371. Brünig, I., et al., *GABAergic terminals are required for postsynaptic clustering of dystrophin but not of GABA(A) receptors and gephyrin.* J Neurosci, 2002. **22**(12): p. 4805-13.
372. Hendriksen, R.G., et al., *Dystrophin Distribution and Expression in Human and Experimental Temporal Lobe Epilepsy.* Front Cell Neurosci, 2016. **10**: p. 174.
373. Cotton, S.M., N.J. Voudouris, and K.M. Greenwood, *Association between intellectual functioning and age in children and young adults with Duchenne muscular dystrophy: further results from a meta-analysis.* Dev Med Child Neurol, 2005. **47**(4): p. 257-65.
374. Wingeier, K., et al., *Neuropsychological impairments and the impact of dystrophin mutations on general cognitive functioning of patients with Duchenne muscular dystrophy.* J Clin Neurosci, 2011. **18**(1): p. 90-5.
375. Steele, M., et al., *Mental health of children and adolescents with Duchenne muscular dystrophy.* Dev Med Child Neurol, 2008. **50**(8): p. 638-9.
376. Billard, C., et al., *Cognitive functions in Duchenne muscular dystrophy: a reappraisal and comparison with spinal muscular atrophy.* Neuromuscul Disord, 1992. **2**(5-6): p. 371-8.
377. Snow, W.M., M. Fry, and J.E. Anderson, *Increased density of dystrophin protein in the lateral versus the vermal mouse cerebellum.* Cell Mol Neurobiol, 2013. **33**(4): p. 513-20.
378. Hinton, V.J., et al., *Selective deficits in verbal working memory associated with a known genetic etiology: The neuropsychological profile of Duchenne muscular dystrophy.* Journal of the International Neuropsychological Society, 2001. **7**(1): p. 45-54.
379. Sesay, A.K., et al., *Spatial learning and hippocampal long-term potentiation are not impaired in mdx mice.* Neurosci Lett, 1996. **211**(3): p. 207-10.
380. Vaillend, C., et al., *Spatial discrimination learning and CA1 hippocampal synaptic plasticity in mdx and mdx3cv mice lacking dystrophin gene products.* Neuroscience, 1998. **86**(1): p. 53-66.
381. Hayward, G.C., et al., *Characterization of Alzheimer's disease-like neuropathology in Duchenne's muscular dystrophy using the DBA/2J mdx mouse model.* FEBS Open Bio, 2022. **12**(1): p. 154-162.
382. Tracey, I., et al., *Brain abnormalities in Duchenne muscular dystrophy: phosphorus-31 magnetic resonance spectroscopy and neuropsychological study.* Lancet, 1995. **345**(8960): p. 1260-4.
383. Tracey, I., J.F. Dunn, and G.K. Radda, *Brain metabolism is abnormal in the mdx model of Duchenne muscular dystrophy.* Brain, 1996. **119 (Pt 3)**: p. 1039-44.
384. Xu, S., et al., *Abnormalities in brain structure and biochemistry associated with mdx mice measured by in vivo MRI and high resolution localized (1)H MRS.* Neuromuscul Disord, 2015. **25**(10): p. 764-72.
385. Kreis, R., et al., *Brain metabolite composition in relation to cognitive function and dystrophin mutations in boys with Duchenne muscular dystrophy.* NMR Biomed, 2011. **24**(3): p. 253-62.
386. Tuon, L., et al., *Mitochondrial respiratory chain and creatine kinase activities in mdx mouse brain.* Muscle & Nerve, 2010. **41**(2): p. 257-260.

387. Comim, C.M., et al., *Oxidative variables and antioxidant enzymes activities in the mdx mouse brain.* Neurochemistry International, 2009. **55**(8): p. 802-805.
388. Copeland, E.N., *Characterization of SERCA function in the hippocampal and prefrontal cortex regions of the brain from C57 and D2 mx mice*. Brock University.
389. Tupling, A.R., et al., *HSP70 binds to the fast-twitch skeletal muscle sarco(endo)plasmic reticulum Ca2+ -ATPase (SERCA1a) and prevents thermal inactivation.* J Biol Chem, 2004. **279**(50): p. 52382-9.
390. Gu, Y., et al., *Hsp70 inducer, 17-allylamino-demethoxygeldanamycin, provides neuroprotection via anti-inflammatory effects in a rat model of traumatic brain injury.* Exp Ther Med, 2016. **12**(6): p. 3767-3772.
391. Woodward Hopf, F. and R.A. Steinhardt, *Regulation of intracellular free calcium in normal and dystrophic mouse cerebellar neurons.* Brain Research, 1992. **578**(1): p. 49-54.
392. Drachman, D.B., K.V. Toyka, and E. Myer, *Prednisone in Duchenne muscular dystrophy.* Lancet, 1974. **2**(7894): p. 1409-12.
393. Griggs, R.C., et al., *Prednisone in Duchenne dystrophy. A randomized, controlled trial defining the time course and dose response. Clinical Investigation of Duchenne Dystrophy Group.* Arch Neurol, 1991. **48**(4): p. 383-8.
394. Mendell, J.R., et al., *Randomized, double-blind six-month trial of prednisone in Duchenne's muscular dystrophy.* N Engl J Med, 1989. **320**(24): p. 1592-7.
395. McDonald, C.M., et al., *Long-term effects of glucocorticoids on function, quality of life, and survival in patients with Duchenne muscular dystrophy: a prospective cohort study.* Lancet, 2018. **391**(10119): p. 451-461.
396. Shieh, P.B., et al., *Meta-analyses of deflazacort versus prednisone/prednisolone in patients with nonsense mutation Duchenne muscular dystrophy.* J Comp Eff Res, 2021. **10**(18): p. 1337-1347.
397. Griggs, R.C., et al., *Efficacy and safety of deflazacort vs prednisone and placebo for Duchenne muscular dystrophy.* Neurology, 2016. **87**(20): p. 2123-2131.
398. Reitter, B., *Deflazacort vs. prednisone in Duchenne muscular dystrophy: trends of an ongoing study.* Brain Dev, 1995. **17 Suppl**: p. 39-43.
399. Zhang, T. and X. Kong, *Recent advances of glucocorticoids in the treatment of Duchenne muscular dystrophy (Review).* Exp Ther Med, 2021. **21**(5): p. 447.
400. Hanaoka, B.Y., et al., *Implications of glucocorticoid therapy in idiopathic inflammatory myopathies.* Nat Rev Rheumatol, 2012. **8**(8): p. 448-57.
401. Schakman, O., et al., *Mechanisms of muscle atrophy induced by glucocorticoids.* Horm Res, 2009. **72 Suppl 1**: p. 36-41.
402. Quattrocelli, M., et al., *Intermittent glucocorticoid steroid dosing enhances muscle repair without eliciting muscle atrophy.* J Clin Invest, 2017. **127**(6): p. 2418-2432.
403. Hammers, D.W., et al., *Glucocorticoids counteract hypertrophic effects of myostatin inhibition in dystrophic muscle.* JCI Insight, 2020. **5**(1).
404. Bushby, K., et al., *Diagnosis and management of Duchenne muscular dystrophy, part 2: implementation of multidisciplinary care.* The Lancet Neurology, 2010. **9**(2): p. 177-189.
405. Jansen, M., et al., *Assisted Bicycle Training Delays Functional Deterioration in Boys With Duchenne Muscular Dystrophy.* Neurorehabilitation and Neural Repair, 2013. **27**(9): p. 816-827.
406. Voet, N.B., et al., *Strength training and aerobic exercise training for muscle disease.* Cochrane Database Syst Rev, 2013(7): p. Cd003907.

407. van Deutekom, J.C., et al., *Antisense-induced exon skipping restores dystrophin expression in DMD patient derived muscle cells.* Hum Mol Genet, 2001. **10**(15): p. 1547-54.
408. Wilton, S.D., et al., *Antisense oligonucleotide-induced exon skipping across the human dystrophin gene transcript.* Mol Ther, 2007. **15**(7): p. 1288-96.
409. Cirak, S., et al., *Exon skipping and dystrophin restoration in patients with Duchenne muscular dystrophy after systemic phosphorodiamidate morpholino oligomer treatment: an open-label, phase 2, dose-escalation study.* Lancet, 2011. **378**(9791): p. 595-605.
410. Koo, T. and M.J. Wood, *Clinical trials using antisense oligonucleotides in duchenne muscular dystrophy.* Hum Gene Ther, 2013. **24**(5): p. 479-88.
411. Verhaart, I.E.C. and A. Aartsma-Rus, *Therapeutic developments for Duchenne muscular dystrophy.* Nat Rev Neurol, 2019. **15**(7): p. 373-386.
412. Helderman-van den Enden, A.T., et al., *Becker muscular dystrophy patients with deletions around exon 51; a promising outlook for exon skipping therapy in Duchenne patients.* Neuromuscul Disord, 2010. **20**(4): p. 251-4.
413. van Deutekom, J.C., et al., *Local dystrophin restoration with antisense oligonucleotide PRO051.* N Engl J Med, 2007. **357**(26): p. 2677-86.
414. Lim, K.R., R. Maruyama, and T. Yokota, *Eteplirsen in the treatment of Duchenne muscular dystrophy.* Drug Des Devel Ther, 2017. **11**: p. 533-545.
415. Sheikh, O. and T. Yokota, *Restoring Protein Expression in Neuromuscular Conditions: A Review Assessing the Current State of Exon Skipping/Inclusion and Gene Therapies for Duchenne Muscular Dystrophy and Spinal Muscular Atrophy.* BioDrugs, 2021. **35**(4): p. 389-399.
416. Mendell, J.R., et al., *Eteplirsen for the treatment of Duchenne muscular dystrophy.* Annals of Neurology, 2013. **74**(5): p. 637-647.
417. Mendell, J.R., et al., *Longitudinal effect of eteplirsen versus historical control on ambulation in Duchenne muscular dystrophy.* Ann Neurol, 2016. **79**(2): p. 257-71.
418. Erkut, E. and T. Yokota, *CRISPR Therapeutics for Duchenne Muscular Dystrophy.* Int J Mol Sci, 2022. **23**(3).
419. Kupatt, C., et al., *Genome editing for Duchenne muscular dystrophy: a glimpse of the future?* Gene Therapy, 2021. **28**(9): p. 542-548.
420. Olson, E.N., *Toward the correction of muscular dystrophy by gene editing.* Proceedings of the National Academy of Sciences, 2021. **118**(22): p. e2004840117.
421. Boutin, S., et al., *Prevalence of serum IgG and neutralizing factors against adeno-associated virus (AAV) types 1, 2, 5, 6, 8, and 9 in the healthy population: implications for gene therapy using AAV vectors.* Hum Gene Ther, 2010. **21**(6): p. 704-12.
422. Buyse, G.M., et al., *Long-term blinded placebo-controlled study of SNT-MC17/idebenone in the dystrophin deficient mdx mouse: cardiac protection and improved exercise performance.* Eur Heart J, 2009. **30**(1): p. 116-24.
423. Buyse, G.M., et al., *Idebenone as a novel, therapeutic approach for Duchenne muscular dystrophy: results from a 12 month, double-blind, randomized placebo-controlled trial.* Neuromuscul Disord, 2011. **21**(6): p. 396-405.
424. Buyse, G.M., et al., *Efficacy of idebenone on respiratory function in patients with Duchenne muscular dystrophy not using glucocorticoids (DELOS): a double-blind randomised placebo-controlled phase 3 trial.* The Lancet, 2015. **385**(9979): p. 1748-1757.
425. Buyse, G.M., et al., *Effects of glucocorticoids and idebenone on respiratory function in patients with duchenne muscular dystrophy.* Pediatr Pulmonol, 2013. **48**(9): p. 912-20.

426. Buyse, G.M., et al., *Treatment effect of idebenone on inspiratory function in patients with Duchenne muscular dystrophy.* Pediatr Pulmonol, 2017. **52**(4): p. 508-515.
427. Sharma, K.R., M.A. Mynhier, and R.G. Miller, *Cyclosporine increases muscular force generation in Duchenne muscular dystrophy.* Neurology, 1993. **43**(3 Pt 1): p. 527-32.
428. Bordet, T., et al., *Olesoxime (TRO19622): A Novel Mitochondrial-Targeted Neuroprotective Compound.* Pharmaceuticals (Basel), 2010. **3**(2): p. 345-368.
429. Bordet, T., et al., *Identification and characterization of cholest-4-en-3-one, oxime (TRO19622), a novel drug candidate for amyotrophic lateral sclerosis.* Journal of Pharmacology and Experimental Therapeutics, 2007. **322**(2): p. 709-720.
430. Clemens, L.E., et al., *Olesoxime suppresses calpain activation and mutant huntingtin fragmentation in the BACHD rat.* Brain, 2015. **138**(Pt 12): p. 3632-53.
431. Gouarné, C., et al., *Olesoxime protects embryonic cortical neurons from camptothecin intoxication by a mechanism distinct from BDNF*. Br J Pharmacol, 2013. **168**(8): p. 1975-88.
432. Eckert, G.P., et al., *Olesoxime improves cerebral mitochondrial dysfunction and enhances Aβ levels in preclinical models of Alzheimer's disease.* Experimental Neurology, 2020. **329**: p. 113286.
433. Abitbol, J., et al. *Safety and pharmacokinetics of repeated doses of TRO19622, a drug candidate for the treatment of amyotrophic lateral sclerosis and spinal muscular atrophy*. in *MND International Symposium, Yokohama, Japan*. 2006.
434. Abitbol, J., et al. *TRO19622 is well tolerated and achieves target plasma concentrations in a Phase Ib study in ALS patients*. in *SOC NEUROSCI ANN MEET*. 2007.
435. Martin, L.J., *Olesoxime, a cholesterol-like neuroprotectant for the potential treatment of amyotrophic lateral sclerosis.* IDrugs, 2010. **13**(8): p. 568-80.
436. Krause, M.P., K.J. Milne, and T.J. Hawke, *Adiponectin-Consideration for its Role in Skeletal Muscle Health.* Int J Mol Sci, 2019. **20**(7).
437. Schraw, T., et al., *Plasma adiponectin complexes have distinct biochemical characteristics.* Endocrinology, 2008. **149**(5): p. 2270-2282.
438. Fruebis, J., et al., *Proteolytic cleavage product of 30-kDa adipocyte complement-related protein increases fatty acid oxidation in muscle and causes weight loss in mice.* Proceedings of the National Academy of Sciences, 2001. **98**(4): p. 2005-2010.
439. Fiaschi, T., et al., *Globular adiponectin activates motility and regenerative traits of muscle satellite cells.* PloS one, 2012. **7**(5): p. e34782.
440. Wang, Y., et al., *Post-translational modifications of adiponectin: mechanisms and functional implications.* Biochemical Journal, 2008. **409**(3): p. 623-633.
441. Richards, A.A., et al., *Adiponectin multimerization is dependent on conserved lysines in the collagenous domain: evidence for regulation of multimerization by alterations in posttranslational modifications.* Molecular endocrinology, 2006. **20**(7): p. 1673-1687.
442. Peake, P.W., et al., *The metabolism of isoforms of human adiponectin: studies in human subjects and in experimental animals.* European Journal of Endocrinology, 2005. **153**(3): p. 409-417.
443. Yamauchi, T., et al., *Adiponectin stimulates glucose utilization and fatty-acid oxidation by activating AMP-activated protein kinase.* Nature Medicine, 2002. **8**(11): p. 1288-1295.
444. Tomas, E., et al., *Enhanced muscle fat oxidation and glucose transport by ACRP30 globular domain: Acetyl–CoA carboxylase inhibition and AMP-activated protein kinase activation.* Proceedings of the National Academy of Sciences, 2002. **99**(25): p. 16309-16313.

445. Iwabu, M., et al., *Adiponectin and AdipoR1 regulate PGC-1alpha and mitochondria by Ca(2+) and AMPK/SIRT1.* Nature, 2010. **464**(7293): p. 1313-9.
446. Yan, W., et al., *Adiponectin regulates SR Ca2+ cycling following ischemia/reperfusion via sphingosine 1-phosphate-CaMKII signaling in mice.* Journal of molecular and cellular cardiology, 2014. **74**: p. 183-192.
447. Inoue, A., et al., *Exercise restores muscle stem cell mobilization, regenerative capacity and muscle metabolic alterations via adiponectin/AdipoR1 activation in SAMP10 mice.* Journal of cachexia, sarcopenia and muscle, 2017. **8**(3): p. 370-385.
448. Tanaka, Y., et al., *Adiponectin promotes muscle regeneration through binding to T-cadherin.* Scientific Reports, 2019. **9**(1): p. 16.
449. Fiaschi, T., et al., *Globular adiponectin induces differentiation and fusion of skeletal muscle cells.* Cell Res, 2009. **19**(5): p. 584-97.
450. Ito, R., et al., *Activation of adiponectin receptors has negative impact on muscle mass in C2C12 myotubes and fast-type mouse skeletal muscle.* PLoS One, 2018. **13**(10): p. e0205645.
451. Shibata, R., et al., *Adiponectin protects against myocardial ischemia-reperfusion injury through AMPK- and COX-2-dependent mechanisms.* Nat Med, 2005. **11**(10): p. 1096-103.
452. Chandrasekar, B., et al., *Adiponectin blocks interleukin-18-mediated endothelial cell death via APPL1-dependent AMP-activated protein kinase (AMPK) activation and IKK/NF-kappaB/PTEN suppression.* J Biol Chem, 2008. **283**(36): p. 24889-98.
453. Ziccardi, P., et al., *Reduction of inflammatory cytokine concentrations and improvement of endothelial functions in obese women after weight loss over one year.* Circulation, 2002. **105**(7): p. 804-9.
454. Luo, Y. and M. Liu, *Adiponectin: a versatile player of innate immunity.* J Mol Cell Biol, 2016. **8**(2): p. 120-8.
455. Wolf, A.M., et al., *Adiponectin induces the anti-inflammatory cytokines IL-10 and IL-1RA in human leukocytes.* Biochem Biophys Res Commun, 2004. **323**(2): p. 630-5.
456. Abou-Samra, M., et al., *Potential Therapeutic Action of Adiponectin in Duchenne Muscular Dystrophy.* Am J Pathol, 2017. **187**(7): p. 1577-1585.
457. Abou-Samra, M., et al., *Involvement of adiponectin in the pathogenesis of dystrophinopathy.* Skeletal Muscle, 2015. **5**(1): p. 25.
458. Otvos, L., Jr., et al., *Design and development of a peptide-based adiponectin receptor agonist for cancer treatment.* BMC Biotechnol, 2011. **11**: p. 90.
459. Achari, A.E. and S.K. Jain, *Adiponectin, a Therapeutic Target for Obesity, Diabetes, and Endothelial Dysfunction.* Int J Mol Sci, 2017. **18**(6).
460. Richter, E.A. and N.B. Ruderman, *AMPK and the biochemistry of exercise: implications for human health and disease.* Biochem J, 2009. **418**(2): p. 261-75.
461. Wu, Z., et al., *Mechanisms controlling mitochondrial biogenesis and respiration through the thermogenic coactivator PGC-1.* Cell, 1999. **98**(1): p. 115-24.
462. Okada-Iwabu, M., et al., *A small-molecule AdipoR agonist for type 2 diabetes and short life in obesity.* Nature, 2013. **503**(7477): p. 493-9.
463. Balasubramanian, P., et al., *Adiponectin receptor agonist AdipoRon improves skeletal muscle function in aged mice.* eLife, 2022. **11**: p. e71282.
464. Abou samra, M., et al., *AdipoRon, a new therapeutic prospect for Duchenne muscular dystrophy.* Journal of Cachexia, Sarcopenia and Muscle, 2020. **11**.
465. Otvos, L., Jr., et al., *Development of second generation peptides modulating cellular adiponectin receptor responses.* Front Chem, 2014. **2**: p. 93.

466. Kumar, P., et al., *Adiponectin agonist ADP355 attenuates CCl4-induced liver fibrosis in mice.* PLoS One, 2014. **9**(10): p. e110405.
467. Wang, H., et al., *Adiponectin-derived active peptide ADP355 exerts anti-inflammatory and anti-fibrotic activities in thioacetamide-induced liver injury.* Sci Rep, 2016. **6**: p. 19445.
468. Li, J., et al., *Stat3 Signaling Pathway: A Future Therapeutic Target for Bone-Related Diseases.* Front Pharmacol, 2022. **13**: p. 897539.
469. Pepping, J.K., et al., *Designer adiponectin receptor agonist stabilizes metabolic function and prevents brain injury caused by HIV protease inhibitors.* J Neuroimmune Pharmacol, 2014. **9**(3): p. 388-98.
470. Rasola, A. and P. Bernardi, *Mitochondrial permeability transition in Ca(2+)-dependent apoptosis and necrosis.* Cell Calcium, 2011. **50**(3): p. 222-33.
471. Rasola, A. and P. Bernardi, *The mitochondrial permeability transition pore and its involvement in cell death and in disease pathogenesis.* Apoptosis, 2007. **12**(5): p. 815-33.
472. Beutner, G., et al., *Complexes between hexokinase, mitochondrial porin and adenylate translocator in brain: regulation of hexokinase, oxidative phosphorylation and permeability transition pore.* Biochem Soc Trans, 1997. **25**(1): p. 151-7.
473. Sokolova, N., et al., *ADP protects cardiac mitochondria under severe oxidative stress.* PLoS One, 2013. **8**(12): p. e83214.
474. Gizatullina, Z.Z., et al., *Effects of extramitochondrial ADP on permeability transition of mouse liver mitochondria.* Biochim Biophys Acta, 2005. **1706**(1-2): p. 98-104.
475. Datler, C., et al., *CKMT1 regulates the mitochondrial permeability transition pore in a process that provides evidence for alternative forms of the complex.* J Cell Sci, 2014. **127**(Pt 8): p. 1816-28.
476. Perry, Christopher G.R., et al., *Inhibiting myosin-ATPase reveals a dynamic range of mitochondrial respiratory control in skeletal muscle.* Biochemical Journal, 2011. **437**(2): p. 215-222.
477. Fisher-Wellman, K.H., et al., *Novel role for thioredoxin reductase-2 in mitochondrial redox adaptations to obesogenic diet and exercise in heart and skeletal muscle.* The Journal of Physiology, 2013. **591**(14): p. 3471-3486.
478. Tsien, R.Y., *Fluorescent Probes of Cell Signaling.* Annual Review of Neuroscience, 1989. **12**(1): p. 227-253.
479. Bessman, S.P. and A. Fonyo, *The possible role of the mitochondrial bound creatine kinase in regulation of mitochondrial respiration.* Biochem Biophys Res Commun, 1966. **22**(5): p. 597-602.
480. Monge, C., et al., *Regulation of respiration in brain mitochondria and synaptosomes: restrictions of ADP diffusion in situ, roles of tubulin, and mitochondrial creatine kinase.* Molecular and Cellular Biochemistry, 2008. **318**(1): p. 147.
481. Goldberg, E.J., et al., *Tissue-specific characterization of mitochondrial branched-chain keto acid oxidation using a multiplexed assay platform.* Biochem J, 2019. **476**(10): p. 1521-1537.
482. Emery, A., *Genetic heterogeneity in Duchenne muscular dystrophy.* Am J Med Genet, 1987. **26**(1): p. 235-6.
483. Petrof, B.J., *The molecular basis of activity-induced muscle injury in Duchenne muscular dystrophy.* Molecular and Cellular Biochemistry, 1998. **179**(1): p. 111-124.
484. Bertini, E., et al., *Safety and efficacy of olesoxime in patients with type 2 or non-ambulatory type 3 spinal muscular atrophy: a randomised, double-blind, placebo-controlled phase 2 trial.* Lancet Neurol, 2017. **16**(7): p. 513-522.

485. Jethwa, S., *Roche Releases Community Statement on Olesoxime Program*. 2018: Cure SMA.
486. Muntoni, F., et al., *Long-term follow-up of patients with type 2 and non-ambulant type 3 spinal muscular atrophy (SMA) treated with olesoxime in the OLEOS trial.* Neuromuscul Disord, 2020. **30**(12): p. 959-969.
487. Holmes, D.J., *DBA/2 Mouse.* Science of Aging Knowledge Environment, 2003. **2003**(44): p. as3-as3.
488. Xiao, W.H., et al., *Olesoxime (cholest-4-en-3-one, oxime): analgesic and neuroprotective effects in a rat model of painful peripheral neuropathy produced by the chemotherapeutic agent, paclitaxel.* Pain, 2009. **147**(1-3): p. 202-9.
489. Butchbach, M.E., et al., *A novel method for oral delivery of drug compounds to the neonatal SMNDelta7 mouse model of spinal muscular atrophy.* J Neurosci Methods, 2007. **161**(2): p. 285-90.
490. Gibbs, E.M., Crosbie-Watson, and R. H., *A Simple and Low-cost Assay for Measuring Ambulation in Mouse Models of Muscular Dystrophy.* JoVE, 2017(130): p. e56772.
491. Fajardo, V.A., et al., *Diaphragm assessment in mice overexpressing phospholamban in slow-twitch type I muscle fibers.* Brain and behavior, 2016. **6**(6): p. e00470-e00470.
492. Gregorevic, P., D.R. Plant, and G.S. Lynch, *Administration of insulin-like growth factor-I improves fatigue resistance of skeletal muscles from dystrophic mdx mice.* Muscle Nerve, 2004. **30**(3): p. 295-304.
493. Moorwood, C., et al., *Isometric and Eccentric Force Generation Assessment of Skeletal Muscles Isolated from Murine Models of Muscular Dystrophies.* JoVE, 2013(71): p. e50036.
494. Méndez, J. and A.B. Keys, *Density and composition of mammalian muscle.* Metabolism-clinical and Experimental, 1960. **9**: p. 184-188.
495. Perry, C.G., et al., *Inhibiting myosin-ATPase reveals a dynamic range of mitochondrial respiratory control in skeletal muscle.* Biochem J, 2011. **437**(2): p. 215-22.
496. Fisher-Wellman, K.H., et al., *Mitochondrial glutathione depletion reveals a novel role for the pyruvate dehydrogenase complex as a key H2O2-emitting source under conditions of nutrient overload.* Free Radic Biol Med, 2013. **65**: p. 1201-1208.
497. Walsh, B., et al., *The role of phosphorylcreatine and creatine in the regulation of mitochondrial respiration in human skeletal muscle.* J Physiol, 2001. **537**(Pt 3): p. 971-8.
498. Perry, C.G., et al., *Methods for assessing mitochondrial function in diabetes.* Diabetes, 2013. **62**(4): p. 1041-53.
499. Ydfors, M., et al., *Modelling in vivo creatine/phosphocreatine in vitro reveals divergent adaptations in human muscle mitochondrial respiratory control by ADP after acute and chronic exercise.* J Physiol, 2016. **594**(11): p. 3127-40.
500. Bloemberg, D. and J. Quadrilatero, *Rapid Determination of Myosin Heavy Chain Expression in Rat, Mouse, and Human Skeletal Muscle Using Multicolor Immunofluorescence Analysis.* PLOS ONE, 2012. **7**(4): p. e35273.
501. Dam, A.D., et al., *Elevated skeletal muscle apoptotic signaling following glutathione depletion.* Apoptosis, 2012. **17**(1): p. 48-60.
502. McMillan, E.M. and J. Quadrilatero, *Differential apoptosis-related protein expression, mitochondrial properties, proteolytic enzyme activity, and DNA fragmentation between skeletal muscles.* American Journal of Physiology-Regulatory, Integrative and Comparative Physiology, 2011. **300**(3): p. R531-R543.

503. Mandel, E.R., et al., *The superoxide dismutase mimetic tempol does not alleviate glucocorticoid-mediated rarefaction of rat skeletal muscle capillaries.* Physiol Rep, 2017. **5**(10): p. e13243.
504. Schlattner, U., et al., *Creatine kinase and creatine transporter in normal, wounded, and diseased skin.* J Invest Dermatol, 2002. **118**(3): p. 416-23.
505. Sloan, R.C., et al., *Mitochondrial permeability transition in the diabetic heart: contributions of thiol redox state and mitochondrial calcium to augmented reperfusion injury.* J Mol Cell Cardiol, 2012. **52**(5): p. 1009-18.
506. Frasier, C.R., et al., *Redox-dependent increases in glutathione reductase and exercise preconditioning: role of NADPH oxidase and mitochondria.* Cardiovasc Res, 2013. **98**(1): p. 47-55.
507. Noble, A., M. Guille, and J.N. Cobley, *ALISA: A microplate assay to measure protein thiol redox state.* Free Radical Biology and Medicine, 2021. **174**: p. 272-280.
508. Howell, D., *Fundamental statistics for behavioral sciences*. 8th ed. 2011, Belmont, California: Wadsworth Cengage Learning 677.
509. Meier, U., *A note on the power of Fisher's least significant difference procedure.* Pharm Stat, 2006. **5**(4): p. 253-63.
510. Perry, C.G., et al., *High-intensity aerobic interval training increases fat and carbohydrate metabolic capacities in human skeletal muscle.* Appl Physiol Nutr Metab, 2008. **33**(6): p. 1112-23.
511. Schlattner, U., M. Tokarska-Schlattner, and T. Wallimann, *Mitochondrial creatine kinase in human health and disease.* Biochim Biophys Acta, 2006. **1762**(2): p. 164-80.
512. Schlattner, U., et al., *Mitochondrial kinases and their molecular interaction with cardiolipin.* Biochimica et Biophysica Acta (BBA) - Biomembranes, 2009. **1788**(10): p. 2032-2047.
513. Bernardi, P., M. Carraro, and G. Lippe, *The mitochondrial permeability transition: Recent progress and open questions.* Febs j, 2021.
514. Imawati Budihardjo, et al., *Biochemical Pathways of Caspase Activation During Apoptosis.* Annual Review of Cell and Developmental Biology, 1999. **15**(1): p. 269-290.
515. Bock, F.J. and S.W.G. Tait, *Mitochondria as multifaceted regulators of cell death.* Nature Reviews Molecular Cell Biology, 2020. **21**(2): p. 85-100.
516. Ventura-Clapier, R., et al., *Functional coupling of creatine kinases in muscles: species and tissue specificity.* Mol Cell Biochem, 1998. **184**(1-2): p. 231-47.
517. Perry, C.G., et al., *Mitochondrial creatine kinase activity and phosphate shuttling are acutely regulated by exercise in human skeletal muscle.* J Physiol, 2012. **590**(21): p. 5475-86.
518. Ventura-Clapier, R. and G. Vassort, *Role of myofibrillar creatine kinase in the relaxation of rigor tension in skinned cardiac muscle.* Pflügers Archiv, 1985. **404**(2): p. 157-161.
519. Jones, D.P., *Radical-free biology of oxidative stress.* American Journal of Physiology-Cell Physiology, 2008. **295**(4): p. C849-C868.
520. Sies, H., *Oxidative stress: a concept in redox biology and medicine.* Redox biology, 2015. **4**: p. 180-183.
521. Weber, J.J., et al., *Olesoxime in neurodegenerative diseases: Scrutinising a promising drug candidate.* Biochem Pharmacol, 2019. **168**: p. 305-318.
522. Eckmann, J., et al., *Mitochondrial Membrane Fluidity is Consistently Increased in Different Models of Huntington Disease: Restorative Effects of Olesoxime.* Molecular Neurobiology, 2014. **50**(1): p. 107-118.

523. Weber, J.J., et al., *The calpain-suppressing effects of olesoxime in Huntington's disease.* Rare Dis, 2016. **4**(1): p. e1153778.
524. Ciafaloni, E., et al., *Age at onset of first signs or symptoms predicts age at loss of ambulation in Duchenne and Becker Muscular Dystrophy: Data from the MD STARnet.* J Pediatr Rehabil Med, 2016. **9**(1): p. 5-11.
525. Cohn, R.D. and K.P. Campbell, *Molecular basis of muscular dystrophies.* Muscle Nerve, 2000. **23**(10): p. 1456-71.
526. Bridges, L.R., *The association of cardiac muscle necrosis and inflammation with the degenerative and persistent myopathy of MDX mice.* J Neurol Sci, 1986. **72**(2-3): p. 147-57.
527. Maury, E. and S.M. Brichard, *Adipokine dysregulation, adipose tissue inflammation and metabolic syndrome.* Mol Cell Endocrinol, 2010. **314**(1): p. 1-16.
528. Ouchi, N. and K. Walsh, *Adiponectin as an anti-inflammatory factor.* Clin Chim Acta, 2007. **380**(1-2): p. 24-30.
529. Maeda, N., et al., *Diet-induced insulin resistance in mice lacking adiponectin/ACRP30.* Nat Med, 2002. **8**(7): p. 731-7.
530. Liu, Y. and G. Sweeney, *Adiponectin action in skeletal muscle.* Best Practice & Research Clinical Endocrinology & Metabolism, 2014. **28**(1): p. 33-41.
531. Otvos, L., Jr., *Potential Adiponectin Receptor Response Modifier Therapeutics.* Frontiers in endocrinology, 2019. **10**: p. 539-539.
532. Morrison, J., et al., *T-cell-dependent fibrosis in the mdx dystrophic mouse.* Laboratory investigation, 2000. **80**(6): p. 881-891.
533. Sung, H.K., et al., *ALY688 elicits adiponectin-mimetic signaling and improves insulin action in skeletal muscle cells.* American Journal of Physiology-Cell Physiology, 2022. **322**(2): p. C151-C163.
534. Da Eira, D., et al., *Effects of the adiponectin mimetic compound ALY688 on glucose and fat metabolism in visceral and subcutaneous rat adipocytes.* Adipocyte, 2020. **9**(1): p. 550-562.
535. Boland, B.J., et al., *Skeletal, cardiac, and smooth muscle failure in Duchenne muscular dystrophy.* Pediatric Neurology, 1996. **14**(1): p. 7-12.
536. Aartsma-Rus, A. and M. van Putten, *Assessing functional performance in the mdx mouse model.* J Vis Exp, 2014(85).
537. Pratt, S.J.P. and R.M. Lovering, *A stepwise procedure to test contractility and susceptibility to injury for the rodent quadriceps muscle.* Journal of Biological Methods, 2014. **1**(2): p. e8.
538. Mouisel, E., et al., *Muscle weakness and atrophy are associated with decreased regenerative capacity and changes in mTOR signaling in skeletal muscles of venerable (18-24-month-old) dystrophic mdx mice.* Muscle Nerve, 2010. **41**(6): p. 809-18.
539. Hurd, T.R. and M.P. Murphy, *Biological Systems Relevant for Redox Signaling and Control*, in *Redox Signaling and Regulation in Biology and Medicine*. 2009. p. 13-43.
540. Robb, E.L., et al., *Control of mitochondrial superoxide production by reverse electron transport at complex I.* J Biol Chem, 2018. **293**(25): p. 9869-9879.
541. Bernardi, P. and F. Di Lisa, *The mitochondrial permeability transition pore: molecular nature and role as a target in cardioprotection.* J Mol Cell Cardiol, 2015. **78**: p. 100-6.
542. Rasola, A. and P. Bernardi, *Mitochondrial permeability transition in Ca2+-dependent apoptosis and necrosis.* Cell Calcium, 2011. **50**(3): p. 222-233.

543. Lecompte, S., et al., *Skeletal muscle secretome in Duchenne muscular dystrophy: a pivotal anti-inflammatory role of adiponectin.* Cellular and Molecular Life Sciences, 2017. **74**(13): p. 2487-2501.
544. Sung, H.K., et al., *ALY688 elicits adiponectin-mimetic signaling and improves insulin action in skeletal muscle cells.* Am J Physiol Cell Physiol, 2022. **322**(2): p. C151-c163.
545. Xin, X., et al., *APPL1 mediates adiponectin-stimulated p38 MAPK activation by scaffolding the TAK1-MKK3-p38 MAPK pathway.* Am J Physiol Endocrinol Metab, 2011. **300**(1): p. E103-10.
546. de Alvaro, C., et al., *Tumor Necrosis Factor a; Produces Insulin Resistance in Skeletal Muscle by Activation of Inhibitor kB Kinase in a p38 MAPK-dependent Manner* Journal of Biological Chemistry, 2004. **279**(17): p. 17070-17078.
547. Akimoto, M., et al., *Antidiabetic adiponectin receptor agonist AdipoRon suppresses tumour growth of pancreatic cancer by inducing RIPK1/ERK-dependent necroptosis.* Cell Death Dis, 2018. **9**(8): p. 804.
548. Zhang, M., et al., *Sudden cardiac death of Duchenne muscular dystrophy with NT-proBNP in pericardial fluid as a useful biomarker for diagnosis of the cause of death: a case report.* Forensic Sciences Research, 2020. **5**(2): p. 165-169.
549. Silva, M.C., et al., *Myocardial Fibrosis Progression in Duchenne and Becker Muscular Dystrophy: A Randomized Clinical Trial.* JAMA Cardiology, 2017. **2**(2): p. 190-199.
550. Guiraud, S. and K.E. Davies, *Pharmacological advances for treatment in Duchenne muscular dystrophy.* Current Opinion in Pharmacology, 2017. **34**: p. 36-48.
551. Tandon, A., et al., *Myocardial Fibrosis Burden Predicts Left Ventricular Ejection Fraction and Is Associated With Age and Steroid Treatment Duration in Duchenne Muscular Dystrophy.* Journal of the American Heart Association, 2015. **4**(4): p. e001338.
552. Forcina, L., et al., *Signals from the Niche: Insights into the Role of IGF-1 and IL-6 in Modulating Skeletal Muscle Fibrosis.* Cells, 2019. **8**(3).
553. O'Reilly, S., et al., *Interleukin-6, its role in fibrosing conditions.* Cytokine & Growth Factor Reviews, 2012. **23**(3): p. 99-107.
554. Greenwel, P., et al., *Induction of an acute phase response in rats stimulates the expression of alpha 1(I) procollagen messenger ribonucleic acid in their livers. Possible role of interleukin-6.* Lab Invest, 1995. **72**(1): p. 83-91.
555. Duncan, M.R. and B. Berman, *Stimulation of collagen and glycosaminoglycan production in cultured human adult dermal fibroblasts by recombinant human interleukin 6.* J Invest Dermatol, 1991. **97**(4): p. 686-92.
556. Pantelidis, P., et al., *Analysis of tumor necrosis factor-alpha, lymphotoxin-alpha, tumor necrosis factor receptor II, and interleukin-6 polymorphisms in patients with idiopathic pulmonary fibrosis.* Am J Respir Crit Care Med, 2001. **163**(6): p. 1432-6.
557. Salvator, H., et al., *Contrasting Effects of Adipokines on the Cytokine Production by Primary Human Bronchial Epithelial Cells: Inhibitory Effects of Adiponectin.* Frontiers in Pharmacology, 2020. **11**.
558. Zhao, J., S. Turpin-Nolan, and M.A. Febbraio, *IL-6 family cytokines as potential therapeutic strategies to treat metabolic diseases.* Cytokine, 2021. **144**: p. 155549.
559. Juban, G., et al., *AMPK Activation Regulates LTBP4-Dependent TGF-β1 Secretion by Pro-inflammatory Macrophages and Controls Fibrosis in Duchenne Muscular Dystrophy.* Cell Reports, 2018. **25**(8): p. 2163-2176.e6.

560. Fang, F., et al., *The adipokine adiponectin has potent anti-fibrotic effects mediated via adenosine monophosphate-activated protein kinase: Novel target for fibrosis therapy.* Arthritis research & therapy, 2012. **14**: p. R229.
561. Wan, Y.Y. and R.A. Flavell, *'Yin-Yang' functions of transforming growth factor-beta and T regulatory cells in immune regulation.* Immunol Rev, 2007. **220**: p. 199-213.
562. Sanjabi, S., S.A. Oh, and M.O. Li, *Regulation of the Immune Response by TGF-β: From Conception to Autoimmunity and Infection.* Cold Spring Harb Perspect Biol, 2017. **9**(6).
563. Batlle, E. and J. Massagué, *Transforming Growth Factor-β Signaling in Immunity and Cancer.* Immunity, 2019. **50**(4): p. 924-940.
564. Luo, Y. and M. Liu, *Adiponectin: a versatile player of innate immunity.* Journal of Molecular Cell Biology, 2016. **8**(2): p. 120-128.
565. Fang, F., et al., *The adipokine adiponectin has potent anti-fibrotic effects mediated via adenosine monophosphate-activated protein kinase: novel target for fibrosis therapy.* Arthritis Research & Therapy, 2012. **14**(5): p. R229.
566. Lo Mauro, A. and A. Aliverti, *Physiology of respiratory disturbances in muscular dystrophies.* Breathe (Sheff), 2016. **12**(4): p. 318-327.
567. Medoff, B.D., et al., *Adiponectin deficiency increases allergic airway inflammation and pulmonary vascular remodeling.* Am J Respir Cell Mol Biol, 2009. **41**(4): p. 397-406.
568. von Haehling, S., A.J.S. Coats, and S.D. Anker, *Ethical guidelines for publishing in the Journal of Cachexia, Sarcopenia and Muscle: update 2021.* J Cachexia Sarcopenia Muscle, 2021. **12**(6): p. 2259-2261.
569. Mele, A., et al., *A long-term treatment with taurine prevents cardiac dysfunction in mdx mice.* Translational Research, 2019. **204**: p. 82-99.
570. Livak, K.J. and T.D. Schmittgen, *Analysis of relative gene expression data using real-time quantitative PCR and the 2(-Delta Delta C(T)) Method.* Methods, 2001. **25**(4): p. 402-8.
571. Hughes, M.C., et al., *Mitochondrial Bioenergetics and Fiber Type Assessments in Microbiopsy vs. Bergstrom Percutaneous Sampling of Human Skeletal Muscle.* Front Physiol, 2015. **6**: p. 360.
572. Pesta, D. and E. Gnaiger, *High-Resolution Respirometry: OXPHOS Protocols for Human Cells and Permeabilized Fibers from Small Biopsies of Human Muscle*, in *Mitochondrial Bioenergetics: Methods and Protocols*, C.M. Palmeira and A.J. Moreno, Editors. 2012, Humana Press: Totowa, NJ. p. 25-58.
573. Rae, M.G. and D. O'Malley, *Cognitive dysfunction in Duchenne muscular dystrophy: a possible role for neuromodulatory immune molecules.* J Neurophysiol, 2016. **116**(3): p. 1304-15.
574. Balaban, B., et al., *Corticosteroid treatment and functional improvement in Duchenne muscular dystrophy: long-term effect.* Am J Phys Med Rehabil, 2005. **84**(11): p. 843-50.
575. DeSilva, S., et al., *Prednisone treatment in Duchenne muscular dystrophy. Long-term benefit.* Arch Neurol, 1987. **44**(8): p. 818-22.
576. Marden, J.R., et al., *Real-world outcomes of long-term prednisone and deflazacort use in patients with Duchenne muscular dystrophy: experience at a single, large care center.* J Comp Eff Res, 2020. **9**(3): p. 177-189.
577. Kim, S., et al., *Corticosteroid Treatments in Males With Duchenne Muscular Dystrophy: Treatment Duration and Time to Loss of Ambulation.* J Child Neurol, 2015. **30**(10): p. 1275-80.
578. Brown, E.S., et al., *Effects of chronic prednisone therapy on mood and memory.* J Affect Disord, 2007. **99**(1-3): p. 279-83.

579. Bloemer, J., et al., *Adiponectin Knockout Mice Display Cognitive and Synaptic Deficits.* Front Endocrinol (Lausanne), 2019. **10**: p. 819.
580. Denninger, J.K., B.M. Smith, and E.D. Kirby, *Novel Object Recognition and Object Location Behavioral Testing in Mice on a Budget.* J Vis Exp, 2018(141).
581. Leger, M., et al., *Object recognition test in mice.* Nat Protoc, 2013. **8**(12): p. 2531-7.
582. Herbst, E.A. and G.P. Holloway, *Permeabilization of brain tissue in situ enables multiregion analysis of mitochondrial function in a single mouse brain.* J Physiol, 2015. **593**(4): p. 787-801.
583. Roth, K. and M.W. Weiner, *Determination of cytosolic ADP and AMP concentrations and the free energy of ATP hydrolysis in human muscle and brain tissues with 31P NMR spectroscopy.* Magn Reson Med, 1991. **22**(2): p. 505-11.
584. Gwinn, D.M., et al., *AMPK phosphorylation of raptor mediates a metabolic checkpoint.* Mol Cell, 2008. **30**(2): p. 214-26.
585. Mueller, M.C., B.J. Baranowski, and G.C. Hayward, *New Insights on the Role of Residue 673 of APP in Alzheimer's Disease.* The Journal of Neuroscience, 2018. **38**(3): p. 515-517.
586. Mishra, E. and M.K. Thakur, *Alterations in hippocampal mitochondrial dynamics are associated with neurodegeneration and recognition memory decline in old male mice.* Biogerontology, 2022. **23**(2): p. 251-271.
587. Jacobs, R.A., et al., *Erythropoietin promotes hippocampal mitochondrial function and enhances cognition in mice.* Communications Biology, 2021. **4**(1): p. 938.
588. Domise, M., et al., *AMP-activated protein kinase modulates tau phosphorylation and tau pathology in vivo.* Sci Rep, 2016. **6**: p. 26758.
589. Zhang, S., et al., *Adiponectin/AdiopR1 signaling prevents mitochondrial dysfunction and oxidative injury after traumatic brain injury in a SIRT3 dependent manner.* Redox Biol, 2022. **54**: p. 102390.
590. Pei, J.-J., et al., *P70 S6 kinase mediates tau phosphorylation and synthesis.* FEBS Letters, 2006. **580**(1): p. 107-114.
591. Zhang, D., et al., *Adiponectin Stimulates Proliferation of Adult Hippocampal Neural Stem/Progenitor Cells through Activation of p38 Mitogen-activated Protein Kinase (p38MAPK)/Glycogen Synthase Kinase 3β (GSK-3β)/β-Catenin Signaling Cascade *.* Journal of Biological Chemistry, 2011. **286**(52): p. 44913-44920.
592. Chan, K.-H., et al., *Adiponectin is Protective against Oxidative Stress Induced Cytotoxicity in Amyloid-Beta Neurotoxicity.* PLoS ONE, 2012. **7**(12): p. e52354.
593. He, K., et al., *Adiponectin alleviated Alzheimer-like pathologies via autophagy-lysosomal activation.* Aging Cell, 2021. **20**(12): p. e13514.
594. Tuncay, A., et al., *RedoxiFluor: A microplate technique to quantify target-specific protein thiol redox state in relative percentage and molar terms.* Free Radical Biology and Medicine, 2022. **181**: p. 118-129.
595. Tokarska-Schlattner, M., et al., *Acute toxicity of doxorubicin on isolated perfused heart: response of kinases regulating energy supply.* Am J Physiol Heart Circ Physiol, 2005. **289**(1): p. H37-47.
596. Koufen, P., et al., *Free radical-induced inactivation of creatine kinase: influence on the octameric and dimeric states of the mitochondrial enzyme (Mib-CK).* Biochem J, 1999. **344 Pt 2**(Pt 2): p. 413-7.
597. Schlattner, U., et al., *C-terminal lysines determine phospholipid interaction of sarcomeric mitochondrial creatine kinase.* J Biol Chem, 2004. **279**(23): p. 24334-42.

598. Vacheron, M.J., et al., *Mitochondrial creatine kinase interaction with phospholipid vesicles.* Arch Biochem Biophys, 1997. **344**(2): p. 316-24.
599. Liu, P., et al., *Formation of nitric oxide, superoxide, and peroxynitrite in myocardial ischemia-reperfusion injury in rats.* Am J Physiol, 1997. **272**(5 Pt 2): p. H2327-36.
600. Yuan, G., et al., *Decrease in heart mitochondrial creatine kinase activity due to oxygen free radicals.* Biochim Biophys Acta, 1992. **1140**(1): p. 78-84.
601. Minajeva, A., R. Ventura-Clapier, and V. Veksler, *Ca2+ uptake by cardiac sarcoplasmic reticulum ATPase in situ strongly depends on bound creatine kinase.* Pflugers Arch, 1996. **432**(5): p. 904-12.
602. Steeghs, K., et al., *Altered Ca2+ responses in muscles with combined mitochondrial and cytosolic creatine kinase deficiencies.* Cell, 1997. **89**(1): p. 93-103.
603. de Groof, A.J., et al., *The creatine kinase system is essential for optimal refill of the sarcoplasmic reticulum Ca2+ store in skeletal muscle.* J Biol Chem, 2002. **277**(7): p. 5275-84.
604. Hughes, M.C., et al., *Mitochondrial-Targeted Peptide SBT-20 Improves Mitochondrial Bioenergetics In Duchenne Muscular Dystrophy In a Mitochondrial Creatine Kinase Dependent Manner.* The FASEB Journal, 2017. **31**(S1): p. 696.7-696.7.
605. Jortay, J., et al., *Adiponectin and skeletal muscle: pathophysiological implications in metabolic stress.* Am J Pathol, 2012. **181**(1): p. 245-56.
606. Fang, X. and G. Sweeney, *Mechanisms regulating energy metabolism by adiponectin in obesity and diabetes.* Biochem Soc Trans, 2006. **34**(Pt 5): p. 798-801.
607. Boursereau, R., et al., *Downregulation of the NLRP3 inflammasome by adiponectin rescues Duchenne muscular dystrophy.* BMC Biol, 2018. **16**(1): p. 33.
608. Muller, J., et al., *Comparative evolution of muscular dystrophy in diaphragm, gastrocnemius and masseter muscles from old male mdx mice.* J Muscle Res Cell Motil, 2001. **22**(2): p. 133-9.
609. Dupont-Versteegden, E.E. and R.J. McCarter, *Differential expression of muscular dystrophy in diaphragm versus hindlimb muscles of mdx mice.* Muscle Nerve, 1992. **15**(10): p. 1105-10.
610. Sekiguchi, M., *The role of dystrophin in the central nervous system: a mini review.* Acta Myol, 2005. **24**(2): p. 93-7.
611. Stephenson, K.A., M.G. Rae, and D. O'Malley, *Interleukin-6: A neuro-active cytokine contributing to cognitive impairment in Duchenne muscular dystrophy?* Cytokine, 2020. **133**: p. 155134.
612. He, C., R. Sumpter, Jr., and B. Levine, *Exercise induces autophagy in peripheral tissues and in the brain.* Autophagy, 2012. **8**(10): p. 1548-51.
613. He, Y., et al., *Adiponectin inhibits cardiac arrest/cardiopulmonary resuscitation-induced apoptosis in brain by increasing autophagy involved in AdipoR1-AMPK signaling.* Mol Med Rep, 2020. **22**(2): p. 870-878.
614. Won, J.S., et al., *Involvement of AMP-activated-protein-kinase (AMPK) in neuronal amyloidogenesis.* Biochem Biophys Res Commun, 2010. **399**(4): p. 487-91.
615. Trojanowski, J.Q., et al., *Altered tau and neurofilament proteins in neuro-degenerative diseases: diagnostic implications for Alzheimer's disease and Lewy body dementias.* Brain Pathol, 1993. **3**(1): p. 45-54.
616. Itoh, K., et al., *Multifocal glial nodules in a case of Duchenne muscular dystrophy with severe mental retardation.* Neuropathology, 1999. **19**(3): p. 322-327.

617. Iqbal, K., et al., *Tau in Alzheimer disease and related tauopathies.* Curr Alzheimer Res, 2010. **7**(8): p. 656-64.
618. Xu, Z.P., et al., *Adiponectin Attenuates Streptozotocin-Induced Tau Hyperphosphorylation and Cognitive Deficits by Rescuing PI3K/Akt/GSK-3β Pathway.* Neurochem Res, 2018. **43**(2): p. 316-323.
619. Bellucci, A., et al., *Induction of inflammatory mediators and microglial activation in mice transgenic for mutant human P301S tau protein.* Am J Pathol, 2004. **165**(5): p. 1643-52.
620. Bromley-Brits, K., Y. Deng, and W. Song, *Morris water maze test for learning and memory deficits in Alzheimer's disease model mice.* J Vis Exp, 2011(53).
621. Pons, F., et al., *Does utrophin expression in muscles of mdx mice during postnatal development functionally compensate for dystrophin deficiency?* J Neurol Sci, 1994. **122**(2): p. 162-70.
622. Pastoret, C. and A. Sebille, *mdx mice show progressive weakness and muscle deterioration with age.* J Neurol Sci, 1995. **129**(2): p. 97-105.
623. Ng, R., et al., *Animal models of muscular dystrophy.* Prog Mol Biol Transl Sci, 2012. **105**: p. 83-111.
624. Spencer, M.J., et al., *Helper (CD4(+)) and cytotoxic (CD8(+)) T cells promote the pathology of dystrophin-deficient muscle.* Clin Immunol, 2001. **98**(2): p. 235-43.
625. Kourakis, S., et al., *Targeting Nrf2 for the treatment of Duchenne Muscular Dystrophy.* Redox Biol, 2021. **38**: p. 101803.
626. Capitanio, D., et al., *Comparative proteomic analyses of Duchenne muscular dystrophy and Becker muscular dystrophy muscles: changes contributing to preserve muscle function in Becker muscular dystrophy patients.* J Cachexia Sarcopenia Muscle, 2020. **11**(2): p. 547-563.
627. Carroll, J.E., A. Villadiego, and M.H. Brooke, *Increased long chain acyl CoA in Duchenne muscular dystrophy.* Neurology, 1983. **33**(11): p. 1507-1507.
628. Bell, E.L., et al., *PPARδ modulation rescues mitochondrial fatty acid oxidation defects in the mdx model of muscular dystrophy.* Mitochondrion, 2019. **46**: p. 51-58.
629. Shirokova, N. and E. Niggli, *Cardiac phenotype of Duchenne Muscular Dystrophy: insights from cellular studies.* J Mol Cell Cardiol, 2013. **58**: p. 217-24.
630. Mazur, W., et al., *Patterns of left ventricular remodeling in patients with Duchenne Muscular Dystrophy: a cardiac MRI study of ventricular geometry, global function, and strain.* Int J Cardiovasc Imaging, 2012. **28**(1): p. 99-107.
631. Hor, K.N., et al., *Circumferential strain analysis identifies strata of cardiomyopathy in Duchenne muscular dystrophy: a cardiac magnetic resonance tagging study.* J Am Coll Cardiol, 2009. **53**(14): p. 1204-10.
632. Hagenbuch, S.C., et al., *Detection of progressive cardiac dysfunction by serial evaluation of circumferential strain in patients with Duchenne muscular dystrophy.* Am J Cardiol, 2010. **105**(10): p. 1451-5.
633. Schlattner, U., et al., *Divergent Enzyme Kinetics and Structural Properties of the Two Human Mitochondrial Creatine Kinase Isoenzymes.* 2000. **381**(11): p. 1063-1070.

Appendix

A Force Protocols

A1 In Vitro Diaphragm Force Protocol

In Vitro Diaphragm Force Production Protocol

Updated: June 2020 CAB

***Protocol based on (1)

See attached paper for set-up procedure with videos (2). Practice of the dissection is crucial for this technique as changes in force development could be a result of technical skill of experimenter, before a study make sure you can consistently produce normal forces. When performing dissection, do so under dissection microscope in cold Tyrodes (also called Ringers) buffer on an ice pack, pining muscle when necessary. Use surgeons' knots to tie off central tendon and loop before attaching to force transducer.

Ensure you bath is filled with Tyrodes solution and oxygenated for 30mins with attached 95% O_2/ 5% CO_2 tank, with water circulator turned on and maintained at 25°C prior to start of surgery. This ensures the bath and muscle has enough oxygen since we are relying on diffusion of oxygen into the muscle and not perfusion through blood supply. CO_2 provides necessary buffering of pH during contraction. Limit strip width to 2mm (maximum 4mm) as wider strips have difficulties with diffusion limitations of O_2. 25°C is used over 37°C as oxygen has poor solubility at higher temperatures.

If you were previously doing in-vivo force

In vitro force is measured in force production (mN) not moment of Force (mN-m)—this is TORQUE
To change units: setup→ Channel set up→ force in device→ select mN
repeat with length (should appear in mm)
setup→ Channel set up →length in → select mm

Have Bath temperature to 25°C- this is to ensure oxygen stays dissolved in the bath

Protocol:

1. Create folder to save files for each animal→ File→ set up autosave folder→ open folder created→click "current folder"
2. Set up Instant Stim→ this will be used for length optimization and stim optimization
    a. Pulse Frequency : 1Hz (this is a single twitch; can increase if you want to provide tetanus stimulus)
    b. Pulse width: 0.2ms (how long the stimulus is given)
    c. Number of pulses: 3 (again giving single twitch)
    d. Train Frequency: 0.1Hz (If you are using multiple twitches this gives 10s of rest between stimuli)
    e. Run time: 1 second (amount of time of data collection)
    ** currently I have a better instant stimulation for optimizing current saved (the settings are saved in a photo on force computer)

3. Open live data monitor (File→ open live data monitor); Instant stim orange button will be available for use.
    a. Set time to 10mins (can see protocol or optimization) (screen will automatically scroll)

4. Let diaphragm strip acclimatize for 20-30mins with some tension applied (will appear at 0mm on length in monitor at the end of acclimatization)
    a. This will allow resting tension in the muscle to relax and will reduce background tension; I typically have it resting with some tension on it (6-10mm) and will give it a tetanus stimulus to fully relax the fibres before optimizing length for full data collection.

5. Optimize the current
    a. Range: **1A (50-70%)** (in vitro force stimulation requires a much higher amperage or voltage than in-situ or in-vivo force stimulation since this is a field stimulation- don't be afraid to have it at a high amperage)
    b. Run Instant Stim and check force development
    c. Increase range to ensure all fibres are recruited- if you see an increase in force development then more fibres have been recruited and you are not at a supramaximal current. Use 3 twitches in a row with increasing current (30s rest between) where force does not increase.
    d. Set supramaximal current by increasing current by 15% (this will ensure you have all fibres being activated in the muscle strip).

6. Optimize the length (necessary to make sure maximal amount of cross bridges are forming) YOU NEED TO RECORD THIS LENGTH AT THE END OF DATA COLLECTION
    a. Gradually increase length of diaphragm strip and apply instant stim. Provide 30s of rest to avoid fatigue.
    b. Continue to increase length of diaphragm until you obtain maximal twitch force.
    c. You will need to increase the length of the diaphragm quite considerably compared to an upright bath since this bath is flat- but be careful of drastic changes in length this will increase basal tension of diaphragm strip. Use ¼ turns of fine adjustment knob and use gross only when necessary.
    d. If you want to collect this data load a single twitch protocol in DMC software and enable autosave- this is optional but for training purposes would be beneficial to look at the shape of the twitch. Can also do this with tetanus to
    e. Measure the length of the diaphragm and record, this is L_o and can be input on the main DMC screen and will be used for analysis
        i. Setup normalization- enter the reference length in mm
    f. Allow some time (approx. 5min) for muscle to rest before starting force frequency curve

7. Optimal current and length have now been set, protocol is ready to begin.

8. Load "Diaphragm in-vitro force frequency" sequence
    a. Frequencies of 1 Hz, 10Hz, 20Hz, 40Hz, 80Hz, 100 Hz, 120Hz, 140Hz,160Hz & 200Hz
        i. Initial delay : 0.2ms (this is the rest period prior to stim)

ii. Pulse Frequency: the above frequencies
iii. Pulse Width: length of stimulus
iv. Duration: **400ms** (inputted in s in protocol editor) *might consider increasing this but 400ms provides tension to return to baseline recording following contraction (Tupling lab uses a 1 sec- 600-800ms might be sufficient).

b. 60s rest in between; avoids fatigue

9. Allow 5 mins recovery for the muscle to avoid fatigue in max force test
10. Load tetanic protocol at the frequency that produces the highest force during force frequency test (label this as pre-fatigue max force test)
11. Perform Pre-Fatigue Max-Force Test
12. Allow 2 mins recovery
13. Load "**Diaphragm In Vitro Fatigue**" sequence
    a. 70Hz (350ms stim, 0.2ms pulse width) every 2 seconds for 5 mins
14. Allow 5 minutes recovery from fatigue
15. Perform a second max force test at the same frequency used in Prefatigue max force test- this assesses recovery from fatigue and can be labelled as **5-min-post-fatigue max** force test.
16. Allow 5 minutes recovery
17. Perform third max force test; label as **10min-post-fatigue-max**
18. Allow 5 minutes recovery
19. Perform Fourth max Recovery test label as **15min-post-fatigue-max**
20. MAKE SURE YOU HAVE RECORDED LENGTH!!!
21. Remove muscle from bath and remove from central tendon and ribs before weighing. Obtain weight in mg.
22. Data will be normalized to Cross sectional area : mass X length X density
    a. Mammalian skeletal muscle density =1.06g/cm^3 (Mendez and key, 1960); this is commonly used in the field as it. CSA in short allows you to compare differing muscle weights and lengths of muscle. Normalizing to CSA is a way of controlling for sarcomeres in parallel and normalizing to muscle length during shortening contractions is a way of controlling for the number of sarcomeres in series.
    b. "If you need a visual -think of a rope. How strong is a single rope- now cut it in half so you have 2 shorter ropes. Lay them beside each other and glue them together. You now effectively have a new stronger rope with twice the CSA of the first rope, but it weighs the exact same. Cut the rope again and stick the two pieces together again. Repeat as many times as you want. You now have a rope which has a much larger CSA than the original rope, and it can handle much more load than the original rope but weighs the same and is much shorter. Replace rope with contracting muscle fibres and you probably get the idea. "- Ian Smith 2018

A2 In Situ Quadriceps Force Protocol

In Situ Quadriceps Force Production Protocol
Updated: June 2020 CAB

See attached paper for step up procedure with videos (1).

A good rule of thumb is to have practiced this surgery at least 10-15 times and be able to get consistent data with previous literature. If you are doing a new model establish your own normal values in a pilot data set.

Protocol

1. Create a folder to save files for each animal - Setup: Autosave Folder, open folder you created; click "current folder"
2. Setup: Instant Stim
    a. Pulse Frequency: 1Hz
    b. Pulse Width: 0.2ms
    c. Number of Pulses: 1
    d. Train Frequency: 0.1Hz
    e. Run Time: 1 second

** I have a train frequency that does 3 twitches with a delay between that I find most useful for optimizing current

3. Open Live Data monitor and set time to 10 minutes
4. Optimize Current
    a. Range:10mA -100mA (if you can get the right placement this can go to 10mA, but if you struggle can go to 10% of 100mA- still 10mA)
    b. Run instant stim
    c. Adjust range to ensure all muscle fibres are being recruited – obtain 3 twitches in a row where force does not increase (run instant stim and increase current between twitches (wait about 30 seconds in between twitches)
    d. Set supramaximal current by increasing current by 15%
5. Optimize Resting Length
    a. Before officially setting optimal length, you will need to toggle the thread from the quad to the hook with forceps- this will reduce any basal tension in the line

b. Increase/decrease length of quad until maximal twitch force is achieved, wait about 30 seconds in between twitches to avoid fatigue

c. Time and keep basal tension about constant in the study

Once optimal current and length have been set, protocol is ready to begin

6. Load **"Quad In Situ Force Frequency"** sequence
    a. Frequencies of 40Hz, 60Hz, 80Hz, 100Hz, 120Hz, 140Hz, 160Hz,180Hz, 200Hz, 220Hz
        i. Initial Delay: 0.2ms
        ii. Pulse Frequency: ____Hz (above frequency)
        iii. Pulse Width: 0.2ms
        iv. Duration: 300ms
    b. 45 seconds in between (can extend up to 1 min)
7. Allow 5 minutes of recovery
8. Load the tetanic protocol at the frequency that produced the highest force during step 6
9. Perform Pre Fatigue Max Force Test – make sure to save this file!
10. Allow 2 minutes recovery
11. Load "**Quad In Situ Fatigue"** sequence for your study (Fatigue protocols are varied in the literature- find one that works for your study
    a. 60 Hz, stim every second for 120 seconds (2mins)
    b. 60Hz, stim every 1.5 seconds for 120 contractions (3mins)
12. Allow 5-minute recovery from fatigue
13. Perform a second max force test at the same frequency used in step 8 – this assesses recovery from fatigue- label as **5min-post-fatigue**
14. Allow 5 minute recovery; perform another max force-label as **10min-post-fatigue**
15. Allow 5 minutes recovery; perform last max force-label as **15min-post-fatigue**
16. Harvest muscle and before freezing **MAKE SURE TO RECORD MUSCLE WEIGHT**

Data will be normalized muscle weight

A3 6 minute Movement Tracker

6 min Movement Tracker Protocol

** make sure to perform this test well before or well after functional testing depending on study protocol

SET UP & RECORDING

1. Take iPhone and switch it to video mode.
2. Place grate on top of chamber (white bin) and align camera on grate to view the bottom of the chamber.
3. Place mouse into the chamber
4. Record the animal for 6 mins
5. Once complete remove animal from the chamber and return the mouse to its cage.

VIDEO CONVERSION

1. On iPhone, open iMovie and start a project
2. Insert video into project
3. Click on bottom reel
4. If needed trim video down to 6mins
5. On timing setting speed up video to 2x (this reduces the number of frames per second)
6. On top corner click on magnifying glass and pinch to expand or zoom out of the video (typically need to zoom in on the bottom of bin)
7. Once complete click done on top left corner
8. Export video by saving video to phone
9. Save in videos (can export as 1080p video)
10. Save to computer by plugging in phone

VIDEO ANALYSIS

1. Open video in Kinovea software program.
2. To set calibration- open line tool and draw a line from the top of the bin to the bottom- Vertical line
3. On this line, right click and select calibrate; insert 32.39cm as line distance- click OK
4. Switch to the cursor/hand tool and move cursor to the base of the animal's tail.
5. Right click and select track path
6. Press the right arrow key to progress the video. Additionally, you may press the space bar to let the video play and pause it when tracker correction is required.
7. If the tracker moves from the base of the tail, manually move the tracker to the base of tail. You may need to go back several frames and correct the tracker. Continue to manually fix the tracker frame by frame until the tracker is in the correct position. Once the tracker is fixed you can continue to play the video.
8. When the tracking of the video is complete, save the video and tracing overlay.
9. Export the positional data by selecting file→export to spreadsheet→excel ms

DATA ANALYSIS

1. Open the positional data in excel. The movement analysis software reports the X, Y and time of the coordinate position of the mouse in each frame.
2. It is important to only select 0:00:00 to 3:00:00. Take the X,Y data and copy it into the analysis spreadsheet.
3. The analysis spreadsheet calculates the distance moved between each frame and summing the total distance moved between each frame. The following formula is used in the spreadsheet:

$$distance = \sqrt{(x_2 - x_1)^2 + (y_2 - y_1)^2}$$

x_2 is the x position of frame 2
x_1 is the x position of frame 1
y_2 is the y position of frame 2
y_1 is the y position of frame 1

4. The distance moved needs to be summed to identify the total distance moved. The next column sums the above formula.
5. Take the total distance moved and paste into summary sheet in correct column.

B.1 - SkyScan 1278 – Scanning an Animal

1. Open Skyscan 1278
2. Click X-Ray button – if this is the first time the machine has been used in a while, it can take up to 10 minutes for the x-ray to warm up
3. With nothing in the machine, you must update the bright and dark flat field
    a. Option: Update flat field for current mode
    b. Want background of mouse to be grey colour not white – want average to be 90% not 100%, 100% is saturated
4. Set your parameters
    a. Resolution (# of pixels): 50, 100 or 200 microns
    b. Filter (energy, controls x-ray voltage): 0, 0.5mm, 1mm aluminum or low dose
5. Load mouse, make sure mouse is centered and arms and legs are taped down
6. Click the TV screen icon to turn on x-ray and bring up live image of mouse
7. Right click to bring up transmission values
    a. Want a minimum value of 20-30%, if this is too high, lower the filter in the bottom right corner
    b. If you change any parameter values, you must update the flat field
8. Click the green arrow to bring up scanning parameters
    a. For 50 + 100 microns – use step and shoot
    b. For 200 microns – use continuous acquisition
    c. For a mouse, use 180°. For a rat, use 360°

**** Make sure the parameters used are the same for entire study**

9. Click scan

B.2 - SkyScan 1278 μCT - % Body Fat

Step 1) Open the reconstructed images made in NRecon software. They are saved in the folder containing the original scans. Click on the firs image and press open.

Step 2) Click on the icon of square with magnifying glass. This opens the profile tab (sometimes the profile tab do not fully open and gets hidden on top of palette tab. You can open the profile tab by double clicking on it). Click on the icon of black square with snowflake on it (it is called maximum intensity projection). This opens the maximum intensity projection tab. Click on Ok button. This will generate a coronal view of the animal so that you can navigate better. Click on the icon of magnifying glass with the arrow next to it (called send image into projection window) and then click on the icon on the right (called close window).

Step 3) This step is called “thresholding”. Click on the icon of black and white cactus (called binary selection preview) on the top. This will open the binary selection tab (next to raw images tab) in the top, and the histogram tab in the bottom. When you perform these steps, the transverse view of the animal turns into a black and white (binary) preview. This view is hard to highlight fat. Click on the colored cactus image with a red dot in background (called toggle half tone view)

in the histogram tab. This will bring back the original transverse preview of the animal under a green filter. Open “from dataset” tab in the histogram tab. On the binary view, scroll down to the very bottom slice (or any slice that shows fat clearly). Highlight fat accurately using the selectors on top and bottom of the histogram (the highlighted area will be red in the transverse view). Sometimes, a part of the lung will stay in slices after reconstruction. To check for that, scroll to the top slices in binary selection. The lung usually appears in the top few slices. They have to be removed because they get highlighted as fat. To do so, find the first slice from the top in the binary selection that does not contain the lungs. Left click on that slice and select “set the top of the selection”. This will eliminate the slices that contain lungs. Then click on the icon of histogram with an arrow on top (called automatic thresholding). This will highlight the entire animal together with isoflurane tube and the mouse housing.

Step 4) In this step, we separate the isoflurane tube and the housing from the animal. To do so, we need to create a region in space that **only** contains the animal called region of interest (ROI). Click on the hexagonal colored cactus icon (called regions of interest preview). This will open the regions of interest tab next to raw images tab. In this step, the transverse view is colored red. This makes it hard to visualize the animal. From the palette tab, select the filter that works best for you (from experience, “color” shows the fat better, but “color 2” shows the edges better than the “greyscale”).

Step 5) In this step we create the ROI. To create the ROI we draw shapes around the mouse every few slides from bottom to top. Software will generate a 3D space by connecting these shapes along the longitudinal axis of the animal. This space separates the animal from the housing and the isoflurane tube. Shapes are drawn manually by mouse. You need to hold the right click while drawing the shapes. When drawing the shapes, make sure to avoid the tube and the housing. If you need to remove a shape, click on the scissors icon (called cut ROI) on the top. Go up and down inslices to make sure ROI contains **all** of the animal and **non** of the tube and the housing.

Step 6) Click on the icon of the face on the top (called custom processing preview). This will open the custom processing tab, next to binary selection tab, and the plug-ins tab on the bottom. Go to the internal tab in the plug-ins tab. Click on the thresholding section. This will open threshold tab. Leave the setting as global and check the default box. Then click ok. To run every step in internal tab, you need to press play and then press continue. his will highlight everything that you selected in the thresholding step and turn it into binary.

Step 7) In this step, we remove the isoflurane tube and the housing from the animal. The internal tab has 4 views. You can navigate them using 4 icons on the right. These views, from left to right, are “Image”, “Image inside ROI”, “ROI”, and “Clipboard”. From the internal tab, click on the “Bitwise operations”. The way that bitwise operations works is similar to Venn diagrams with the same logical rules of “and”, “or”, “not” etc. Bitwise operations allow you to modify the “Image” using the shapes in other views. When you click on the bitwise operations, it will open bitwise operation tab. Put the settings in the following way:
Image = Image AND Region of Interest.
This will remove the isoflurane tube and housing.

Step 8) In this step, you need to modify the image. Parts of the housing or the tube might still stay in the image that must be removed. Click on "Despeckle". Select the settings according to the image (in the remove section, the largest object is the highlighted animal). Click on the play icon to run the despeckle. Some parts of the tube or the housing may still be attached to the animal. To remove them click on the "Morphological operations". Select the settings according to the image and press ok. Always despckle after any morphological operation to remove any speckles that might be created. You need to save the image after the modifications. Software allows you to save the image only in the clipboard view. To do so, click on the "bitwise operations". Set the setting as follow:
Clipboard = Image AND Image.

Step 9) In this step, we turn the image into a solid region. To do that, click on the "ROI shrinkwrap". Make sure that it is applied to 2D space. The default should be to keep "stretch over the holes" unchecked. But, if there are dips in the image you need to check that box. You also need to assign a diameter measured in pixels. The diameter should be set as the lowest number possible because this will increase the ROI volume. The right diameter is found through trial and error. Start with a high diameter (20 pixels) and work your way down. When you click on OK, a solid shape that has all the holes filled will be created in the ROI view in the internal tab. If the dip is covered, click on the bitwise operations and put the settings as follow: Image = clipboard AND clipboard. This will load the image again. Go back the "ROI shrink-wrap and put a lower diameter. Repeat these steps until you reach the lowest diameter that covers all the dips.
Until now, we have created a space in ROI that consist of the entire mouse. This space will be the total volume which is the denominator in the percent body fat formula. Now we need to select the fat.

Step 10) Click on the bitwise operation and put the setting as follow: Image = region of interest AND region of interest. Then click OK.

Step 11) In this step, we threshold the fat. Go back to the binary selection tab. Scroll down to the very bottom slice (or any slice that shows fat accurately). Use the selectors on top and bottom of the histogram and highlight fat (it should be the same thresholding values as you found in step 3).

Step 12) Go back to the custom processing tab. Click on the internal tab. Click on the "Reload". This will open the reload tab. Set apply to "Image" and then click OK. This will load the original image in the transverse view (make sure you are in the image view of the internal tab).
Click on thresholding and then click OK. This will highlight the parts of the animal (fat) that was selected in step 11 and turn the entire image into binary. Click on the bitwise operations and put the settings as follow:
Image = Image AND Region of Interest.
This will remove the isoflurane tube and the housing from the selected area of the animal.

Step 13) Click on the "3D Analysis" in the internal tab. This will open 3D analysis tab. Leave the settings as it is and click on OK. This step will perform the 3D calculations to measure the percent body fat. To see the results, go to the Output/Report tab and click on the first Open from the top. This will open a text file containing the results. Scroll down to the very bottom and you can find the results. Measurements are made in mm^3. Total VOI volume is the volume of ROI. It is the total volume of the animal that was selected which is the denominator of the percent body

fat formula. Object volume is the volume of fat, the numerator of the percent body fat formula. Percent object volume is the percent body fat which is calculated by dividing object volume by total VOI volume.

B.3 - SkyScan 1278 μCT - Analyzing Hind-Limb Muscle Volume

Step 1) Open the reconstructed images made in NRecon software. They are saved in the folder containing the original scans. Click on the firs image and press open.

Step 2) Click on the icon of square with magnifying glass. This opens the profile tab (sometimes the profile tab do not fully open and gets hidden on top of palette tab. You can open the profile tab
by double clicking on it). Click on the icon of black square with snowflake on it (it is called maximum intensity projection). This opens the maximum intensity projection tab. Click on Ok button. This will generate a coronal view of the animal so that you can navigate better. Click on the icon of magnifying glass with the arrow next to it (called send image into projection window) and then click on the icon on the right (called close window).

Step 3) Click on the image of black and white cactus (called binary selection preview). Click on the "from dataset" tab in histogram tab. Go to the top slices in the binary tab. Scroll up and down until you find the knee joint. In the transverse view (superior part of the tibia has a curved shape in coronal view; therefore, it will be shown like two parallel ovals in transverse view). Left click on the slice that it the top of the tibia and select "set the top of selection". This will eliminate the higher slices from the selection.

Use the selectors on top and bottom of the histogram to select muscle. Muscle is usually the second spike after on the right of the spike for fat. Use the top slices to highlight muscle.

Step 4) In this step, we separate the isoflurane tube and the housing from the animal's leg. To do so, we need to create a region in space that **only** contains the animal called region of interest (ROI).
Click on the hexagonal colored cactus icon (called regions of interest preview). This will open the
regions of interest tab next to raw images tab. In this step, the transverse view is colored red. This makes it hard to visualize the animal. From the palette tab, select the filter that works best for you (from experience, "color" shows the fat better, but "color 2" shows the edges better than the "greyscale").

Step 5) In this step we create the ROI. To create the ROI we draw shapes around the leg every few
slides from bottom to top. Software will generate a 3D space by connecting these shapes along the
longitudinal axis of the animal. This space separates the animal's leg from the housing and the isoflurane tube.
Shapes are drawn manually by mouse. You need to hold the right click while drawing the shapes.

When drawing the shapes, make sure to avoid the tube and the housing. If you need to remove a shape, click on the scissors icon (called cut ROI) on the top. Go up and down in slices to make sure ROI contains **all** of the animal's leg and **non** of the tube and the housing.

Step 6) Click on the icon of the face on the top (called custom processing preview). This will open
the custom processing tab, next to binary selection tab, and the plug-ins tab on the bottom. Go to the internal tab in the plug-ins tab. Click on the thresholding section. This will open threshold tab.
Leave the setting as global and check the default box. Then click ok.
To run every step in internal tab, you need to press play and then press continue.
This will highlight everything that you selected in the thresholding step and turn it into binary.

Step 7) In this step, we remove the isoflurane tube and the housing from the animal's leg. The internal tab has 4 views. You can navigate them using 4 icons on the right. These views, from left to right, are "Image", "Image inside ROI", "ROI", and "Clipboard".
From the internal tab, click on the "Bitwise operations". The way that bitwise operations works is similar to Venn diagrams with the same logical rules of "and", "or", "not" etc. Bitwise operations allow you to modify the "Image" using the shapes in other views. When you click on the bitwise operations, it will open bitwise operation tab. Put the settings in the following way:
Image = Image AND Region of Interest.

Step 8) Click on the "3D Analysis" in the internal tab. This will open 3D analysis tab. Leave the settings as it is and click on OK.
To see the results, go to the Output/Report tab and click on the first Open from the top. This will open a text file containing the results. Scroll down to the very bottom and you can find the results.
Measurements are made in mm^3. Object Volume is the hind limb muscle volume.

C Histology
C1 Picrosirius Red Staining

Principle – Directly from Junqueira et al., Histochemical Journal, 11 (1979), 447-455

The interaction between collagen and sirius red is due mainly to the reaction of its sulphonic acid groups with the basic groups of collagen. The role of picric acid in the staining of collagen is not known. When omitted from the staining solution, all tissue components stain red. Picric acid, therefore, seems to somehow prevent the indiscriminate staining of non-collagenous structures by Sirius Red. When picric acid is not used, despite the overall red stain, only collagen showed an enhancement of birefringency.

Summary

Picrosirius red stains collagen (red) and cytoplasm (yellow).
(Haematoxylin stains nuclei (brown)-optional.

Notes:

- For Brightfield staining, using distilled water is fine. For immunohistochemistry use deionized water. Deionized water is ultra-purified water that has no ions other than H^+ and OH^-.
- Can also use isopropanol as a substitute for ethanol at all steps.
- Stir PSR solution for ~24 hours continuously prior to use. At least 4 hours if you want to use the same day. This helps prevent any precipitate from creating staining artefacts.
- USE A HUMIFIED BOX for staining duration to prevent PSR from drying out .

Solutions and Reagents:

Modified Harris Hematoxylin - OPTIONAL

Harris Modified Method Hematoxylin Stain with Acetic Acid (Fisher Chemical Cat. No. SH26-500D).

Acidified Water:

Glacial Acetic Acid (Fisher Chemical Cat. No. A38-500) ……. 5 ml

Distilled Water ……. 995 ml

Make fresh.

Working PSR:

Direct Red 80 (Sigma Cat. No. 365548-5G)...……. 0.5 g

Saturated aqueous solution of picric acid (1.3% in H_2O) …….. 500 ml final volume[1]
Keeps for at least 3 years and can be used many times.

[1] Always make sure to use saturated picric acid (1.3% in H2O); picric acid is very explosive in a dried state and in concentrated state so always look for crystallization

ALWAYS STAIN ALL YOUR SAMPLES AT THE SAME TIME IF YOU ARE MAKING COMPARISONS BETWEEN THEM.

Procedure:

Figure 1. Glass slide rack

Paraffin Embedded Tissue

Deparaffinize Sections

1. Xylene (#1) for 2 minutes.
2. Xylene (#2) for 2 minutes.
3. Xylene (#3) for 2 minutes.
    - Always move the glass slide rack to a new xylene staining dish at each step. Do **not** backtrack.
    - Just submerge the slides, no need to agitate.
    - Xylene is a clearing agent that removes the paraffin.

Re-hydration in Ethanol

4. 100% Ethanol (#1) for 2 minutes.
5. 100% Ethanol (#2) for 2 minutes.
6. 95% Ethanol for 2 minutes.
7. 70% Ethanol for 2 minutes.
8. Distilled water for 2 minutes.

OCT Embedded Tissue

1. Air dry OCT embedded tissues for 5-10 minutes before staining

Staining

1. OPTIONAL- Stain in Modified Harris Hematoxylin for 10 minutes. [2]
2. Wash in running distilled water until no more dye comes off.
3. Rinse for 10 minutes under running distilled water or rinse with agitation and change water multiple times (i.e. 1-2 min).
4. Stain in picrosirius red (pH >4) for 60 minutes inside a humidified box.
5. Quickly dip in acidified water.
6. Wash in new acidified water with constant agitation for 2 minutes using Columbia jar filled until all samples are covered (not the entire slide).
7. Repeat wash in new acidified water with constant agitation for 2 minutes.
    - Physically remove most of the water from the slides by vigorous shaking.
8. 95% Ethanol for 2 minutes.
    - Use the 95% Ethanol from step 6. Discard when finished.
9. 100% Ethanol (#2) for 2 minutes.

[2] Steps are optional. You may not want to use Hematoxylin if you are more interested in fibrosis, but you need to do it if you want to quantify CSA.

- Use the 100% Ethanol from step 5.

10. 100% Ethanol (#1) for 2 minutes.
    - Use the 100% Ethanol from step 4.
11. Xylene (#4) for 3 minutes.
12. Xylene (#5) for 3 minutes.
13. Mount with Permount (xylene-based mounting medium) and cover slip. Press out any visible bubbles and allow to dry.

Analyzing Protocol:

1. Analyzing images is done through the "ImageJ" application. It is free to download and readily available online for both Mac and PC. If using a laptop, it is much more efficient and convenient to use a mouse than the mousepad (you will be doing a lot of clicking). When analyzing PSR stains, it is easier to use the non-stitched images that randomly selected throughout the whole image rather than the whole stitched image but in some cases you can use the whole section. Choose 5-10 non-stitched sections or regions of interest(keep the number consistent) for each sample and analyze each one separately.

2. ** If you are analyzing smaller images of the entire section, it is important that you select sections that are representative of the whole image (that you are not focusing solely on damaged or healthy areas to skew the results). Additionally, select images that highlight the "middle" portions of the whole image as opposed to the "outer" sections that will contain the background of the slide which you will have to account for. If you decide to analyze the entire image, you need to remove any tendon, ie in the plantaris.

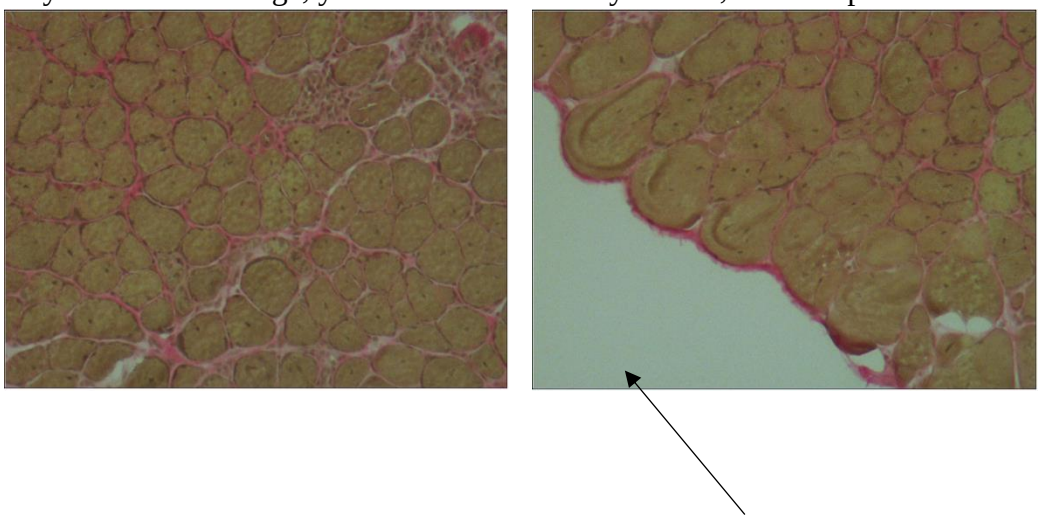

Select images that do not contain much (if any) of the slide background to make it easier to analyze

3. Below is the link to a YouTube tutorial that is a fantastic resource when analyzing differences in area on histological stains. It is recommended that you watch this video prior to beginning your analysis: https://www.youtube.com/watch?v=nLfVSWcxMKw&t=642s

4. Open ImageJ
5. Go to FILE and click on OPEN to open the desired image
   NOTE: it should be in jpeg format

6. Zoom in and out of the image with the + and – buttons on your keyboard and move along with image with the hand function ( ) selected in the ImageJ toolbar
7. Select Analyze and under its options tab, select set scale. In the scale screen, select to remove the scale and then click on OK.

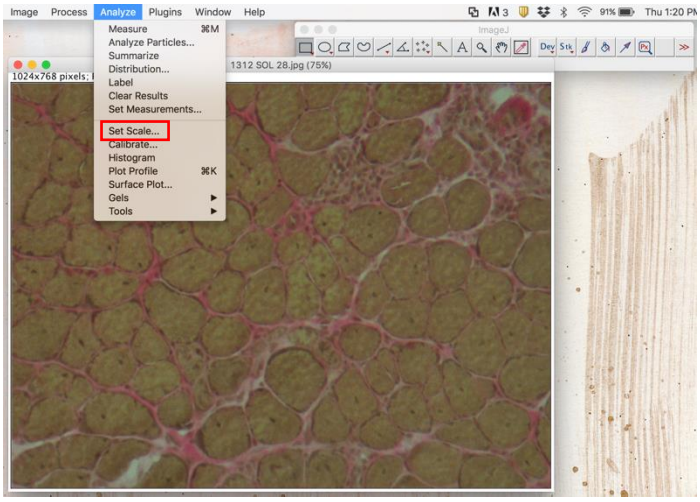

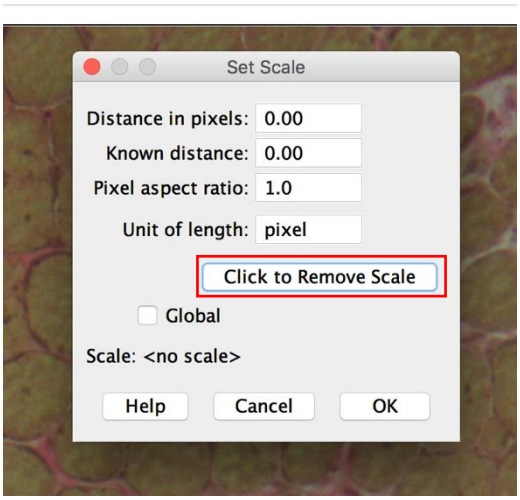

8. Select Image and under its option tab, select adjust. In the adjust screen, select color threshold.

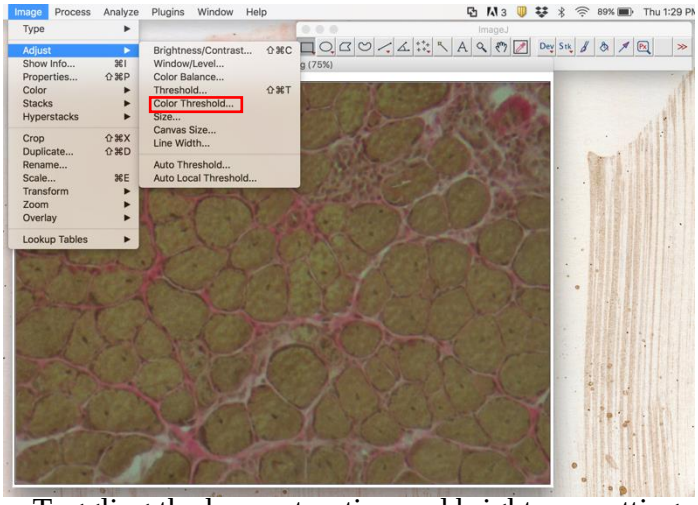

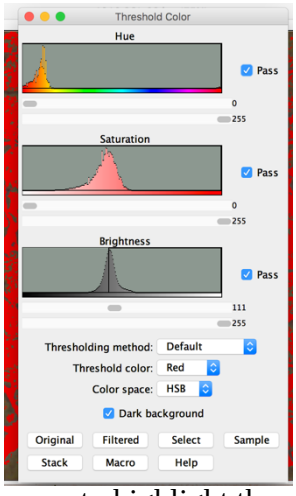

9. Toggling the hue, saturation and brightness settings will enable you to highlight the area of the whole image, as well as, the area of collagen and the muscle fibre area. Ideally, the collagen and muscle fibre areas should add up to (or be very close to) the whole image area

a. toggle the hue, saturation and brightness levels until the entire image is highlighted in red.

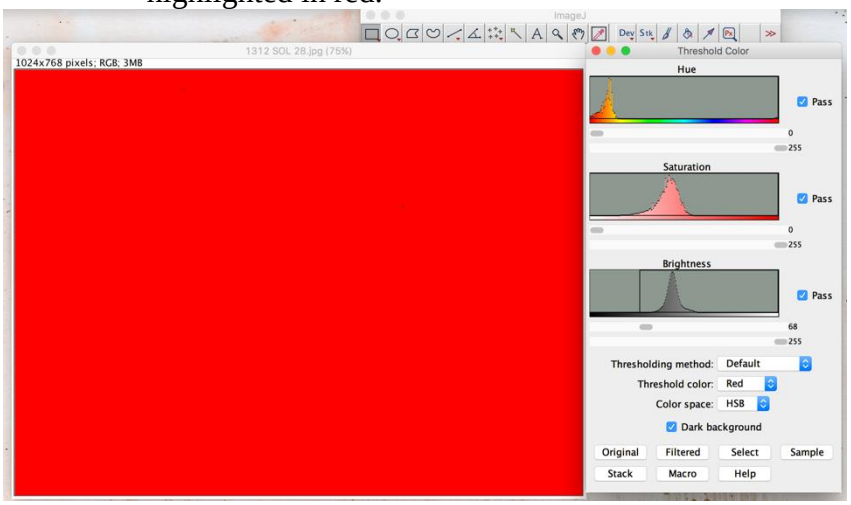

b. select Analyze and under its option tab, select measure to obtain the area of the entire image. This area can then be saved in an excel spreadsheet

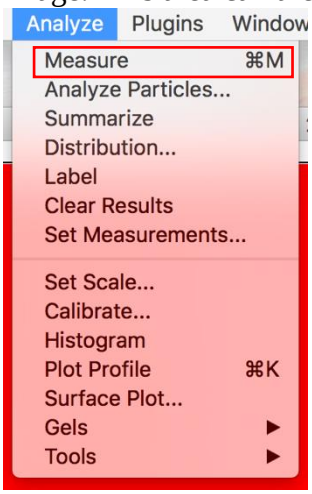

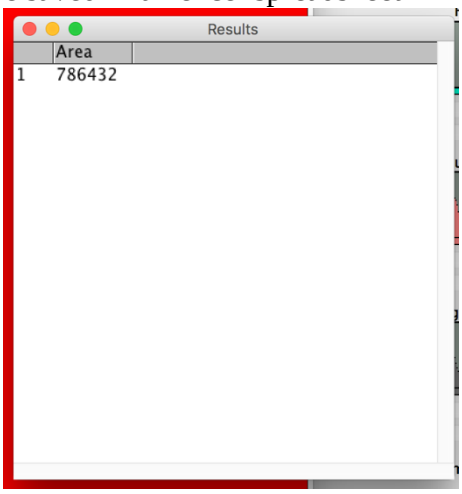

NOTE: you can customize the measurement tab depending on what values you require. To do so, click on the results window and select Results, under its option tab, select set measurements.

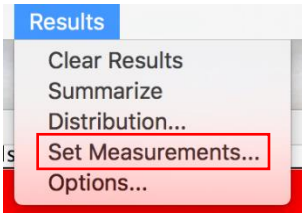

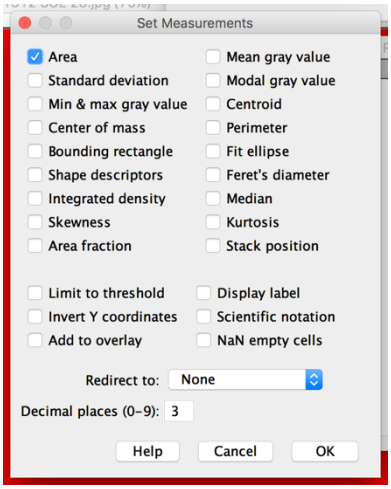

c. adjust the hue, saturation and brightness to highlight ONLY the muscle fibres and obtain their area. Press select to highlight the area outlined in red.

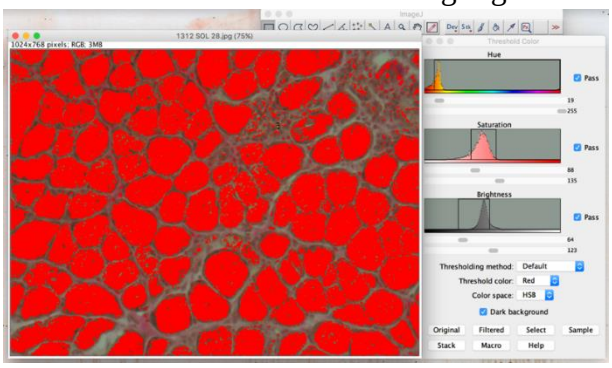

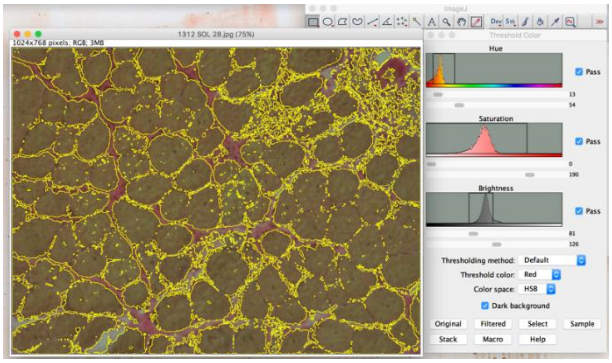

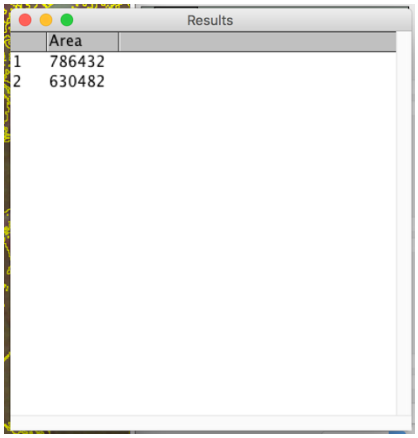

d. adjust the hue, saturation and brightness to highlight ONLY the collagen invasion and obtain that area. Press select to highlight the area outlined in red.

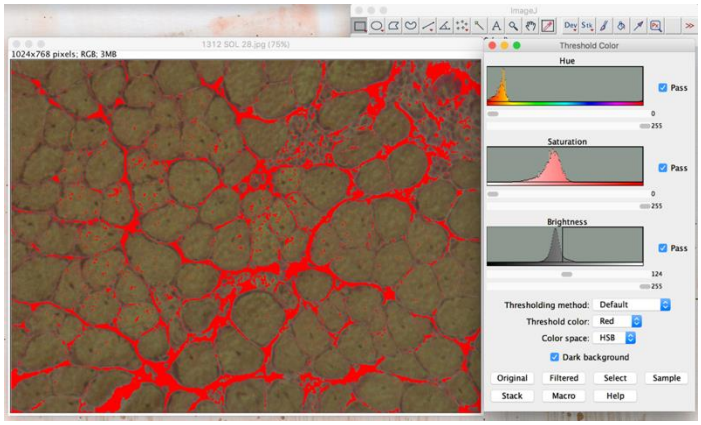

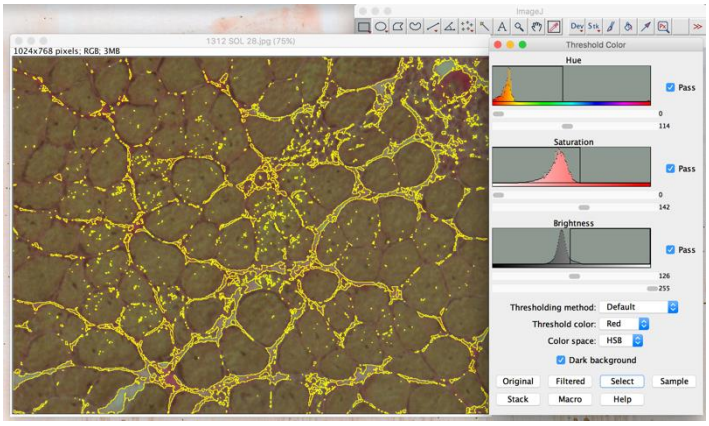

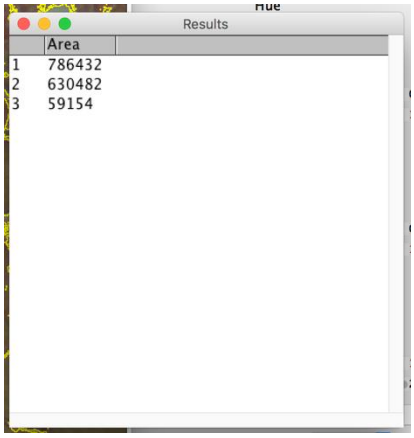

10. Repeat the above steps for at least 5 non-stitched images per section. NOTE**: if you to decide to analyze the entire section then you only will have 1 row of data per individual.

1213	Total Area:	Fibrotic Area:	Normal Area:		**1411**	Normal Area:	Fibrotic Area:	Total Area:
	756260	34497	717995			649684	113893	786248
	706016	51516	757532			642399	144033	786432
	707760	44867	782572			602230	160026	762256
	679185	65866	782657			617961	107673	786267
Total:	2849221	196746	3040756			657468	205017	778450
						3169742	730642	3899653
1312	Normal Area:	Fibrotic Area:	Total Area:		**1512**	Normal Area:	Fibrotic Area:	Total Area:
	629190	105146	734336			533857	168198	780898
	704873	100871	784533			553587	131988	780568
	661534	96411	784620			519729	198384	785327
	693686	124479	786038			577918	185844	783840
	630162	169541	785694			585635	197482	782860
Total:	3319445	596448	3875221		Total:	2770726	881896	3913493

Below is an example of how to organize an excel spreadsheet per section:

11. Using the totals from each non-stitched image per section, you can then determine the percentage of fibrosis:

% Fibrosis = (Fibrotic Area / Total Area) * 100

ID:	Normal Area:	Fibrotic Area:	Total Area:	% Fibrosis:
1213	2849221	196746	3040756	6.47029883
1312	3319445	596448	3875221	15.3913286
1314	3179569	951250	3928777	24.2123694
1322	2677664	340124	3144000	10.8181934
1411	3169742	730642	3899653	18.7360773
1512	2770726	881896	3913493	22.5347535
1513	2845386	104756	3029538	3.45782096
1514	2417322	944935	3917149	24.1230293
1522	1401148	111708	1693596	6.59590599
1523	1592246	152746	1909231	8.00039388

Hematoxylin & Eosin Illustrated Protocol

Summary Report:

The Hematoxylin & Eosin (H&E) stain is the gold standard for recognizing various tissue types and the morphologic changes incurred by various disorders. It is one of the principal histological stains because it can be applied to numerous tissues, it works well with a variety of fixatives and displays a broad range of cytoplasmic, nuclear, and extracellular matrix features. The stain is consisted of two components:

i. *Hematoxylin*: a basic/positive, dark blue or violet stain that binds to basophilic substances (such DNA/RNA in the nucleus, and RNA in ribosomes in the rough endoplasmic reticulum).

Both DNA and RNA are acidic because the phosphate backbones of nucleic acids are negatively charged. These negatively charged backbones will form salts with basic dyes that contain positive charges. As such, hematoxylin (and other positive stains) will bind to DNA and RNA and stain them violet.

ii. *Eosin*: is an acidic/negative, red or pink stain that binds to acidophilic substances such as positively charged amino acid side chains (e.g. lysine, arginine).

Most proteins in the cytoplasm of some cells are basic because they are positively charged due to the arginine and lysine amino acid residues. These will form salts with acid dyes that possess negative charges. Therefore, eosin will bind to these amino acids/proteins and stain them pink.

In this lab, the H&E stain is used to examine muscle morphology and nuclei location in skeletal muscle. As explained above, the hematoxylin will stain the nuclei violet and eosin will stain the muscle fibres pink. Additionally, infiltrating immune cells will also be stained purple. In healthy skeletal muscle tissue, muscle fibres are multinucleated with the nuclei located around the periphery of the fibres. During the degenerative process the nuclei will move to a more central location within the muscle fibre. Similarly, during muscle fibre regeneration, the nuclei begin in a central location and move to the periphery as the fibres mature. As such, the proportion of peripherally to centrally located nuclei is indicative of muscle fibre health, and provides us with a histological assessment of muscle turnover (muscle fibre degeneration/regeneration). In healthy muscle, the proportion of centralized nuclei is ~ 2 – 3%. In contrast, in skeletal muscle disease (such as Duchenne muscular dystrophy) the proportion of centralized nuclei is upwards of ~ 60 – 70%.

To date, the muscles examined in this lab have been the soleus, extensor digitorum longus (EDL), tibialis anterior and diaphragm. These muscles produce sections of differing amounts of fibres and thus different sizes. For instance, the soleus sections will have ~ 500 fibres whereas the diaphragm will have ~ 2000. In these cases, it is appropriate to count the entire soleus section, however, it would be best to select five random and well-spaced areas of the diaphragm and only count those.

Do not be alarmed if there are differences in staining between sections on the same slide or if the stain on an individual section is uneven. Always select the best image per slide to analyze.

Stain Protocol:

1. Remove two slides from the freezer and allow to air dry for 5 min

    NOTE: if there is any residual moisture, remove with a kim wipe but be careful not to wipe away muscle section

    NOTE: only do two slides at a time

2. Prepare your staining workbench as depicted in the figure below:

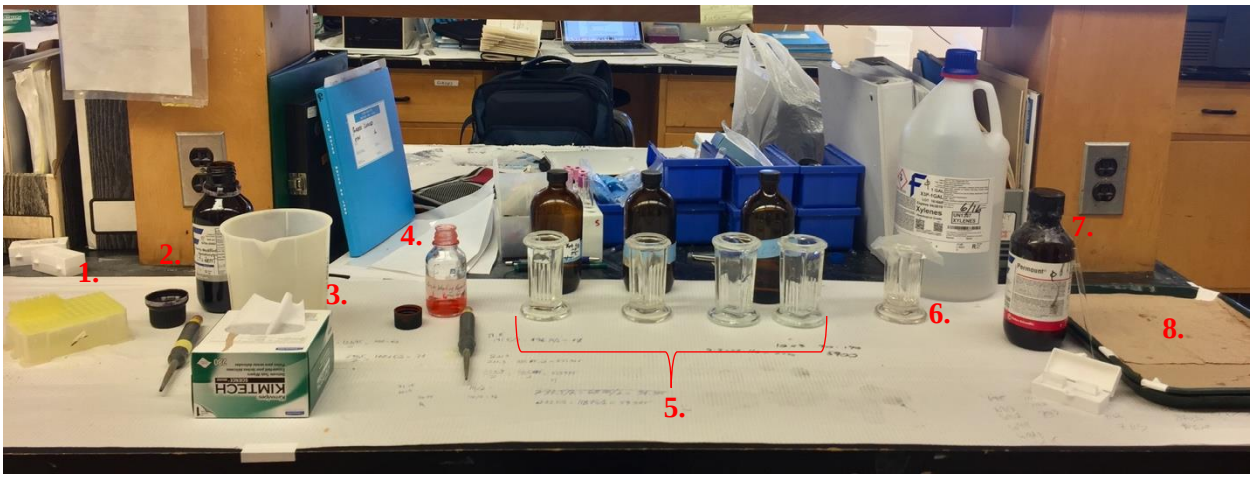

1. Have a box of pipette tips ready, these do not need to be autoclaved. Use the 100 uL pipettes, you will need two (one for the hematoxylin and one for the eosin).

2. The Harris hematoxylin stain is stored at room temperature, pour a small amount into the lid and pipette from there.

3. Use a PLASTIC beaker to dip the slides in. Tapping glass slides on the side of a glass beaker will cause the slides to crack and break, therefore a plastic beaker is more suitable.

4. The eosin stain is stored at room temperature, pour a small amount into the lid and pipette from there.

5. 70%, 95% and 100% EtOH are stored at room temperature. Pour enough ethanol into the Columbia jar to cover the portion of the slide that contains sections. However, dipping the entire slide in ethanol will cause the slide ID to smudge off, therefore, be careful with how much ethanol there is in the jar and how far you are dipping slide in the ethanol.

6. Xylene is stored at room temperature in the cabinet in the chemical room. The smell of this solvent resembles paint thinner and is dangerous if inhaled, as such the lid should be

on and sealed when not in use and the Columbia jar should be covered with parafilm at all times, unless you are dipping the slides in xylene.

7. Permount is stored at room temperature. It is very viscous. Dip a long Pasteur pipette in the permount and carefully use this pipette to add a drop of permount to the slide. Immediately place a cover slip on the slide.

8. Place the finished slides on a plastic tray covered with paper towels to dry.

NOTE: as you can see in this image, it is imperative that you are prepared and have all of the reagents and supplies that you need (and arranged in the proper order) before you take your slides out of the freezer.

3. Use a 100 uL staining pipette to add hematoxylin stain to the slides, leave for on 1 min

NOTE: use an excess amount than is needed to ensure that the sections are completely covered

NOTE: be careful to NOT touch the tip of the pipette to the section as this will compromise the section

NOTE: while waiting to remove the stain, remove the next two sets of slides from the freezer so that they have air dried by the time you finish (only start them once the first set of two slides has been completed)

4. Dip and swirl the slides in warm tap water five times to remove any excess hematoxylin stain

5. Wipe away excess water from the back and top of the slide, be sure NOT to wipe away muscle section

NOTE: this will prevent dilution of the eosin stain

6. Use a 100 uL staining pipette to add the eosin stain to the slides, leave for on 30 seconds

NOTE: use an excess amount than is needed to ensure that the sections are completely covered

NOTE: be careful to NOT touch the tip of the pipette to the section as this will compromise the section

NOTE: remove as much excess stain as possible before Step 7

7. Arrange slides back to back, dip and swirl 5 times each in:

a. 70% ethanol

b. 95% ethanol

c. 100% ethanol

d. 100% ethanol

e. xylene

NOTE: shake off slides in between each a – e step

NOTE: don't dry off too much of the xylene, it helps the permount spread and prevents the formation of bubbles (wipe back of slide and a circle/square around the sections)

8. Add a drop of permount with the Pasteur pipette to the middle of the sections and place a #2 coverslip on top

NOTE: use the tip of a pipette tip to *gently* push away any of the bubbles that may have formed

9. Place finished slides on a tray. The slides are now ready to be imaged

How to Analyze H&E Staining

Updated June 2 2021 by CB

H&E staining is commonly used for identifying the cytoplasm/membrane (eosin) and the nuclei (hematoxylin) in a variety of histological sections including skeletal muscle. Commonly in skeletal muscle histology, cross sections of a sample are taken to identify muscle fibre size (cross sectional area, minimal ferret diameter), regeneration status of the muscle (centrally nucleated fibres) or areas of muscle damage (necrosis).

In order to analyze for **centralize nuclei** we use the following procedure using Image J:

1. Open the image using imageJ
2. Using the box tool

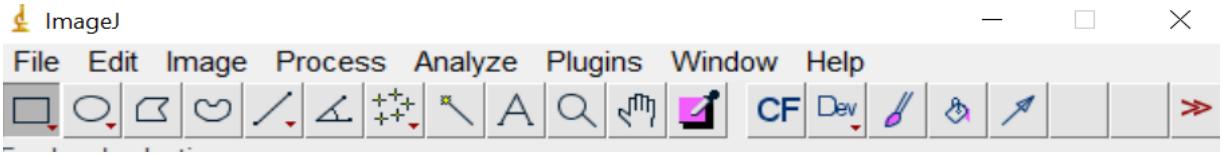

3. Create 4-6 large boxes across the entire section. On average we use 5 but smaller sections may only require four, while larger ones require 6. If you have areas of freezer burn (also known as freezing artifact) on the section try to avoid them if possible. If the section is entirely freezer burnt then make a note of it in the analysis spreadsheet and move onto another image. In the image below, healthy properly frozen muscle will look like A and B (but note A does look better then B but B is still fine to analyze). C and D have varying levels of freezing artifact so try and avoids areas like this when analyzing. Freezing artifact happens when either water in the muscle or water on top of the muscle freezes too quickly and creates holes in the section. This care interfere with your identification of

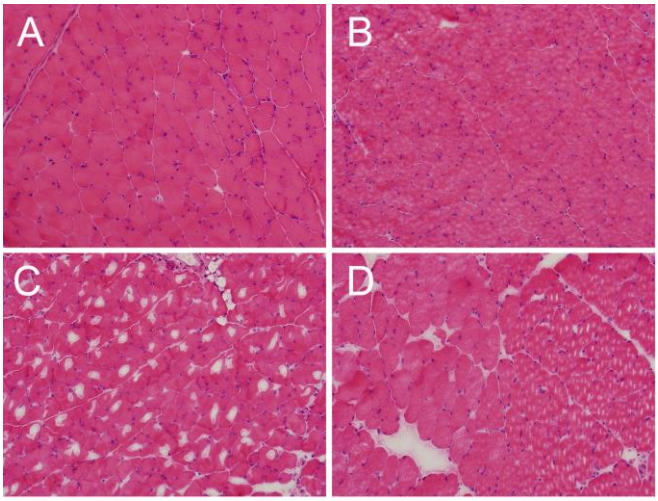

fibres and nuclei.

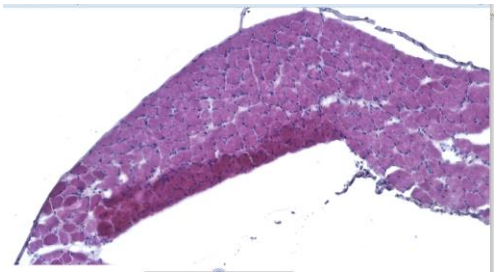

4. Create your boxes throughout your section and duplicate the image (control+shift+D) to create a separate file for the box you will count. I find it easiest to create all my boxes at the beginning and then analyze them one by one.

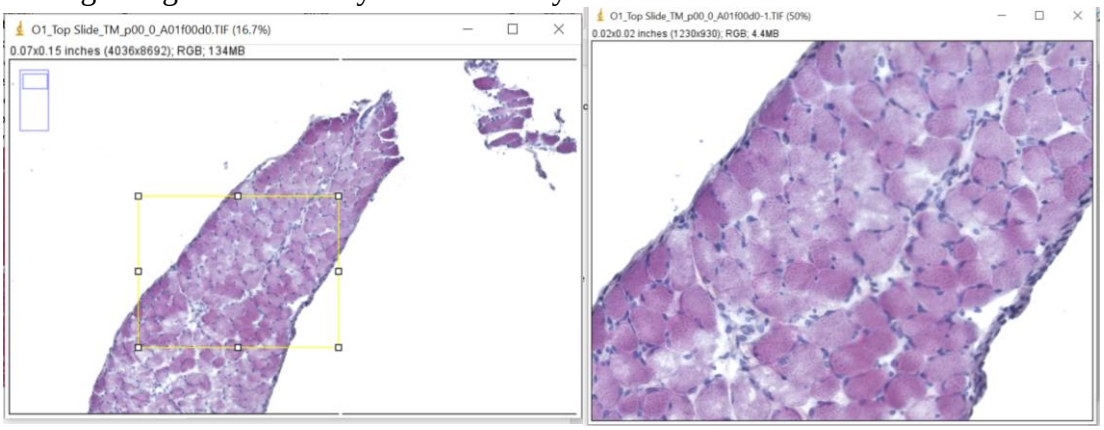

5. Using the multipoint tool (looks like 5 stars in the upper menu-Image 1) you will count all the centrally nucleated fibres you can see. Centrally nucleated fibres often have a clear nucleus directly in the center of the fibre. Sometimes they are slightly off center but they

should be clear nuclei and not likely speckled dots.

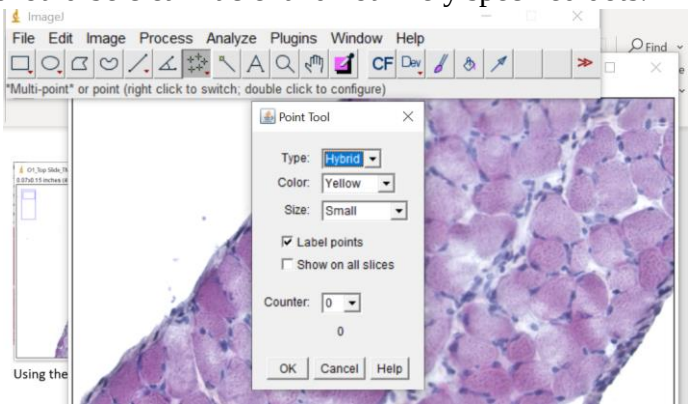

6. Examples of Centrally nucleated fibres you can count (below). You should be able to see cytoplasm (pink) around all edges of the fibre. For the most part the nuclei are right in the middle of the fibre (image 2). Some nuclei can often be faint so make sure you zoom in when you need. When a nuclei is slightly off center it could be migrating back to the periphery of the fibre (Image 1).

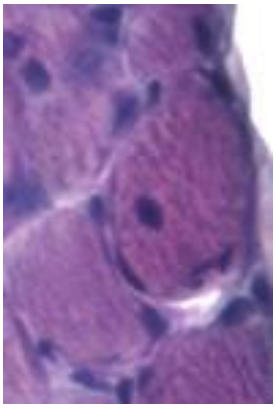

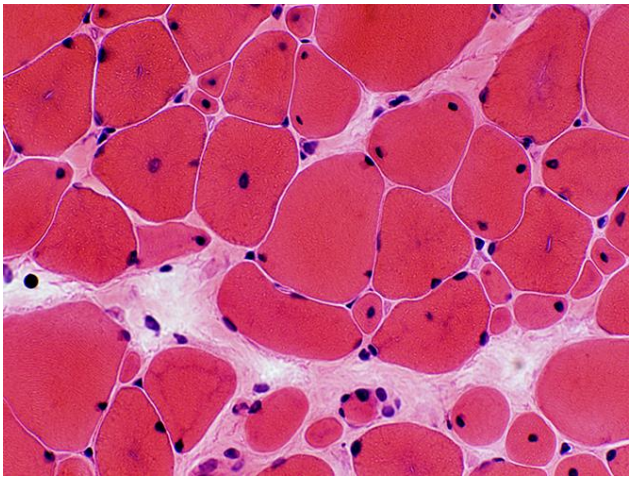

7. Examples of things NOT TO COUNT as centrally nucleated fibres(below): Make sure not to count nuclei that are on the periphery of the muscle fibre as a centrally nucleated fibre(you should see pink all the way around the nuclei). Also do not count degenerating fibres (broken/fuzzy membranes- typically a darker pink colour but you will see tons of nuclei in or around them). Also watch out for these weird spots (image 3) these aren't nuclei but are an artifact of the staining process but you will notice they are too small and perfect a circle to be a nuclei:

Healthy : 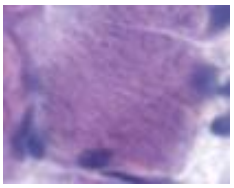 Count as non-centrally located 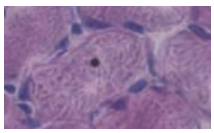

Do NOT Count: 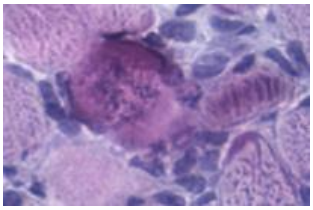

8. Once you have counted all the centrally nucleated fibres, switch the marker you are using in the multi-point tool and count all other visible fibres. Fibres on boarders of the image can be difficult to count but if you can see most of the fibre then you can count it. If you can only see a bit of the fibre do not count it. Finally image will look something like this: It's a good idea to keep these smaller images either by saving the image as a tiff file or by print screening the image to an excel document. This helps another counter verifying your selections and also provides material for when you train others.

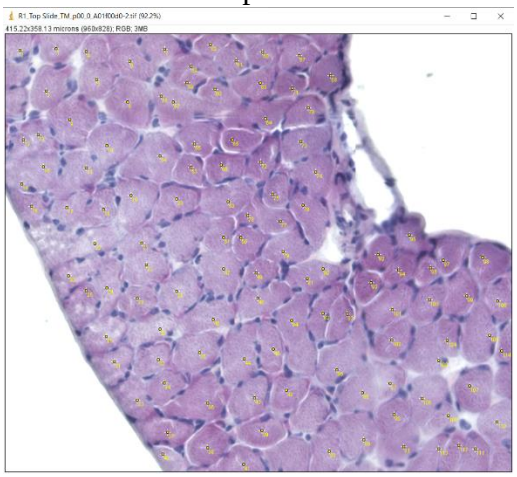

9. Record both centrally nucleated counts in the excel spreadsheet. Repeat these steps with the rest of the boxes you have created. All boxes will be averaged together to be representative of the entire section.

11					
12	CENTRALIZED NUCELI				
13	M1	CN	Non CN f	Total Fib	% CN
14	1	7	119	126	5.555556
15	2	10	146	156	6.410256
16	3	9	146	155	5.806452
17	4	3	174	177	1.694915
18	5	13	189	212	6.132075
19	AVERAGI	8.4	154.8	165.2	5.084746
20	SD	3.714835	27.27086	31.83866	1.941725
21	SEM	1.661325	12.1959	14.23868	0.868366
22					
23					

How to Analyze Necrosis:

1. Necrosis is expressed as a function of total area so you need to circle the entire section using the polygon tool in the upper tool bar. Once you have circled the entire image you

can “M” to measure the image’s area. Copy this area into the total area section in the spread sheet. NOTE: if there are any large holes in the image make sure you circle those so you can subtract them from total area. Its easiest to analyze this image without a calibration (ie the one you use in CSA/MFD) so the area that use measure is just pixels. Remember we normalize area of necrosis to total area, so it is expressed as a percentage.

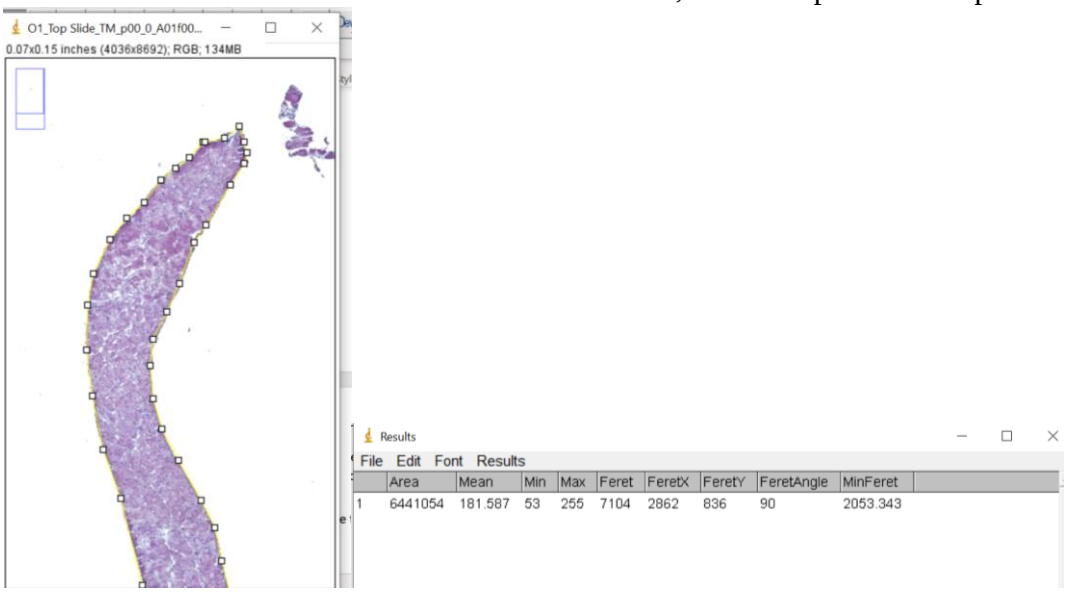

2. Going through the entire section circle areas of necrosis. This is measured as areas of fibres with fragmented sarcoplasm and/or areas of inflammatory cells (accumulations of mononuclear cells). Dystrophic tissue also has areas of calcification (darkly stained aggregates) so depending on if you are analyzing “unhealthy tissue” or necrotic tissue you may need to include this area. To analyze only necrotic tissue do not include calcified tissue.

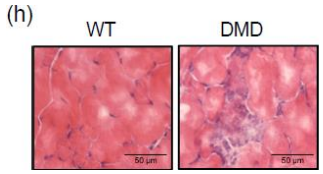

3. When you have circled a necrotic region, click “t” to add this area to your ROI manager. In ROI manager make sure the “show all” box is clicked (it will keep track of all the areas your have circled). Continue circling necrotic regions and clicking “t” to mark them. Once you have all necrotic regions circled you can highlight all regions in ROI manager and click measure.

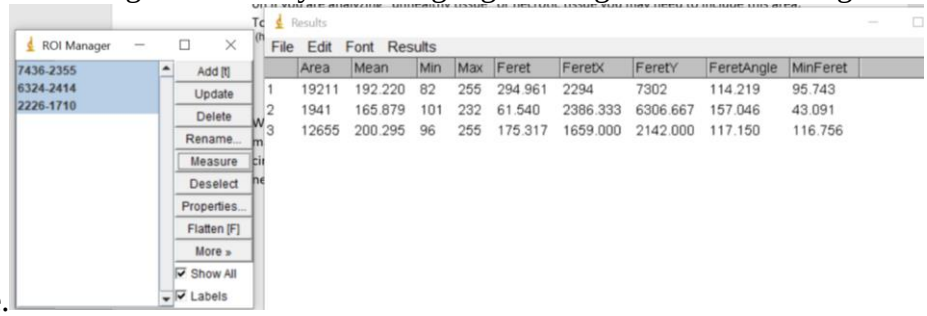

4. Copy all the areas into the spreadsheet. In the example below you can see that the holes are subtracted from total area (first number) by adding a minus sign on top. The total ROW at the bottom is just the sum of the cells above it.

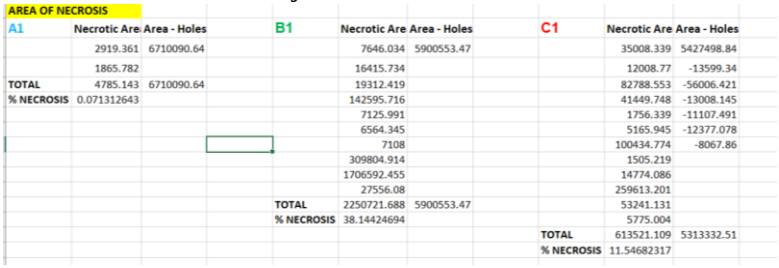

AREA OF NECROSIS									
A1	Necrotic Are	Area - Holes		B1	Necrotic Are	Area - Holes		C1	Necrotic Are	Area - Holes
	2919.361	6710090.64			7646.034	5900553.47			35008.339	5427498.84
	1865.782				16415.734				12008.77	-13599.34
TOTAL	4785.143	6710090.64			19312.419				82788.553	-56006.421
% NECROSIS	0.071312643				142595.716				41449.748	-13008.145
					7125.991				1756.339	-11107.491
					6564.345				5165.945	-12377.078
					7108				100434.774	-8067.86
					309804.914				1505.219	
					1706592.455				14774.086	
					27556.08				259613.201	
				TOTAL	2250721.688	5900553.47			53241.131	
				% NECROSIS	38.14424694				5775.004	
								TOTAL	613521.109	5313332.51
								% NECROSIS	11.54682317	

C3 Immunofluorescent Detection of Myosin Heavy Chain

Immunofluorescence Fiber Typing Illustrated Protocol

Summary Report:

Immunofluorescence allows detection of multiple antigens of interest on a single section, as long as the 1˚ antibodies are of differing immunoglobulin isotype and we have appropriately conjugated 2˚ antibodies that fluoresce at different colours. We can therefore incubate sections with a cocktail of up to 3 different antibodies simultaneously (1 of each isotype: cannot do 2 green or 2 reds at the same time).

Rat and mouse muscle sections can be adequately fiber-typed using a cocktail of antibodies against MHCl, MHClla, and MHCllb (BA-F8, SC-71, and BF-F3). In this way, type I fibers are blue, type I/IIA are blue/green, type IIA are green, type IIA/IIX are faintly green, type IIX are blank, type IIX/IIB are faintly red, and type IIB are red. To confirm these type IIX fibers, a serial section is stained for MHClla and MHCllx (SC-71 and 6H1).

For human tissue, the MHClla antibody SC-71 shows cross-reactivity with IIX fibers. In order to confirm these fibers as pure IIX and not IIA/IIX, sections are incubated with “not llx” antibody BF-35.

1˚Antibody Dilutions:

Mouse tissue sections: (1-hour incubation for each individually or when used as a cocktail.)

MHCl (BA-F8) @ 1:25 – IgG2b (@ 1:1000): **blue**

MHClla (SC-71) @ 1:500 – IgG1 (@ 1: 1000): **green**

MHCllb (BF-F3) @ 1:50 – IgM (@ 1: 1000): **red**

MHCllx (6H1) @ 1:100 – IgM (@ 1: 1000): **red**

“not llx” (BF-35) @ 1:200 – IgG1(@ 1: 1000): **green**

Staining Protocol:

All section/slide incubations for this procedure are done at room temperature (RT), on the shaker (220rpm), and with 50-100µL of solution (only large sections/areas require 100µL). Make sure slides are as flat/level as possible when they are in the incubation container. Also, when blotting slides, even though it is important to remove as much of the solution as possible, the Kimwipes will leave fabric fibers on the sections which show up very brightly blue on the microscope. So, avoid touching the pap pen area with the Kimwipe. Finally, make up antibody dilutions immediately before they are applied.

1. Before beginning, determine the number of slides you will be staining and calculate how much blocking solution will need to be made using the sample calculation below:

eg.

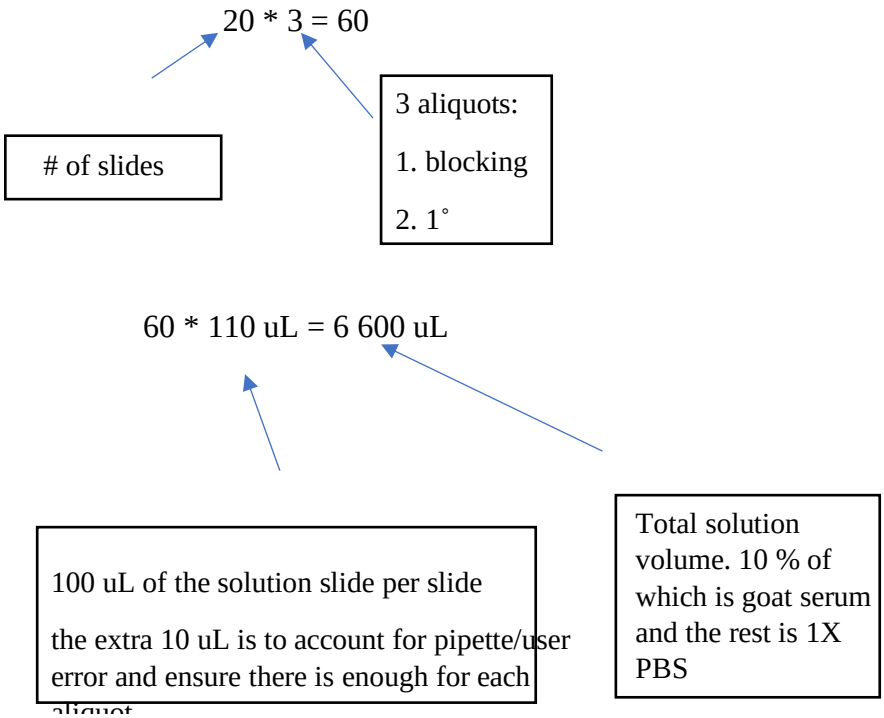

660 uL GS + 5 940 uL 1X PBS = 6 600 uL

2. Remove slides from -80°C freezer and allow to air dry slides for 5 – 10 minutes at room temperature

NOTE: if there is any residual moisture, remove with a kim wipe but be careful not to wipe away muscle section

NOTE: outline sections with a sharpie if this makes it easier to visualize the sections

3. Place a moist paper towel on the bottom of the tray and cover it with parafilm, place dry slides on top of the parafilm

NOTE: this is used to prevent the slides from drying out during the overnight incubation

4. Make the blocking solution and aliquot the blocking solution while the slides are thawing

NOTE: a clear 1.5 mL Eppendorf tube can be used for the blocking and 1˚ aliquots, however, a solid black 1.5 mL Eppendorf tube must be used for the 2˚ aliquot because it is light sensitive

5. Using a 100 uL pipette, add 100 uL of blocking solution to each slide (add a drop to each section and then carefully connect them). Incubate sections for 1 hour while shaking

NOTE: be careful to NOT touch the tip of the pipette to the section as this will compromise the section

6. Determine the volumes needed to make up the 1˚ working solution. Do not make up the solution in advance, do so prior to the end of the incubation period.

7. Shake off blocking and add 1˚ immediately. Incubate slides in 1˚ antibodies appropriately diluted in blocking solution **overnight** at room temperature while shaking.

NOTE: give the stock antibody tubes a quick shake/inversion before pipetting out of them.

8. Place slides back to back and wash slides 3 x 5 minutes in a Columbia jar with 1X PBS

NOTE: wrap tinfoil around the jars to protect from light

9. Blot dry slides. Incubate sections in appropriate 2˚ antibodies diluted 1:500 in blocking solution for 1 hour at room temperature in the dark.

NOTE: precipitate forms in the stock tubes which show up as bright spots on the microscope; centrifuge for 15 seconds before pipetting out of stock tubes. Ensure as little light as possible makes contact with the 2˚ antibodies and sections from this point

10. Place slides back to back and wash slides 3 x 5 minutes in a Columbia jar with 1X PBS

NOTE: wrap tinfoil around the jars to protect from light

11. Blot dry slides. Apply 15µL of Prolong to each slide and mount with a #1 coverslip

NOTE: cut the tip of the pipette off, will make it easier to pipette the Prolong

NOTE: perform this step in the microscope room in almost total darkness

NOTE: the coverslip can be pressed gently to remove bubbles, but do not apply pressure direction above sections, they will squish.

12. Tack the corners of the coverslip down with nail polish and place in a labeled, light-proof slide box.

13. Slides can be imaged after the nail polish has dried (5 to 10 minutes), but next day imaging seems to work better as the Prolong is allowed to set

NOTE: Slides should be imaged no longer than 2 days after staining.

D1 RNA Isolation

RNA Extraction Protocol

This applies for animal tissue

Reagents:

Procedure:

1. Add 4 volumes (80 mL) of 95-100% ethanol to the low stringency wash solution before INITIAL use. It is provided as a 5x concentrate.
2. Reconstitute the DNase I by adding 250 uL 10 mM Tris pH 7.5 and mix by pipetting up and down. You can make a 1M Tris-HCl stock and dilute down with Molecular grade water.
3. Keep samples under liquid nitrogen and record each weight.
4. Place samples in sterile 2 mL Eppendorf tubes provided in Aurum Extraction kit from Bio-Rad.
5. Clean all pipettes, tip boxes and garabe containers with RNAse off spray. Clean gloved hands with RNAse off as well. This will help with preventing RNA degradation.
6. In the fume hood, add 1 mL Trizol reagent to each tube.
7. Homogenize for 10 seconds at speed 3, or until fully liquefied. Homogenize for another 10 seconds if necessary.** use bladed homogenizer from Ceddia lab or equivalent system.
8. Centrifuge the samples at 12,000xg for 10 minutes at 4°C.
9. Transfer supernatant to new 1.5 mL tubes and incubate for 5 minutes at room temperature.
10. Add 200uL chloroform to each tube and shake vigorously (by hand) for 15 seconds. Samples will become cloudy,
11. Incubate for 15 minutes at room temperature.
12. Centrifuge the samples at 12,000xg for 15 minutes at 4°C. Sample will separate into 3 layers.

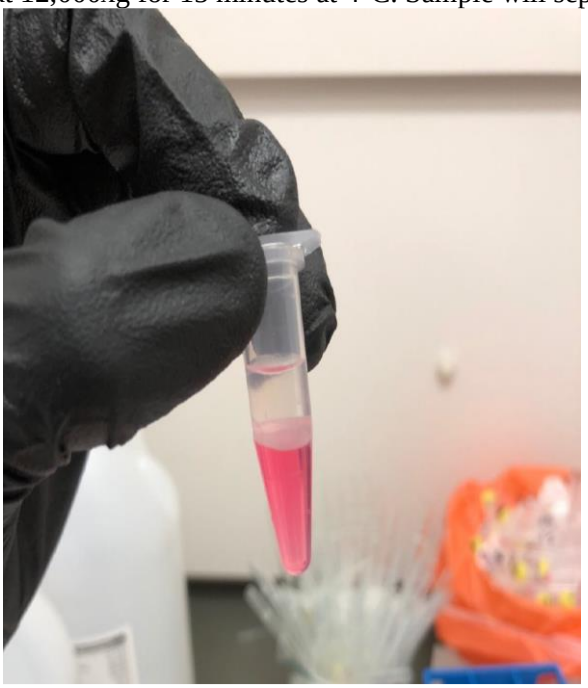

13. Transfer only the clear upper phase to a new 1.5 mL Eppendorf tube (do not take up middle or bottom pink layers).
14. Add 600 uL isopropanol into each tube and mix by hand (invert 15 times).

15. Transfer 700 uL of each sample into an RNA binding column and centrifuge at 12,000xg for 1 minute.
16. Discard the flow-through and pat the bottom of the column dry using a kimwipe.
17. Transfer any remaining sample into the binding column and centrifuge again at 12,000xg for 1 minute. Discard flow through and pat bottom of column dry again.
18. Add 700uL low stringency wash solution from Aurum RNA isolation Kit to each RNA binding column.
19. Centrifuge for 30 seconds (12,000Xg) and discard the flow through.
20. Turn on heat block for elution buffer. Allow to come to temperature before adding in buffer. Heat buffer to 75°C for 3 minutes before use. 50uL per sample plus additional
21. For each RNA binding column used, mix 5 uL of reconstituted DNase I with 75 uL of DNase dilution solution in a 1.5 mL Eppendorf tube. (Multiply by number of RNA binding columns for total volumes).
22. Add 80 uL of the diluted DNase I solution to the membrane stack of each column and incubate for 25 minutes at room temperature.
23. Add 700 uL of high stringency wash solution to each RNA binding column and centrifuge for 30 seconds. Discard the flow through.
24. Add 700 uL of low stringency wash solution to each RNA binding column and centrifuge for 30 seconds. Discard the flow through.
25. Centrifuge again for 2 minutes to remove residual wash solution and discard the flow through.
26. Transfer RNA binding column to a new 1.5 mL capped Eppendorf tube.
27. Add 25 uL of the heated elution solution (refer to step 19) to each RNA binding column and let sit for 1 minute.
28. Centrifuge for 2 minutes. DO NOT discard the flow through.
29. Repeat steps 26-27.

All RNA will be collected in the capped 1.5 mL Eppendorf tube, store at -80°C after using the nanodrop

E1 Glutathione

Buffers:

- **TRIS-BSA:** homogenization buffer with Trizma Base + Boric Acid/Serine/Acivicin to inhibit γ-glutamyltranspeptidase from metabolizing GSH/GSSG.
    - 200mL HPLC grade water
    - 50mM Trizma Base: 1.212g -- (MW=121.14g)
    - 20mM Boric Acid: 0.248g – (MW=61.83g)
    - 2mM L-serine: 0.042g – (MW=105.69g)
    - 20uM Acivicin: (MW=178.57)
    - Acivicin inhibits y-glutamyltranspeptidase, a protein bound to the cell membrane which catabolizes glutathione upon contact
    - pH to 8 with HCL
- DAY OF:
    - Add 25ul 0.2M NEM for every 1ml TRIS-BSA fresh day of use (some suggest NEM is light sensitive, freeze sensitive, not sure if this is true or not, but adding it same day allows for to decide whether you would want to or not add NEM, only time you wouldn't add NEM is if you wanted to measure total glutathione)
    - NEM irreversibly binds to GSH creating a GS-NEM conjugate and inhibits glutathione reductase preventing the auto-oxidation GSH to GSSG

Sample preparation:

- Make up 6 tubes:
    - Tube1 for homogenate/lysis
    - Tube2 for protein assay
        - 5ul homogenate into 45ul buffer/RIPA buffer for cells
        - Poke hole in top of tube
    - Tube3 with TCA
        - 7ul TCA into tube
    - Tube4 PCA
        - 70ul PCA into tube
    - Tube5 labeled GSH
        - Poke hole in top of tube
    - Tube6 labeled GSSG
        - 500ul 0.5M NaOH
- For muscle:
    - Homogenize tissue in TRIS-BSAN at a 1mg-10ul ratio, leave on ice until all samples (I usually do about 10 samples at a time, do samples in random order).
        - Try and get at least 145ul final volume, otherwise need to adjust volumes of TCA and PCA
    - Spin samples at 800g for 10 minutes at 4 degrees
    - Add supernatant to tube 1
- For Cells:
    - Wash cells in PBS-NEM (PBS with 0.5mM NEM – 25ul 0.2M NEM into 10ml PBS)
    - Trypsinize cells, re-suspend in media-NEM (2mM NEM in media)
    - spin at ~1000g for 5 minutes at 4^{o}C
    - Wash cells with PBS-NEM
    - spin at ~1000g for 5 minutes at 4^{o}C
    - aspirate off PBS-NEM carefully, re-suspend in ~155ul TRIS-BSAN

    - Add to tube 1
- Now have cells or muscle homogenate in tube 1
- Take from tube 1:
    - 5ul tube 1 -> tube 2 (protein tube- has 45uL of buffer in it)
        - Freeze in liquid nitrogen
    - 70ul tube 1 -> tube 3 (TCA tube, for GSH)
        - Put onto rocker
    - 70ul tube 1 -> tube 4 (PCA tube, for GSSG)
        - Put onto rocker
    - Vortex tubes 3 and 4 then leave on rocker while working on other samples
- Spin TCA and PCA tubes at 20,000g for 5minutes at 4^{o}C
- Carefully take tubes out of centrifuge, be careful not to dislodge pellet
- From tube 3: Take off supernatant, and transfer to tube 5 (GSH tube)
- From tube 4: take 100ul of tube 4 -> tube 6 (GSSG tube- already has 500uL of 0.5M NAOH)
- Freeze

Determine protein from samples using tube 2 (protein tube)

GSH

Mobile phase solvents

- **GSH mobile phase**
    - Solvent A: 0.25% Glacial Acetic Acid in HPLC grade water
        - 2.5mL glacial acetic acid into 997.5mL water
            - Or 1.25ml glacial acetic acid into 498.75mL water
        - pH to 3.1 by adding in a couple drops of 2M NaOH to bring pH up or glacial acetic acid to bring pH down
        - **Prepare fresh every day**
    - Solvent B: 100% Acetonitrile

GSH Standard

- Every day, run a 4 point standard
- 250uM GSH, 62.5uM GSH, 31.25uM GSH, 15.6uM GSH
- Step 1: Make 50mM GSH in TRIS-BSAN (MW= 307.32g/mol→ 15.3mg in 1ml)
- Step 2: Dilute 50mM GSH -> 5mM GSH in TRIS-BSAN (50uL into 450uL of TRIS-BSAN)
- Step 3: Dilute 5mM GSH -> 0.5mM GSH in TRIS-BSAN (50uL into 450uL of TRIS-BSAN)
- Step 4: Do serial dilutions from 0.5mM (500uM GSH)
    - 500uM GSH -> 250uM GSH -> 125uM GSH -> 62.5uM GSH -> 31.25uM GSH -> 15.6uM GSH (50uL into 50uL of TRIS-BSAN)
- Take 70ul of 250uM GSH, 62.5uM GSH, 31.25uM GSH, 15.6uM GSH tubes, and transfer to new tubes with 7ul TCA (this is to be consistent with treatments of the samples)
- Transfer GSH-TCA tube to HPLC vial, ready to load (label the outside of HPLC vial

GSH determination (UV)

- GSH flow rate at 1.25 ml/min (new HPLC down to 1.05ml/min)
- Sample detected using VWD (UV detector) detector (on HPLC stack) at 265nm
- 94% Mobile phase A, 6% acetonitrile
    - Protocol name on HPLC is TurnbullGSH
- Take GSH tube, transfer total volume into HPLC vial.
- Have machine insert 10ul of sample into machine
    - GSH elutes as two peaks right before NEM spike
        - No idea why is elutes as two peaks, cant find answer (yet) but is reported as common – I think it is likely due to some of the amino acid residues being chimeric (maybe?)
        - Found answer: it is because the configuration of GSH (3 amino acids) can be built in two ways depending on the specific amino acid configuration, I always use 2nd peak because 1st peak is sometimes influenced by other compounds depending on the tissue being analyzed

Day of checklist:

- Make up TRIS-BSAN
    - Thaw 0.2M NEM stock from freezer, add 25ul NEM per 1ml TRIS-BSA
- Make up mobile phase
- Make up standard curve
    - Transfer tubes into HPLC Vials

GSSG

Mobile phase solvents

- **GSSG mobile phase**
  Solvent A: 25mM Na_2HPO_4 in HPLC grade water
  - Make 425ml
    - pH to 6.0 using phosphoric acid
  - Add 75ml MeOH to get final 15% methanol mobile phase

GSSG Standard

- Every day, run a 4 point standard
- 10uM GSSG, 2.5uM GSSG, 1.25uM GSSG, 0.625uM GSSG, 0uM GSSG
- Step 1: Make up 20mM GSSG in TRIS-BSAN
- Step 2: Dilute 20mM GSSG -> 2mM GSSG in TRIS-BSAN
- Step 3: Dilute 2mM GSSG -> 0.2mM GSSG in TRIS-BSAN
- Step 4: Dilute 0.2mM GSSG -> 20uM GSSG in TRIS-BSAN
- Step 5: Do serial dilutions starting from 20uM GSSG
    - 20uM GSSG -> 10uM GSSG -> 5uM GSSG -> 2.5uM GSSG -> 1.25uM GSSG -> 0.625uM GSSG.
- Take 100uL from GSSG standards and transfer to new tube with 500ul 0.5M NaOH
- Add in 37.5ul of 0.1% OPA-MeOH (our fluorophore, which is stored in -20^{o}C freezer)
- Incubate standards in the dark for at least 15 minutes

GSSG determination (fluorescent)

- Excitation/Emission 350/420nm
- Flow rate at 0.5 ml/min
- Sample elutes as a single peak
- Injection volume: 50ul
- Protocol is set up as TurnbullGSSG
- Take tube 6 out of freezer
- When thawed, add in 37.5ul of 0.1% OPA (our fluorophore, which is stored in -20^{o}C freezer)
- Incubate samples in the dark for at least 15 minutes
- After incubation, transfer to HPLC vial, ready for run.

Day of checklist:

- Make up TRIS-BSAN
    - Thaw 0.2M NEM stock from freezer, add 25ul NEM per 1ml TRIS-BSA
- Make up mobile phase
- Make up standard curve
- Incubate with OPA for 15 minutes before transfer tubes to HPLC vials

F Western Blotting and Redox Status

F1 Western Blotting

WESTERN BLOTTING PROTOCOL

CASTING A GEL
**** make sure you have 1.5mm Backplates**

1. In 50mL falcon tubes make running gel and stacking gel (1 column makes 2 gels)
   ***DO NOT ADD TEMED UNTIL READY TO LOAD**
   *HINT: if polymerization is slow check the age of the APS
2. Take 1 short plate and one spacer plate and clean both sides of glass with methanol and kimwipe
3. Place clean short plate on top of spacer place and place both in mounting apparatus, ensuring the edge of the plates are lined up against the bench top
4. Place plates in apparatus on foam piece in gel stand (press down gently to ensure firm seal)
5. Place 3 transfer pipettes and falcon tube with methanol close to gel stand
6. Add TEMED to running gel and invert falcon tube 1-2 times (TEMED will polymerize the gels) (or mix with 5mL pipette by drawing up and down very slowly)
7. Using transfer pipette, fill space between glass plates with running gel until solution reaches the top of the green doors
8. Using new transfer pipette add methanol to top of plate to create an even line along the top of the gel removing any bubbles
9. Let sit until remaining running gel has hardened in the falcon tube
10. Once gel has set, invert gel to remove any excess methanol (allow to air dry while you prepare stacking gel.
11. Add TEMED to stacking gel and invert 1-2 times
12. Using transfer pipette, add stacking gel to top of glass plates, use methanol transfer pipette to remove any bubbles
13. Add comb to top of gel and allow to set
    **At this point gels can be stored overnight for use the <u>NEXT DAY</u> but since gels polymerize quickly its easiest to make gels the day off

RUNNING

1. Prepare diluted samples by combining sample, water and Laemmeli's buffer + 2-mercaptoehtanol (**100 µl 2-mer: 900 µl Lam**)
    a. **Example of dilution to load 50µg protein at a concentration of 1µg/ µl**

Sample	Corr Prot (ug/ul)	Aliquot (ug)	Sample (ul)	H20	4X Laem (1:9 2-Mercap:Laemmeli)	Vol for 1 Well
-						
EXAMPLE1	**4.599**	50	**10.9**	26.6	12.5	50

2. Boil samples at 95 °C for 5 minutes*** DEPENDS ON THE PROTEIN DO NOT BOIL FOR OXPHOS
3. Spin down samples for 5 seconds on tabletop centrifuge to bring volume down
4. Make 1X running buffer in 1000mL graduated cylinder (make double if running 4 gels)
5. Remove combs from gels in biorad dish filled with running buffer and place gels in gasket (helps to limit any gel stuck to combs from blocking lane)
6. Place gasket with gels in tank and add 1X running buffer until it fills the top of gasket and tank
7. Load wells with desired concentration of samples
8. Run for desired time (40-75 minutes) at 160mV (or desired voltage)
   ** Hint: best to write how long you run gels and at what voltage to stay consistent for protein throughout the study.

TRANSFERRING

9. Thoroughly clean "biorad" dishes with ethanol and ultrapure water and dry off with kimwipes
10. Fill 2 plastic "biorad" dishes, one with methanol (this will activate a PVDF membrane- remember to mark the dish) and one with transfer buffer (this will acclimatize membrane)
11. Place 2 transfer packs in dish of transfer buffer and place membrane in dish of methanol (we cut one pack in half for smaller gels)
12. After 2-3 minutes place first transfer pack on bottom of transfer case
13. Place membrane in transfer buffer for 10-15 seconds
14. Place membrane on top of transfer pack ensuring no air bubbles
15. Remove short plate from gel, cut off stacking gel and place gel face down on membrane.
    ** NOTE: because the unit transfers the proteins down into the membrane it should not make difference if you place the gels up or down on the unit. Personally, I always

keep my ladder on the left when I transfer (because my first lane is always the ladder) so this just helps me keep the gel oriented when I transfer)

** HINT: Mark your membranes top right corner by cutting off the corner or cutting a notch into it. This will help you identify the top of your membrane in the event you cut off specific markers in the ladder.

16. Place second transfer pack on top of membrane
    ** HINT: if you have multiple gels on the membrane try and have a small space between gels to limit bubbles on edges of gels.
17. Using roller, roll from one side of transfer pack to the other to remove air bubbles
18. Hold firmly down in the middle of the transfer pack and remove excess liquid
19. Put lid on transfer case and run transfer (standard setting is 1.5mm gel for 10 minutes)

DETECTION

20. Following transfer remove membrane and place in dish with blocking buffer (50% Odyssey Blocking Buffer, 50% TBS or 50% PBS made from tablets) for 1 hour, rocking at room temperature
    ** NOTE: it does not matter if this is TBS or PBS, it just needs to be a neutral solution. Because our blocking buffer is made with PBS I tend to use PBS (that is a sterile as possible- can filter this as well)
21. After 1 hour pour blocking buffer back into falcon tube (it can be reused multiple times) and add primary antibody
22. Place membrane in primary in fridge overnight, rocking (seal all openings of cassette with parafilm)
    NOTE: you might be able to do a primary incubation for 1 Hour at RT but you should test for best conditions)
23. In the morning remove primary and pour back into falcon tube (can be reused)
24. Add TBST to dish and complete 3x5 minute TBST washes rocking at room temperature.
25. Add corresponding secondary antibody and leave rocking at room temperature for 1 hour
26. Remove secondary and place back in falcon tube (can be reused)
27. Complete 3 more 3x5 minute TBST washes
28. Detect using LiCOR Infrared Imager (in LBS 4th Floor – Mike Scheid's Lab)
    a. ***84 uM, on membrane setting, correct for length & height of membrane***
    b. ***Place facing down on glass, Top left hand corner will align on bottom left corner of machine (will see specific start point on ruler on glass)***

WESTERN BLOTTING – PREPARATION OF BUFFERS

10 X Running Buffer:

	500 ml	**1 L**	**2 L**
Tris	15 g	30 g	60 g
Glycine	72 g	144 g	288 g
SDS	5 g	10 g	20 g

1 X Running Buffer: 10 X Running buffer 100 ml
dH_2O 900 ml

---

1 X Western Transfer Buffer: 5 X BIORAD Transfer buffer 200 ml
Ethanol 200 ml
dH_2O 600 ml

---

10 X TBS (Tris Buffered Saline):

	500 ml	**1 L**
Tris	12.1 g	24.2 g
NaCl	40 g	80 g
Adjust to pH 7.6 with HCl		

1 X TBST:

	1 L	**2 L**
10 X TBS	100 ml	200 ml
dH_2O	900 ml	1800 ml
Tween 20	1ml	2 ml

Note: Ensure solution is stirring when adding Tween

Wet Transfer Buffer

		1L
Tris	Tris	
Glycine	190mM	
Methanol	20%	

NOTE: Check pH to 8.3

Can reduce methanol to 10%

For proteins larger than 80kDa use SDS to a final concentration of 0.1%

Gel Preparation:

Blocking

- Blocking Buffer (50%)
- PBS (50%)

Primary

	Stacking	**Running**				
		5%	**6%**	**8%**	**10%**	**12%**
dH_2O	6.8 ml	11.4	10.6 ml	9.4 ml	8 ml	6.7 ml
1.5M Tris-Base, pH 8.8 (made in house)	***	5 ml	5 ml	5 ml	5 ml	5 ml
1M Tris-Base, pH 6.8 (made in house)	1.25 ml	***	***	***	***	***
30 % Acrylamide %T= 30%, %C= 2.7%) (Cat # : 1610158)	1.70 ml	3.4 ml	4 ml	5.3 ml	6.7 ml	8 ml
10 % SDS	100 µl	200 µl	200 µl	200 µl	200 µl	200 µl
10 % APS	100 µl	200 µl	200 µl	200 µl	200 µl	200 µl
Temed	**20 µl**	**20 µl**	**20 µl**	**20 µl**	**20 µl**	**20 µl**

- Blocking Buffer
- .1% Tween
- .01% SDS

Secondary

- Blocking Buffer
- .1% Tween
- .01% SDS

F2 Redox Status of Specific Protein

Evaluating Redox Status of Specific Protein

Optimized for IP of MtCK

Lysis Buffer: COBLEY LYSIS

For 200mL solution at pH 7.5

Reagent	Amount	Concentration	Molecular Weight
HEPES pH 7.5	1.906g	40mM	238.3
NaCl	1.403g	120mM	58.44
EDTA Na_2	74.4mg	1mM	372.2

$NaHP_2O_7$ ●10 H_2O pyrophosphate	892mg	10mM	446.1
B-glycerophosphate	432mg	10mM	216.04
NaF	420mg	50mM	41.99
CHAPS	0.6g	0.30%	

Stock Solutions

	Catalog number	**Molecular Weight (g/mole)**	**Amount (g)**	**Volume of Solvent**
IR Dye – 8.4mM Licor, 929-80020	1191 0.5mg	DMSO	50ul	*5ul aliquots
	Dilute to 60uM Stock – freeze 60uM stock, can be reused several times 1uL of 8.4mM Dye into 140uL DMSO			
H_2O_2 – 0.1M Fresh	Sigma-95321-100ml	34.01	113ul (of 3%)	WATER 887ul
NaI – 100% Fresh	Sigma-217301-100G	185.92	0.1g	WATER 100ul
TCEP – 0.1M Fresh	Fisher - 20490	286.65	1mg	WATER 34.9ul

Tissue Homogenization

N.B: The IRDye-Maleimide should be protected from light at all time

Day 1

1. Weigh **2x 60 mg** of tissue (one will be labeled and the other one will be used for controls)
2. Place 60mg of tissue into 0.6 ml ice cold Cobley buffer + protease inhibitors (standard homogenization protocol) and homogenize for 3x10seconds
3. Spin at 800g for 10 minutes (4°C)
4. Transfer supernatant to new tube
5. Determine protein concentration using standard BCA protein assay kit
6. Determine exact volume of lysate and calculate total protein in sample
   **Use prepared excel sheet*
7. Add 100nM dye/200ug protein (60uM stock)
8. Mix gently on nutator overnight at 4°C

Day 2

9. Remove excess Dye by passing the lysate over 2 successive 2ml desalting Zeba columns. Use the same column twice.
   a. Remove bottom closure and place column in 15ml Eppendorf tube
   b. Unscrew red cap
   c. Spin down for 2 minutes at 1000g to remove storage

    d. Mark with sharpie the side of the column that has resin slanted upwards – always place this side facing outwards in the centrifuge
    e. Add 1ml of water to column and spin down again for 2min at 1000g
    f. Place zeba column in new 15ml Eppendorf
    g. Slowly load up to 700ul of sample onto filter bed
    h. Spin down for 2 minutes at 1000g
10. Collect the cleaned sample
11. Determine protein concentration using BCA
12. Proceed to the IP

Immunoprecipitation Protocol – *based on BioRad SureBeads Protocol*

1. Vortex SureBeads in their solution and transfer 100ul (1mg of beads) of SureBeads to 1.5ml tubes – 1 tube/sample
2. Magnetize beads and aspirate off supernatant using pipette (aspirator is too aggressive and sucks up beads)
3. Wash with 1ml PBS-T (PBS + 0.1% Tween 20)
    a. Add PBS-T to Eppendorf running liquid overtop of beads
    b. Rotate Eppendorf 180 degrees, let bead sit, rotate another 180 degrees and allow beads to gather
4. Magnetize beads and aspirate off supernatant (always using pipette)
5. Repeat steps 3 and 4 three times
6. Remove tubes from magnet (should have no liquid) and add 200-volume of antibody ul PBS-T over beads
7. Add desired concentration of antibody (usually between 1 and 10ug) and vortex well
    a. Total volume in tube should be 200ul
8. Rotate for 10 minutes at room temperature
9. Spin down to remove liquid from the cap
10. Wash with 1ml PBS-T (PBS + 0.1% Tween 20)
    a. Add PBS to Eppendorf running liquid overtop of beads
    b. Rotate Eppendorf 180 degrees, let bead sit, rotate another 180 degrees and allow bead to gather
11. Magnetize beads and aspirate off supernatant
12. Repeat steps 10 and 11 three times
13. Remove tube from magnet (beads should have no liquid in tube)
14. Add desired volume/concentration of lysate
15. Rotate for overnight at room temperature
16. Spin down to remove liquid from lid
17. Magnetize beads and keep supernatant as unbound sample
18. Wash with 1ml PBS-T (PBS + 0.1% Tween 20)
    a. Add PBS to Eppendorf running liquid overtop of beads
    b. Rotate Eppendorf 180 degrees, let bead sit, rotate another 180 degrees and allow bead to gather
19. Magnetize beads and aspirate off supernatant
20. Repeat steps 18 and 19 three times
    a. Before last magnetization, transfer the re-suspended beads to a new tube
21. Spin down tube for several seconds
22. Magnetize beads and aspirate residual buffer from the tubes

Elution:

1. Add 20mM Glycine (pH 2.0) – 20ul and incubate for 5 minutes at room temperature
2. Magnetize beads and move eluent to a new vial
3. Neutralize eluent with 2ul (10% of total volume) with 1M Phosphate Buffer, pH 7.4
   ** This elution strategy is used for IR Dye to avoid boiling and subsequent denaturing of proteins. If not using IR dye, standard Laemmli buffer plus boiling can be used to elute protein of interest
4. Proceed to Western Blot Sample Preparation – do not boil
   a. 22ul total sample +
   b. 10ul of 4x Sample Buffer (1/10 2-Mercap, 9/10 4x Laemellis) +
   c. 8ul of H2O
5. Spin samples down to remove bubbles
6. Load 35ul of sample into lane

Controls

Day 1

1. Homogenize in CHAPS buffer as above for samples.
2. Run samples through zeba desalting column twice to remove any glutathione
   a. Use 0.5ml zeba column to reduce protein loss that occurs when sample is spun through the large 2ml column
   b. Remove bottom closure and place column in 1.5ml Eppendorf tube
   c. Unscrew red cap
   d. Spin down for 1 minute at 1500g to remove storage
   e. Mark with sharpie the side of the column that has resin slanted upwards – always place this side facing outwards in the centrifuge
   f. Place zeba column in new 1.5ml Eppendorf
   g. Slowly load up to 130ul of sample onto filter bed
   h. Spin down for 2 minutes at 1500g
3. After spin, run protein assay with standard BCA kit
4. Divide sample into 3 aliquots of 4.167ug/ul diluted in CHAPS (total volume 200ul)
   a. Use prepared excel sheet for calculations
5. Add 5mM H_2O_2 + 0.5% NaI to oxidized sample – **this sample should turn yellow! Make sure you added H2O2 and NaI at the same time!**
   a. 5mM H_2O_2 = 10ul of 0.1M
   b. 0.5% NaI = 1ul of 100%
6. Add 1mM TCEP to control sample
   a. 1mM TCEP = 2ul of 0.1M
7. Incubate at room temperature on nutator for 5 minutes along with non-treated control
8. Spin all samples through zeba column to remove excess reagent - twice
9. Run Protein Assay using reducing agent compatible BCA kit
10. Determine volume of remaining lysates – calculate total protein in sample
11. Add 100nM/200ug protein dye (60uM Stock)
12. Mix gently on nutator overnight at 4°C

Day 2

13. Remove excess Dye by passing the sample over 2 consecutive desalting Zeba columns (0.5mL columns). Use same column twice.
14. Collect the cleaned sample
15. Determine protein content using Reducing Agent Compatible BCA protein assay kit
16. Prepare samples for western blot – will need 2.5ug Protein

Western Sample Preparation

** Do not boil

**1/10 2-Mercaptoethanol; 9/10 4x Laemellis Buffer

G Permeabilized Fibre Bundles & Bioenergetic Protocols

G1 Buffers

BIOPS BUFFER (Extracellular)

Chemical	Stock Solution	Molecular Weight	Final Concentration	Addition to *2 Litre* Final Volume
CaK_2EGTA*	100mM		2.77mM	55.4mL
K_2EGTA*	100mM		7.23mM	144.6mL
Na_2ATP		555.1	5.77mM	6.41g
$MgCl_2 \cdot 6H_2O$		203.3	6.56mM	2.67g
Taurine		125.1	20mM	5.02g
Na_2Phosphocreatine		327.14	15mM	9.81g
Imidazole		68.1	20mM	2.72g
Dithiothreitol (DTT)		154.2	0.5mM	0.154g
MES Hydrate		195.2	50mM	19.52g

*__**ALWAYS**__ double check molecular weights for supplier-specific chemicals (n=m/M.W.)

BIOPS contains the following ion concentrations		**EXTRACELLULAR RANGE**
Ca^{2+} free	0.1uM	Rat: 7.6mM Mouse: 1.3mM
Mg^{2+} free	1mM	
Na^+	41mM	Human: 133-143mM
K^+	20mM	Human: 4.5mM
Cl^-	13mM	Rat: 160mM Mouse: 95-120mM
MgATP	5mM	
Ionic Strength	160mM	
Osmolality	295 mOsm	

*Ionic strength is the sum of all ions
*Buffers do not perfectly reflect extracellular conditions
*Species-specific extracellular ranges exist

*Ranges are expressed as mmol/L (refer to ion concentration summary chart)

CaK_2EGTA: Dissolve 2.002g of $CaCO_3$ in 100mM hot (80°C) solution of EGTA (7.608g of EGTA in 200mL ddH_2O). Add 2.3g of KOH and adjust pH to 7.0 using KOH. Freeze unused portions.

K_2EGTA: Dissolve 7.608g EGTA and 2.3g KOH into 200mL ddH_2O. Adjust pH to 7.0 using KOH. Freeze unused portions.

To make BIOPS:

1. Add approximately 1500mL of ddH_2O to 2000mL beaker
2. While constantly stirring add stock solutions of CaK_2EGTA and K_2EGTA
3. Weigh and add all powder chemicals
4. Adjust pH to 7.1 using KOH pellets
5. Using graduated cylinder, bring total volume to 2000mL
6. Filter and then aliquot into 50mL falcon tubes
7. Freeze falcon tubes

MiRO BUFFER (Intracellular)

Chemical	Stock Solution	Molecular Weight	Final Concentration	Addition to *2 Litre* Final Volume
EGTA		380.4	0.5mM	0.38g
$MgCl_2 \cdot 6H_2O$		203.3	3mM	1.22g
K-Lactobionate*	0.5M	358.3 free acid	60mM	240mL
Taurine		125.1	20mM	5.02g
KH_2PO_4		136.1	10mM	2.72g
HEPES		238.3	20mM	9.54g
Sucrose		342.3	110mM	75.3g
BSA		154.2	1g/L	2.0g

*__ALWAYS__ double check molecular weights for supplier-specific chemicals (n=m/M.W.)

MiRO contains the following ion concentrations		**INTRACELLUAR RANGE**
Ca^{2+} free	0.0uM	Human: 30nM – 60nM SR: 5.7-20mmol/L Free Ca^{2+} in SR 0.2-0.5mM Rat: 7.76-11.11 ueq/g dry wt
Mg^{2+} free	2.1mM	
Na^+	0.0mM	Human: 6-13mM Rat: 7.10-21.9mmol/L
K^+	90mM	Human: 130 – 164mmol/L Rat: 117 – 149mmol/L
Cl^-	6mM	Rat: 4.97-16.57mmol/L
PO_4^{3-}	10mM	
EGTA free	0.46mM	
Ionic Strength	95mM	
Osmolality	330 mOsm	

*Ionic strength is the sum of all ions

*Buffers do not perfectly reflect extracellular conditions

*Species-specific intracellular ranges exist
*Ranges are expressed as mmol/L (refer to ion concentration summary chart)

K-Lactobionate: Dissolve 71.6g lactobionic acid in 300mL ddH_2O, adjust pH to 7.0, adjust final volume to 400mL with ddH_2O

To make MiRO:

1. Add approximately 1500mL of ddH_2O to 2000mL beaker
2. While constantly stirring add stock solution of K-Lactobionate
3. Weigh and add all powder chemicals
4. Adjust pH to 7.1 using KOH pellets
5. Using graduated cylinder, bring total volume to 2000mL
6. Filter and then aliquot into 50mL falcon tubes
7. Freeze falcon tubes

BUFFER Z (Intracellular) USED FOR H_2O_2

Chemical	Molecular Weight	Final Concentration	Addition to *500mL* Final Volume
K-MES	233.33	105mM	12.26g
KCl	74.55	30mM	1.12g
KH_2PO_4	136.08	10mM2	0.7g
$MgCl_2 \cdot 6H_2O$	203.3	5mM	0.51g
EGTA	380.35	1mM	0.19g
BSA	154.2	5mg/mL	2.5g

*__**ALWAYS**__ double check molecular weights for supplier-specific chemicals (n=m/M.W.)

Buffer Z contains the following ion concentrations		**INTRACELLULAR RANGE**
Ca^{2+}	0.0uM	Human: 30nM – 60nM SR: 5.7-20mmol/L Free Ca^{2+} in SR 0.2-0.5mM Rat: 7.76-11.11 ueq/g dry wt
Mg^{2+} (total, not free)	5mM	
Na^{+}	0.0mM	Human: 6-13mM Rat: 7.10-21.9mmol/L
K^{+}	145mM	Human: 130 – 164mmol/L Rat: 117 – 149mmol/L
Cl^{-}	40mM	Rat: 4.97-16.57mmol/L
PO_4^{3-}	10mM	
EGTA free	1mM	

*Buffers do not perfectly reflect extracellular conditions
*Species-specific intracellular ranges exist
*Ranges are expressed as mmol/L (refer to ion concentration summary chart)

To make Buffer Z:

1. Add approximately 400mL of ddH_2O to 1000mL beaker
2. Weigh and add all powder chemicals
3. Adjust pH to 7.4 using KOH pellets
4. Using graduated cylinder, bring total volume to 500mL

5. Filter and then aliquot into 50mL falcon tubes
6. Freeze falcon tubes

G2 Permeabilized muscle fibre bundle preparation

Equipment

- Ice blocks
- Dissecting microscope
- Anti-magnetic fine tipped forceps (1 large, 1 small)
- 18mm cell culture dish
- 1.5ml tubes
- gel loading tips

Reagents

- Biops buffer
- MIR05 buffer
- saponin

Protocol

1. Prepare a Styrofoam container with ice and 5ml tubes filled with biops buffer (see section for preparation instructions)
2. Prepare 40µg/ml saponin dissolved in biops (saponin tubes)
    a. Dilute 7µL of 10mg/mL saponin into 1.5mL of biops
3. Prepare equal amounts of 1.5mL tubes 1) with 40µg/mL saponin + biops and 2) MIR05 buffer (see section for preparation instructions) (wash tubes)
4. Harvest tissue and immediately submerge into ice cold biops buffer
5. Decant tissue with biops into a 18mm dish and place on an ice block under a dissecting microscope
6. Cut all connective tissues and remove blood and fat
7. Gently begin separating fibers ~1-3mg wet weight fiber bundles
8. Place muscle bundles into saponin tubes and rock at 4°C for 30 minutes
9. Transfer permeabilized muscle fiber bundles (PmFB) to wash tubes and rock at 4°C for 15 minutes
10. PmFB are ready for bioenergetic assays
    a. See appendix for respiration experimental protocols (A4.1) and buffer preparation (A4.2-A4.3)
    b. See appendix for H2O2 emission experimental protocols (A4.4) and buffer preparation (A4.5 – 4.8)
    c. See appendix for calcium retention capacity experimental protocols (A4.7) and buffer preparation (A4.8)

G3 Sample Respiration Protocol

MOUSE QUAD- 20mM CR				
Substrate	**Event Code**	**STOCK**	**Titration Volume (µL)**	**Final Concentration in Chamber**
MiRO5 Lights Out BLEB Fibre	 F10 BLEB Fibre	20mM Cr 10 mM BLEB	 1	 5 µM
Stop stir bar, turn on lights and verify fibre is in chamber/not stuck on side wall **Hit F10 (lights out)**				
100% O_2	O		Injection	250-275 µM
Pyruvate Malate	P M	**2M** **1M**	**5** **4**	5 mM 2 mM
ADP	25 µM D	**5 mM**	**10**	25 µM
ADP	100 µM D	**50 mM**	**3**	100 µM
ADP	500 µM D	**50 mM**	**16**	500 µM
ADP	5 mM D	**500 mM**	**18**	5 mM
Cyto c	Cyto c	**4 mM**	**5**	10 µM
Succinate	20 mM S	**2M**	**20**	20 mM

G4 Reactive Oxygen Species Emission & Attenuation Protocol
** 35uM (5uL of 10.5mM Stock) in Saponin Tubes for Tubes 1 & 2

PYRUVATE & MALATE- Complex I Forward Flow

Assay Buffer	**Pre-experiment**		**Substrates**		**ADP**		**ADP**		**ADP**	
20mM Creatine	**1U/mL HRP** 2uL of 500U/mL Fibre	3 min	**10mM Pyruvate** 5uL of 1M **2mM Malate** 2uL of 1M	3 min *add ADP before slope starts to decline	**25uM** 5uL of 5mM	2min	**100uM** 1.5uL of 50mM	2min	**500uM** 0.8uL of 500uM	2min
20mM Creatine	**1U/mL HRP** 2uL of 500U/mL Fibre	3 min	**10mM Pyruvate** 5uL of 1M **2mM Malate** 2uL of 1M	3 min *add ADP before slope starts to decline	**25uM** 5uL of 5mM	2min	**100uM** 1.5uL of 50mM	2min	**500uM** 0.8uL of 500uM	2min

SUCCINAte- Complex I Reverse Flow

Assay Buffer	**Pre-experiment**		**Substrates**		**ADP**		**ADP**		**ADP**	
20mM Creatine	**1U/mL HRP** 2uL of 500U/mL Fibre	3 min	**10mM Succinate** 5uL of 2M	5 min	**25uM** 5uL of 5mM	2min	**100uM** 1.5uL of 50mM	2min	**500uM** 0.8uL of 500uM	2min
20mM Creatine	**1U/mL HRP** 2uL of 500U/mL Fibre	3 min	**10mM Succinate** 5uL of 2M	5 min	**25uM** 5uL of 5mM	2min	**100uM** 1.5uL of 50mM	2min	**500uM** 0.8uL of 500uM	2min

G5 Calcium Retention Capacity Assay

Chemical	Final Concentration	Addition to *120mL* final volume
Buffer Y (freshly made)		120mL
Creatine	20mM	0.358g
EGTA	40uM	9.6uL of 0.5M
BLEB	5uM	60uL of 10mM
Calcium Green*	1uM	400uL of 0.3mM
Tharpsigargin**	2uM	160uL of 1.5mM

CRC Assay Buffer – 900uL aliquots

* Dissolve 0.5mg CG5N in 1.398mL water

** 1mg vial, make 1mL, aliquot into 165uL stocks and freeze

Create a stock of 50mM $CaCl_2$ dissolved in water and store in 50uL aliquots in freezer

Procedure:

** cuvette on stir plate and fill with ddH2O and 10uL EGTA (0.5M Stock)

1. Harvest muscle and place in ice cold **BIOPS**
2. Separate fibres into bundles (larger than those used for respiration).
3. Permeabilize for 30 minutes in BIOPS with 30ug/mL saponin
4. WASH 1: 10 minutes in 1.5mL Buffer Y + 1mM EGTA (3uL of 0.5M)
5. Turn on fluorometer to allow lamp to heat up
6. WASH 2: 10 minutes in 1.5mL Buffer Y + 10uM BLEB (1.5uL of 10mM BLEB)
7. Aspirate out water from cuvette but DO NOT RINSE (keep cuvette lined with EGTA)
8. Select Calcium Uptake Assay Protocol on PTI Software. Make sure the following parameters are set:
    a. Excitation: 506
    b. Emission: 532
    c. Duration – 3000 seconds
    d. Slit Widths: Excitation 3nM
       Emission 3nM
    e. x-axis window: 2000 seconds
    f. y axis max and min: 200 000 and 500 000

Substrate	Stock Concentration	Addition to cuvette	Final Concentration in Cuvette
CRC Assay Buffer		300uL	
Glutamate	2M	1.5uL	10mM
Malate	1M	1.5uL	5mM
ADP	500mM	3uL	5mM
Fibre ** make sure fibre is at the bottom of cuvette attached to stir bar**			

Collect 400 second background to establish "F-Min"			
$CaCl_2$	5mM	2.5uL	8nmol
Wait 5 minutes or until steady state			
$CaCl_2$	5mM	1.25uL	12nmol (4nmol pulse)
Wait 5 minutes in between pulses and continue pulsing until pore opens			
$CaCl_2$	50mM	3uL	0.5mM Pulse (F-Max)
Wait 3 minutes before final addition, this should establish F-Max but last addition is to make sure			
$CaCl_2$	50mM	3uL	0.5mM Pulse (F-Max)

* for each addition remove cuvette from holder and ensure fibre has not been disrupted
**Make sure y axis is no more than 300 000 units or you will miss opening

After opening, remove bundle and save for freeze drying

H Caspase Activity Assay

Caspase 3, 8 and 9 Activity in Skeletal Muscle – York 2017

Chemicals:

Homogenisation buffer: 500 ml

Chemical	Molecular Weight	Concentration	Amount added
Sucrose	342.3	250 mM	42.8g
Tris	121.14	50 mM	3.03g
DTT	154.25	1 mM	0.077g
EDTA	372.24	1 mM	0.186g
$MgCl_2$	203.3	5 mM	0.51g
Glycerol		10%	50mL

pH 7.5

Incubation buffer: 100 ml

Chemical	Molecular Weight	Concentration	Amount added
HEPES	283.3	100 mM	2.38g
Sucrose		10%	10g
DTT	154.25	1 mM	0.015g

pH 7.5

Fluorescent substrates for Caspase activities:

Caspase 3: AC-DEVD-AMC (Enzo - **ALX-260-031-M001)**

1mg into 1.48 mL DMSO for 1mM Stock

Caspase 3 Inhibitor: AC-DEVD-CHO (Enzo - **ALX-260-030-M001)**

1mg into 2mL DMSO for 1mM Stock

Caspase 8: AC-IETD-AMC (Enzo - **ALX-260-042-M001)**

1mg into 1.48 mL DMSO for 1mM Stock

Caspase 8 Inhibitor: AC-IETD-CHO (Enzo - **ALX-260-043-M001)**

1mg into 2mL DMSO for 1mM Stock

Caspase 9: AC-LEHD-AMC (Enzo - **ALX-260-080-M001)**

1mg into 1.45 mL DMSO for 1mM Stock **different MW from 3 and 8

Caspase 9 Inhibitor: AC-LEHD-CHO (Enzo - **ALX-260-079-M001)**

1mg into 1.86mL DMSO for 1mM Stock

** Aliquot Substrates into 300uL, Aliquot inhibitors into 10uL. Store in black tubes at -20

Experimental procedures

Preparation of lysosome and proteasome fractions:

Homogenise muscle biopsy using tapered pestle with a muscle:homogenate ratio of 10mg:100uL.
** note homogenization is different because we do not add protease inhibitors

Centrifugation steps: (P = pellet; S = supernatant)

700×g 10 min at 4 degrees **P1** (nuclei, myofibrils)

S1 ↓

16,300×g 20 min at 4 degrees **P2** (lysosomes, mitochondria)

S2 (bound and free proteasomes)

S2: divide into 100 µl portions to be used for **CASPASE AND CALPAIN ASSAYS**

Freeze all fractions at -80ºC

Protein determination:

Protein determination is done with the BCA method **USING THE REDUCING AGENT COMPATIABLE KIT** because homogenization buffer has high [DTT] resulting in the reduction of Cu2+ to Cu1+ making you unable to determine protein concentration**.**

Pierce BCA Protein Assay Microplate Kit- reducing agent compatible (product number 23252) (From Thermofisher - Smartbuy)

Protein Assay – BCA

1. Create standards by diluting BSA in homogenization buffer
   Standards (BSA):

   0 mg/mL (buffer)

   0.0625 mg/mL

   0.125 mg/mL

   0.25 mg/mL

0.50 mg/mL

0.75mg/mL

1.00 mg/mL

2. Dilute 5 µL of each sample in 45 µL of homogenization buffer- can do this when you homogenize samples or when you run caspase assay- do this prior to the actual run of the assay

KEY CONSIDERATIONS: you need at minimum 40-45uL of sample for caspase (30 for measurement and 5uL for protein) so ensure during homogenization you have enough sample

Reducing Agent Compatible Kit

Use when buffer has high [DTT] or other reducing agent

1. Take total number of wells to be loaded and multiple x 4ul – this gives you the total volume of reconstitution buffer you will need
   EXAMPLE: full plate 96 wells x 4uL is 384uL
2. Take the total volume and /100. Round up to the nearest whole number. This tells you how many vials of compatibility agent you need.
   EXAMPLE: 384uL/100 = 3.84 ROUND TO 4
3. From the foil package, cut out the required number of vials.
   EXAMPLE: 4 vials are required
4. Poke a hole in the top of each vial using a pipette tip.
5. Add 100ul of reconstitution buffer to each vial and pipette vigorously to mix
6. Combine all vials in one Eppendorf tube and protect from light until use (must be used same day- sample in fridge stored in the dark for 8 hours)
7. Load 10ul of standards/diluted lysate samples in designated wells
8. Add 4ul of compatibility agent buffer to each well
9. Incubate plate at 37 degrees for 15 minutes (keep lid of plate on or seal with parafilm)
10. Add 186ul of mixed Solution A/Solution B (from above) (this brings volume to 200uL in each wheel)
11. Incubate plate at 37 degrees for 30 minutes
12. Read plate at 562nm on a plate reader (BCA reader).

Caspase Activity:

1. Dilute 1mM stock of each substrate into 100µM using incubation buffer – make up total volume needed for all samples plus 200µL extra (see loading table in excel)
2. Add 10uL of protein from S2 into the wells
3. Add 100 uL of diluted caspase 3 substrate to 1 well of sample
4. Repeat step 3 using Caspase 8 and Caspase 9 substrate
5. Add 3uL of Caspase 3 inhibitor to well if required
6. Repeat step 5 for Caspase 8 and 9 inhibitors
7. Read every 2 minutes for 1 hour

**Do not need to run inhibitor well for every sample, just use as a check (typically only run one additional sample with inhibitor)

Fluorometer measurements:

Prepare the fluorometer settings before adding standards, muscle extracts and substrates into the micro plates.

Temperature 37ºC; Excitation filter 360 nm; Emission filter 460 nm

Gain 80 % of max value

Read every 2 min for 1 hour

I Novel Object Recognition

Novel Object Recognition

Acclimatization

1. Place animal in open field box (40cmX 40cm X 40cm) and allow to freely move for 5 minutes each day for 4 consecutive days prior to testing
2. This should be repeated at the same time every day in relative silence
3. Sanitize the container after animal is complete

Habituation

1. Using similar sized objects to the animal, place 2 identical objects (object 1) in opposite corners of the arena
2. Place animal into container and allow to explore for 10 minutes- RECORD this session
3. Once complete, remove animal from the container and place into a neutral cage for 30 minutes
4. Sanitize the container

Testing

5. Replace one of the objects with a new (novel) object (object 2) and allow animal to explore for 10 minutes- RECORD this session
6. Once complete, put animal back into home cage

Analysis

1. Open the recordings and count the duration in which the mouse interacts with the object
2. Object exploration time is defined as the time the mouse interacted with the object, defined by sniffing or touching the object when the mouse is less than 2 cm from the object
3. Sitting or standing on the object was not included unless the mouse sniffed the object while climbing on it.
4. For the trial to be considered the animal must have interacted with the object for greater than 20 seconds.
5. Discrimination ratio (DR) was calculated as follows:

   DR = (Time (object 2) –Time (object 1))/Total time.

Important considerations

- Large disturbances (voices/talking/people walking in and out of the room) should be avoided & testing performed roughly the same time every day
- Males may have some effect on this result- so if possible, have a female researcher perform this task
- Across different animals, use different combinations of objects
- Objects should be a similar size to animals tested
- Optimization for length of testing is required.